

SYNTHESIS AND CHARACTERIZATION OF A RUTHENIUM-EDTA
DIMER BY SPECTRAL AND ELECTROCHEMICAL TECHNIQUES

Thesis by
Roger Bennett Baar

In Partial Fulfillment of the Requirements
for the Degree of
Doctor of Philosophy

California Institute of Technology
Pasadena, California

1985

(Submitted July 7, 1983)

© 1985

Roger Bennett Baar

All Rights Reserved

To my parents,
Anita and Stanley

Acknowledgements

I want to thank my advisor, Fred Anson, for his help and encouragement during the many trying moments involved in these studies. His insights enabled a truer course to be followed during the darker days of my investigations. I also want to thank the many people that I have had the fortune of meeting and knowing while at Caltech. My life is so much the richer because of them.

I would especially like to thank a few people that have offered me the most encouragement and friendship during the past few years. Two of my oldest friends, Dr. Mark Dershwitz, PhD., and Debra Ack have been a constant source of friendship and joy. Mark kept me on my toes about science, girls and stereo equipment (not necessarily in that order), and helped me to have some of the largest phone bills imaginable. Debbie has shown me what there is to know about Los Angeles and all of its varied places and people. She has also been someone I could talk with when times were tough.

During my stay at Caltech, I have come to know many people who have enriched my life. The following people have enriched my life during my stay here and I would like to thank them all: Dr. Jane Raymond, Professor Harry Gray and The Rocky Horror Picture Show, John and Sandy Padgett, Noboro Oyama, Mark Paffett, Frances Foley, Brian Willett, Rich Durand, Dan Buttry, Chi-Ming, all of my basketball and baseball cronies, and the many post-docs and the other members of the Anson group that I have had the pleasure of

meeting.

I have also been most fortunate to meet and to know Linda Nann. She has been a source of help, inspiration, and a wonderful friend during my most trying times. She has been a true friend and companion when I have needed someone the most.

Finally, I would especially like to thank Bill Gross. His generosity in allowing me to use his computer to write this thesis is greatly appreciated. In addition, the past few years of my life have been filled with many memories shared with him and his wife, Lori. One that I will particularly remember was the time we put together the ultimate "Ride of the Valkyries" off the top of Thomas during Spring finals of 1981 to the delight of the throngs of people below, as well as to anybody within one mile ear shot of the campus. I want to thank him for making my stay at Caltech one of much joy. I consider myself truly fortunate to be able to call him my friend.

Abstract

Section I

The synthesis of a ruthenium-edta dimer is described. The dimer is shown to be the one-electron oxidized product of two $[\text{Ru(III)edta(OH}_2)]^-$ monomers. The dimer was shown to contain one unpaired spin by magnetic susceptibility and esr spectroscopy indicating spin pairing between the two ruthenium metal centers. A band was detected in the near infrared that analyzed for a Class III complex indicating that the dimer is truly delocalized and that the oxidation state on each ruthenium is 3.5. The band was much narrower than predicted for a delocalized, Class II complex and its position did not exhibit any solvent dependence. The optical spectrum indicated some similarity with other formally Ru(III)-Ru(IV) dimers indicating that the formation of this type of dimer is favored regardless of the type of auxiliary ligands attached to the ruthenium.

The change in the optical spectrum upon raising the pH indicated a pKa of 10.32 for the dimer. This, taken in conjunction with the infrared, the raman and the nmr results indicated that the dimer was μ -oxo bridged at low pH and was, most likely, μ -oxo, μ -hydroxo bridged at higher pH.

When an excess of Ce(IV) was added to a solution of the dimer the catalytic evolution of dioxygen was observed. The dimer also catalyzed the disproportionation of hydrogen peroxide.

Section II describes the electrochemistry of Ru(III)edta

and the dimer. Cyclic voltammetry, polarography and rotating ring-disk electrode (RRDE) voltammetry were used to characterize the oxidation and reduction of each of the two complexes. The electrochemical oxidation of Ru₃Y produced the dimer after one Faraday per two moles of ruthenium. The catalytic evolution of dioxygen was also observed at a platinum electrode. The step-wise reduction of the dimer to produce Ru(II)edta is also described. The combined use of the RRDE with digital simulations of the mechanism of reduction yielded the rate constants for the rate of breakup of the intermediates. A spectro-electrochemical experiment also showed that the dimer can be oxidized further to produce a Ru(IV)-Ru(IV) dimer.

TABLE OF CONTENTS

SECTION I. SPECTRAL AND CHEMICAL ANALYSES

1. Introduction.....	1
2. Experimental.....	17
A. Spectroscopic Measurements.....	17
B. Magnetic Measurements.....	17
C. Miscellaneous Techniques.....	18
D. Electrochemical Measurements.....	19
E. Computer Simulations.....	21
3. Materials.....	24
4. Conductivity.....	30
5. Magnetic Susceptibility.....	31
6. Formation of the [34] Dimer.....	32
7. Titration of the [34] Dimer with Base.....	42
8. Optical Studies of the Ru-edta System.....	53
A. [34] Dimer.....	53
B. Ru (III)-edta Optical Spectra Results	79
C. Addition of Various Ligands to the...	85
[34] Dimer.....	
D. Equilibration Studies of the [34]....	89
Dimer.....	
9. Titrations of Ru ₃ Y-OH ₂ with Cerium (IV).....	92
10. Dioxygen Addition to Ru ₃ Y-OH ₂	99
11. Catalysis of Peroxide Disproportionation.....	105
12. Infrared and Raman Spectroscopy.....	112
13. ESR Spectroscopy.....	122

TABLE OF CONTENTS

14.	NMR Spectroscopy.....	129
15.	Summary aand Conclusions.....	138
SECTION II. ELECTROCHEMISTRY		
16.	Cyclic Voltammetry and Electrolysis of the... Ru-edta System.....	144
17.	Polarography.....	168
18.	Spectro-electrochemistry.....	187
19.	Rotating Ring-Disk Electrode Voltammetry.....	197
20.	Summary and Conclusion.....	261
21.	RRDE Simulation and Discussion.....	269
22.	Appendix.....	304
	A. PH Titration Program Listing and.....	304
	Sample Output.....	
	B. Catalytic Program Listing and.....	309
	Sample Output.....	
	C. Scheme X Program Listing and Sample..	316
	Output.....	
23.	References.....	324
24.	Propositions.....	337

LIST OF FIGURES

1.	OTTLE Cell Dimensions.....	22
2.	Optical Spectrum of Ru3Y-OH ₂ + Hydrogen.....	33
	Peroxide at pH 5.50.....	
	A. 230-600 nm.....	
	B. 500-800 nm.....	
3.	Titration Results for [34] Dimer Formation.....	36
	A. Plot of μeq of Base vs. μeq of.....	
	H ₂ O ₂	
	B. Plot of Absorbance (632 nm) vs. ...	
	μeq of H ₂ O ₂	
	C. Plot of Absorbance (393 nm) vs. ...	
	μeq of H ₂ O ₂	
4.	Optical Spectra of [34] Dimer vs. pH.....	43
5.	Plot of $\log\left(\frac{A_{\text{HA}} - A_{\lambda}}{A_{\lambda} - A_{\text{A}}}\right)$ vs. pH for the.....	47
	[34] Dimer at 393 nm.....	
6.	Plot of Observed, and Simulated Titration.....	50
	Curve of the [34] Dimer with Base.....	
7.	Potential Energy vs. Nuclear Configuration.....	58
	for Symmetric, Mixed-valence Complexes.....	
	A. Class I Complex.....	
	B. Class II Complex.....	
	C. Class III Complex.....	

LIST OF FIGURES

8.	Near-infrared Spectra of [34] Dimer.....	62
	A. pD 5.0.....	
	B. pD 13.0.....	
9.	Dunitz-Orgel Diagrams.....	71
	A. Ru-O-Ru Linear Model (12.....	
	Electrons: [44]).....	
	B. Ru-O-Ru Bent Model (13.....	
	Electrons: [34]).....	
10.	Optical Spectra of Ru ₃ Y-OH ₂ vs. pH.....	82
11.	Optical Spectra of the [34] Dimer.....	86
	+ Added Ligands.....	
	A. [34] + Thiocyanate.....	
	B. [34] + Histidine.....	
12.	Optical Spectra of [34] Dimer Equilibrations... ..	90
	A. pH 5.42 Acetate Buffer (50 <u>mM</u>).....	
	B. pH 8.42 Phosphate Buffer (50 <u>mM</u>)... ..	
	C. pH 11.65 Phosphate Buffer.....	
	(50 <u>mM</u>).....	
13.	Reappearance of [34] Dimer after Addition of....	93
	Excess Ce(IV).....	
14.	Dioxygen Evolution from [34] Dimer.....	106
	Catalyzed Peroxide Disproportionation.....	
15.	Infrared Spectra.....	114
	A. IR of HRU ₃ Y-OH ₂ (KBr Pellet).....	
	B. IR of K ₃ [34] (KBr Pellet).....	

LIST OF FIGURES

16.	Raman Spectra of the [34] Dimer.....	118
	A. pH 6.....	
	B. pH 12.....	
17.	ESR Spectra at pH 5.....	123
	A. [34] Dimer.....	
	B. Ru3Y.....	
18.	ESR Spectra of the [34] Dimer at pH 13.....	126
	A. High pH [34] Dimer at LN2.....	
	Temperature.....	
	B. High pH [34] Dimer at Liquid.....	
	Helium Temperature.....	
19.	Nmr Spectra of the [34] Dimer.....	131
20.	Cyclic Voltammogram of Ru3Y-OH ₂ at pH 5.50.....	145
21.	Cyclic Voltammogram of Ru3Y-OH ₂ at pH 7.70.....	150
22.	UV/Vis Spectrum of the [34] Dimer after.....	154
	Electrolysis at +1.100 V at pH 7.70.....	
23.	Cyclic Voltammogram of the [34] Dimer.....	159
	at pH 9.96.....	
24.	UV/VIS Spectrum of a [34] Dimer Solution.....	165
	Containing the "Impurity" after.....	
	Reduction at -1.050 V at pH 9.96.....	
25.	Plot of E ₁ vs. pH for the [34] Dimer and Ru3Y...	173
26.	Normal Pulse Polarograms of the [34] Dimer.....	175
	at pH 8.51.....	

LIST OF FIGURES

27.	Wave Shape Analysis Plots of pH 8.51 Tact.....	178
	Polarogram.....	
28.	Spectro-electrochemical Response of the.....	188
	[34] Dimer at pH 1.....	
29.	Nernst Plot of the Oxidation of the.....	193
	[34] Dimer.....	
30.	RRDE of RU3Y-OH_2 at pH 1.....	199
	A. Disk Scan Range: +0.400 --->.....	
	-0.500 V.....	
	B. Scan Range: +0.400 ---> +1.300 V...	
31.	Levich Plots of RU3Y-OH_2 at pH 1.00.....	202
32.	RRDE of RU3Y-OH_2 at pH 7.70.....	206
	A. Scan Range: +0.400 ---> -0.600 V...	
	B. Scan range: +0.200 ---> +1.400 V...	
33.	Levich plot of RU3Y-OH_2 at pH 7.70.....	208
34.	Simulated Collection Efficiency, N, vs. XKTC....	215
	For Scheme III and Scheme V.....	
35.	Oxidative RRDE Behavior of the [34] Dimer.....	222
	at pH 1.....	
36.	Reductive RRDE Behavior of the [34] Dimer.....	224
	A. pH 1.00.....	
	B. pH 7.70.....	
37.	Levich Plots of the [34] Dimer.....	226
	A. pH 1.00.....	
	B. pH 7.70.....	

LIST OF FIGURES

38.	Simulated Collection Efficiency, N , vs. XKT	242
	for Scheme VIII.....	
39.	Simulation Data for Scheme IX.....	249
	A. Collection Efficiency, N_k , vs. XKT ..	
	B. Disk Current, ZD , v_s . XKT	
40.	Simulation Data for Scheme X.....	256
	A. Collection Efficiency, N_k , vs. $XKTC$.	
	B. Disk Current, ZD , vs. $XKTC$	
41.	Comparison of Simulations for the Catalytic.....	277
	Mechanism for the Bard and Prater.....	
	Electrode (54).....	
	A. Collection Efficiency, N_k , vs. $XKTC$.	
	B. Disk Current, ZD , vs. $XKTC$	
42.	Program Listing and Output for pH Titration.....	306
	Simulation.....	
43.	Catalytic Program Listing and Output.....	310
44.	Scheme X Program Listing and Sample Output.....	317

LIST OF TABLES

1.	Comparison of the Substitution Rates.....	6
	of Ruthenium Systems.....	
2.	Analytical Results.....	26
	A. Elemental Analysis.....	
	B. Conductivity.....	
3.	Near-infrared Results for [34] Dimer.....	64
4.	Electronic Spectra of Various Ru Dimers.....	68
	and Trimers.....	
5.	Optical Spectra Data of Ruthenium (III).....	79
	Complexes.....	
6.	Dioxygen Addition to Ru ₃ Y.....	101
7.	Hydrogen Peroxide Disproportionation Data.....	108
8.	Nmr Shift Data for the [34] Dimer vs.	133
	Temperature.....	
9.	Polarography Results for Ru ₃ Y and the [34].....	170
	Dimer.....	
10.	RRDE Wave Shape Analysis of Ru ₃ Y-OH ₂ and the....	210
	[34] Dimer.....	
11.	Simulation Data for E _r C _{cat} Mechanism.....	230
12.	Simulation Data for E _r C _i E _{cat} Mechanism.....	234
13.	Data for the Breakup of the [34] Dimer.....	244
	A. pH 1.00.....	
	B. pH 5.00.....	
	C. pH 7.70.....	
	D. pH 9.25.....	

LIST OF TABLES

14.	Experimental RRDE Data for Scheme X.....	258
15.	RRDE Catalytic Simulation Results for..... Skinner (57) Data.....	282
16.	RRDE Catalytic Simulation Results for Bard..... and Prater Data (54).....	289
17.	RRDE Catalytic Simulation Results for..... Skinner Data (57) of Copper System.....	291
18.	Simulated Catalytic Mechanism for a Cobalt-..... Cyclam Complex Studied by Geiger and Anson.	299

LIST OF ABBREVIATIONS

edta, Y	ethylenediamminetetra-acetate
tedta	thio-bis, ethylenediamminetetra-acetate
NaTFA	sodium trifluoroacetate
RRDE	rotating ring-disk electrode
CV	cyclic voltammetry
Ru ³⁺ -OH ₂	Ru(III)edta(OH ₂) ⁻
[34]	([Ru(edta)] ₂ O) ³⁻
[34]-OH	([Ru(edta)] ₂ (O)(OH)) ⁴⁻
DSS	sodium 2,2-di-methyl-2-silapentane- 5-sulfonate

SECTION I SPECTRAL AND CHEMICAL ANALYSES

1. INTRODUCTION

The late 1960's saw the synthesis and identification of $H[Ru(edta)(OH_2)]$ (abbreviated by $HRu3Y-OH_2$) by groups in Japan and Russia (1,2). The study of the complex's spectral, substitutional, and electrochemical properties was not made in earnest until the 1970's (3-8). By this time, a vast amount of data had been accumulated on the ruthenium (III/II) ammine, and bipyridyl systems identifying the redox properties, the electronic interactions between the metal center and the ligands, and the substitutional properties of these metal complexes (9-25). The extensive study of the ruthenium systems had much to do with the general inertness of the $Ru(III)$ and $Ru(II)$ oxidation states, thereby facilitating studies of electron transfer reactions and the effect of a metal center's electronic structure on its interaction with various types of saturated, and unsaturated ligands (16,19).

Synthetic procedures were developed that permitted the incorporation of a variety of incoming ligands into the RuL_5-OH_2 , or the $RuL_4(OH_2)$ complexes to study sigma and pi-type interactions between the metal center and the incoming ligand. The substitution was generally found to proceed via a dissociative mechanism (25). Ruthenium (II) was found to favor coordination to ligands capable of pi-type interactions, especially molecules possessing unoccupied,

pi-acceptor anti-bonding orbitals, while the ruthenium (III) center exhibited a propensity for sigma and pi donor molecules (11,22). This behavior was explained by considering the different electronic structure of ruthenium (II), d^6 low-spin, and ruthenium (III), d^5 low-spin configurations. Ruthenium (II), having a filled t_2 set of d orbitals of pi symmetry would be expected to be a poor pi acceptor. If one of these orbitals were to mix with an unoccupied orbital of a ligand molecule of similar symmetry, they would form a new pair of molecular orbitals that, when filled with the electrons from the initial atomic orbitals, would yield a net bonding interaction (11,22). This interaction, coupled with the sigma interaction of the incoming pair of ligand electrons leads to a synergistic, back-bonding (22) molecular orbital scheme resulting in an overall, more stable configuration. Ruthenium (III), on the other hand has a vacancy in its t_2 set of orbitals that enables it to interact more strongly with pi-donating ligand orbitals, but without the benefit of the added stability due to back-bonding.

When a comparison is made between the relative stability of the incoming ligand for a coordinated water position in the two oxidation states, pi-acceptor ligands tend to stabilize the ruthenium (II) state, while pi-donator ligands tend to stabilize the ruthenium (III) state.



(where L is ammonia, a saturated ammine, or a bipyridine-type ligand.)

The relative stability can be measured by comparing the shift in the reduction potential for the substituted species to that for the aquo form (12).

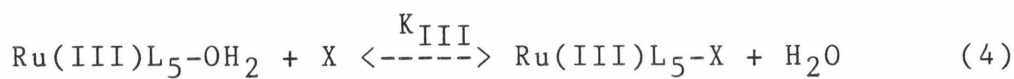
When the substitutional and electrochemical properties of $\text{Ru}^{3+}/\text{Y-OH}_2$ were compared with those of the ammine and bipyridyl systems, very glaring differences were found (5,7,42). The ruthenium (III) state was found to be up to ten orders of magnitude more labile towards substitution for the edta system than in the other systems. The backwards rate constant for the loss of the ligand, X, was also up to four orders of magnitude higher for a given incoming ligand. The mechanism of substitution also differed, and was found to be very pH dependent and associative in nature. The substitutional properties of the ruthenium (II) state for the edta system were not affected as dramatically, and the substitutional rates were within one to two orders of magnitude; its back-bonding properties seeming to predominate over any effects due to the already coordinated ligands. Thus, the relative stability of Ru(III)-edta substituted complexes exhibited an enhanced stability when compared to the other Ru(III) systems, while Ru(II)-edta substituted complexes retained, roughly, the same stability.

A comparison of the shift in the redox potential for the

substituted ruthenium complex, compared to the unsubstituted complex, is a measure of the relative stability of the two oxidation states in the substituted complex.



$$K_{\text{II}} = \left(\frac{[\text{Ru(II)L}_5\text{-X}]}{[\text{Ru(II)L}_5\text{-OH}_2][\text{X}]} \right) \quad (3)$$



$$K_{\text{III}} = \left(\frac{[\text{Ru(III)L}_5\text{-X}]}{[\text{Ru(III)L}_5\text{-OH}_2][\text{X}]} \right) \quad (5)$$

$$\begin{aligned} \Delta E &= \Delta E^\circ + \left(\frac{0.059}{n} \right) \log \left(\frac{[\text{Ru(III)L}_5\text{-OH}_2][\text{Ru(II)L}_5\text{-X}]}{[\text{Ru(II)L}_5\text{-OH}_2][\text{Ru(III)L}_5\text{-X}]} \right) \quad (6) \\ &= \Delta E^\circ + \left(\frac{0.059}{n} \right) \log \left(\frac{K_{\text{II}}}{K_{\text{III}}} \right) \end{aligned}$$

where,

ΔE = the difference between the potentials for

the unsubstituted, and substituted RuL_5 complex

The enhanced stability of the Ru(III)-edta complexes thus lead to smaller shifts in the redox potential of the substituted complexes, when compared to the unsubstituted, aquo complexes for Ru-edta , than for other ruthenium systems. This makes electrochemistry a very powerful means of comparing the substitutional properties of ruthenium complexes.

As an example of the enhanced reactivity of $\text{Ru}_3\text{Y-OH}_2$, during the synthesis of the $\text{L}_5\text{Ru(III)-X}$ system the following procedures are generally followed:



The substitutional inertness of the ruthenium (III) state then allows for the isolation of the final, oxidized product. The enhanced lability of the YRu(III)-OH_2 system, however, allows for the direct substitution of the desired ligand onto ruthenium (III) without having to resort to the involved procedure of the other ruthenium systems (see Table 1 for a comparison of the substitution properties of several Ru (III) complexes).

The substitution rates of the $\text{Ru}_3\text{Y-OH}_2$ system are also highly pH sensitive (5,7,8) and exhibit a maximum rate at about pH 5, with a fall-off to $\frac{1}{2}$ of the maximum rate at the pKa for the dangling acetate arm of the potentially, hexa-coordinate edta (pKa=2.90), and of the coordinated water (pKa=7.65). The substitution rate drops off very fast past these pH ranges. The reason for the dropoff after the second pKa is attributed to the poor leaving-group ability of a coordinated hydroxide. The reason for the lower substitution rate at pH's more acidic than the first pKa

Table 1

Comparison of the substitution rates
of ruthenium systems

Table 1

<u>Complex + ligand</u>	<u>$k_1, \text{M}^{-1} \text{s}^{-1}$</u>	<u>k_{-1}, s^{-1}</u>	<u>$K = k_1 / k_{-1}, \text{M}^{-1}$</u>
<u>Ru(III)edta^a</u>			
thiocyanate	270	0.5	540
isonicotinamide	8300	0.7	12000
pyrazine	20000	2.0	10000
<u>Ru(II)edta^a</u>			
thiocyanate	2.7	2.1 E-4	1.3 E+4
isonicotinamide	30	4 E-6	7 E-6
pyrazine			1.7 E+8
<u>Ru(III)(NH₃)₅^b</u>			
chloride			110
dimethyl sulfide			$\geq 1.6 \text{ E-2}$
pyrazine	$\leq 2 \text{ E-6}$		
<u>Ru(II)(NH₃)₅^b</u>			
chloride			0.4
thiocyanate	4.0		$K_{\text{II}} / K_{\text{III}} = 14$
isonicotinamide	0.11		$K_{\text{II}} / K_{\text{III}} = 1.8 \text{ E+5}$
pyrazine	0.056		$K_{\text{II}} / K_{\text{III}} = 4 \text{ E+6}$
dimethyl sulfide	8 E-2	4.2 E-6	$> 1 \text{ E+5}$

* a. ref 7; b. ref 15 and the references therein

are less clear. Creutz has cited the importance of the assistance of the free, dangling acetate group as being important (7). Some manner of anchimeric assistance involving the unprotonated carboxylate group and the incoming ligand was suggested.

The necessity of having a free-dangling acetate group for an increase in the rate of substitution is not unique to ruthenium. Several other metal-edta complexes have exhibited rate enhancements when compared with the substitutional properties of the metal with ammine, or bipyridine type ligand environments (eg. Cr(III), Os(III), Co(III), Rh(III)) (7,27). In the Cr(edta) case, an associative mechanism was also observed (27).

Oyama and Anson also demonstrated the necessity of having a free acetate arm on Ru3Y-OH_2 to observe enhanced substitution rates (27-29). They covalently attached Ru3Y-OH_2 to a functionalized carbon disk electrode via an amide linkage formed between the carboxylate of the free acetate arm and the ammine groups on the electrode. The rate of the substitution of isonicotinamide in this system was 4 E-4 sec^{-1} (29), compared with 0.7 sec^{-1} (27) for the unbound, Ru3Y-OH_2 (7). The substitution behavior of the anchored Ru3Y-OH_2 now mirrored that of the other ruthenium (III)/(II) systems. In addition, the hedta ligand (one of the acetate arms on edta is now a hydroxy ethyl group), when coordinated to ruthenium, was also observed to behave more like "normal" ruthenium (III) (31). This further emphasizes

the necessity of having a free acetate arm for a substitution rate enhancement onto ruthenium (III).

At the time of my joining the Anson group, a supply of an edta modified ligand, tedta, a thioether modified analog of edta that incorporated a bis-methylene, sulfide moiety symmetrically between the nitrogens of the ethylenediammine backbone was made available (32).

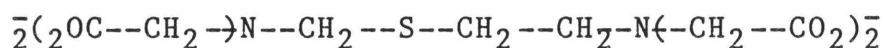


DIAGRAM 1.

TEDTA

It was proposed that by making the Ru(tedta) complex that the propensity that ruthenium (II) was shown to have for thioethers (19,25,33-35) would aid in producing a stable complex with a Ru-SR₂ bond. The enhanced stability of the Ru-SR₂ bond has been attributed to back-bonding of the ruthenium (II) to unoccupied, low-lying, anti-bonding orbitals on the thioether sulfur (33-35). Using this complex, it was hoped that it would then be possible to form an adsorbed complex on mercury and thereby study the surface characteristics of the complex and its electron transfer properties (32,36).

In the course of the above study, many complications arose concerning the isolation, and characterization of Ru(tedta), especially as is related to its meager electrochemical response. It was decided that an understanding of the reactivity and properties of Ru^{3+/2+} and simple thioethers would aid in untangling the mysteries of

Ru(tedta). The reactions between Ru₃Y-OH₂ and a few thioethers were studied and it was found that the enhanced reactivity of the Ru₃Y-OH₂ complex also applied to these ligands as well. An enhanced stability of thioethers towards coordination to Ru₃Y was observed and actually yielded an equilibrium constant greater than 100 M^{-1} (31). In general, for ruthenium amines, this value is 0.01 M^{-1} (19,25). While pursuing an understanding of the thioether-Ru₃Y system, it was noted that, under conditions that were not initially reproducible, the appearance of an intense, yellow-green species appeared in solution--and not always in the presence of any additional ligand. The presence of this species also affected the substitutional and electrochemical properties exhibited by Ru₃Y in the presence of the thioethers. Since the color of the Ru(tedta) complex was also green, while the color of Ru₃Y-SR₂ systems were yellow, to orange, it was felt that an investigation of the conditions necessary for the evolution of the "green" species in the presence of Ru_{3/2}Y was warranted. The existence of a mysterious "green" complex had also been noted in passing in a paper concerning the electrochemistry of Ru₃Y-OH₂ at a mercury electrode (3) and in the substitution properties of Ru₂Y-OH₂ with Π -acceptor ligands (42). I also observed that the amount of the "green" complex increased in neutral pH's upon prolonged exposure to air (31). Concomitant with the appearance of the "green" complex, a "pre-wave" appeared in the cyclic voltammogram of

the reduction of $\text{Ru}_3\text{Y-OH}_2$. An understanding of these phenomena was important for a clear description of the redox behavior of the $\text{Ru}_3\text{Y-OH}_2$.

Starting in the late 1960's, a series of articles appeared in the Russian literature concerning the product of the reaction of $\text{Ru}_3\text{Y-OH}_2$ with various chemical oxidants (2,37-41). At pH's below 5, it was found that hydrogen peroxide reacted with $\text{Ru}_3\text{Y-OH}_2$ to produce an intensely green solution, while at pH's above 7, dioxygen reacted with $\text{Ru}_3\text{Y-OH}$ to produce a green complex of a similar nature. The possibility of the existence of a dimeric ruthenium complex was proposed, but the properties, and the proposed structure of the "green" complex varied from paper to paper.

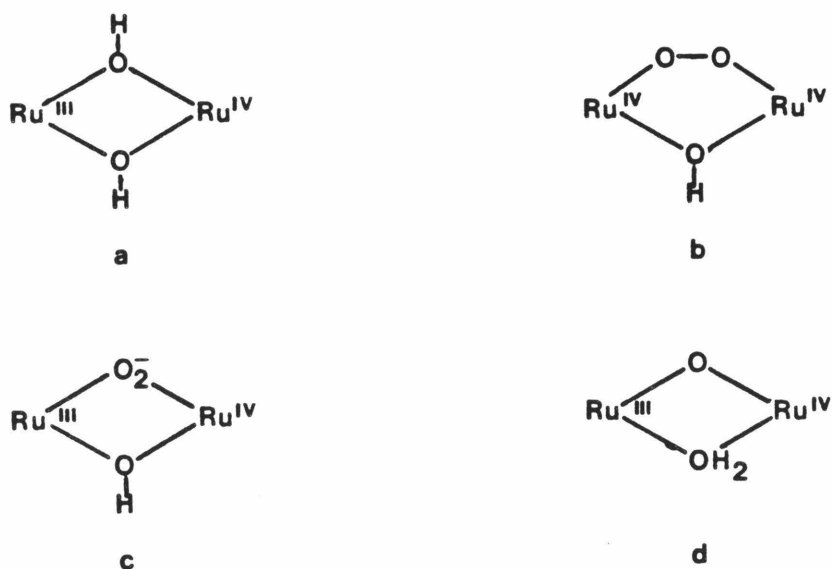


Diagram 2. Proposed ruthenium-edta dimer structures
by Ezerskaya

The various structures proposed included a doubly-bridged di-hydroxy, a peroxy- and a hydroxy-, a dioxo- and a hydroxy-, and an oxo- and an aquo, as bridging groups. The oxidation states of the rutheniums were never clearly identified, and varied depending upon the type of bridge invoked.

During the writing of this thesis, a note appeared by Khan and Ramachandraiah (43) concerning the reaction of $\text{Ru}_3\text{Y-OH}_2$ with dioxygen at pH 5. This was not the pH region that Ezerskaya noted that dioxygen reacted with $\text{Ru}_3\text{Y-OH}_2$. My observations agreed with those of Ezerskaya, and, exactly what conditions were used by Khan and Ramachandraiah is unclear, even though some of the spectral features they reported were similar to what Ezerskaya and I observed.

Very recently, two short articles appeared concerning the oxidation of $\text{Ru}_3\text{Y-OH}_2$. One appeared in the Japanese literature and concerned the reaction of chlorate ions with $\text{Ru}_3\text{Y-OH}_2$ to produce a green species (44). The other article was by Khan (45), who proposed that dioxygen was bound by $\text{Ru}_3\text{Y-OH}_2$ to form a peroxy-bridged dimer. Sato, et al (44) reported spectral properties similar to those of Ezerskaya but the proposed structure was not any of Ezerskaya's suggestions, but of a μ -oxo bridged ruthenium dimer. This structure was based on analogy with the systems characterized by Meyer, et al (18,46,47), for the ruthenium-bipyridine and the ruthenium ammine systems. No direct evidence, however, was presented to establish the oxo-

bridged structure for the Ru(edta) dimer. Sato, et al, observed a net, one electron per two rutheniums oxidation yielding a dimer with the formal oxidation states, formally, Ru(III)-O-Ru(IV).

The reaction of Ru₃Y with dioxygen at neutral pH's also suggested the possibility of catalytically reducing dioxygen to water. The reasons for pursuing this system were also made more interesting by the observation in the Russian series of papers that the "green" complex exhibited peroxidase, and catalase activity (37-40).

The task of characterizing the mysterious and mercurial "green" complex was thus undertaken. The main body of this work will be concerned with the evolution of the "green" complex in solution, its isolation, its subsequent characterization, and its spectral, electrochemical, and catalytic activity. This effort precluded any further work on the ruthenium-sulfur system.

The use of the rotating ring-disk electrode (RRDE) was employed as a powerful tool to help unravel the mysteries of the dimer's electrochemistry (48,49). For a simple, diffusion and convection controlled, electron-transfer reaction, the so-called, Levich behavior is expected (50).

$$i_{\text{disk,lim}} = 0.62nFACv^{-\frac{1}{6}}D^{\frac{2}{3}}\omega^{\frac{1}{2}} \quad (10)$$

n = the number of electrons involved

F = Faraday's constant (96,485 coulombs/equivalent)

A = the area of the disk electrode (cm^2)

C = the bulk concentration of the electroactive species (moles/cm^3)

v = solution kinematic viscosity (cm^2/sec)

D = diffusion coefficient (cm^2/sec)

ω = rotation rate (Hz)

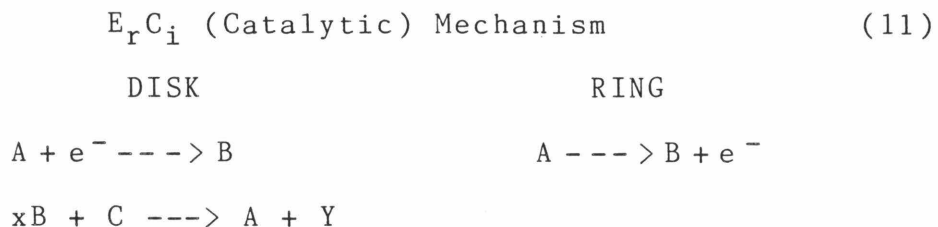
A linear plot of the disk current vs. the square root of rotation rate with an origin intercept is indicative of a simple, mass-transfer controlled (diffusion and convection), electron-transfer process (Levich behavior).

For a simple, mass-transfer controlled, electron-transfer reaction, the ring current is also linear in response with respect to the square root of the rotation rate and has an origin intercept. Monitoring of the ring current and the collection efficiency ($N_k = -i_{\text{ring}}/i_{\text{disk}}$) was employed to aid further in characterizing the electrochemical behavior of $\text{Ru}_3\text{Y-OH}_2$ and the green dimer. It is important to note that the collection efficiency is a function of only the ring-disk electrode's geometry and is independent of the rotation rate for systems free of kinetic complications.

Chemical or electrode kinetics complications can show up in the form of collection efficiencies that are a function

of rotation rate. Unfortunately, to extract the rate constant of the chemical step from the data is difficult at best and only a few, simple first-order reaction mechanism systems can be approximated using numerical methods (49-51). Digital simulation of the RRDE, however, has been shown to be a powerful means of separating the chemical and electron transfer processes (52-54). The simulations enable second-order chemical rate processes, multiple-step electrochemical reactions and the effect of different diffusion coefficients for the reactive species to be taken into account.

To obtain rate constants, and unravel the chemical processes of the ruthenium dimer in solution, computer simulation programs were employed. The "box-method" of finite element analysis developed by Feldberg (55) and Bard and Prater (52-54) for the rotating ring-disk electrode was utilized with modification of the kinetic term according to the method of Marcoux (56). Coupled electron-transfer and chemical reactions not addressed by Bard and Prater were also studied. In addition, some new corrections to the Bard and Prater programs, as well as, the "correction" for stoichiometry discussed by Skinner (57) for the catalytic system were made.



In the first step of the catalytic system, species A is reduced to produce species B. In the absence of any substrate (C), the Levich current at the disk is observed. When the substrate is introduced, it can react with B to regenerate A and produce a reduced, electro-inactive product (Y). The factor (x) in front of B accounts for the number of one-electron species (B) necessary to reduce C to Y. The influence of the chemical step is then reflected in the measurement of greater disk and lesser ring currents. Improper use of the programs in previous articles is cited, and corrected, and rate constants for the catalyzed disproportionation of hydrogen peroxide by iron(II) are recalculated. The resulting, corrected values for the two papers are in closer agreement with each other, as well as with the measurements of this rate as determined by stopped-flow methods. A discussion of the use of the programs occurs at the end of this work. An appendix is included with a summary of the systems simulated and with the program listings for these simulations.

2. EXPERIMENTAL

A. SPECTROSCOPIC MEASUREMENTS

Ultraviolet/ Visible measurements were performed using a Cary 219, or a Hewlett-Packard HP-8450 spectrophotometer. Spectra obtained on the Hewlett-Packard were digitized and stored on cassette. Samples were routinely measured in 1 cm, or 1 mm cells. When an inert atmosphere was required, a stoppered, deaerated cell was used. The sample was introduced by a gas-tight syringe. Kinetic runs were performed by programming the HP-8450 to scan the sample during a given interval (minimum of 1 second) and the full spectra (200-800 nm) was digitized and the data stored on cassette.

Near-infrared spectra were recorded on a Cary 17 in 1 cm cells and were corrected for background solvent absorbances.

Infrared spectra were taken of KBr pellets using a Beckman IR 4240 spectrometer. Resonance Raman spectra were performed on dilute, aqueous solutions using a Spectra Physics Tunable Laser with a SPEX DPC-2 spectrometer run by a SCAMP controller and stored on floppy disk.

B. MAGNETIC MEASUREMENTS

Magnetic susceptibility measurements were performed at ambient temperatures on solid samples with a Cahn Faraday Magnetic Susceptibility instrument. Corrections were made

using $\text{HgCo}(\text{SCN})_4$ as a standard. Diamagnetic corrections were made using Pascal's constants (59).

Electron Paramagnetic Resonance spectra were obtained on a Varian E-Line Centruy Series EPR with a Heli-Tran Temperature Controller. Some of the spectra were digitized and stored on floppy disk using a Digital PDP8A. The samples were either dilute solids (1% w/w in KCl), or dissolved in buffered, aqueous, or deuterio-media. Temperatures between 10-297 K were used routinely.

Nuclear Magnetic Resonance proton spectra were performed on a Bruker 500 instrument at the Southern California NMR Facility in buffered, deuterio-media with DSS (sodium 2,2-dimethyl-2-silapentane-5-sulfonate) as an internal reference. Variable temperature experiments were performed using a Bruker Temperature Controller. All data were digitized and stored on floppy disk.

C. MISCELLANEOUS TECHNIQUES

pH measurements were performed using a Beckman 39501 pH Electrode and an Orion Research 701A Digital Ionalyzer. Dissolved dioxygen concentrations were measured with a YSL O_2 probe and a Fluke 8000A Digital Multimeter. The electrode was calibrated by measuring the voltage generated in dioxygen saturated, air saturated, and argon saturated solutions and taking the the dioxygen saturated value as 1.4 mM in an acidic solution. The air saturated value was measured, and taken, as 1/5 of the dioxygen value. A linear

relationship down to zero (argon saturated value) was assumed and the resulting dioxygen concentration of an unknown solution was calculated.

Conductivity measurements were performed at ambient temperatures using a conductance cell consisting of four platinized, platinum plates with a 1 mm spacing (area 4 cm²) connected to a Beckman RC 1632 Conductivity Bridge. Measurements were made in deionized water that had been passed through a Barnsted Nanopure system.

Whenever an inert atmosphere was required, pre-scrubbed argon was used. The argon was passed through two zinc amalgam containing vanadous towers, and then through a tower of deionized water. A gas line with detachable bubblers was used to carry out the deaeration. Each bubbler had sidearms for the introduction and removal of solutions by syringe techniques, the transfer of solutions by Teflon tubing, the removal of gases by hypodermic needles, or the introduction of monitoring devices.

D. ELECTROCHEMICAL MEASUREMENTS

Rotating ring-disk measurements were performed using a Pine RDE-3 Bipotentiostat, ASR Speed Control, ASR-2 Analytical Rotor, DT-6 basal plane graphite (BPG) disk (area 0.458 cm²) and a platinum ring electrode (collection efficiency of 0.176) and plotted on a Hewlett-Packard 7046A XYY recorder. Measurements were performed using standard

techniques (60) with a 400 ml beaker that had been modified with a Teflon plug cap and sidearms for the reference and auxiliary electrodes. The sidearms were separated by fine, sintered-glass frits. Separate sidearms were used for the introduction and the removal of desired substances. Before using, the electrode was polished with alumina on a fine grade of Buehler Microcloth and then rinsed with Nanopure water, cleaned in a Sonicator sonicator, re-rinsed with deionized water and dried with a Kimwipe.

Cyclic voltammograms and controlled potential electrolyses were performed using a Princeton Applied Research (PAR) 175 Universal Programmer, 173 Potentiostat/Galvanostat, 179 Digital Coulometer, 178 Electrometer Probe and recorded with a Houston 2000 XY recorder. Standard H cells were employed for voltammetric measurements with a platinum wire auxiliary electrode, a saturated Calomel electrode (SCE), and either a Metrohm Hanging Mercury Drop Electrode (HMDE), or a basal plane graphite (BPG) disk mounted in a glass tube with heat shrinkable tubing. Electrical contact to the graphite was made by using a mercury pool on top of the BPG plug. A copper wire extended out of the tube for electrical contact. A new surface for the BPG electrode was obtained by cleaving the disk with a razor blade. The area of the HMDE could be dialed out by calibrated amounts. Electrolyses were performed using either a large mercury pool, or a platinum gauze as the working electrode.

Polarographic measurements were performed with a PAR 174A Polarographic Analyzer using an H-cell and a mercury column constructed by standard techniques (61). The mercury column was calibrated for the mercury reservoir at a given height and for a given drop time by standard techniques (61).

Spectroelectrochemical measurements were made using the Hewlett-Packard HP-8450, PAR 174A, and a modified, optically-transparent thin-layer electrode (OTTLE) using a tin oxide coated glass plate instead of a gold minigrid as the working electrode (64,65). A platinum wire was used as an auxiliary electrode. The reference electrode was a Sargent-Welch SCE (miniature, Pt junction, #S-30080-17) (see figure 1 for the dimensions). The cell was introduced into the spectrometer's light path and left in place for the duration of the experiment. A baseline correction routine was applied by the HP-8450 and used to determine the pathlength of 0.4 mm when compared to the same solution in a 1 mm, or 1 cm cell.

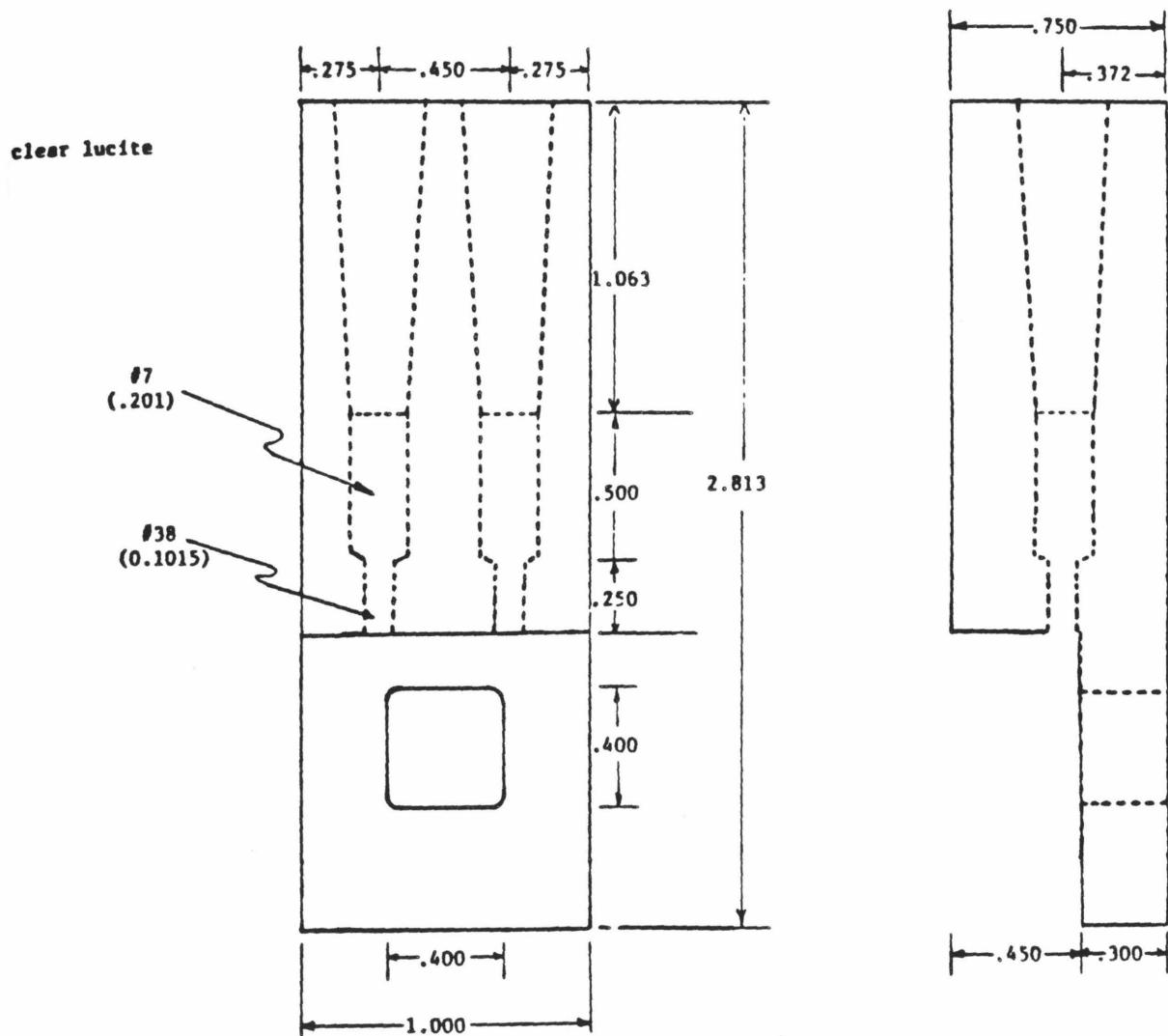
E. COMPUTER SIMULATION

The rotating ring-disk simulations were performed on a Digital Electronics Corporation VAX PDP 11/780 by modifying (56) the programs first developed by Feldberg (55), and Bard and Prater (52-54) and Skinner (57).

Figure 1

OTTLE cell dimensions

Figure 1



3. MATERIALS

$\text{H}[\text{Ru}(\text{III})\text{edta}(\text{OH}_2)]$ was prepared by modified literature methods (1). 1.0 gram of $\text{K}_2\text{RuCl}_5\text{OH}_2$ (2.67 mmoles) was dissolved in 50 ml of a pH 2 solution of trifluoroacetic acid (HTFA). The ruthenium solution was covered with a watchglass and heated to near boiling for 30 minutes. A 5% molar excess of $\text{Na}_2\text{H}_2(\text{edta})$ was dissolved in 50 ml of water. The edta solution was added to the ruthenium solution, recovered, and heated to near boiling for 45 minutes. The solution was then uncovered, and evaporated slowly on a lower heat until a light, yellow precipitate started to form. At this point, 50 ml of ethanol was added and the solution was allowed to cool to room temperature. The resulting yellow solid was filtered and washed several times with ethanol and air dried. The yellow solid was reprecipitated after redissolving in hot, 0.1 M HTFA. The solution was evaporated slowly with gentle heating until near dryness. An excess of ethanol was added to induce precipitation, and the solution was filtered. The yellow powder was washed several times with ethanol and then ether, and then air dried. This procedure was repeated until a silver ion test for chloride in the mother liquor was negative. The final yield was typically about 90% per mole of ruthenium. The equivalent weight of the fine yellow powder was determined to be $204_{\pm 2}$ by titrating with standardized base. The ruthenium content was analyzed by a modified literature method (66). In a typical analysis, 5

mg of the compound was dissolved in 10 ml of 2 M KOH and heated while stirring. Approximately 100 mg of potassium persulfate was added and the solution was covered and heated to near boiling for 30 minutes. The resultant solution was cooled and diluted to 25 ml with 2 M KOH and the absorbance at the isosbestic point for ruthenate/perruthenate at 415 nm ($\epsilon = 1047 \text{ cm}^{-1} \text{ M}^{-1}$) was used to determine the amount of ruthenium present. A blank run on the edta ligand showed no interference at this wavelenth. Carbon, hydrogen, and nitrogen analyses were performed by the Caltech Analytical Lab. The fine yellow powder analyzed for (also see Table 2) Ru,24.2; C,29.3; H,3.71; N,6.97; in good agreement with the calculated values for $\text{RuC}_{10}\text{H}_{15}\text{N}_2\text{O}_9$, MW=408; Ru,24.75; C,29.44; H,3.71; N,6.87.

$\text{K}_3[\text{Ru}(\text{edta})]_2 \cdot x\text{H}_2\text{O}$ was prepared by several methods depending upon the pH, and whether or not a solid was desired. At pH's above 7.5, exposure of a $\text{Ru}_3\text{Y}-\text{OH}_2$ solution to dioxygen yielded the dimer over a period of several hours. Vigorous bubbling of dioxygen was necessary to effect complete conversion of the monomer to the dimer. No solid was isolated from this method.

At lower pH's, titration of $\text{Ru}_3\text{Y}-\text{OH}_2$ with $\text{Ce}^{4+}(\text{aq})$, $\text{MnO}_4^-(\text{aq})$, or hydrogen peroxide, or by electrolysis yielded the dimer. For synthetic ease, the addition of hydrogen peroxide to a pH 5.0 solution of the monomer was used. A 50 ml solution of 10 mM $\text{HRu}_3\text{Y}-\text{OH}_2$ (0.86 g, 0.5 meq) was

Table 2

Analytical Results

A. Elemental Analysis

B. Conductivity

Table 2

A. Elemental Analysis

<u>Complex</u>		<u>C</u>	<u>H</u>	<u>N</u>	<u>RU</u>	<u>K</u>	<u>O</u>
HRu3Y-OH ₂	%Calc	29.44	3.71	6.87	24.75		
	%Obsd	29.3	3.71	6.97	24.2		
K ₃ [34]•6H ₂ O	%Calc	23.55	3.56	5.49	19.80	11.50	36.08
	%Obsd	22.84	3.21	5.39	19.1	12.65	34.94



B. Conductivity

<u>Complex</u>	<u>Λ_M, μmhos</u>
KCl	149
KMnO ₄	133
Ru(bipy) ₃ Cl ₂	226
Ru(NH ₃) ₆ Cl ₃	482
K ₃ Fe(CN) ₆	496
K ₄ Fe(CN) ₆	681
K ₃ [34]•6H ₂ O	426

prepared by dissolving the solid in warm water (40°C). The pH was adjusted to 5 by the addition of 1 M potassium hydroxide. Fifteen μl of 30% H_2O_2 (0.30 meq) was then added by calibrated pipette to the solution. Addition of a 10% stoichiometric excess of hydrogen peroxide was found to yield the purest product. Upon addition of the peroxide, the solution immediately turned a very dark-green and the pH dropped to less than 2. The reaction was allowed to proceed for one hour. The pH was readjusted to 7 with potassium hydroxide, and the solution was slowly evaporated by gentle heating to about one-fifth of its original volume. The solution was then allowed to cool to room temperature. With stirring, a ten-fold volume excess of ethanol was rapidly added, precipitating a fluffy, green solid. If the ethanol was not added rapidly, or the solution had been allowed to evaporate to near dryness, an oily liquid formed which had to be redissolved with water before precipitation would occur. The green solid was then washed several times with ethanol, then ether, and air dried. The yield after reprecipitation from water was approximately 80%. Elemental analysis for C,H,N, was performed by the Caltech Analytical Lab, or Galbraith Labs, for C,H,N,K,O,Cl, and sometimes Ru. The ruthenium content was typically determined by the spectroscopic method described above. For the formula, $\text{K}_3[(\text{Ru}(\text{edta}))_2\text{O}] \cdot 6\text{H}_2\text{O}$ (MW = 1020) the following percentages are calculated (also see Table 2): ($\text{K}_3\text{Ru}_2\text{C}_{20}\text{H}_{38}\text{N}_4\text{O}_{23}$) K,11.50; Ru,19.80; C,23.55; H,3.56; N,5.49; O,36.08. The

following percentages were obtained for the green solid, which are in agreement with the calculated values for the formula $K_3[(Ru(edta))_2O] \cdot 6H_2O$ (also see Table 2): K, 12.65; Ru, 19.1; C, 22.84; H, 3.21; N, 5.39; O, 34.94.

$HCr(edta)(OH)_2$ (27), $NaFe(edta)$ (67), $[Ru(bipy)_2(NO_2)]_2O$ (68), and $K_4[C_{15}Ru)_2O]$ (68) were all prepared by literature methods. The purity was determined by analyzing the sample for metal-ion content by standard procedures (70). The synthesized complex was then dissolved in water and its visible spectrum compared with the literature values. All of the complexes had been reprecipitated at least once.

$Ru(NH_3)_6Cl_3$ is commercially available and was purified by dissolving it in warm, 0.1 M HCl, filtering, and precipitating by the addition of excess acetone. This procedure was repeated a total of three times. The purity was determined by analyzing for ruthenium content.

All of the starting materials and the standard compounds were of the highest available quality and were used without further purification.

4. CONDUCTIVITY

To identify the charge of the anionic ruthenium-edta dimer, the conductivity of the potassium salt was measured. A 0.200 mM solution of the dimer (two times the ruthenium concentration) was measured in Nanopure water. For comparison, and calibration, 0.200 mM solutions of the following complexes were also measured: KCl, KMnO_4 , $\text{Ru}(\text{bipy})_3\text{Cl}_2$, $\text{Ru}(\text{NH}_3)_6\text{Cl}_3$, $\text{K}_3\text{Fe}(\text{CN})_6$, and $\text{K}_4\text{Fe}(\text{CN})_6$. The results are listed in Table 2.

The conductivity of the dimer was similar to that of ferricyanide indicating the presence of a tri-anion and three cationic potassium's. The slightly lower value for the dimer was most likely due to the slower ionic mobility of the larger, ruthenium dimer than the smaller, monomeric ferricyanide.

Considering the total formal charges of the two ruthenium centers (7+), and the two, deprotonated edta's (8-), the charge of the bridging group would have to be doubly-negative. A single oxo-bridge is compatible with this result. Other possible di-negative, oxygen-containing bridges include two hydroxides, or even a peroxide. The characterization of the dimer and its bridging group is described in the following sections.

5. MAGNETIC SUSCEPTIBILITY

The magnetic susceptibility of a solid sample of the ruthenium-edta dimer was measured at room temperature using the Guoy method and then corrected for diamagnetism using Pascal's constants (59). The corrected value is 1.79 Bohr Magnetons per dimer indicating the presence of one, unpaired-spin. A solid sample of $\text{HRu}_3\text{Y-OH}_2$ yielded a corrected value of 1.96 Bohr Magnetons, which also indicates the presence of one, unpaired-spin. The latter result is due to the low spin, \underline{d}^5 configuration of ruthenium (III).

In the case of the dimer, the formal oxidation states of the two rutheniums are (III) and (IV). For discrete metal centers with weak coupling, a value higher than 1.79 Bohr Magnetons is expected.

In a system with weak coupling between the two rutheniums, the expected magnetic behavior would be that for both a low-spin, \underline{d}^4 , and a low-spin, \underline{d}^5 system. The spin only value for the latter configuration is 1.73 B.M., while it is 2.83 B.M. for the latter. The expected magnetic susceptibility would then be 3.22 B.M. for the dimer. The value of 1.79 B.M. per dimer indicates that there must be spin pairing between the two rutheniums.

6. FORMATION OF THE [34] DIMER

A titration of Ru3Y-OH₂ with hydrogen peroxide was performed to establish the stoichiometry of the oxidation reaction to produce the "green" dimer. A 1.01 mM solution of Ru3Y-OH₂ was prepared and the pH was then adjusted to 5.50 with 1.00 M sodium hydroxide. At this pH, the proton on the dangling acetate arm (pKa = 2.90) has been neutralized, while the coordinated water remains fully protonated. Small increments of 48.3 mN hydrogen peroxide were then added to the Ru3Y-OH₂ and the pH was measured and was observed to decrease after each addition. Since hydrogen peroxide consumes protons upon reduction, the drop in Ph indicates that more than one proton per equivalent of peroxide was being generated.



The amount of acid generated upon each addition of peroxide was measured by back-titrating with 0.100 N NaOH to pH 5.50 and then a visible spectrum was recorded. The spectrum continued to change upon each addition of peroxide with bands growing in at 393 nm and 632 nm (see Figure 2). (The glitches at 240, 380 and 400 nm are problems associated with the HP-8450 spectrophotometer.) Two isosbestic points were observed; one at 271 nm ($\epsilon_{271} = 2,780 \pm 80 \text{ M}^{-1} \text{ cm}^{-1}$) and the other at 288 nm ($\epsilon_{288} = 2,710 \pm 80 \text{ M}^{-1} \text{ cm}^{-1}$) indicating the presence of only two species in solution. The value for the extinction coefficients for the dimer would be twice these.

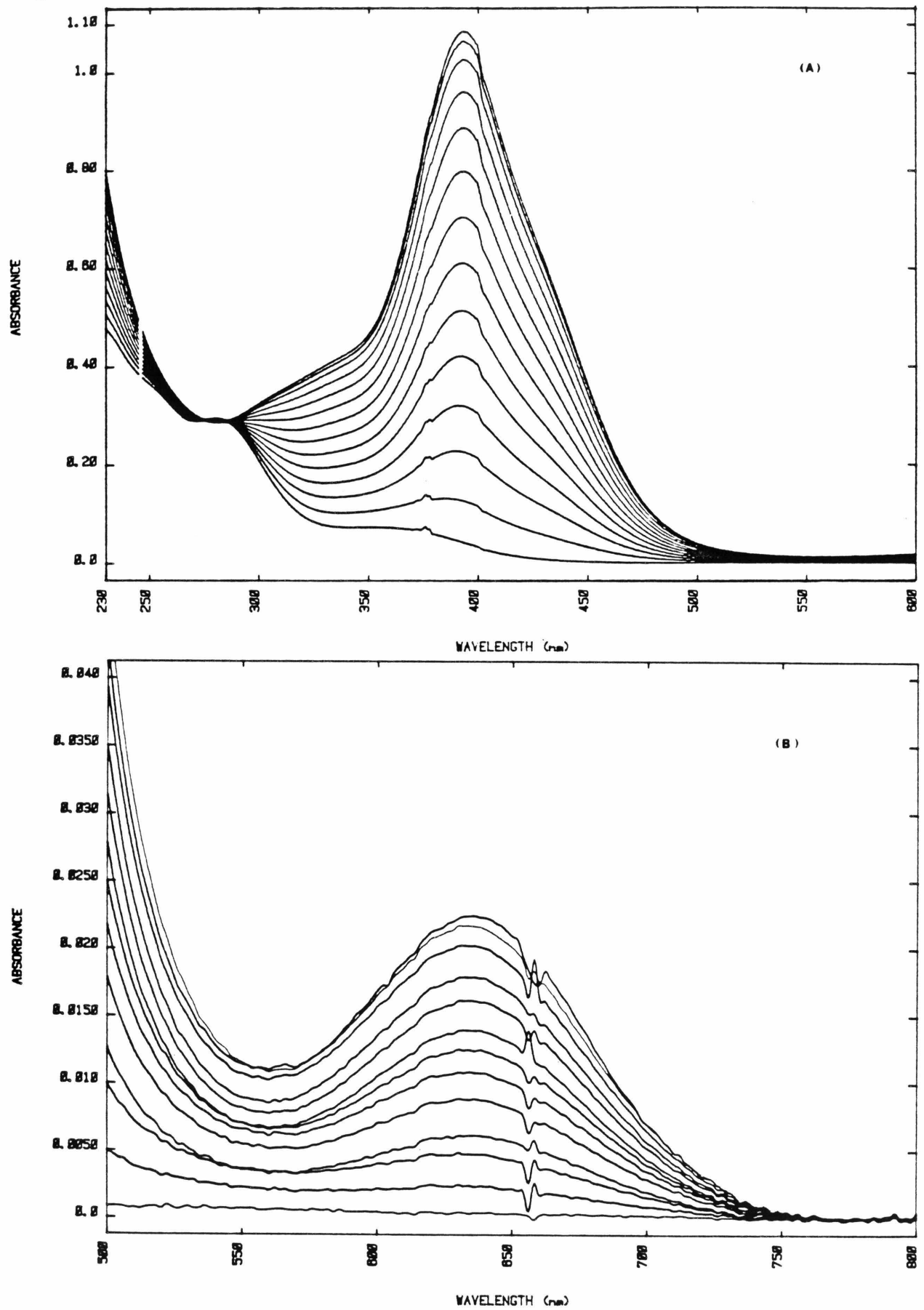
Figure 2

Optical spectrum of Ru3Y-OH₂ + hydrogen peroxide
at pH 5.50

Conditions: 1.01 mM Ru3Y-OH₂
pH 5.00 acetate buffer (50 mM)
total ionic strength = 0.200 N with NaTFA
total volume: 25.00 ml
H₂O₂ concentration: 48.3 mN
H₂O₂ additions: 25 microliters

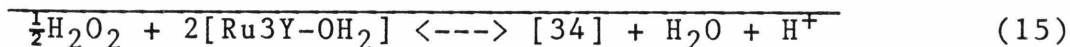
- A. 230-600 nm
- B. 500-800 nm

Figure 2



The dimerization is therefore rapid and, apparently, free of any complicating initial side reactions. Maxima were observed at 393 nm ($\epsilon_{393}=10,200\pm 310 \text{ M}^{-1}\text{cm}^{-1}$) and 632 nm ($\epsilon_{632}=210\pm 7 \text{ M}^{-1}\text{cm}^{-1}$) where the calculated extinction coefficients were based upon the initial concentration of Ru3Y-OH₂. Plots of the absorbance at 393 and 632 nm vs. the number of equivalents of peroxide added yielded straight lines with a slope of 1.05 equivalents per two moles of Ru3Y-OH₂ (see Figure 3). No further changes occurred in the spectrum after the addition of one equivalent of peroxide per two moles of rutheniums.

A plot of the equivalents of hydroxide used to back-titrate the acid generated by the addition of the peroxide yielded a straight line with a slope of one proton per equivalent of peroxide with the cessation of proton generation occurring at one equivalent of peroxide per two moles of ruthenium (see Figure 3). This, coupled with the proton consumption by the peroxide, yielded a net evolution of two protons per equivalent of peroxide. The overall stoichiometry for production of the [34] dimer was then,



[34] = ruthenium-edta dimer with the formal
oxidation states of Ru (III) and Ru (IV).

Figure 3*

A. Plot of μeq of base vs. μeq of H_2O_2

r^2 : 0.9998

intercept: $-47.1 \text{ E-}3$

slope: $0.924 \text{ eq OH}^-/\text{eq H}_2\text{O}_2$

B. Plot of absorbance (632 nm) vs. μeq of H_2O_2

r^2 : 0.9993

intercept: 0.0007

slope: $0.00165 \text{ abs}/\mu\text{eq H}_2\text{O}_2$

C. Plot of absorbance (393 nm) vs. μeq of H_2O_2

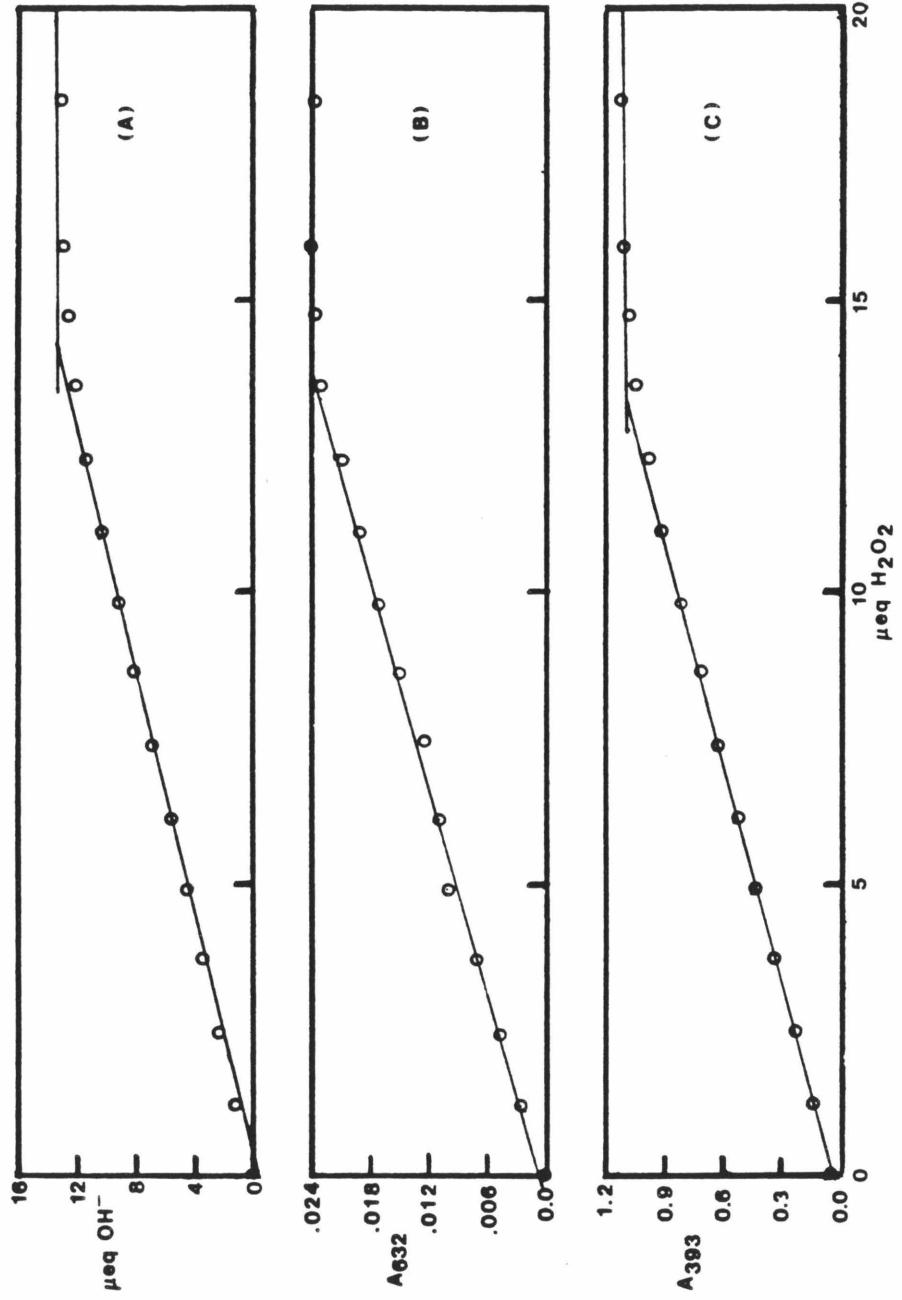
r^2 : 0.9998

intercept: 0.0391

slope: $0.785 \text{ abs}/\mu\text{eq of H}_2\text{O}_2$

* Data were fit with a linear regression program
supplied with an HP-41C calculator

Figure 3



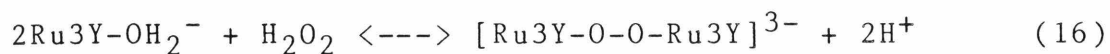
Further additions of hydrogen peroxide yielded no change in the electronic spectrum, nor any consumption, or generation, of protons. The formation of bubbles was also observed upon addition of a large excess of peroxide. The catalytic disproportionation of hydrogen peroxide to yield dioxygen and water by the [34] dimer will be discussed later.

Similar titration results were obtained when 0.100 M permanganate was used as the oxidant at pH's 3-5 and when 0.05824 M Ce(IV) was used at pH's 1-5. The electrolysis of a buffered, pH 5 solution of Ru₃Y-OH₂ at E = +1.000 V vs. SCE in pH 5, also required the same number of equivalents as above to produce the spectrum in Figure 2. Electrochemical details will be discussed in a later section. These redox titrations show that the oxidation of Ru₃Y-OH₂ leads to a green dimer and requires one electron per two moles of ruthenium.

These results agree with the observations of the production of a green complex upon oxidation of Ru₃Y-OH₂ by peroxide, dioxygen, or chlorate, reported by Ramanchandraiah (43), Ikeda, et al (44), and previously by Ezerskaya, et al (37-40). In all of these studies, however, the oxidation state of the rutheniums and the nature of the bridging group was unambiguous.

One possible structure could involve the formation of a peroxy-bridged ruthenium-edta dimer. Khan has recently reported the binding of dioxygen to Ru₃Y-OH₂ to form a

dimeric, Ru(III)-peroxo-Ru(III), complex. The possibility of a bridging peroxide in my experiments was ruled out by the stoichiometry determined by the titration. If the peroxide were just bridging two Ru3Y monomers, then the molar ratio of H₂O₂/Ru3Y-OH₂ should have been 1:2, while the ratio of H⁺/Ru3Y-OH₂ should have been 1:1 (see equation 16).



My results showed a peroxide to ruthenium molar ratio of 1:4, while the proton to ruthenium ration was 1:2. A mixed-valence peroxide bridged species would also not be compatible with the observed stoichiometry, since even more peroxide would have been required. The formation of the green complex by the other chemical oxidants also ruled out a peroxide-bridged species since these oxidants are not thermodynamically capable of oxidizing water to peroxide (70). The bridging group(s) must then be either a μ -oxo, or di- μ -hydroxy. This also suggests that the oxidized complex is a Ru(III)-Ru(IV), mixed-valence dimer.

Upon sitting for several days, the absorbances of the band maxima for the green complex (see Figure 2) were observed to decrease, but without any bands disappearing, or any new bands growing in. The cause of the decreased absorbance was not clear, but it may be due to an instability of the ruthenium-edta dimer induced by light. A similar change in the spectrum of the ruthenium-edta dimer isolated by Ikeda, et al, was also reported (44).

The absorbance maxima for the green complex reported in this study are the same as those reported for the green complexes reported previously (37,40,43,44), but my molar extinction coefficients are larger. It is felt that the reason for this is due to the rapid isolation of a more pure complex. When a solution of the green complex had been allowed to sit for several hours, or overnight, before isolating a solid, then less intense (by up to 20%) peak absorbances were observed when the solid was redissolved. The pure dissolved solid was also found to obey Beer's Law for concentrations between 0.1 μM - 1.5 μM for the band at 393 nm and 0.1 μM - 5.0 μM for the band at 632 nm. The slopes of the lines for the redissolved dimer exhibited molar extinction coefficients within 5% of those observed for the mother liquor.

When the pH was lowered to one, a decrease in the intensity of the band maxima (approximately 10%) was observed. A new band was also seen to grow in near 300 nm. Adjusting to the original pH restored the initial spectrum. The origin of these spectral changes was unclear, but similar results are also observed in the visible spectrum of Ru3Y-OH_2 (31). For the monomer, the free-acetate arm (pKa 2.90) is fully protonated at pH 1. If protonation of the carboxylate group led to the breaking of the hydrogen bond between it and the coordinated water (7), or the removal of the acetate group from a seventh coordination position for Ru3Y-OH_2 , then either of these effects could also be

occurring for the dimer. My guess is that a free acetate arm is interacting with the metal center(s), thereby causing a minor change in the ligand field about the ruthenium and leading to a decrease in the intensity of the band maxima. This also means that for quantitative comparison of spectra of ruthenium-edta dimer samples (as well as for Ru3Y-OH₂ samples), the pH of the solutions must be the same.

Recently, Khan and Ramachandraiah (43,45) reported that they observed a reaction between Ru3Y-OH₂ and dioxygen to form a green complex that has some spectral similarities to the [34] dimer I have described. In contrast to their results, I found that even continuous bubbling of dioxygen into a solution of Ru3Y-OH₂ for several days that was buffered at pH 5, did not produce a change in the visible spectrum. They did not mention the use of a buffered solution, only that the reaction occurred at pH 5. The exact conditions, however, that Khan and Ramachandraiah used in the production of their green complex, were unclear; the articles were not specific on this matter. If the pH was raised above 7 in the presence of air, I observed that the solution turned green (Ezerskaya noted similar behavior to mine (37)). It is possible that Khan and Ramachandraiah allowed the pH to rise above 7 during the production of the green dimer. A discussion of the quantitative reaction between dioxygen and Ru3Y at pH 7.7 occurs later in this report.

7. TITRATION OF THE [34] DIMER WITH BASE

When the pH of a solution of the [34] dimer was raised to greater than 8, dramatic changes occurred in the visible spectrum. To investigate this behavior, a 0.500 mM solution of the [34] dimer was titrated with standardized base and the visible spectrum recorded after each addition. The initial solution had a pH of 6.70, and its spectrum remained unchanged as the pH was increased, until about pH 8.70 (see Figure 4). The original spectrum consisted of the characteristic bands at 393 nm ($\epsilon_{393} = 20,400 \text{ M}^{-1}\text{cm}^{-1}$ based on the molar concentration of dimer) and 632 nm ($\epsilon_{632} = 420 \text{ M}^{-1}\text{cm}^{-1}$) with a broad shoulder at 310 nm ($\epsilon_{310} = 7,200 \text{ M}^{-1}\text{cm}^{-1}$), and a small shoulder at 424 nm (masked).

During the titration, an isosbestic point appeared at 284 nm ($\epsilon_{284} = 5,510 \text{ M}^{-1}\text{cm}^{-1}$), indicating the existence of just two species in solution. The titration was stopped at pH 12 where a stable spectrum (several hours) was recorded, with two band maxima at 324 nm ($\epsilon_{324} = 5,200 \text{ M}^{-1}\text{cm}^{-1}$) and 414 nm ($\epsilon_{414} = 4,000 \text{ M}^{-1}\text{cm}^{-1}$). A new band at >800 nm also appeared.

Due to the high pKa of the dimer, the pH titration curve was featureless, resembling that for the addition of a strong base to pure water. Only by analyzing the absorbance data with the assumption of a simple acid-base equilibrium was it possible to determine the dimer's pKa. The absorbance data at 393 nm were inserted into the Henderson-Hasselbach

Figure 4

Optical spectra of [34] dimer vs. pH

Conditions: 0.500 mM [34] dimer

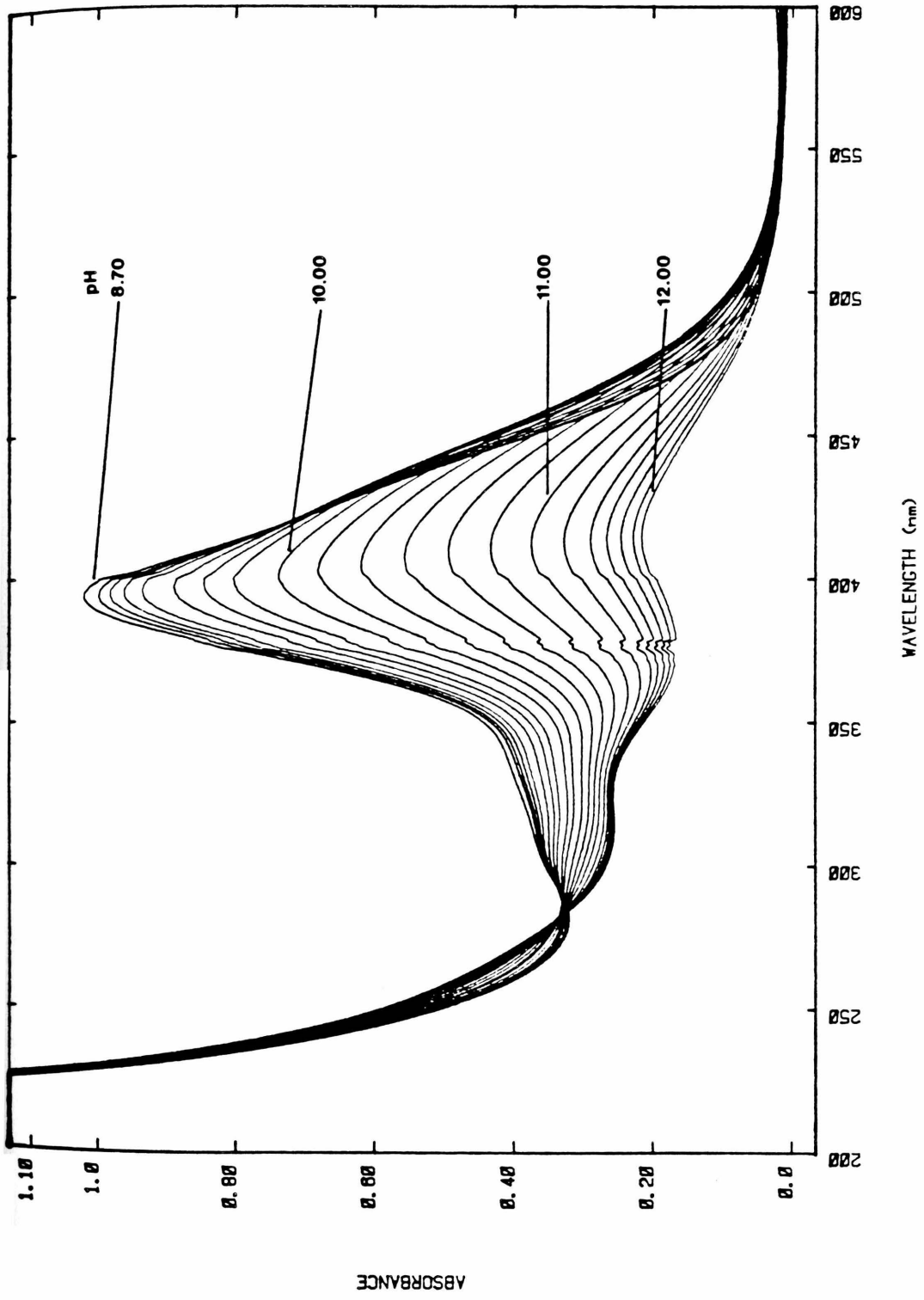
200-600 nm

Cell pathlength: 1.00 mm

Initial pH: 8.70

Final pH: 12.00

Figure 4



equation (70) to estimate the pKa in the following way:

$$\text{pKa} = \text{npH} - \log\left(\frac{[A]}{[HA]}\right) \quad (17)$$

The following assumptions were made to include the use of absorbance data in the above equation.

$$C_T = [HA] + [A] \quad (18)$$

$$A_\lambda = b(\epsilon_{HA}[HA] + \epsilon_A[A]) \quad (19)$$

where,

C_T = total dimer concentration

$[HA]$ = concentration of the acid form of the dimer

$[A]$ = concentration of the base form of the dimer

A_λ = absorbance at a given wavelength

ϵ_i = molar extinction coefficient at a given wavelength for an absorbing species

b = cell pathlength

These equations can be rearranged to give:

$$[HA] = \left\{ \frac{b\epsilon_A C_T - A_\lambda}{(\epsilon_A - \epsilon_{HA})b} \right\} \quad (20)$$

$$[A] = \left\{ \frac{A_\lambda - b\epsilon_{HA} C_T}{(\epsilon_A - \epsilon_{HA})b} \right\} \quad (21)$$

and substituting them into (17) yields,

$$\text{pKa} = \text{npH} - \log\left(\frac{b\epsilon_{HA} C_T - A_\lambda}{A_\lambda - b\epsilon_A C_T}\right) \quad (22)$$

when $\epsilon_A \neq \epsilon_{HA}$.

The term, $b\epsilon_{HA}C_T$, is the absorbance of the solution for the fully protonated form of the dimer, A_{HA} , while, $b\epsilon_A C_T$, is the absorbance of the solution for the fully deprotonated form, A_A . The former value was determined by measuring the absorbance of the solution at a pH just before the spectrum started to change during the titration with base, while the latter term was taken as the absorbance at a pH just after the spectrum stopped changing during the titration. Equation 22 assumes that the acid/base pair are at equilibrium. It was observed that the spectrum changed immediately upon addition of base and was stable for at least 15 minutes (the length of time between additions). The system also lacked any hysteresis upon back-titrating with acid. This latter procedure was carried out three times on the same solution. The spectrum, normalized for concentration, was identical for any pH in each of the titrations. The final concentration of dimer, after the the repetitive titrations with acid and base, was one-half the concentration of the initial base titration product. The expression used to determine the pKa was:

$$pKa = npH - \log \left(\frac{A_{HA} - A_{\lambda}}{A_{\lambda} - A_A} \right) \quad (23)$$

A plot of the log term vs. pH (Figure 5) yielded a pKa of 10.32 ± 0.02 . A general acid-base titration curve program

Figure 5

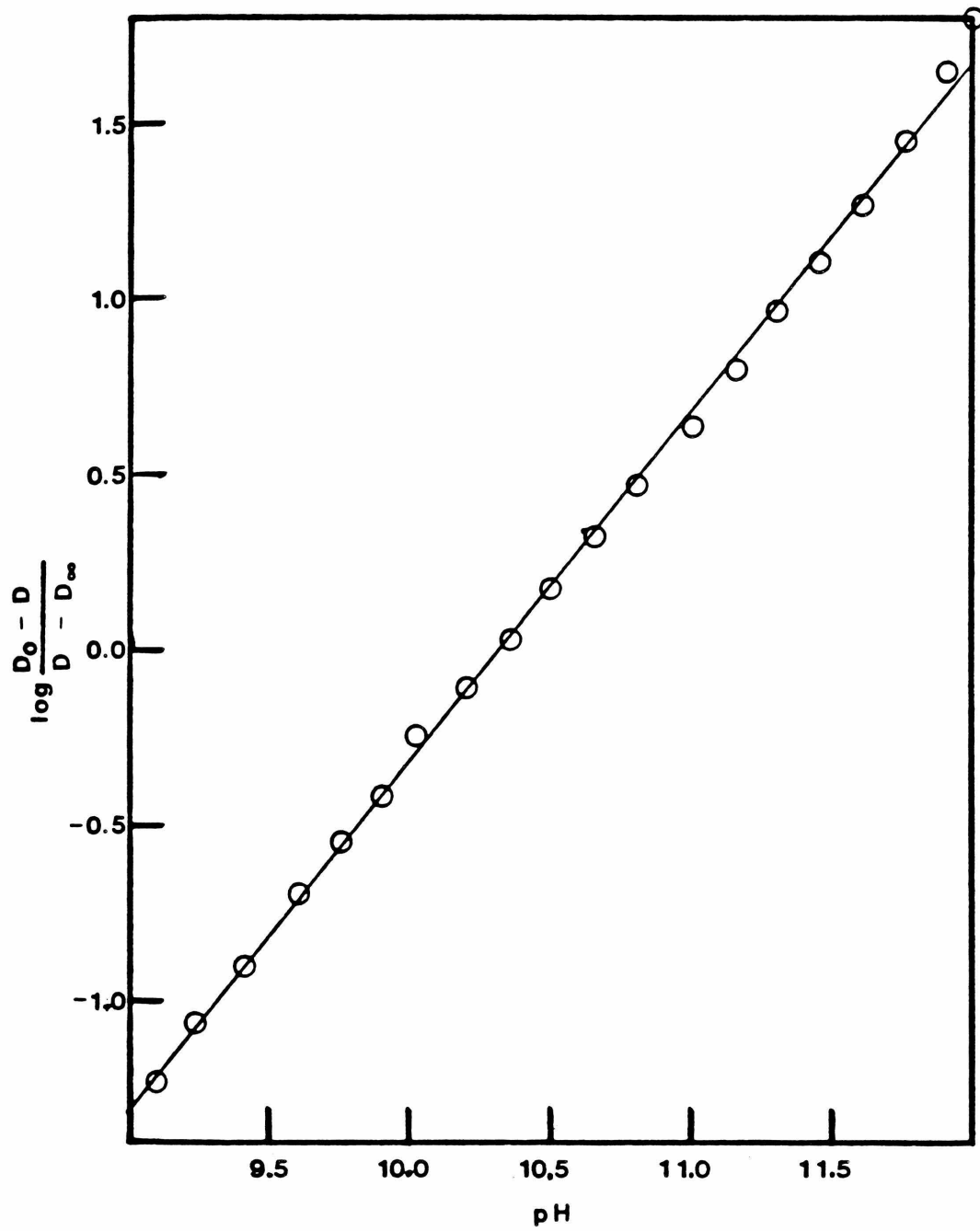
Plot of $\log\left(\frac{A_{\text{HA}} - A_{\lambda}}{A_{\lambda} - A_{\text{A}}}\right)$ vs. pH for [34] dimer at 393 nm

$$R^2 = 0.9994$$

$$\text{Intercept} = 10.32$$

$$\text{Slope} = 1.010$$

Figure 5



(71), modified to run on a Hewlett-Packard HP41C calculator, was written to simulate the data (see appendix for program listing). The pH titration curve for one of the titrations of a 0.500 mM solution of the [34] dimer, and with 0.110 N NaOH was fit very well by this program and gave a pKa of 10.32. A comparison of the simulation with the experimental results are shown in Figure 6.

The presence of one titratable proton, taken with the oxidation stoichiometry presented earlier suggested three possible structures for the [34] dimer.

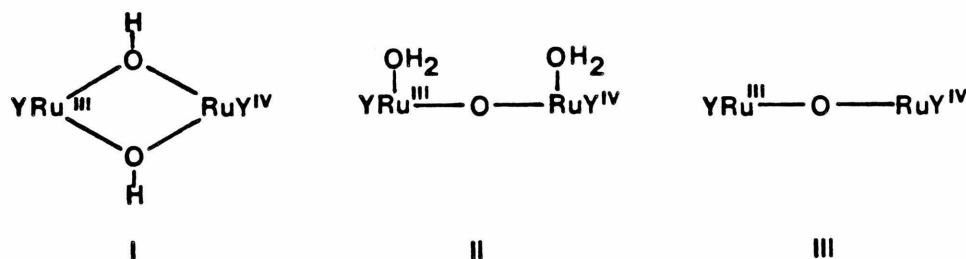


Diagram 3. Possible [34] dimer structures

In all cases, the remaining positions on the ruthenium are occupied by Y (edta). For structure I, the pKa of 10.3 would correspond to the deprotonation of one of the bridging hydroxide groups. For II, a proton of one of the coordinated water molecules would be removed, while for III, the hydroxide could displace a carboxylate group on one ruthenium center, or form a bridge between both rutheniums centers. The latter would yield a structure identical to the deprotonated form of I.

For structure III, the large difference between the

Figure 6

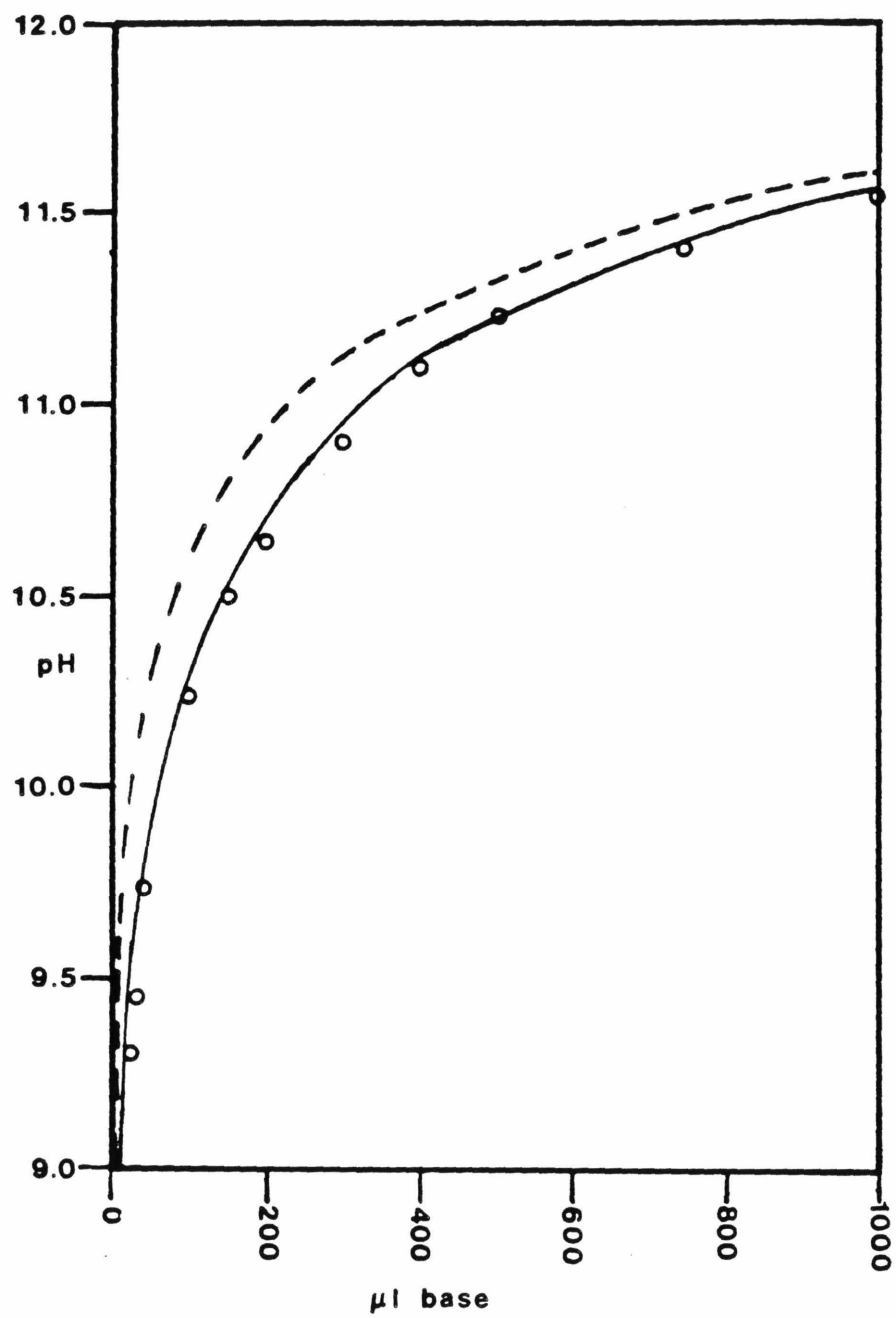
Plot of observed, and simulated titration curve of
the [34] dimer with base

Conditions: 0.500 mM [34] dimer
0.100 N NaOH
Volume: 25.00 ml

Legend:

solid line: simulated titration curve
pKa = 10.3
circles: experimental results
dashed line: titration of pure water with
base

Figure 6



spectra of the [34] dimer at high and low pH could be attributed to the big change in the structure resulting from the formation of the double bridge. The displacement of an acetate group by a hydroxide ion has been proposed for Cu and Hg edta complexes and was supported by infrared spectroscopy (72). Infrared studies of the [34] dimer, detailed later, showed similar results. For structure I, deprotonation would also lead to structural changes due to the bridge asymmetry. Structure II suggests that deprotonation is localized on only one of the rutheniums leading to asymmetry in the overall structure of the [34] dimer. In this case, it is most likely that the hydroxide would be centered on the Ru(IV) center due to the stronger acid character of ruthenium in successively higher oxidation states.

Asymmetry in the [34] dimer at high pH would also be expected to lead to a localization of the electronic spin so that the two rutheniums would have different electronic structures. The existence of the mixed-valence dimers also suggested the possibility of an intervalence transition (73). For ruthenium systems, these transitions generally appear in the near infrared region (800-2000 nm), and a study was, therefore, made of the protonated, and the unprotonated forms of the dimers in this region.

8. OPTICAL STUDIES OF THE RU-EDTA SYSTEM

A. [34] DIMER

Before presenting the results of the near infrared study of the [34] dimer, a brief review of mixed-valence metal complexes, and the theory used to study them by optical spectroscopy, is presented. The theory of Hush (73-74) will be considered and used to analyze the results for the [34] dimer. The spectral results for several other ruthenium-containing, mixed-valence complexes will be considered for comparison.

The study of mixed-valence metal complexes has received considerable attention over the past few decades (73-98). One of the most prevalent means of characterizing these complexes has been by studying their optical properties, especially in the visible and the near infrared regions. Mixed-valence ruthenium complexes have figured rather prominently in these studies owing to the fact that they are generally, substitution inert in their lower oxidation states, and that they exhibit electronic transitions easily measured by optical methods. The bulk of these studies have consisted of ruthenium-ammine, or ruthenium-bipyridine complexes, with various types of organic, or simple inorganic groups bridging the two metal centers. The main focus of the study of these mixed-valence complexes has been in trying to understand the relationship between the metal centers and the bridging group, and their effects on the

complex's electronic properties.

Even though mixed-valence complexes had been known for nearly a century, it was not until the end of the 1960's that Hush proposed a viable theoretical model to explain their behavior (73-74). He attempted to provide a theoretical basis for the physical properties of mixed-valence complexes and electron transfer reactions in solution. In Hush's model, the mixed-valence complex is considered to consist of two metal centers in different oxidation states connected by some sort of electronic interaction (this may be a bridge consisting of an atom, a molecule, or a direct interaction, like a metal-metal bond). It is assumed that the distance, r , between the two metal centers is such that the electronic coupling, H_{AB} , between them is small and that the auxiliary ligand environment around each metal is the same. The theory predicts that a moderately coupled, mixed-valence complex should exhibit an intervalence charge transfer (a light-induced metal-to-metal charge transfer) absorbance at an energy, E_{Op} , that is simply related to the energy barrier, ΔG_{th} , for thermal electron transfer ($E_{Op} = 4\Delta G_{th}^*$). Hush showed that for a symmetric molecule, and assuming that the two metals are simple harmonic oscillators,

$$E_{Op} = 4\Delta G_{th}^* \quad (24)$$

where,

$$E_{Op} = E_{in} + E_{out} \quad (25)$$

$$E_{in} = n \left(\frac{2f_1 f_2}{f_1 + f_2} \right) (d_1^{\circ} - d_2^{\circ})^2 \quad (26)$$

$$E_{out} = e^2 \left(\frac{1}{2a_1} + \frac{1}{2a_2} + \frac{1}{r} \right) \left(\frac{1}{D_{op}} - \frac{1}{D_s} \right) \quad (27)$$

where,

E_{in} = the energy associated with inner shell rearrangements

E_{out} = the energy associated with outer shell (solvent) rearrangements

n = the number of ligands per metal center

a_1, a_2 = metal-ligand bond lengths

f_1, f_2 = metal-ligand force constants

r = separation between the metal centers

D_{op}, D_s = optical and static dielectric constants of the solvents

These inner, and outer shell environments require nuclear rearrangements, and considering that nuclear motion is on the order of $1 \text{ E-}13$ sec while electronic motion is less than $1 \text{ E-}15$ sec (the Franck-Condon principle), there is a barrier to electron transfer that needs to be overcome. This activation barrier to electron transfer is due to the different metal-ligand bond lengths and their force constants in the two different oxidation states. Dielectric continuum effects are also considered in the model leading to solvent rearrangement contributions to the activation barrier (73-75).

It was also shown that the band width at half intensity

should be a function of the band maximum,

$$\Delta\bar{\nu}_{\frac{1}{2}} = (2310\bar{\nu}_{\max})^{\frac{1}{2}} \text{ cm}^{-1} \quad (28)$$

and that the degree of electronic coupling between the metal centers is related to the band maximum intensity (73,74),

$$H_{AB} = (2.05 \text{ E-}2) \left(\frac{\epsilon_{\max} \Delta\bar{\nu}_{\frac{1}{2}}}{\bar{\nu}} \right) \left(\frac{\bar{\nu}_{\max}}{r} \right) \text{ cm}^{-1} \quad (29)$$

where,

$\bar{\nu}_{\max}$ = molar absorptivity ($\underline{M}^{-1}\text{cm}^{-1}$)

$\Delta\bar{\nu}_{\frac{1}{2}}$ = band width at half intensity

$\bar{\nu}$ = energy of the band maximum

r = distance between the two metal centers (nm)

In an attempt to distinguish between different types of mixed-valence complexes, Robin and Day (75) described three main classes of mixed-valence complexes based on the amount of electronic interaction between the two-metal centers. In a Class I complex, the interaction between the two metal centers is considered weak and is usually due to a large separation of the metal centers, or different ligand environments on the two metals. These compounds exhibit only the sum of the properties of the isolated, mono-nuclear complexes. Class III compounds, on the other hand, exhibit complementary behavior. The interaction between the metal centers is so great that the individual metal complexes properties are now absent and the new spectral properties

characteristic of only the new complex are observable.

For Class II complexes, intermediate behavior between the two extreme classes is observed. Some of the phenomena of the discrete metal monomers may be seen, as well as the appearance of some new features. Equation 24 describes the case when H_{AB} is approximately zero (when the interaction between the two metal centers is negligible--the so-called, weakly coupled case). As the interaction energy increases, the thermal electron transfer barrier is lowered.

$$E_{th} = \left(\frac{E_{op}}{4} \right) - H_{AB} \quad (30)$$

When the interaction becomes very large, the two metal centers lose their individual identity and become strongly coupled (see Figure 7).

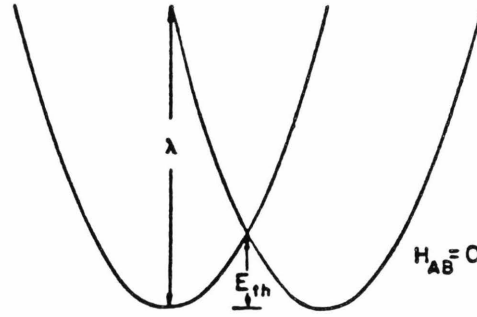
The first case in Figure 7 is a Class I system, where the thermal electron transfer process is non-adiabatic due to the system's two metal centers energy profiles not crossing at the intersection and, thus, having exactly zero electronic interaction. Due to the interaction energy being equal to zero, the intensity of the intervalence transfer band may not be observed. If the interaction energy is increased to slightly above zero ($H_{AB} = 0.05 E_{op}$), a Class II system with the same zero-order conditions as above splits the energy surfaces by $2H_{AB}$ at the intersection. This increases the probability that the system will remain on the lower surface and that the thermal electron transfer

Figure 7

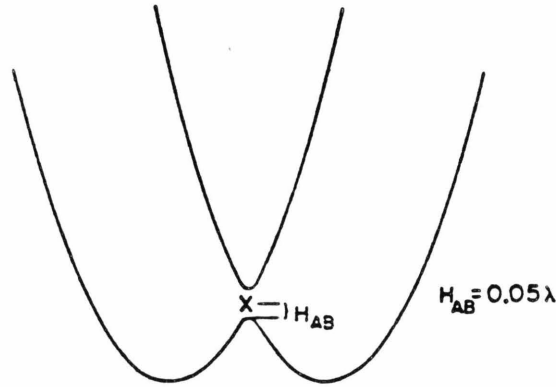
Potential energy vs. nuclear configuration for
symmetric, mixed-valence complexes

- A. Class I complex
- B. Class II complex
- C. Class III complex

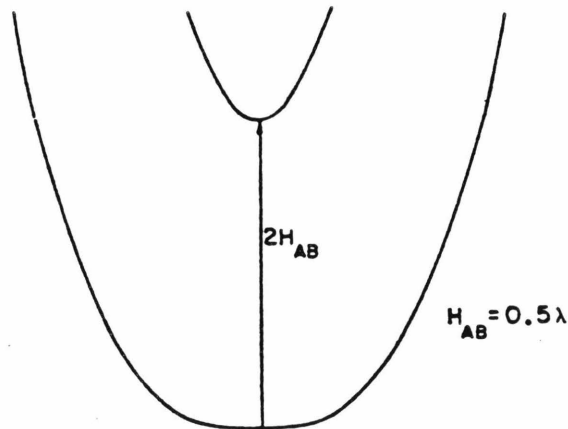
Figure 7



Class I



Class II



Class III

will be adiabatic. The intervalence transfer will now have a measurable intensity which reflects the amount of the interaction (equation 28). When the interaction energy is larger than twice the thermal barrier, then the lower surface possesses only a single minimum and a Class III complex results. In this case, the light absorption is no longer strictly defined as an intervalence transition (since the metal's oxidation states are intermediate between the two formal starting oxidation states), but is a charge transfer process with $E_{op} = 2H_{AB}$. A corollary to this is that the position of a mixed-valence band of a Class II complex is related to E_{th} , but that for a Class III complex the position is related to H_{AB} (80).

The magnitude of the splitting at the intersection of the reactant and product curves is $2H_{AB}$, and is related to the intervalence band intensity through equation 28. For an adiabatic system ($\kappa = 1$),

$$(4.6E-3)(H_{AB}^2)(\bar{\nu}_{max})^{-\frac{1}{2}} > 1 \quad (31)$$

otherwise,

$$\kappa = \left[\frac{2(1-\exp[(-2.3E-3)(H_{AB})^2(\bar{\nu}_{max})^2])}{2-\exp[(-2.3E-3)(H_{AB})^2\bar{\nu}^2]} \right] \quad (32)$$

and the reaction is nonadiabatic (80-82).

To determine which Class (75) the [34] dimer belonged, the near infrared spectra of a pD 8, and a pD 13, unbuffered solution were measured. A 1.84 mM solution of the [34]

dimer produced two fairly intense bands at 1178 nm ($8,500 \text{ cm}^{-1}$, $\epsilon_{478} = 420 \pm 10 \underline{\text{M}}^{-1} \text{cm}^{-1}$) and 632 nm ($15,800 \text{ cm}^{-1}$, $\epsilon_{632} = 420 \pm 10 \underline{\text{M}}^{-1} \text{cm}^{-1}$) at pD 8 (see Figure 8). A portion of the above solution was then adjusted to pD 13 with the addition of concentrated NaOD. The positions and intensities of the two lowest energy bands then changed to 1250 nm ($8,000 \text{ cm}^{-1}$, $\epsilon_{250} = 435 \pm 10 \underline{\text{M}}^{-1} \text{cm}^{-1}$) and 968 nm ($10,300 \text{ cm}^{-1}$, $\epsilon_{968} = 965 \pm 20 \underline{\text{M}}^{-1} \text{cm}^{-1}$) (see Figure 8).

For a Class II complex with a localized bonding scheme, Hush's model predicts that the bandwidth at half-maximum is a function of the band maximum (see equation 28). Using this relationship, and measuring the values at different pD's, it was found that the band widths were too narrow in all cases for a Class II complex (see Table 3). A further test of the Class designation of the dimer is the solvent dependence of the band attributed to the intervalence transition (see equation 27) (73,74,81,93). A solvent study was performed using the tri-potassium salt of the [34] dimer dissolved in dimethyl sulfoxide and ethylene glycol (approximately $0.1 \underline{\text{mM}}$) (the [34] dimer was not soluble in ethanol, methanol, dimethyl formamide, acetone, or propylene carbonate). The energy of the band in the near infrared was not observed to change for either of these solvents. These experiments, thus, indicate that both the protonated and the unprotonated forms of the [34] dimer are Class III ions and they have a symmetric, delocalized ground state.

No direct insight into the nature of the bridging group

Figure 8

Near-infrared spectra of [34] dimer

Conditions: A) 1.00 mM [34] in D₂O

B) 0.500mM [34] in D₂O

Cell pathlength: 1.00 cm

Scan range: 550-1600 nm

A. pD 5.0

B. pD 13.0

Figure 8

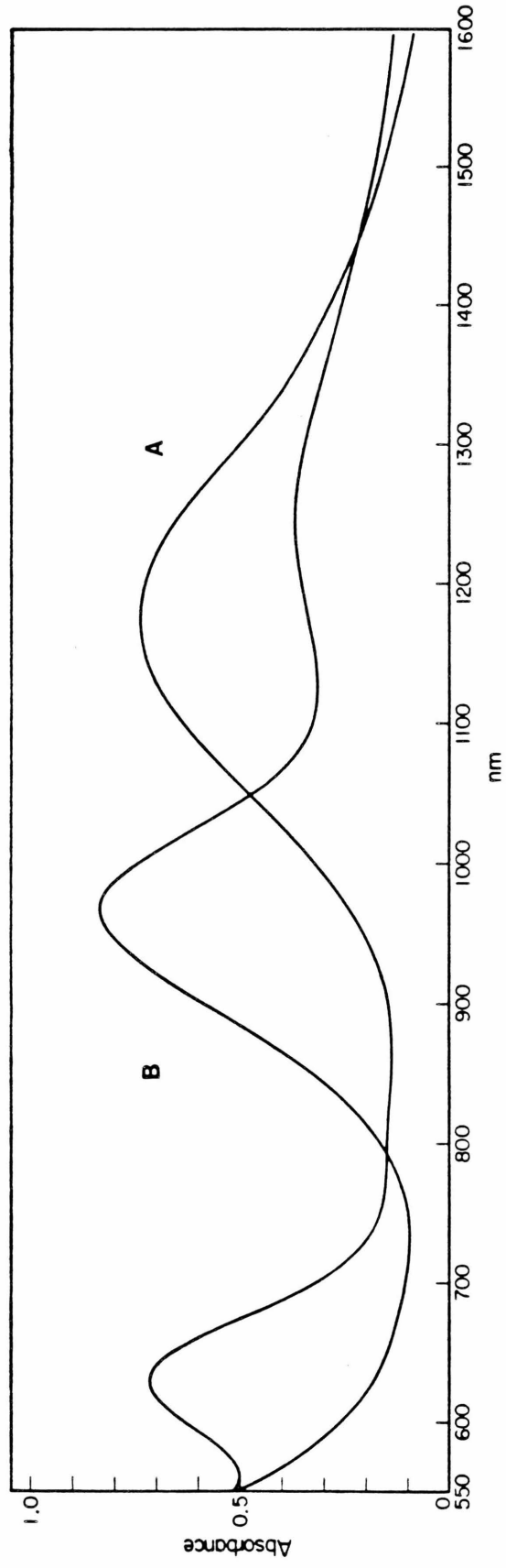


Table 3

Near-infrared results for [34] dimer

Table 3^a

<u>pD</u>	<u>$\bar{\nu}_{\max}$</u>	<u>$\Delta\bar{\nu}_{\frac{1}{2}}(\text{calc})$</u>	<u>$\Delta\bar{\nu}_{\frac{1}{2}}(\text{obsd})$</u>	<u>$\bar{\nu}_{\frac{1}{2}}(\text{calc})$</u>	<u>$\bar{\nu}_{\frac{1}{2}}(\text{obsd})$</u>
5	8490	4430	2440	10700	9830
				6280	7390
	15800	6050	2780 ^b	18800	***
				12800	***
13	8000	4300	2560 ^b	10150	***
				5850	6720
	10300	4800	2400 ^c	12700	11500
				7900	***

a. all values are in cm^{-1}

b. twice the low energy side

c. twice the high energy side

between the rutheniums was obtained by these results, however, but the likelihood of just a simple deprotonation of one of the coordinated water molecules for Structure II in Diagram 3 appears to be ruled out. As mentioned earlier, a non-bridging hydroxide would favor coordination to Ru(IV), while a coordinated water molecule would favor Ru(III). This would then be expected to lead to a localization of the charge on the rutheniums, producing a Class II ion. A Class II designation has been ruled out by the band analysis described above for the high pH form of the [34] dimer. The more symmetric μ -oxo, μ -hydroxo bridged dimer may be the form that exists upon deprotonation.

Several other ruthenium systems are already known to produce μ -oxo bridged dimers (46,47,68,106), although there is some question as to whether or not di- μ -hydroxo bridging occurs (8,104). Dwyer (104) felt that the dimer formed by $[(\text{phen})_2(\text{OH}_2)_2\text{Ru}]^{3+}$ in an aqueous media, contained di- μ -hydroxy bridging groups, while Meyer, et al (18), proposed a single μ -oxo bridge (see Diagram 3, Structures I and III). Without a crystal structure, it is very difficult to distinguish between these two structures. Cases exist for both bridging modes (99-104), but second and third row metals tend to prefer oxo-bridging over hydroxo linkages (99). A crystal structure was obtained for $[(\text{bpy})_2(\text{NO}_2)\text{Ru}]_2\text{O}(\text{PF}_6)_2$ (68) indicating a slightly bent single μ -oxo bridge. A comparison of the aqueous solution spectrum of this complex with that observed for Dwyer's

complex were quite similar and Meyer, et al (18) concluded that Dwyer's complex was also μ -oxo bridged (18).

Several of the ruthenium complexes containing aquo, or oxo-ligands dimerize in their higher oxidation states. These dimers are all apparently, μ -oxo bridged. Examples with known crystal structures include ruthenium red $([(\text{NH}_3)_5\text{RuORu}(\text{NH}_3)_4\text{ORu}(\text{NH}_3)_5]^{6+})$, formally a [343] trimer (105), $([\text{Cl}_5\text{Ru}]_2\text{O}]^{4-})$, which is formally a [44] dimer (106), and $([(\text{bipy})_2(\text{NO}_2)\text{Ru}]_2\text{O}]^{2+})$, which is a [33] dimer. By analogy to these systems, ruthenium brown [434], the one-electron, oxidized product of ruthenium red, $([(\text{NH}_3)_5\text{RuORu}(\text{NH}_3)_5]^{4+/5+})$, both the [33] and the [34] forms (46) and the [34] dimer of the ruthenium-bipyridine system are postulated as being oxo-bridged. There is no comparison possible between $([\text{Cl}_5\text{Ru}]_2\text{O}]^{4-})$ and its reduced form since the latter complex is not stable upon reduction and decomposes to form the $([\text{Cl}_5\text{RuOH}_2]^{2-})$ monomer. One last important example of a high oxidation state ruthenium complex that does not exist as a monomer is ruthenium dioxide, one of the best known compounds for the catalytic evolution of the dioxygen from water. Ruthenium dioxide consists of a chain-like array of ruthenium (IV) units linked together by oxo-bridges in a rutile structure (107,108). For comparison, the electronic absorptions for these systems are listed in Table 4.

The molecular orbital bonding scheme that has been proposed for these systems was first introduced by Dunitz

Table 4

Electronic spectra of various Ru dimers and trimers

Table 4

<u>Complex</u>	<u>Ox. St.</u>	<u>λ, nm</u>	<u>E, cm^{-1}</u>	<u>ϵ, $\text{M}^{-1}\text{cm}^{-1}$</u>	<u>Ref.</u>
$([(\text{NH}_3)_5\text{Ru}]_2\text{O})^{4+}$	[33]	503	19900	16230	46
		386	25900	5430	
$([(\text{NH}_3)_5\text{Ru}]_2\text{O})^{5+}$	[34]	616	16300	271	46
		342	29300	25280	
		255	39200	2100	
$(\text{Cl}_5\text{Ru}]_2\text{O})^{4-}$	[44]	500	20000	5000	112
$([(\text{NH}_3)_5\text{Ru}]_2\text{Ru}(\text{NH}_3)_4)^{6+}$	[343]	532	18800	69000	66
$([(\text{bipy})_2\text{ClRu}]_2\text{O})^{2+}$	[33]	672	14900	17900	18
$([(\text{bipy})_2\text{ClRu}]_2\text{O})^{3+}$	[34]	470	21300	19700	18
$([(\text{bipy})_2(\text{OH}_2)\text{Ru}]_2\text{O})^{4+}$	[33]	660	15150	25000	18
		410	24400	9500	
$([\text{RuY}]_2\text{O})^{3-}$, pH 5	[34]	1178	8500	420	*
		632	15800	420	
		393	25400	20400	
$([\text{RuY}]_2(\text{O})(\text{OH}))^{4-}$, pH 13	[34]	1250	8000	420	*
		968	10300	965	
		414	24150	4000	
		324	30900	5200	
$(\text{Ru}_3\text{Y}-\text{OH}_2)^-$, pH 5	[3]	350	28600	663	*
		281	35600	2800	
		255	39200	3130	
		227	44050	4180	
$(\text{Ru}_3\text{Y}-\text{OH})^{2-}$, pH 9	[3]	532	18800	53	*
		298	33500	2160	
		232	43100	4200	

* this work

and Orgel (109,110) in the early 1950's. The model helped to explain the observed diamagnetism, the short, linear Ru-O-Ru bonds (1.80 Å vs. 1.98 Å for single bond character), and the normal Ru-Cl bond lengths (2.34 Å) of $[(Cl_5Ru)_2O]^{4-}$ (see Figure 9). In this bonding scheme, the p_x , and p_y orbitals of the oxygen combine with the d_{xz} and d_{yz} orbitals of each ruthenium to form molecular orbitals of π symmetry in a D_{4h} crystal field. The remaining d_{xy} pair of orbitals are considered to not interact with the bridging oxygen, or with each other, due to their orientation and the separation of the metal centers (3.6 Å). They formally possess δ bond character. Filling the new molecular orbitals with the twelve electrons from the three interacting atoms fills the six lowest energy orbitals, leaving the two π^* orbitals unoccupied. All of the electrons are now paired, accounting for the complex's diamagnetism. The structural features are now seen to be attributable to the net-bonding interactions through the Ru-O-Ru π system. In an analysis of the visible, Raman and infrared spectra of $[(Cl_5Ru)_2O]^{4-}$, Clark pointed out that the lowest allowed transitions involved excitation of the π non-bonding electrons to the π^* level and was not the $\pi^* \leftarrow \pi^b$ transition (69,111). Using the orbital symmetry in the D_{4h} point group he noted that $e^* \leftarrow b_1^u$ was a forbidden, electric dipole transition, while two other transitions from the π non-bonding level were formally allowed ($e_u^* \leftarrow b_{2g}$, e_g). The $e_u^* \leftarrow e_b$ transition is also electric dipole

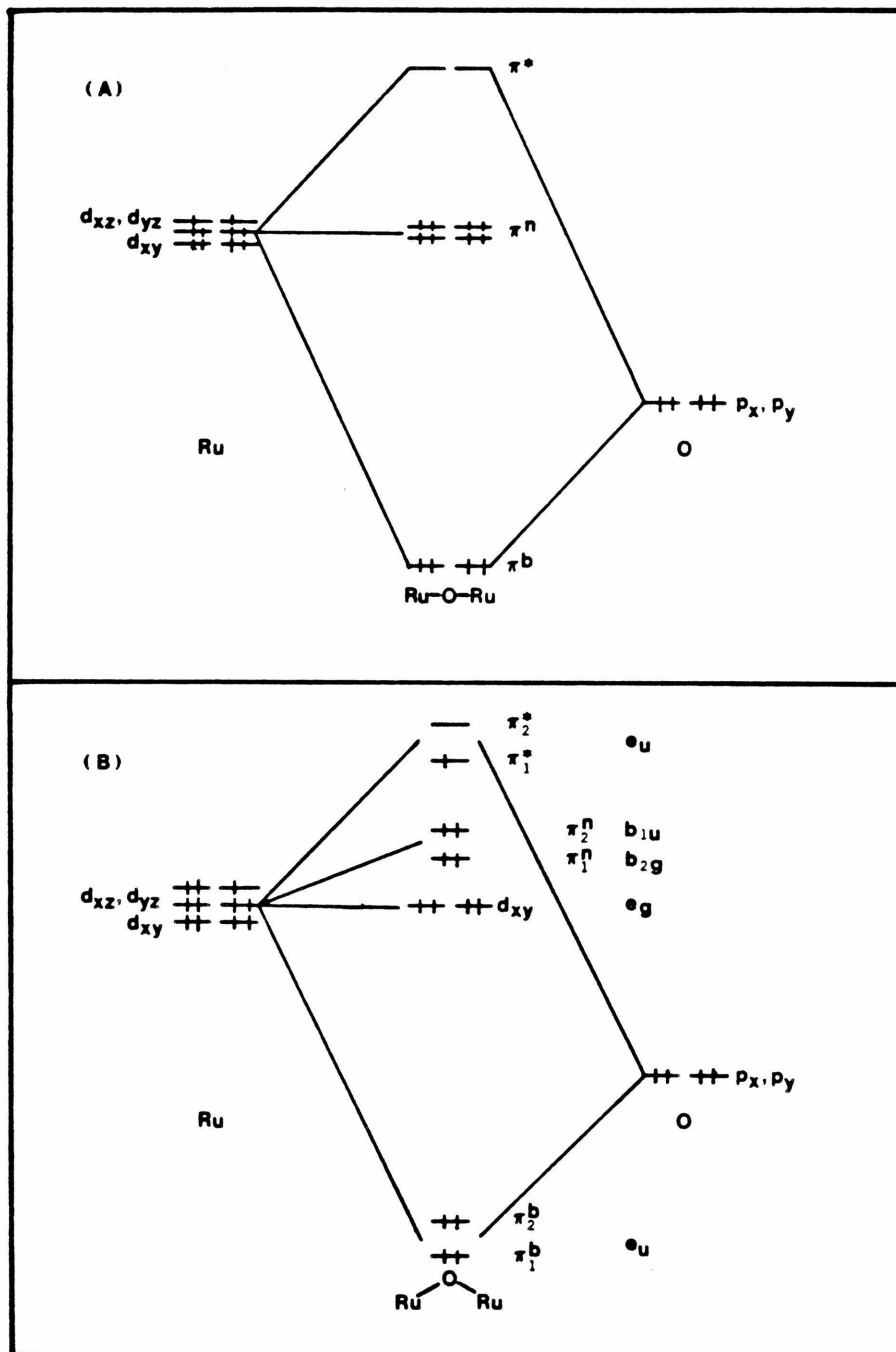
Figure 9

Dunitz-Orgel diagrams

A. Ru-O-Ru linear model (12 electrons: [44])

B. Ru-O-Ru bent model (13 electrons: [34])

Figure 9



forbidden. Clark then assigned the observed electronic transition at $20,000 \text{ cm}^{-1}$ to the metal-localized transitions from the π non-bonding orbitals to π^* .

By analogy, Baumann and Meyer (46) assumed a slightly bent Ru-O-Ru structure for the ruthenium 4+ and 5+ decaammine dimers ([33] and [34]) and used the Dunitz-Orgel scheme for assigning their spectra and the spectra of the ruthenium-bipyridine μ -oxo bridged dimers (18,47). In the case of the decaammine system, there are 14 and 13 total electrons for the [33] and [34] dimers, respectively. The former complex is diamagnetic at low temperatures and attained more paramagnetic behavior as the temperature was increased. This implies a splitting of the π^* levels leading to a pairing of the two highest energy electrons at low temperatures and to the observed paramagnetism at higher temperatures. The splitting of the Π^* states was found to be 170 cm^{-1} .

A comparison of the spectra of the ruthenium-edta dimers with the spectra of the other ruthenium oxo-bridged dimers shows some similarities between them, as well as some glaring differences. The band at 632 nm ($15,800 \text{ cm}^{-1}$) for the [34] ruthenium-edta dimer is similar in energy and intensity to the decaammine system, as are the bands at 393 nm ($25,500 \text{ cm}^{-1}$) and 424 nm ($23,600 \text{ cm}^{-1}$) and the obscured band(s) in the 300 nm ($33,300 \text{ cm}^{-1}$) region. Meyer's studies of the ruthenium-bipyridine systems also mention a green, mixed-valence [34] dimer, but did not provide any details

about this complex. The difference between the ruthenium-edta system and the others occurs in the near infrared region where the ruthenium-edta [34] dimers are the first ones in the group to exhibit a transition.

A mixed-valence [34] dimer is apparently the favored product upon oxidation of ruthenium (III). The different [34] dimers all appear to have a characteristic green color due to a band near 650 nm. This indicates that the formation of the mixed-valence dimer is favorable in several different systems, and that electronic interactions appear to dominate over other factors, such as the auxiliary ligands and the overall charge on the molecule. All of the [34] dimers that have been studied also appear to have a band in the ultraviolet region near 350 nm with very large intensity. The appearance of a band in the near infrared for the ruthenium-edta [34] dimers thus makes these complexes stand out from the others. Either the ruthenium-edta system has a special property that differentiates it from the other dimeric systems, or a reinvestigation of the near infrared system for the other systems needs to be performed.

If a simple, Dunitz-Orgel orbital scheme is considered as the basis for the ruthenium [34] dimers, some problems arise in assigning the transitions observed for the ruthenium-edta system. Clark and Meyer have both concluded that the intense band in the spectra of the dimers was attributable to the two $\pi^* \leftarrow \pi^n$ electric dipole allowed

transitions. For the mixed valence complexes studied by Meyer, the low intensity band in the visible was described as a $\sigma^* \leftarrow \pi^*$ "d-d" type transition. No evidence of a transition in the near infrared was mentioned in the reports on any of these complexes. If these assignments are followed for the ruthenium-edta [34] dimer, then the origin of the near infrared band is unclear.

One possibility could be that some type of ligand interaction causes the π_2^n orbitals to be of higher energy upon dimerization. Ligand-field effects, such as a trigonal perturbation of the d-orbitals caused by the different ligand field strengths of a carboxylate compared to an ammine, and a non-linear Ru-O-Ru structure could cause these changes. The possibility of a seven coordinate ruthenium must also be considered. The $e_u \leftarrow b_{1u}$ transition would then be allowed due to the lower symmetry of the complex. A second $\sigma^* \leftarrow \pi^*$ transition might also be expected with the reordering of the energy levels. There is evidence of several bands on the low, and high energy sides of the large 393 nm band which may be attributable to these other transitions. The inapplicability of the Dunitz-Orgel model for these systems should also be considered. The lack of any structural data and any detailed spectral measurements (such as low temperature, optical polarization studies) however, makes any definitive assignments for these transitions very tenuous and a rigorous study is required before any conclusions about the bonding scheme can be made

(for this and the other ruthenium dimers.)

Even with structural data and detailed spectral measurements, there is still controversy over the origin of the transitions in some oxo-bridging systems (112-116). The $[\text{ORe}(\text{CN})_4\text{ORe}(\text{CN})_4\text{O}]^{4-}$ ion has a linear $\text{O}=\text{Re}-\text{O}-\text{Re}=\text{O}$ structure, but is not fit well by the Dunitz-Orgel model (115,116). Also, the crystal structure of $\text{enH}_2[(\text{FeHEDTA})_2\text{O}]$ exhibits a nearly linear $\text{Fe}-\text{O}-\text{Fe}$ unit (165°), which, upon extensive magnetic and spectral measurements, was concluded to be best described by a high-spin, ligand-field model (113,114), and not by the Dunitz-Orgel model. Great caution must therefore be exercised when assigning the transitions for μ -oxo bridged systems.

The near-infrared spectral response of the ruthenium-edta [34] dimer as the pH was changed also provided some interesting points of comparison (see Figures 4 and 8, and Table 3). Upon raising the pH past the high pK_a (10.32), the two lowest energy transitions shifted to lower energy. The amount of the shift for the lowest energy transition was 500 cm^{-1} ($8,500 \text{ cm}^{-1}$ to $8,000 \text{ cm}^{-1}$), while for the next highest energy transition, the shift was $5,500 \text{ cm}^{-1}$ ($15,800 \text{ cm}^{-1}$ to $10,300 \text{ cm}^{-1}$). The lowest energy transition maintained the same intensity, while the next lowest transition was observed to double in intensity.

The lowering of the energy of the transitions is consistent with the weaker ligand-strength of a hydroxide ion when compared to other type's of oxygen-containing

ligands. The magnitude of the shifts and the change in the extinction coefficient indicate that the effect of the deprotonation, or the hydroxide incorporation, affects these two transitions differently.

A much more dramatic change occurred in the positions and intensities for the higher energy transitions of the [34] dimer when the pH was increased. The dominant charge transfer band at 393 nm ($25,500 \text{ cm}^{-1}$) decreased dramatically in intensity and yielded two lesser intense charge transfer bands at 324 nm ($30,900 \text{ cm}^{-1}$) and 414 nm ($24,150 \text{ cm}^{-1}$) (see Figure 4). The incorporation of a bridging hydroxide (see Diagram 3, Structures I and III) could lead to a significantly different ordering of the dimer's energy levels and the change in the charge transfer spectrum.

An alternative explanation considers the maintenance of the single, μ -oxo bridged structure and the removal of an acetate arm with coordination of a hydroxide to only one of the rutheniums. In this case, the hydroxide would be expected to stabilize the Ru(IV) oxidation state. This would then lead to an asymmetry in the molecule and the possibility of a localization of the electron spins. This would then result in a broadening of the near infrared transition towards that expected for a Class II complex. The latter behavior, however, was not observed. The bandwidth for the two lowest energy transitions of the [34] dimers remained nearly the same at any pH. The narrow bandwidth of the near infrared band suggests, therefore,

that the symmetry of the dimer was maintained at the higher pH. The additional bridging hydroxide group would be most compatible with this result.

B. RU(III)-EDTA OPTICAL SPECTRA RESULTS

For comparison, the effect of the ligand-field strength of a few coordinated ligands on ruthenium(III) are listed in Table 5. As expected, the general trend of the spectrochemical series: $N > O > X^- \approx OH^-$ containing ligands is observed. The values for ligand-metal charge transfer (LMCT) bands also follows the optical electronegativity scale initially proposed by Jorgenson (117,118).

Using these values, it can be seen that the ruthenium(III)-edta system fits into these patterns. The position of the prominent $Ru3Y-OH_2$ bands are shifted to lower energy relative to the hexaquo complex, but are similar in energy to those for the tris-oxalato complex. In addition, the presence of two high energy shoulders are also discernable on the charge transfer band at 281 nm ($35,600 \text{ cm}^{-1}$) (see Figure 10). Their prominence was observed at pH's above $HRu3Y-OH_2$'s first pKa (pH 3-5), and upon an anaerobic oxidation of $Ru2Y-OH_2$ at pH 5. With time, the prominence of the bands diminished. The exact origin of these transitions remains unclear, but they may be indicative of a labilization of the three, coordinated acetate arms with assistance of the fourth, free acetate arm, since ruthenium acetate complexes exhibit transitions

Table 5

Optical Spectra Data of Ruthenium (III) Complexes

Table 5

<u>Complex</u>	<u>λ, nm</u>	<u>E, cm^{-1}</u>	<u>ϵ, $\text{M}^{-1}\text{cm}^{-1}$</u>	<u>Assignment</u>
$\text{Ru}(\text{NH}_3)_6^{3+}$ a	320	31300	100	
	275	36400	479	
$\text{Ru}(\text{ox})_3^{3-}$ a	631	15850	11	${}^4\text{T}_{1g} \leftarrow {}^2\text{T}_{2g}$
	490	20400	28	${}^4\text{T}_{2g} \leftarrow {}^2\text{T}_{2g}$
	376	26600	350	${}^2\text{A}_{2g} \leftarrow {}^2\text{T}_{2g}$
	288	34700	320	${}^2\text{T}_{1g} \leftarrow {}^2\text{T}_{2g}$
RuCl_6^{3-} a	349	28650	3000	LMCT
$\text{Ru}(\text{OH}_2)_6^{3+}$ a	600	16700	0.6	${}^4\text{T}_{1g} \leftarrow {}^2\text{T}_{2g}$
	392	25500	60	${}^2\text{A}_{2g}, {}^2\text{T}_{1g} \leftarrow {}^2\text{T}_{2g}$
	225	44400	2480	LMCT
$\text{Ru}(\text{OH}_2)_5\text{Cl}^{2+}$ a	318	31500	661	LMCT
$\text{Ru}(\text{OH}_2)_5\text{Br}^{2+}$ a	385	26000	536	LMCT
$\text{Ru}(\text{OH}_2)_5\text{OH}^{2+}$ a	290	34500	1650	LMCT
$\text{Ru}3\text{Y-OH}_2^-$, pH5 b	350	28600	663	
	281	35600	2800	
	255	39200	3130	
	227	44050	4180	
$\text{Ru}3\text{Y-OH}^{2-}$, pH9 b	532	18800	53	
	298	33500	2160	
	232	43100	4200	

a. ref 119, and the references, therein.

b. this work

in this region. This sort of assistance has been cited by Creutz to explain the observation of a second thiocyanate coordinating to Ru3Y-OH_2 (7). If these transitions are ascribed to LMCT transitions due to the coordinated acetate arms, then any isomerization, or the degree of coordination would affect them.

As the pH is raised from 5, isosbestic points appear in the optical spectra of Ru3Y-OH_2 . The two highest energy isosbestic points actually coincide with the maxima of the high-energy shoulders at pH 5. These maxima were extracted from a derivative spectrum of the absorbance data using the Hewlett-Packard HP-8450. The presence of only two species in solution was substantiated by the presence of the isosbestic points.

The shift to lower energy for Ru3Y-OH^{2-} vs. Ru3YOH_2^- for all of the transitions parallels the hexa-aquo complexes. For the deprotonated form, the presence of a weak band at 532 nm ($\epsilon_{532} = 50 \text{ M}^{-1}\text{s}^{-1}$, $18,800 \text{ cm}^{-1}$) was observed. This transition is most likely spin-forbidden, and use of the detailed analysis of Harzion (119) would help in assigning the ligand field parameters, Dq and B.

Using the values of Harzion and Navon (119) for the hexa-aquo system, the shifts upon deprotonation of a water in the charge transfer band are found to be almost $10,000 \text{ cm}^{-1}$ towards lower energy. The changes for the Ru3Y-OH_2 system shows a shift of $2,000 \text{ cm}^{-1}$ for the only prominent band, while the highest energy bands are no longer

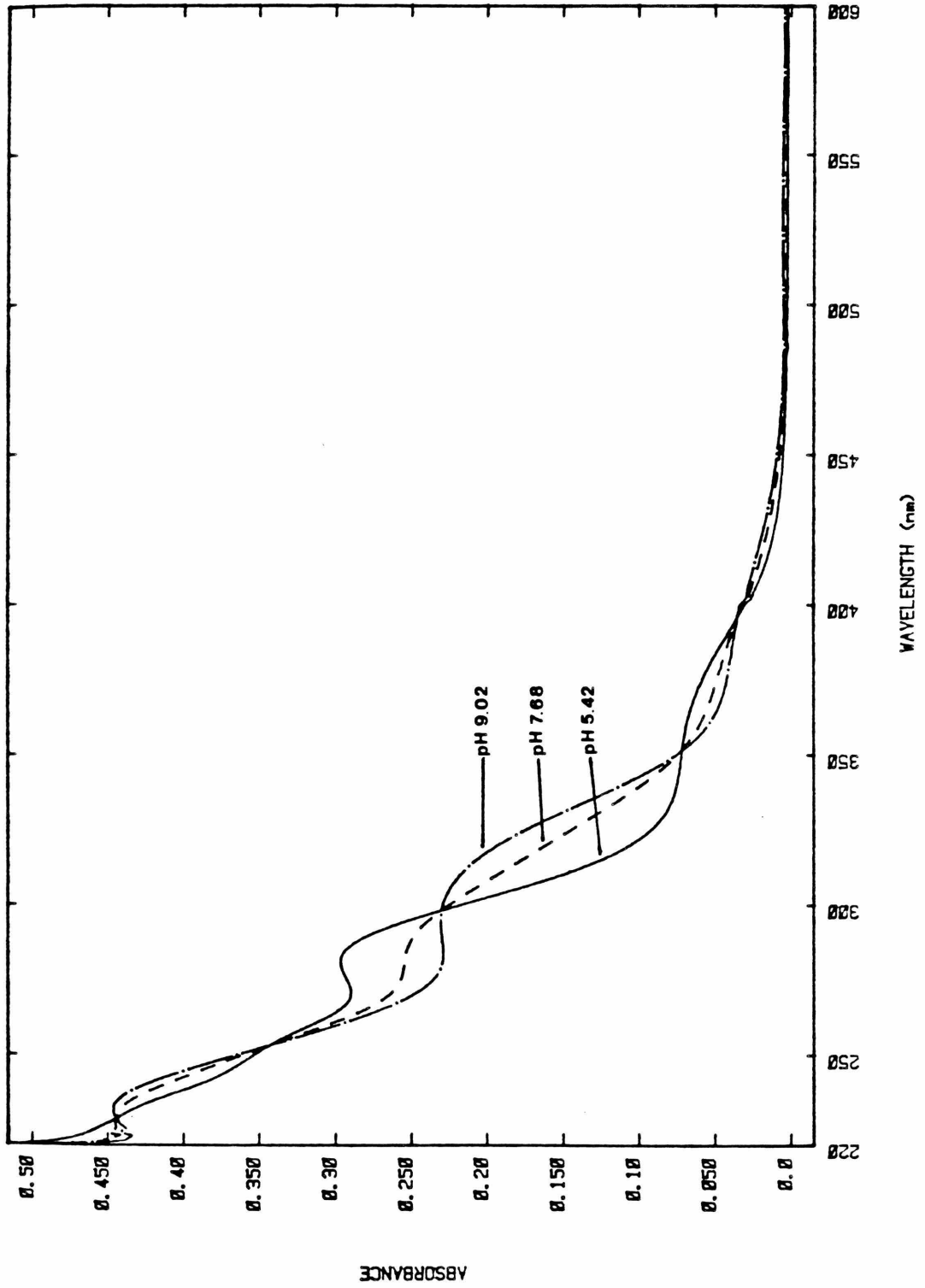
Figure 10

Optical spectra of Ru3Y-OH₂ vs. pH

Conditions: 1.00 mM Ru3Y in de-aerated H₂O

Cell pathlength: 1 mm

Figure 10



discernable. The spin-allowed, ligand field bands for the deprotonated species are apparently obscured by the shifted LMCT bands in both the hexa-aquo and the Ru3Y systems. It was also observed that the shifts for the ligand field bands were generally only several hundred cm^{-1} for aquo vs. hydroxide coordination (141).

Reconsidering the spectra for the Ru-edta [34] dimer, the shift in the band in the near infrared is only about 500 cm^{-1} . This could indicate a simple deprotonation of an already coordinated water molecule. It could also be due to the substitution of a hydroxide for a carboxylate on a single ruthenium. The shift in the 632 nm ($15,800 \text{ cm}^{-1}$) band to 968 nm ($10,300 \text{ cm}^{-1}$) is, however, larger ($5,500 \text{ cm}^{-1}$) than is generally observed for a coordinated hydroxide vs. a coordinated water ligand field transition. The intensity increase to $1,000 \text{ M}^{-1}\text{cm}^{-1}$ from $420 \text{ M}^{-1}\text{cm}^{-1}$ also indicates that this is not just a simple ligand-field transition and that it most likely involves some ligand charge transfer character. Taken in conjunction with the large changes in the intensities of the transitions in the ultraviolet region a simple deprotonation, or hydroxide substitution seems to be ruled out. My guess is that significant structural changes occur, accounting for the dramatic change in the [34] dimer's spectrum upon raising the pH. The incorporation of a bridging hydroxide, in addition to the bridging oxide could account for this. One other possibility that cannot be ruled out is that each

ruthenium is seven coordinate. Seven coordinate edta-containing complexes are known (150,151) for Fe(III) and Os(IV). This type of coordination would then alter the ligand field about each metal center, which could then lead to the chemical and spectral properties observed.

An attempt was also made to see if there was any evidence of dimer formation at high concentrations of the aquo, and hydroxide forms of Ru3Y in the absence of air. The absorbance maxima for both monomeric complexes obeyed Beer's Law between 0.1 mM and 20 mM. This is unlike the behavior exhibited by Fe(edta)⁻, where a dimer is formed at higher pH. The [33] form of the ruthenium-edta dimer is therefore not as stable as its iron analog, nor as the other cationic ruthenium [33] dimers observed by Meyer.

C. ADDITION OF VARIOUS LIGANDS TO THE [34] DIMER

To test for the existence of an open coordination site on the [34] dimer, several ligands were added in greater than 100-fold excess to 0.50 mM [34] dimer solutions buffered at pH 7.7. The added ligands included thiocyanate, pyrazine, imidazole and histidine (see Figure 11). Over a period of hours, to days, the spectra of the solutions changed to yield the ligand-substituted Ru3Y complex. When 0.50 mM each of the [34] dimer and the ligands was allowed to react for several days, however, then there was very little indication of coordination. It is possible for thiocyanate and imidazole to chemically reduce the dimer,

Figure 11

Optical spectra of the [34] dimer + added ligands

Conditions: 0.500 mM [34] Dimer

pH 7.70 phosphate buffer (50 mM)

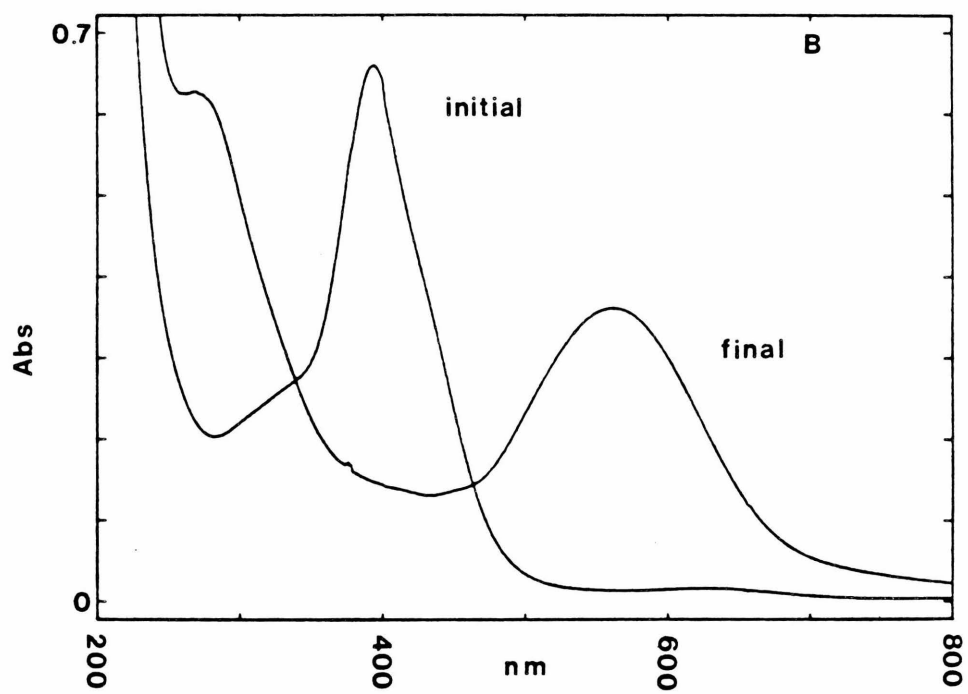
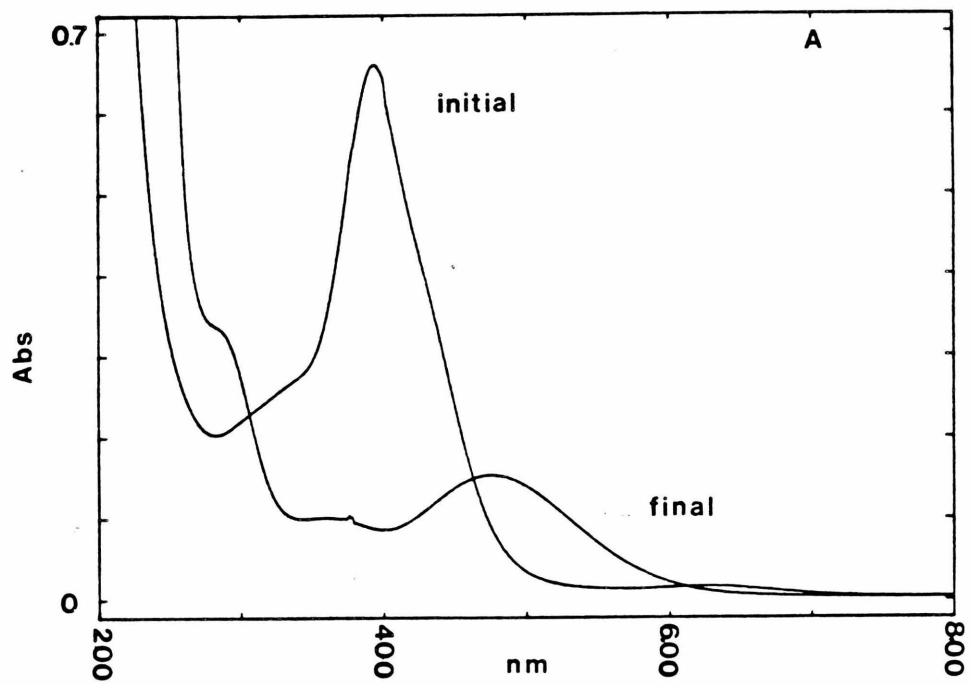
Total ionic strength = 0.200 N with NaTFA

Added ligands are 50 mM

A. [34] + thiocyanate

B. [34] + histidine

Figure 11



but this is not possible for histidine or pyrazine. Either there is a coordinated water position available for substitution (as well as to be titrated), or else the coordinated, acetate arms are somewhat labile and can be substituted. The latter type of behavior was observed by Matsubara and Creutz (7) for $\text{Ru}_3\text{Y}-\text{OH}_2$ where a second thiocyanate was observed to coordinate to a 1.00 mM Ru_3Y - (thiocyanate) solution when a large excess of thiocyanate was present.

The appearance of the substituted, Ru_3Y complex upon addition of the ligands indicates that a redox reaction had also occurred. If the added ligands were not acting directly as reducing agents, then by substituting one of them onto a ruthenium, the stability of the dimer was diminished. The dimer could then split up to form substituted Ru_3Y and Ru_4Y . The substituted Ru_4Y could then oxidize an unreacted ligand, the coordinated edta, or the solvent. A lack of time prevented further study of these reactions and the results are presented here for future reference.

D. EQUILIBRATION STUDIES OF THE [34] DIMER

The stability of the [34] dimer was tested by preparing buffered solutions of the [34] dimer at several pH's. Buffered solutions at pH 1,5,6,7,8,9,10,11 and 13 were prepared and allowed to stand in volumetric flasks for up to nine months on an open shelf. The solutions immediately attained the colors characteristic of the [34] dimer at the

appropriate pH. The color of the solutions remained stable for several days. Over several months, however, decomposition of the [34] dimer to the Ru₃Y monomer was observed, except at neutral to slightly basic pH's, where a totally new spectrum appeared (see Figure 12). The identity of the new complex was not able to be determined by its spectrum and a product was not isolated to enable further studies. Whether the [34] dimer is kinetically unstable, or photolytically reduced is not clear from these results, although Ikeda, et al (44) reported that the [34] dimer was photosensitive and decomposed. They did not, however, present any experimental data, nor did they mention what the decomposition products were. The length of time necessary for the decomposition to occur precluded any further studies in this area. An investigation of the photochemistry of the [34] dimer was outside the scope of this project, but it may prove to be interesting since some species is being oxidized during the decomposition of the [34] dimer and it is possible that dioxygen is being produced from water.

Figure 12

Optical Spectra of [34] dimer equilibration

Conditions: [34] concentrations are roughly 1 mM

Total ionic strength = 0.200 N with NaTFA

Final spectra are after 9 months

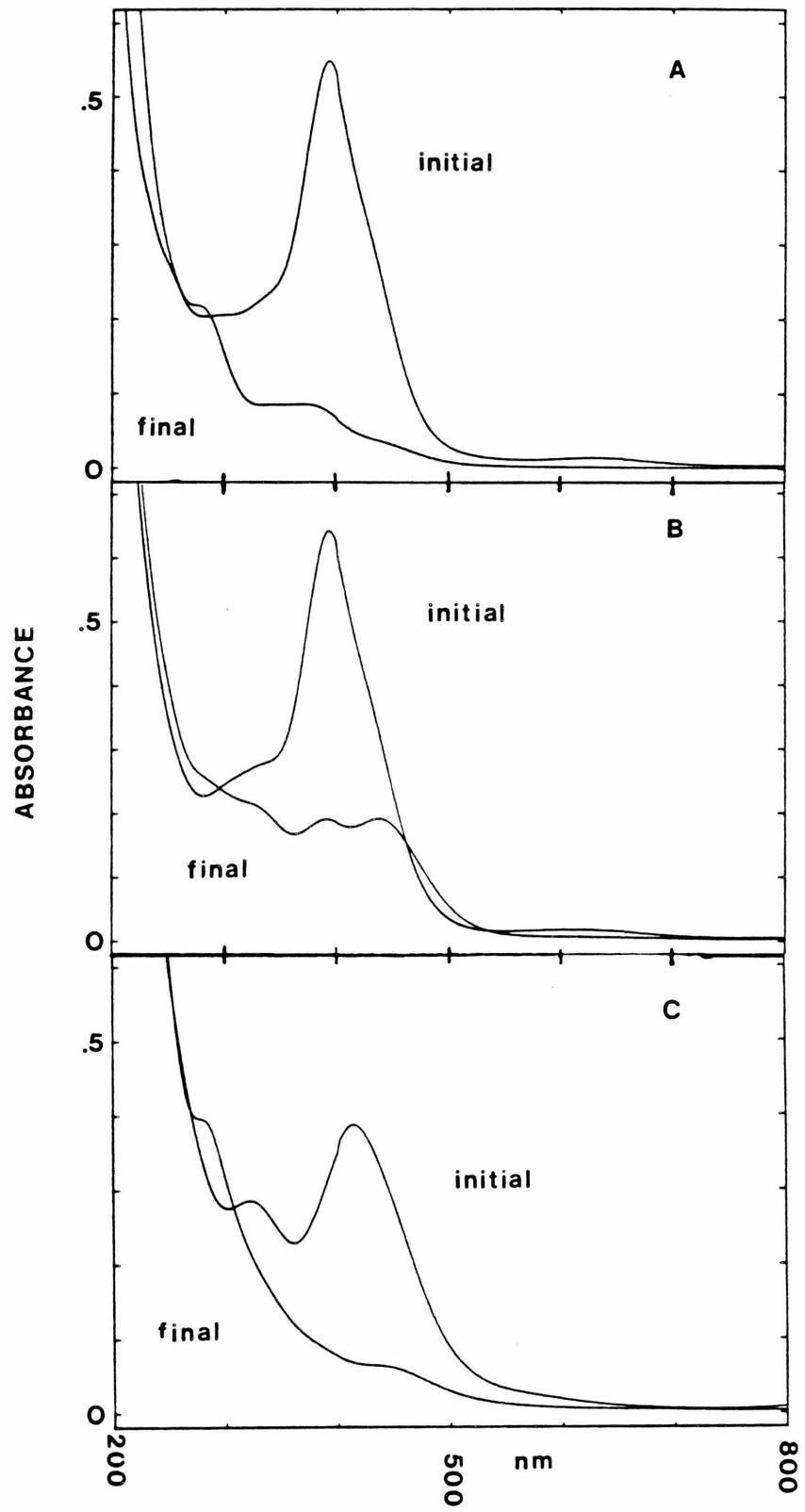
Equilibration

A. pH 5.42 acetate buffer (50 mM)

B. pH 8.42 phosphate buffer (50 mM)

C. pH 11.65 phosphate buffer (50 mM)

Figure 12



9. TITRATIONS OF Ru₃Y-OH₂ WITH CERIUM(IV)

A 1.00 mM solution of Ru₃Y-OH₂ was prepared in a buffered, pH 5.00 acetate media and was then titrated with 0.0584 M Ce(IV). At one equivalent of Ce(IV) per two moles of Ru(III), the same spectrum was obtained as in the titration of Ru₃Y-OH₂ with hydrogen peroxide (see Figure 2). If a ten-fold excess of Ce(IV) was then added, the visible spectrum changed producing the sum of the spectra due to Ce(IV), Ce(III), and one attributable to a new, more highly, oxidized form of the [34] dimer (see Figure 13). Upon standing, the excess Ce(IV) was consumed and the original spectrum of the [34] dimer reappeared. The rate of reappearance of the [34] dimer was then monitored at one of its characteristic band maxima (393 nm), and found to be first order with a rate constant $k=2.0 \times 10^{-5} \text{ sec}^{-1}$.

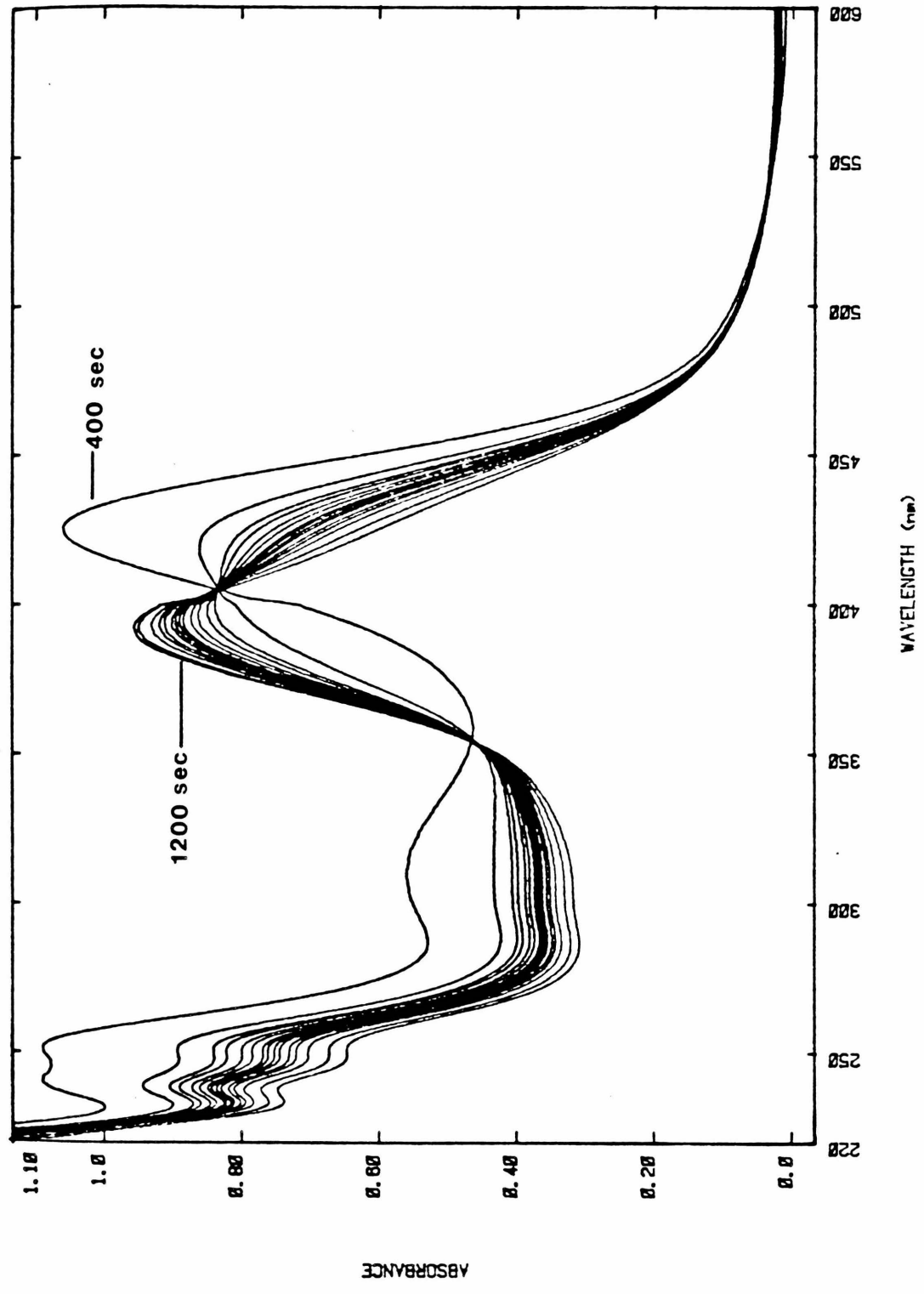
Since the [34] dimer spectrum reappeared after all of the Ce(IV) had been consumed, there must have been some species in solution that was oxidized. The Ce(IV) did not appear to be destroying the edta to any great extent, since after the Ce(IV) had been consumed the maxima in the optical spectrum were within 10% of the initial [34] dimer values. The presence of the two isosbestic points in the optical spectrum during the consumption of excess Ce(IV) also indicated the presence of only the [34] dimer, and its oxidized form in solution. The oxidation state of the oxidized dimer was difficult to determine in this set of experiments but, as will be detailed later, a spectro-

Figure 13

Reappearance of [34] dimer after addition of
excess Ce(IV)

Conditions: 0.500 mM [34] dimer
pH 1.00 with HTFA
total ionic strength = 0.200 N with NaTFA
initail Ce(IV) concentration: 10.0 mM
first measurement: 400 sec
final measurement: 1200 sec

Figure 13



electrochemical experiment indicated it to be the [44] dimer.

Ce(IV) is thermodynamically capable of oxidizing water to dioxygen, but is kinetically limited. It is possible that the [34] dimer, or the [44] dimer could then be catalyzing dioxygen evolution. The possibility of the oxidation of water to dioxygen was then investigated.

To test for this, a fourteen-fold excess of Ce(IV) was added to a 1.0 mM solution of the [34] dimer. The solution had been deaerated with argon for 20 minutes and a YSL oxygen probe inserted into the sealed cell. The argon flow was then stopped and the cell closed to the atmosphere prior to the addition of the Ce(IV). Upon addition of the Ce(IV), the solution immediately turned an orangish-yellow, generating the [44] dimer. Detection of dissolved dioxygen occurred within a few minutes, and proceeded for several minutes longer until all of the Ce(IV) had been consumed, and only Ce(III), and the [34] dimer spectra remained (as analyzed by the periodic withdrawal of small amounts of the solution). Blank experiments had determined that it was impossible to keep atmospheric dioxygen completely out of the cell during this time, which made it difficult to quantitatively detect the amount of dioxygen evolved. Even though this experiment was unable to quantitatively measure the amount of dioxygen produced, it is evident that dioxygen is being produced by Ce(IV) in the presence of the [34] dimer. Meyer (47), and Mills and Zeeman (121) have also observed dioxygen evolution from water with other high

oxidation state ruthenium complexes. Meyer ,et al, reported that $[(\text{bipy})_2\text{Ru}(\text{OH}_2)]_2\text{O}^{4+}$ required four equivalents of Ce(IV) per mole of dimer before catalytic activity occurred. They postulated that this meant a [55] dimer was required before dioxygen evolution occurred. They also noted a decrease in the catalytic reactivity when more Ce(IV) was added and attributed this to the destruction of the catalyst. The final form of the deactivated catalyst was also not characterized. Little quantitative information was given and further studies were reported in progress.

Mills and Zeeman used Ce(IV) to generate dioxygen from water in the presence of a suspension of ruthenium dioxide. They observed the formation of ruthenium (VIII) tetroxide, which is known to be unstable in water, decomposing to dioxygen and ruthenium dioxide (121). No information was given about the rate of the reaction. The hypothesized mechanism included several steps and the formation of RuO_4 , but no substantive proof for the listed steps. They also noted that electrodes coated with ruthenium dioxide also catalytically produce dioxygen without any evidence of RuO_4 formation and concluded that two different mechanisms were involved for the two systems.

The actual mechanism of dioxygen evolution in these, and the ruthenium-edta systems is not known. The requirements appear to be accessible, high oxidation states of ruthenium and, more than likely, a dimeric or polymeric structure. The multiple binding sites of these catalysts

may also allow for the correct binding and orientation of the two reduced oxygen atoms (as water, hydroxide, or oxide) to permit the reaction to proceed efficiently. Decomposition of the coordinated, auxiliary ligands may also be a problem and the possibility of this side-reaction must be considered.

It is unlikely that the two oxygen atoms that finally produce the dioxygen are the result of a bimolecular reaction between one water molecule bound to each ruthenium in any of these ruthenium dimers (see Diagram 3, Structure II). The distance between the two bound water molecules $[\text{Ru}(\text{bipy})_2(\text{OH}_2)]_2^{4+}$ has been shown by crystal structure studies to be approximately 3.6 Å and the Ru-O-Ru bond was found to be nearly linear (165°) (47). The distances of the Ru-O-Ru bond would be expected to shorten very little upon oxidation to a [44] form: $[(\text{Cl}_5\text{Ru})_2\text{O}]^{4-}$ also has a Ru-O-Ru bond length of 3.6 Å (152). If there are coordinated water molecules on the ruthenium-edta dimer, then with a μ -oxo bridge between the two rutheniums, there is little likelihood of the two coordinated waters coming close enough to react with each other. Also, as the dimer is oxidized to higher oxidation states, any coordinated water molecule would be expected to deprotonate to give a bound hydroxide, or even a bound oxo- group. It may be that the oxidized dimer is merely acting as an electron sink to remove one or more electrons from an unbound water molecule, which then reacts with another unbound water molecule to form a peroxo-

species. This peroxo-species can then either disproportionate to give dioxygen and water, or else it can be further reduced to give dioxygen directly.

Another possibility would involve the ruthenium-edta [44] dimer in a di- μ -hydroxo bridge configuration (see Diagram 3, Structure I). This model has the attractive feature of two oxo groups held in close proximity between two oxidizing metals. The scenario for the production of dioxygen then involves the two, or four electron oxidation of the two hydroxides to give hydrogen peroxide, or dioxygen. The remaining ruthenium-edta moieties then pick up a water and form two $\text{Ru}_3\text{Y-OH}_2$, or two $\text{Ru}_2\text{Y-OH}_2$ monomers. These species are then reoxidized to form the [34] dimer. This scenario is conjecture, but it served as a possible structure and mechanism during much of these studies. The determination of the structure of the bridging group between the two rutheniums and how this might affect the catalytic evolution of dioxygen from water was the impetus for many of the studies that follow.

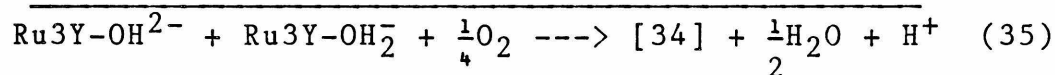
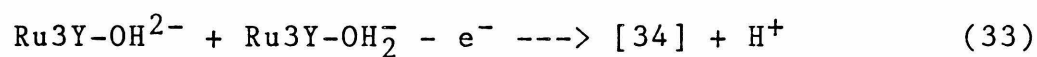
10. DIOXYGEN ADDITION TO Ru3Y-OH_2

Earlier reports by Khan and Ramachandraiah (43,45), and Ezerskaya, et al (2,37-39), have shown that dioxygen reacted with Ru3Y-OH_2 to form a green species with properties similar to the [34] dimer described earlier. My observations have also shown that dioxygen reacted with Ru3Y-OH_2 to form the [34] dimer, but only at pH's > 7.

In an attempt to reproduce the results of Khan and Ramachandraiah, a pH 5, acetate-buffered, 1.00 mM solution of Ru3Y-OH_2 was reacted with a steady stream of dioxygen bubbled through the solution for four days. I observed less than 3% conversion to the [34] dimer. This is in direct contradiction with Khan and Ramachandraiah's results. They did not mention the use of a buffered solution, so that it is possible that the pH in their experiment had been allowed to rise above 7, where the [34] dimer is formed spontaneously in the presence of dioxygen. In light of my observations, it is unclear how Khan and Ramachandraiah obtained any green dimer formation by the addition of dioxygen at pH's less than five.

To quantify the behavior of Ru3Y-OH_2 in the presence of dioxygen above pH 7, a deaerated 0.500 mM solution of Ru3Y-OH_2 was prepared in distilled water and then titrated with deaerated, sodium hydroxide to pH 7.76. A continuous flow of dioxygen that had been prescrubbed in a pH 7, NaTFA bubbler was then introduced to initiate the oxidation reaction. The pH and electronic spectrum were monitored before and during

the reaction. Every 300 seconds, a sample was withdrawn and its spectrum recorded between 200 and 800 nm within one second on the HP-8450 spectrophotometer and then the sample was returned to the bulk solution. An immediate color change was observed upon introduction of the dioxygen. The changes continued for several hours until a final spectrum was reached. The final spectrum was identical to that of the [34] dimer formed at pH 5 by oxidation with hydrogen peroxide (see Figure 2). The pH, however, remained unchanged throughout the duration of the reaction. The constant pH is accounted for by referring to equations 33-35.



At the pKa of the coordinated water in Ru3Y-OH₂ (pH 7.65), equal amounts of the aquo, and the hydroxide, forms of Ru3Y are present. This leads to the evolution of one proton per electron consumed in equation 33. The net stoichiometry (equation 35) would then involve no protons. The rate of reaction was followed by monitoring the appearance of the [34] dimer at its two characteristic maxima at 393 nm and 632 nm, and then analyzing the absorbance data for a first-order reaction. The results are listed in Table 6. The rate constants for the rate of appearance of the [34] dimer were $k = 3.0 \text{ E-4 sec}^{-1}$ (393 nm) and $k = 5.5 \text{ E-4 sec}^{-1}$

Table 6

Dioxygen addition to Ru3Y

Conditions: 0.500 mM Ru3Y

unbuffered, pH 7.76

saturated solution with dioxygen (1.4 mM)

Table 6

<u>t, sec</u>	<u>A₆₃₂</u>	<u>$\ln\left(\frac{A-A_0}{A_\infty-A_0}\right)$</u>	<u>t, sec</u>	<u>A₃₉₃</u>	<u>$\ln\left(\frac{A-A_0}{A_\infty-A_0}\right)$</u>
0	0.0113	-----	0	0.3132	-----
300	0.0184	-2.268	300	0.6971	-0.179
600	0.0263	-1.402	600	0.9620	-0.325
900	0.0342	-0.841	900	1.166	-0.454
1200	0.0409	-0.450	1200	1.334	-0.574
1500	0.0364	-0.707	1500	1.448	-0.665
1800	0.0409	-0.450	1800	1.567	-0.769
2100	0.0440	-0.282	2100	1.666	-0.865
2400	0.0492	-0.005	2400	1.761	-0.966
2700	0.0504	0.056	2700	1.836	-1.055
3000	0.0548	0.289	3000	1.903	-1.140
3300	0.0569	0.403	3300	1.967	-1.230
3600	0.0582	0.475	3600	2.026	-1.230
4200	0.0644	0.837	4200	2.128	-1.499
4800	0.0593	0.536	4800	2.201	-1.650
5400	0.0603	0.593	5400	2.274	-1.827
6000	0.0646	0.849	6000	2.343	-2.030
21000	0.0874	-----	21000	2.65	-----

 $r^2: 0.9472$
 $r^2: 0.9986$

intercept: -1.43

intercept: -2.209

slope: 5.51 E-4

slope: -3.0 E-4

rate of appearance:

 $k = 5.51 \text{ E-4 sec}^{-1}$
 $k = 3.0 \text{ E-4 sec}^{-1}$

(632 nm).

Pseudo-first order conditions were maintained by keeping the solution saturated with dioxygen. Using a saturation concentration of 1.4 mM for dioxygen at pH 7.70, an averaged second-order rate constant of 0.15 M⁻¹s⁻¹ was obtained ($k_{\text{obs}} = 2k_2[\text{O}_2]$). In the oxidation of Ru3Y-OH₂ using chlorate ions, Ikeda, et al (44), reported a second-order rate constant of 5.3 M⁻¹s⁻¹ for the appearance of the [34] dimer at pH 4.7 (roughly 1-2 millimolar in Ru3Y, no chlorate concentration given). This is faster than I observed for dioxygen, but not nearly as fast as either hydrogen peroxide, permanganate, or Ce(IV) oxidations, which were complete upon mixing at, or below, pH 5.

The results of this experiment verify the spontaneous oxidation of Ru3Y by dioxygen to the [34] dimer at pH 7.76, but not for pH ≤5. The spontaneous reaction proceeded slowly, but was quantitative.

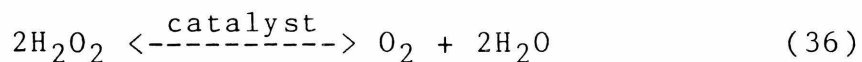
Ezerskaya reported the formation of a green complex with a spectrum similar to the [34] dimer when he bubbled air through an unbuffered solution of Ru3Y-OH at pH 8-9. He observed that the pH eventually dropped to near 7. Given that dioxygen can oxidize Ru3Y-OH to produce the [34] dimer, the net consumption of protons is predicted (see equation 35) since now the Ru3Y is fully deprotonated. The reason Ezerskaya observed a drop in the pH is most likely due to his use of air. Air contains carbon dioxide, which, when dissolved in water produces protons. This acid then

counteracts the consumption of protons by the reduction of dioxygen. Even though the reaction was not carried out, if just dioxygen had been used, the pH would have risen slightly, but not too much, since now the [34] dimer ($pK_a=10.32$) acts to buffer the solution.

It has now been demonstrated that several strong, chemical oxidants (hydrogen peroxide, Ce(IV), permanganate, chlorate and dioxygen) are capable of oxidizing Ru_3Y-OH_2 , or Ru_3Y-OH , to the [34] dimer. The use of dioxygen at $pH = 7.76$ also fixes a minimum potential necessary for the oxidation of Ru_3Y to form the [34] dimer of +0.53 V. An electrochemical study that appears later will shed more light on the oxidation process.

11. CATALYSIS OF PEROXIDE DISPROPORTIONATION

A rapid evolution of bubbles was observed when a large excess of hydrogen peroxide was added to an unbuffered, pH 5 solution of the [34] dimer. There was also no change in the pH, or the optical spectrum of the solution. This suggested the possibility of peroxide disproportionation.



Varying amounts of hydrogen peroxide were added to a sealed, deaerated vessel containing an unbuffered, pH 5 solution of the [34] dimer. The rate of the reaction was monitored by measuring the concentration of dissolved dioxygen by means of a YSL O₂ probe. The experimental results are shown in Figure 14, and listed in Table 7. All of the experimental results exhibited extreme curvature in the amount of dioxygen evolved vs. time. This was most likely due to the gaseous volume above the solution (roughly, of equal dimensions as the solution) and the outgassing of the dissolved dioxygen to equilibrate with the vapor above the solution. Therefore, the initial slopes for the rate of dioxygen evolution were used to analyze for the rate constant. Hydrogen peroxide to [34] dimer molar ratios of 1, 1.3 (twice), 3.3, and 6.5 were measured. For 0.58 mM and 0.45 mM solutions of the [34] dimer, a second-order rate constant of $k = 107 \pm 7 \text{ M}^{-1} \text{ sec}^{-1}$ was calculated.

In comparison, $\text{Fe}(\text{edta})^-$ also catalyzes the

Figure 14

Dioxygen evolution from [34] dimer catalyzed peroxide
disproportionation

Conditions: [34] = 0.581 mM

[H₂O₂] = 0.758 mM

Results: initial slope: 0.046 μM O₂ sec⁻¹

k_{obs} = 0.060 sec⁻¹

k = k_{obs}/[34] = 105 M⁻¹ sec⁻¹

Figure 14

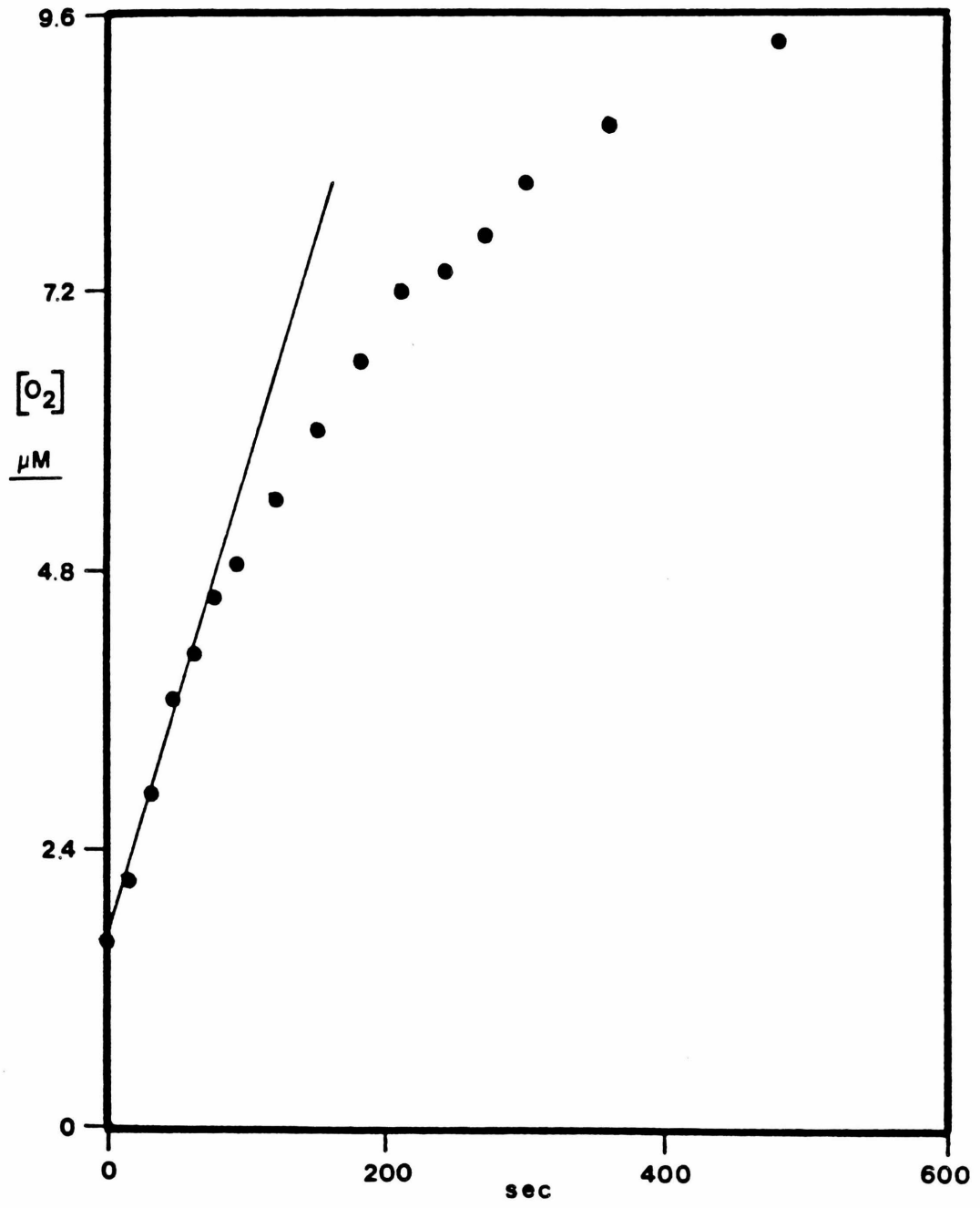


Table 7

Hydrogen Peroxide Disproportionation Data

Table 7

<u>[34], mM</u>	<u>[H₂O₂], mM</u>	<u>rate, $\frac{\text{mM O}_2}{\text{sec}}$</u>	<u>k, M⁻¹s⁻¹</u>
0.450	0.436	2.51E-5	104
0.582	0.760	4.29E-5	97.0
0.581	0.758	4.61E-5	105
0.582	1.90	1.27E-5	115
0.579	3.77	2.48E-4	113

$$k_{\text{ave}} = 107 \pm 7$$

decomposition of hydrogen peroxide. The studies of Walling, et al (137), and the references therein, indicated the presence of a peroxo-bridged Fe(edta) dimer as the catalytic species for $\text{pH} \geq 10$. They also observed the formation of a new, purple species in solution at this pH that was attributed to the peroxo-bridged species. At lower pH's, they observed that uncomplexed edta, and the Fe(edta) complex, decomposed in the presence of peroxide. The decomposition produced carbon dioxide and ammonia, and also lead to the evolution of acid. The rate of peroxide decomposition was found to be a complicated function of the reactants that was first-order in the iron complex, and first, to second-order in peroxide. The kinetic expression was further complicated by the addition of alcohols that functioned as hydroxyl radical traps. It was concluded that a hydroxyl radical was generated, and that it was the reactive species for this and other iron containing systems that catalyzed peroxide disproportionation (137).

There are some similarities between the iron and the ruthenium systems. Both systems exhibit a first-order dependence on peroxide, and, using only the two, limited concentrations used of the ruthenium [34] dimer, they both appear to be first-order in metal complex. Differences occur in that the [34] dimer is not peroxo-bridged and does not generate any acid during the catalysis. The latter result is further evidence that the coordinated edta is not decomposed when the [34] dimer is formed by the addition of

peroxide (and probably as well for Ce(IV)).

The [34] dimer results thus indicate that the peroxide is decomposed by a mechanism similar to the iron system; by the generation of hydroxyl radicals. The effect of added organic substrate, such as short-chained alcohols, was not attempted due to the complexity they introduce to the mechanism (137). Ezerskaya, et al (38), commented that the green complex they isolated exhibited catalase activity, but they gave no experimental results. The recent work of Meyer, et al (137-140) has indicated that ruthenium-bipyridine dimeric complexes also are capable of oxidizing several types of organic substrates. A detailed study of the catalytic properties of the [34] dimer was beyond the scope of this work, but the similarities between the results above indicate that further studies are warranted.

12. INFRARED AND RAMAN SPECTROSCOPY

Solid samples of the [34] dimer were isolated as the acid salt, the tri-potassium salt, or as the deuterio-acid salt. Their infrared spectra were taken as KBr pellets as were the acid, and the deuter-acid salts of $\text{Ru}_3\text{Y-OH}_2$. For comparison, $\text{NaFe}(\text{edta})$, $\text{HCr}(\text{edta})(\text{OH}_2)$, $\text{K}_4[\text{Cl}_5\text{Ru}]_2\text{O}$, $\text{K}_2([\text{bipy}]_2\text{Ru}(\text{NO}_2)]_2\text{O}$, "ruthenium red", $\text{Ru}(\text{bipy})_3\text{Cl}_2$, $\text{Ru}(\text{NH}_3)_6\text{Cl}_3$, and K_2RuCl_6 solid samples were also measured as KBr pellets.

In an attempt to differentiate between the linear, or slightly bent Ru-O-Ru and the doubly-bridged $\text{Ru}(\text{OH})_2\text{Ru}$ structures, infrared spectra were taken of the various [34] dimer salts and of the $\text{Ru}_3\text{Y-OH}_2$ salts. Earlier articles have discussed the two different bonding schemes and the effects they should have on the infrared and Raman spectra (103,112,123,124). In particular, for the M-O-M system the asymmetric stretch should appear at higher energies than the symmetric stretch (approximately, 800 cm^{-1} vs. 250 cm^{-1} for linear systems). If there were any deviation from linearity, then the symmetric stretch would be expected to increase in energy to roughly 500 cm^{-1} . This stretch would now also become infrared active. In addition, there would be a concomitant lowering of energy for the infrared-active, asymmetric stretch to the 700 cm^{-1} region.

The infrared spectrum for the ruthenium-bipyridine dimer showed no evidence of the asymmetric stretch above 800 cm^{-1} . Below this energy, ligand absorption problems made

identification of any bands in this region difficult. Similar observations were reported by Meyer, et al for this complex (18,46).

In the case of the other ruthenium dimers, a band was observed in the 745-790 cm^{-1} region for ruthenium red, while a prominent band was observed for the decachloro-ruthenium complex at 886 cm^{-1} . These values agreed well with Meyer (46), Hewkin and Griffith (123), and Wing and Callahan (103). The decachloro-ruthenium complex is formally a [44] dimer and is known to be linear, while ruthenium red is a [343] trimer and is known to be slightly bent (148).

Other dimeric systems that also exhibit an asymmetric stretch near these energies include $\text{enH}_2[(\text{FeHEDTA})_2\text{O}] \cdot 6\text{H}_2\text{O}$, with a band at 837.5 cm^{-1} (which was attributed to an approximately linear Fe-O-Fe unit (165') (103,114,123,125)), $\text{K}_4(\text{Re}_2\text{OCl}_{10})$ (123), and $[\text{Cr}_2\text{O}(\text{NH}_3)_{10}]\text{Cl}_4$ (123,126).

The oxidation of chromium (II) amines in aqueous solution by dioxygen produces binuclear μ -hydroxo chromium (III) amines (126), which exhibit a strong band at 569 cm^{-1} and shifts to 549 cm^{-1} upon deuteration. This behavior has been taken as evidence for a bent hydroxide bridge structure (126).

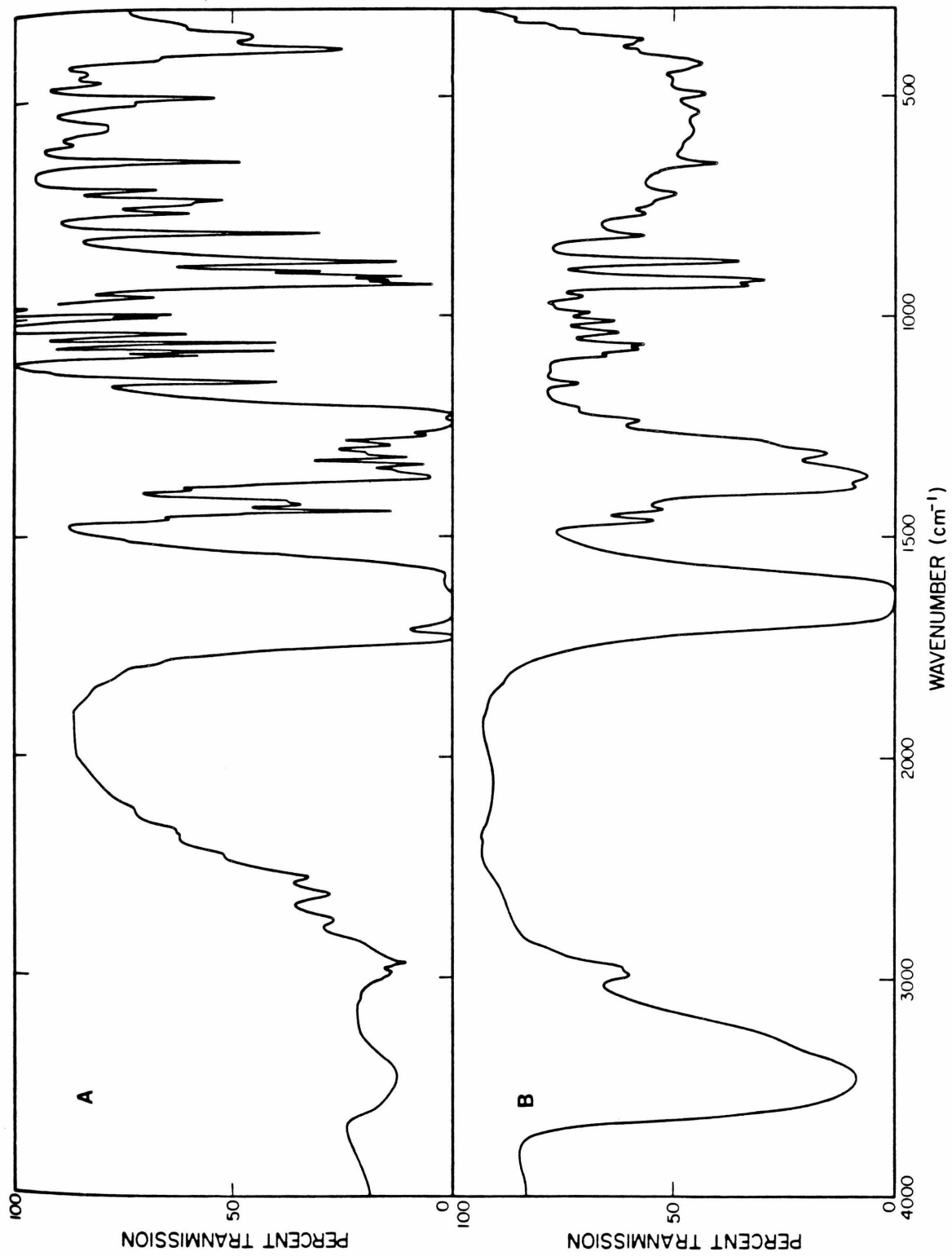
The ruthenium edta system, however, yielded nothing as dramatic as the above results. The spectra of the monomer and the [34] dimer are very similar down to 600 cm^{-1} (see Figure 15). The transitions present near 1200 cm^{-1} have been assigned (100,101) to the $(\text{CH}_2)_{\text{wag}}$ vibrations for an

Figure 15

Infrared Spectra

- A. IR of HRU3Y-OH₂ (KBr pellet)
- B. IR of K₃[34] (KBr pellet)

Figure 15



uncoordinated, protonated, acetate group. They were also present in the spectrum of the acid salt of the [34] dimer. This band was also accompanied by the characteristic carboxyl stretch above 1700 cm^{-1} for a protonated carboxyl group (127).

Below this energy, some differences do appear. A new, weak band appeared at 535 cm^{-1} for the [34] dimer and a band group at 395 cm^{-1} for $\text{Ru}_3\text{Y-OH}_2$ shifted to higher energy for the [34] dimer. The band group shifted back to 395 cm^{-1} when the acid salt of the [34] dimer was used. If this band is assigned to a Ru-N vibration, then protonation of the free acetate group appears to affect this mode. This may be due to a geometry change whereby an acetate arm swings around toward the metal center when it is deprotonated. The change in the coordination geometry would then be expected to affect the Ru-N symmetric stretching mode.

The 535 cm^{-1} band could be due the symmetric Ru-O-Ru stretch which has now become infrared active due to a bent bridge structure. The infrared spectrum of the deuterated [34] dimer, however, showed no shift in this region by any of the bands. This would seem to rule out a di- μ -hydroxide bridge, since if there was a bridging hydroxide, then a shift in energy of the vibration would have been expected upon deuteration. The lack of any change in the band's energy upon deuteration, however, does not provide positive proof of the identity of the vibration. The vibration may also be due to a Ru-O stretch, or even a carbon skeleton vibration that

has now become infrared active due to the change in geometry for the [34] dimer. This latter conclusion was reached by Bhat and Krishnamurthy (128) and Krishnan and Plane (72) for a vibration that occurred in this region in their infrared and Raman studies of Cu-edta systems.

With the hope of observing the symmetric stretch of the Ru-O-Ru, or the Ru₂(OH)₂ moieties, the aqueous and deuterio-spectra of the [34] dimer were measured by resonance Raman spectroscopy using a 454.5, or a 457.9 nm laser line. These wavelengths corresponded to the low energy side of a charge transfer band in both the low and high pH solutions. No enhancement was observed when the 632 nm band was excited.

The pH 6 and pH 12 spectra were inconclusive in delineating the bridging structure (see Figure 16). One difference was a shift in the most prominent peak near 400 cm⁻¹ to 422 cm⁻¹. The Raman shift between the pH 6 and pH 12 samples may be due to the geometry change that accompanied the incorporation of a bridging hydroxide group, but no substantive proof was possible by these experiments.

Previous Raman studies on metal-edta systems have shown that M-N stretches occur in the 400-500 cm⁻¹ range, while the metal carboxylate stretches are not seen at all (72). Krishnan and Plane ascribed the latter result to the electrostatic nature of this bond. They also concluded that the large intensity of the M-N stretch was due to the highly covalent nature of this bond.

The large band in the high pH and pD solutions at

Figure 16

Raman spectra of the [34] dimer

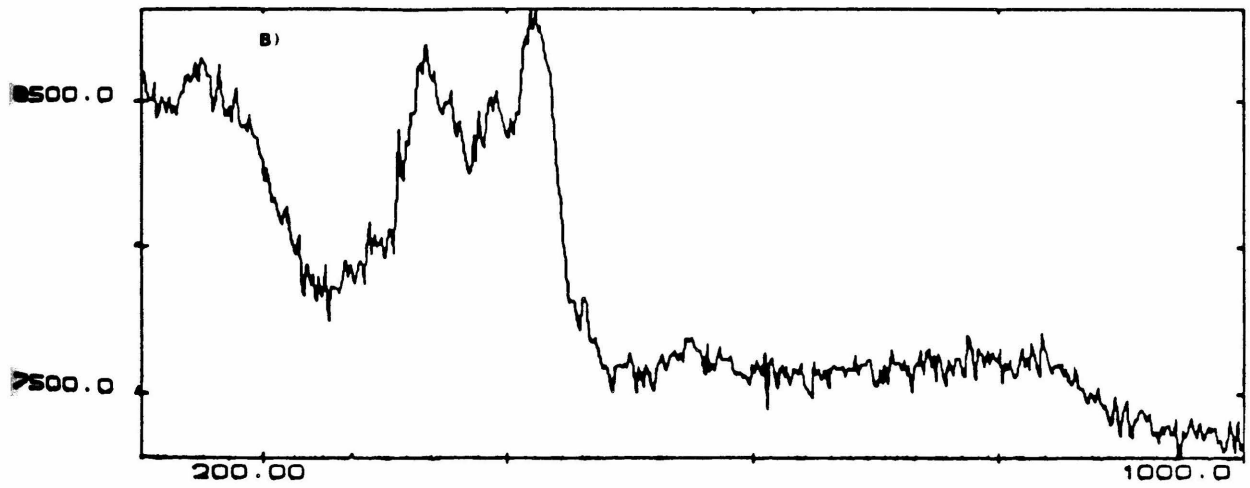
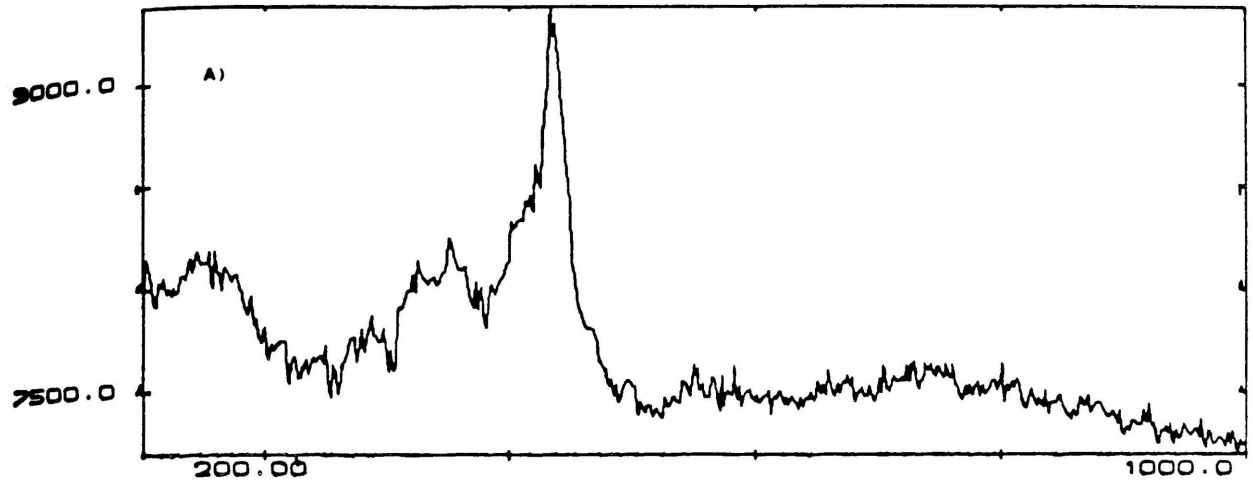
A. pH 6

B. pH 12

Conditions: 0.500 mM [34] dimer

454.5 nm exciting line of Hg laser

Figure 16



334 cm^{-1} was unassigned, but may be due to a symmetric Ru-OH-Ru stretch. The appearance of a band in this region has been observed for monomeric Hg and Cu edta complexes that dimerize at higher pH's (72). There was no discernable shift for the [34] dimer measured upon changing to D_2O , although only a very slight shift would be expected for this vibration due to the small difference in the reduced mass. The poor resolution in this series of experiments may also have masked these small shifts.

The infrared and Raman results do provide some information about the nature of the [34] dimer. As was the case with $\text{Ru}_3\text{Y-OH}_2$, there are uncoordinated acetate arms and whether they are protonated or not has an effect on the geometry of the molecule. When the acetate arms are uncoordinated, then there is the possibility that they could change the overall geometry around the ruthenium metal center, which would then be reflected in a shift in the energy of the vibrations affected by the geometry change.

The high pH optical spectra behavior indicated the possibility of incorporation of a hydroxide that was, most likely, bridging between the two metals. The infrared results do not shed much light on this matter. The raman spectra, however, at low and high pH indicate the possibility of a bridging hydroxide between the two rutheniums. Unfortunately, poor resolution made the positive identity of the vibration difficult.

Conclusive evidence for the structure of the bridging

group in the [34] dimer was, however, not possible by these techniques. The region where μ -oxo, or di- μ -hydroxy vibrations are predicted to occur, were either complicated by ligand vibrations, or else there were no vibrations present. A definitive identification of the bridging group for the ruthenium-edta, the ruthenium-bipyridine, or the ruthenium-ammine dimers is, at this time, not possible by vibrational spectroscopy.

13. ESR SPECTROSCOPY

The ESR of the [34] dimer was investigated to study its magnetic behavior in hopes of establishing the number of unpaired electron spins and the g -values. It was also hoped that coupling between the unpaired spin and the bridging hydroxides (if this was the mode of bridging), and, or the rutheniums ($^{99}\text{Ru}=3/2$ (12.7%) and $^{101}\text{Ru}=5/2$ (17.1%)) would be observed. A solid sample of the tri-potassium salt of the [34] dimer, and of $\text{HRu}_3\text{Y-OH}_2$, in KCl were measured between liquid nitrogen and liquid helium temperatures (see Figure 17). Three discrete g -values near 2.00 were observed for the [34] dimer, while $\text{Ru}_3\text{Y-OH}_2$ exhibited a very broad band near $g=2.00$ and a much weaker one near $g=1.30$. Both complexes indicated the presence of one unpaired spin, but with very different spectra.

The spectrum of $\text{Ru}_3\text{Y-OH}_2$ was similar to other ruthenium (III) complexes with an axial distortion (94,129-132). The presence of the large, broad bands, even at 12K, made the identification of any hyperfine interactions for the monomer impossible. The bands for the dimer were much narrower than for the monomer, but no hyperfine splittings were resolvable.

The general interpretation of non-isotropic Ru(III) spectra assumes a tetragonal, or trigonal distortion that leads to the large, observed, splitting of g_{\perp} and g_{\parallel} . The spin-orbit coupling and ligand field parameters are frequently extracted from these spectra and the orbital

Figure 17

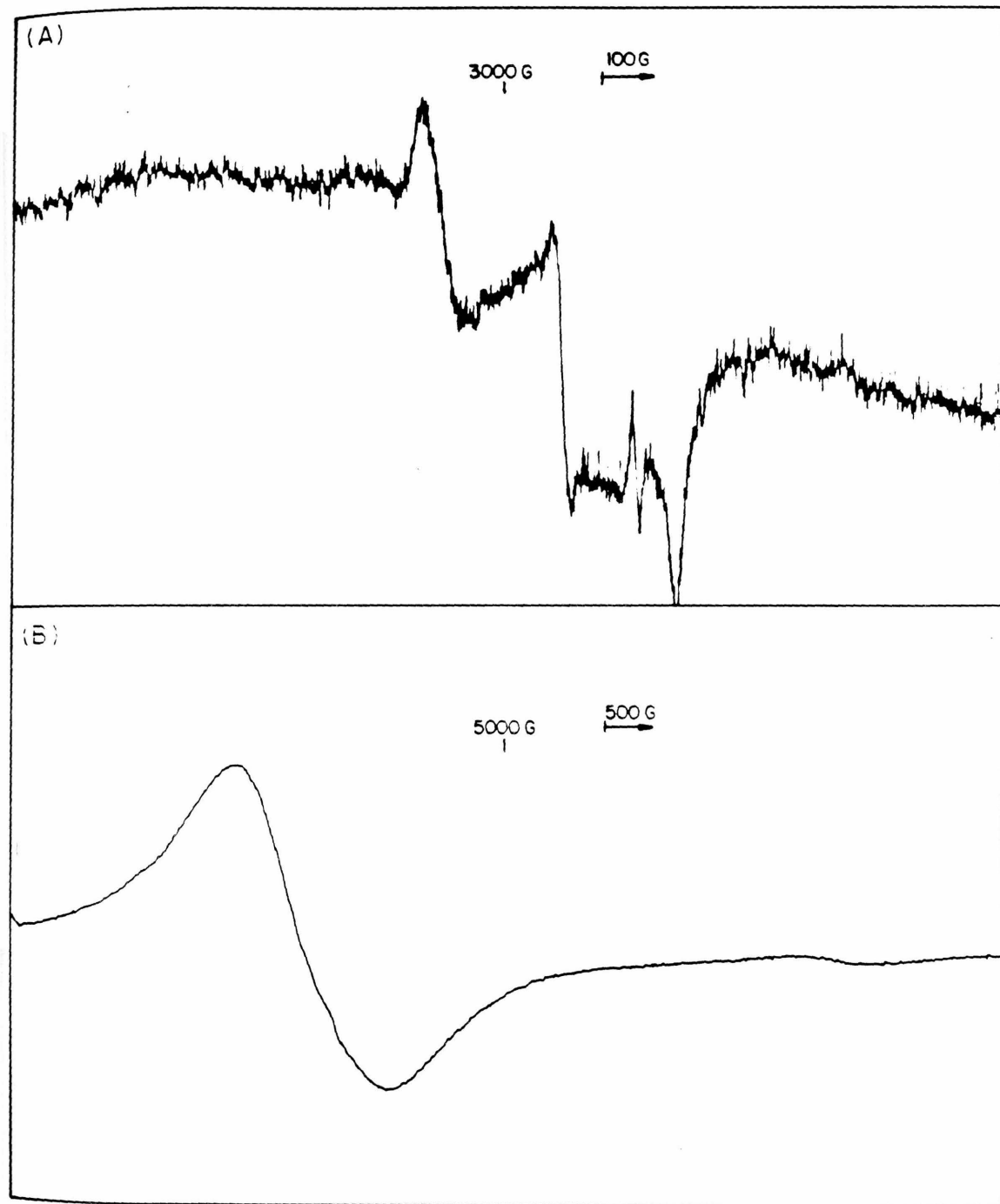
ESR spectra at pH 5

A. [34] dimer

B. Ru3Y

Conditions: 1.00 mM in complex, pH 5

Figure 17



reduction factor, k , determined (133,134). The $\text{Ru}_3\text{Y-OH}_2$ spectrum was not analyzed because of the lack of spectral detail and its similarity to many other Ru(III) spectra. On the other hand, the spectrum of the [34] dimer offered the first opportunity for a mixed-valence ruthenium dimer to be observed in these oxidation states. The splitting pattern of the dimer yielded three g -values (1.96, 2.10 and 2.31) indicating a rhombic distortion. The average g value for the dimer was 2.13. The dilute powder spectrum of the [34] dimer was also measured at 12K with little difference in the spectrum.

The rhombic splitting pattern substantiated the low symmetry of the [34] dimer that was indicated by the visible spectrum. The ability to extract structural information however, would require a crystal. The angular dependence of the g -values could then be measured and fit to the equations for a single, unpaired electron, or electron hole, derived by Stevens (133). This analysis has been used by others to interpret d^5 , and t_{2g} hole systems leading to information about the electron energy-levels (129-131,134,135). Attempts at obtaining a crystal were unsuccessful, and only the g -values are reported here.

ESR spectra were also measured for a pH 12 sample of the [34] dimer. No spectrum was observed at room temperature, but at liquid nitrogen temperatures, and below, spectra different from the pH 5 spectrum were observed (see Figure 18). The spectra were much more complicated and indicated

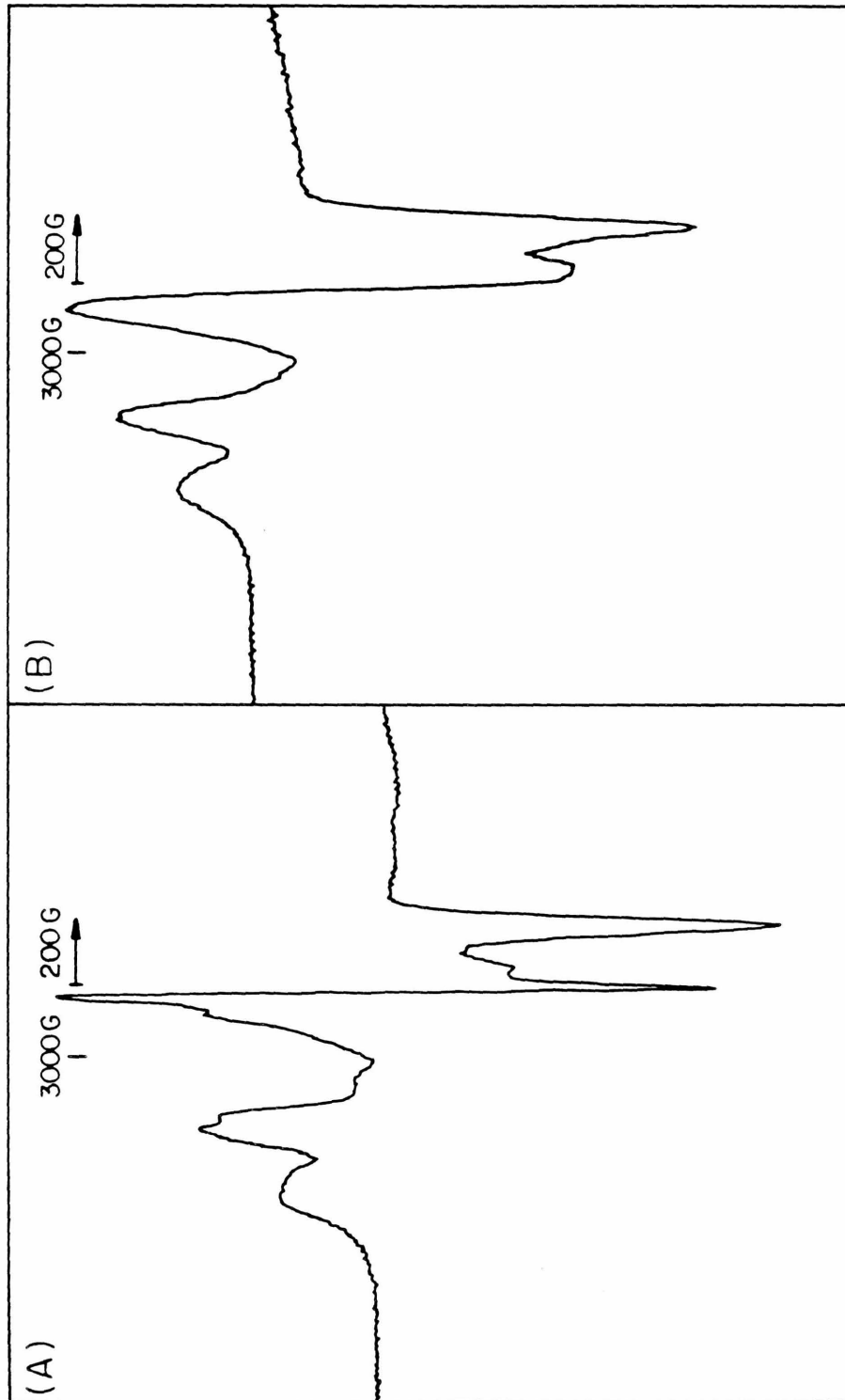
Figure 18

ESR spectra of the [34] dimer at pH 13

A. High pH [34] dimer at LN2 temperature

B. High pH [34] Dimer at liquid helium temperature

Figure 18



the presence of more than one species in solution and several g-values were extracted from these spectra. For the lower temperature, a much simpler spectrum was observed (Figure 18b). Only four g-values were discernable. The two lowest g-values were 1.977 and 2.090, while the two highest values were 2.360 and 2.543. This suggested the presence of two isomers. The exact nature of these isomers remains unclear, but if the dimer is truly doubly-bridged at high pH, then there are several different isomers possible relative to the plane of the two nitrogens on each ruthenium. These different geometric orientations would then lead to different magnetic environments. The same possibilities also exist for a μ -oxo bridged dimer.

This same high pH solution was allowed to warm to room temperature and after 5 days the spectrum was remeasured at liquid nitrogen temperature. The two highest g-values had coalesced into one with a small shoulder, while the lower g-value remained the same. The spectrum was still too complicated to yield any structural information, but indicated that there may be one preferred, stable configuration. There were still, however, at least two species still present.

The lack of any hyperfine splittings made any structural conclusions difficult. The spectra, nevertheless, confirmed the presence of one, unpaired-spin in the [34] dimer, and of a change in the structure of the dimer upon increasing the pH to 10, or greater.

14. NMR SPECTROSCOPY

The application of proton nmr techniques towards the problems of bonding in transition metal complexes has been extensive (146,147). These techniques have generally been applied to diamagnetic transition metals complexes, while their use in the study of paramagnetic transition metal-complexes has been much less extensive (146,147). The reasons for the latter situation have mainly to do with the difficulty in obtaining spectra of paramagnetic transition metals due to the prevalence of line broadening. When signals are present, large upfield and downfield shifts are observed when compared to diamagnetic metal-containing analogs. These large shifts are due to the pseudo-contact, or dipolar shifts, and the scalar, or "contact" shift (141-147). There are difficulties, however, in assigning the relative contribution of each of these effects to the total shift due to anisotropy of the g-tensor and a lack of knowledge of the complex's structure.

Several factors led to the decision to use nmr spectroscopy as a means of determining structural information about the [34] dimer. The classic studies of Reilly, et al (143-145) showed how nmr studies can help in determining the structures of edta-containing, paramagnetic nickel (II) complexes, while a report by Ezerskaya, et al (41), indicated that a proton nmr had been observed for the "green", ruthenium-edta dimer they had isolated. It was also hoped that the greater resolution of the Bruker 500 MHz

instrument would aid in producing a better quality spectrum.

A 20 mM solution of the [34] dimer was prepared in D₂O with DSS used as an internal reference and the spectrum was measured at 295 K. Later, several spectra were measured at higher temperatures. The result of the room temperature measurement is shown in Figure 19.

A very complex spectrum is observed with shifts, both upfield, and downfield of the DSS reference (0 ppm). This is to be contrasted with the typical response for diamagnetic, transition-metal edta complexes which exhibit several overlapping resonances centered around 3.4 ppm. The spectrum of the [34] dimer exhibits 17 distinct resonances, with possibly more obscured by the large water resonance at 4.6 ppm. The integrated area of the discernable peaks for the [34] dimer accounts for 22 of the possible, 24, C-H resonances (see Table 8). These resonances could not be assigned by inspection of this spectrum, but the presence of so many different resonances indicates that most of the protons are inequivalent. The large number of resonances also indicates a low degree of symmetry for the structure of the [34] dimer in solution which coincides with the rhombic spectrum observed in the ESR.

In general, the total isotropic shift is the sum of two contributions, the contact shift, which takes into account the electron-nuclear spin interaction, and the pseudocontact shift, a dipolar effect, which becomes prominent when the g-tensor is anisotropic.

Figure 19

Nmr spectra of the [34] dimer

Conditions: 20 mM [34] dimer in D₂O

pD 6, unbuffered

DSS internal reference

Figure 19

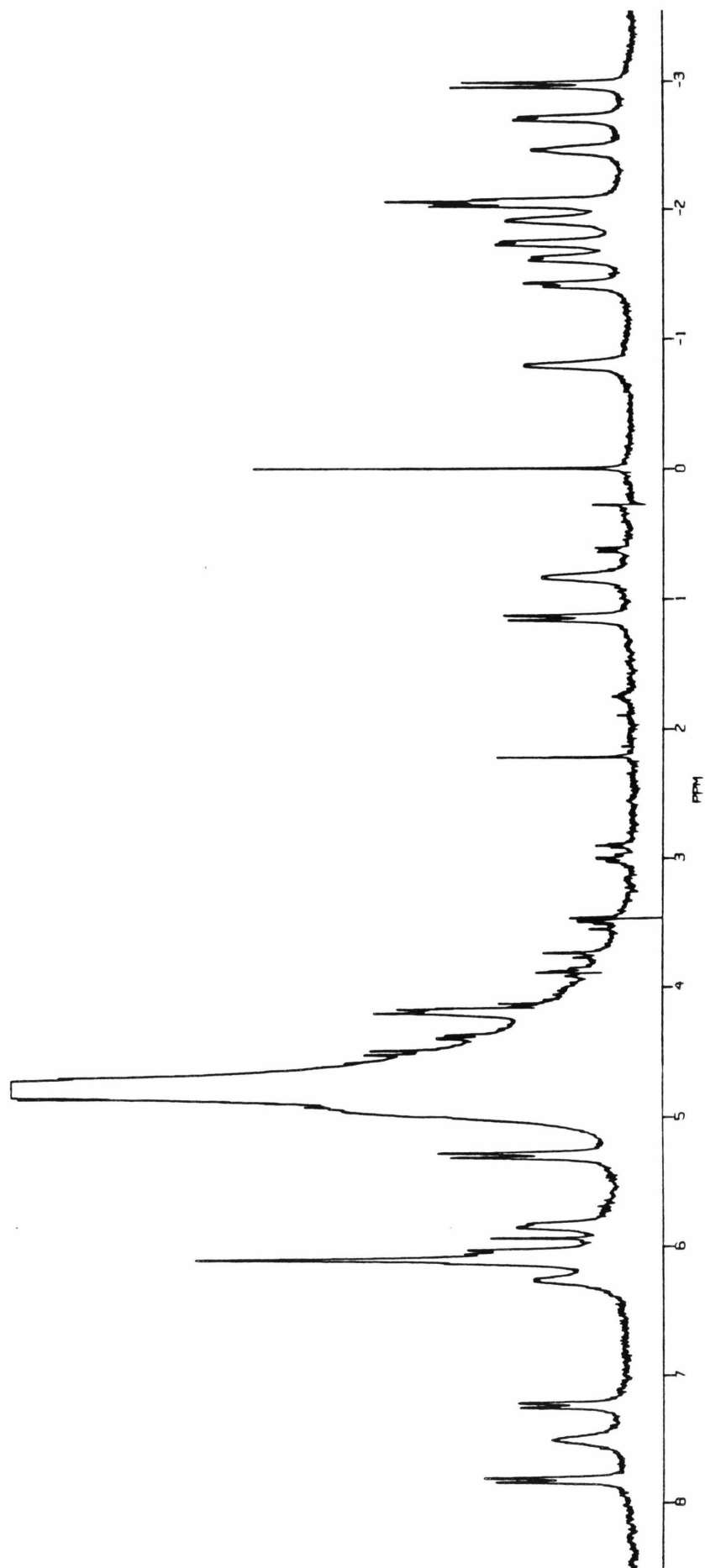


Table 8

Nmr shift data for the [34] dimer vs. temperature

Table 8*

		$\Delta\nu, \text{shift (ppm)}$						
		Temperature, °K						
<u>Band</u>	<u>Area</u>	<u>298</u>	<u>303</u>	<u>313</u>	<u>318</u>	<u>323</u>	<u>328</u>	<u>338</u>
dbl	1	-3.00	-2.88	-2.76	-2.61	-2.57	-2.46	-2.32
		$r^2: 0.9840, \text{ int: } 2.73 \text{ ppm, slope: } -1710 \text{ ppm-}^\circ\text{K}$						
dbl	1	-2.73	-2.65	-2.57	-2.47	-2.45	-2.37	-2.27
		$r^2: 0.9825, \text{ int: } 1.13 \text{ ppm, slope: } -1150 \text{ ppm-}^\circ\text{K}$						
sngl	1	-2.47	-2.39	-2.31	-2.21	-2.19	-2.11	-2.01
		$r^2: 0.9825, \text{ int: } 1.39 \text{ ppm, slope: } -1150 \text{ ppm-}^\circ\text{K}$						
dbl	2	-2.13	-2.06	-1.87	-1.74	-1.70	-1.62	-1.49
		$r^2: 0.9900, \text{ int: } 3.53 \text{ ppm, slope: } -1690 \text{ ppm-}^\circ\text{K}$						
sngl	1	-1.95	-1.86	-1.80	-1.72	-1.69	-1.62	-1.49
		$r^2: 0.9654, \text{ int: } 1.75 \text{ ppm, slope: } -1100 \text{ ppm-}^\circ\text{K}$						
dbl	1	-1.75	-1.69	-1.64	-1.57	-1.54	-1.48	-1.41
		$r^2: 0.9764, \text{ int: } 1.15 \text{ ppm, slope: } -865 \text{ ppm-}^\circ\text{K}$						
dbl	1	-1.69	-1.52	-1.35	-1.17	-1.10	-0.94	-0.73
		$r^2: 0.9861, \text{ int: } 6.35 \text{ ppm, slope: } -2400 \text{ ppm-}^\circ\text{K}$						
dbl	1	-1.44	-1.35	-1.30	-1.20	-1.16	-1.09	-1.00
		$r^2: 0.9666, \text{ int: } 2.23 \text{ ppm, slope: } -1100 \text{ ppm-}^\circ\text{K}$						
dbl	1	-0.79	-0.75	-0.68	-0.59	-0.56	-0.48	-0.40
		$r^2: 0.9794, \text{ int: } 2.80 \text{ ppm, slope: } -1080 \text{ ppm-}^\circ\text{K}$						

-continued on next page-

Table 8*

Band	Area	$\Delta\nu$, shift (ppm)						
		Temperature, °K						
		298	303	313	318	323	328	338
snglt	1	0.78	0.96	1.20	1.39	1.46	1.64	1.88
		r^2 : 0.9942, int: 10.06 ppm, slope: -2770 ppm-°K						
dbltd	1	1.15	1.18	1.20	1.24	1.25	1.27	1.30
		r^2 : 0.9682, int: 2.40 ppm, slope: -372 ppm-°K						
dbltd	1	5.88	5.82	5.75	5.69	5.67	5.62	5.54
		r^2 : 0.9924, int: 3.08 ppm, slope: +833 ppm-°K						
mltpt	3	6.06	6.0	5.95	5.88	5.86	5.82	5.73
		r^2 : 0.9776, int: 3.36 ppm, slope: +806 ppm-°K						
dbltd	1	6.11	6.11	6.11	6.16	6.16	6.17	6.15
		no change with temperature						
dbltd	1	7.27	7.21	7.15	7.09	7.06	7.02	6.94
		r^2 : 0.9894, int: 14.55 ppm, slope: +810 ppm-°K						
snglt	1	7.52	7.52	7.52	7.52	7.52	7.53	7.52
		no change with temperature						
dbltd	1	7.87	7.80	7.72	7.64	7.62	7.56	7.46
		r^2 : 0.9889, int: 4.47 ppm, slope: +1010 ppm-°K						

* snglt = singlet; dbltd = doublet; mlpt = multiplet;
 data are fit to $\Delta\nu$ vs. $1/T$ by a linear regression analysis
 int = intercept

$$\Delta\nu(\text{isotropic}) = \Delta\nu(\text{contact}) + \Delta\nu(\text{pseudocontact}) \quad (37)$$

The contact shift reflects the influence of unpaired spin density which has been delocalized onto the nmr nucleus, while the pseudocontact shift is due to a dipolar contribution to the hyperfine coupling caused by an anisotropic g-tensor. This latter effect is a function of the orientation of the nucleus of interest with respect to the magnetic field caused by the unpaired electron density from the metal (146,147).

Generally, for systems where $g_{zz} > g_{xx}, g_{yy}$, a nucleus that is coaxial with the principal axis will experience an upfield shift, while those nuclei lying in the equatorial region will experience downfield shifts (146). This behavior was observed for the paramagnetic Ni(II) complexes with edta-like ligands studied by Reilly, et al (143-146). The large, observed, upfield and downfield shifts are thus seen to be due to the orientation of the proton nuclei with respect to the principal g-axes (147).

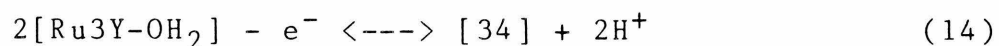
The isotropic shift should exhibit Curie Law behavior (ie. a plot of $\Delta\nu$ vs. $1/T$ should be linear) (146,147). The slope of this plot gives, in the absence of any g-tensor anisotropy, the hyperfine coupling constant, A_i . When a g-tensor anisotropy is present, then the interpretation of the meaning of the slope becomes difficult without some knowledge of the g-values, and the orientation of the nuclei of interest compared to the g-axes.

A Curie plot was made for 17 of the observed resonances,

and the values are listed in Table 8. Several of the resonances exhibited similar slopes, but no interpretation of these slopes was possible due to the g-tensor anisotropy. The data are presented here for future reference.

15. SUMMARY AND CONCLUSIONS

The previous sections have described the synthesis and spectroscopic characterization of the [34] dimer. Several chemical oxidants (hydrogen peroxide, Ce(IV) and permanganate) were used to oxidize $\text{Ru}_3\text{Y-OH}_2$ at $\text{pH} \leq 5$ to produce the [34] dimer. The following stoichiometry was observed:



At neutral pH's, dioxygen was also observed to spontaneously produce the [34] dimer from Ru_3Y . The reaction between dioxygen and $\text{Ru}_3\text{Y-OH}_2$ at lower pH's, however, did not exhibit any production of the [34] dimer. This is in contrast with the results of Khan and Ramachandraiah (43). The reason for the difference was tentatively ascribed to their use of an unbuffered pH 5 solution, which could have drifted to a higher pH where the reaction with dioxygen becomes rapid.

The [34] dimer was then isolated as a solid that analyzed well for $\text{K}_3\text{Ru}_2\text{C}_{20}\text{H}_{36}\text{N}_4\text{O}_{22}$ (MW = 1020). The solid, when redissolved in water, exhibited the conductivity for a tri-anion. The magnetic susceptibility of the solid was 1.79 Bohr Magnetons. This value is less than predicted for discrete Ru(III) and Ru(IV) centers and is indicative of one unpaired spin for the the dimer. The optical spectrum of the [34] dimer was very similar to that reported by Meyer, et al (46) for $([(\text{NH}_3)_5\text{Ru}]_2\text{O})^{5+}$, which is also a [34] dimer. In

both cases, the dimers exhibited a green color. The ruthenium-edta [34] dimer, however, exhibited a band in the near infrared region, which makes it the first example of an oxo-bridged ruthenium dimer with a band in this region (see Table 4).

A band shape analysis using Hush's theory for mixed-valence complexes (73-74) showed that the band in the near infrared (1178 nm) was characteristic of a Class III complex (75). The band width at half-maximum was much narrower than predicted for a Class II, or localized, complex, and when the solid was dissolved in D₂O, dimethyl sulfoxide, or ethylene glycol, there was no change in the position of the band. The [34] dimer was thus concluded to be delocalized with a symmetric ground state and with a formal oxidation state on each ruthenium of 3.5.

The [34] dimer also exhibited variable pH behavior. A pK_a of 10.32 was indicated by an analysis of the the change in the optical spectrum as the pH was varied between 5 and 13 (see Figure 4). The unprotonated form of the [34] dimer was determined to be different from that of the protonated form by the change in the band positions and their intensities.

The unprotonated form of the [34] dimer also exhibited a band in the near infrared. The intensity of this band was the same as for the protonated form, but it was at lower energy (1250 nm). The band at 632 nm also shifted to lower energy, 968 nm, and increased in intensity to 965 $\text{M}^{-1} \text{cm}^{-1}$ from 420 $\text{M}^{-1} \text{cm}^{-1}$. The most dramatic change in the optical

spectrum occurred with the intense charge transfer band at 393 nm, where two lower intensity bands at 414 nm and 324 nm were now observed.

A band-width analysis of the band at 1250 nm showed that the unprotonated form of the [34] dimer was also a Class III complex. This indicated the maintenance of a symmetric ground state for the dimer, which precluded a simple deprotonation of a water coordinated to just one ruthenium. It is possible that a doubly-bridged dimer with μ -oxo, and μ -hydroxo linkages was now present.

Several other spectroscopic techniques were used to try and identify the mode of bridging in the two forms of the [34] dimer. The infrared spectrum of the acid form of the [34] dimer was different from that of the tri-potassium salt in the low energy region (below 600 cm^{-1}), and indicated that there was a change in the Ru-N stretch. This was taken to indicate that protonation of the acetate arms of the [34] dimer affected the coordination geometry of the edta on a ruthenium. My guess is that when the free-acetate arm is deprotonated, it swings around to form either a seven-coordinate ruthenium, or else the edta rearranges around the ruthenium to form a lower-energy six coordinate configuration.

A comparison of the raman spectra for the protonated, and unprotonated forms of the [34] dimer ($\text{pK}_a = 10.3$) also showed changes upon raising the pH. Another change in the Ru-N stretch occurred when the pH was raised. This supported the

optical results that also indicated a change in the structure of the [34] dimer at higher pH. It was hoped that a band attributable to a symmetric Ru-O-Ru stretch, or even a Ru-(OH)-Ru stretch would be observed by this technique, but the poor resolution in the experiments made positive identity of the weak bands below 500 cm^{-1} difficult.

The [34] dimer was also studied by the use of esr and nmr techniques. The esr results indicated that the [34] dimer and its deprotonated form were both rhombic. The spectra for the two forms were also very different. No bridging structure information was able to be extracted from these results, although the presence of two forms of the unprotonated [34] dimer was indicated.

The nmr results were very dramatic and the standard, poorly resolved bands for metal-edta complexes displayed large upfield, and downfield shifts from the usual values for diamagnetic metals. The observed multitude of lines also substantiated the rhombic nature of the [34] dimer. A temperature dependence study also indicated that several of the resonances were affected differently by the unpaired spin. The lack of structural information and a lack of knowledge of the components of the anisotropic g-tensor made a full analysis of the spectrum impossible. No conclusive structural information was possible by this technique other than to substantiate the rhombic nature of the [34] dimer.

During the titration of $\text{Ru}_3\text{Y-OH}_2$ with Ce(IV), the presence of an oxidized form of the [34] dimer was observed.

After the [34] dimer had been formed, the addition of excess Ce(IV) caused a change in the optical spectrum. The excess was observed to be consumed and to eventually yield detectable amounts of dioxygen with the regeneration of the [34] dimer. The original spectrum was observed after all of the Ce(IV) had been consumed indicating that the coordinated edta had not been destroyed. The presence of an isosbestic point during the regeneration of the [34] dimer also indicated that only the [34] dimer and its oxidized form were present in solution. The oxidation state of the oxidized form of the [34] dimer was not able to be determined by the experiment above, but a spectro-electrochemical technique described in the next section identified it as the [44] dimer.

The addition of excess hydrogen peroxide produced a different result. The rapid evolution of dioxygen was observed, but there was no evidence of any higher oxidation state forms of the [34] dimer. The evolution of dioxygen from peroxide was found to be catalyzed by the [34] dimer with a second-order rate constant of $100 \text{ M}^{-1} \text{ sec}^{-1}$.

The optical spectra of $\text{Ru}_3\text{Y-OH}_2$ at higher pH's was also measured in this study to use as comparison with the [34] dimer. A change in the optical spectrum was observed as the pH was raised above the pKa of the coordinated water molecule (pKa 7.65). An isosbestic point was observed indicating that only the coordinated aquo, and hydroxide forms were present in solution. This also indicated that there was no evidence

of the formation of a [33] dimer at any pH, which is unlike the behavior of $\text{Fe}(\text{edta})^-$ (113-114).

The use of several spectral techniques was thus very informative in characterizing the [34] dimer. Details about its formation, its structure and its catalytic properties were able to be described. More about its redox behavior will be described in the following section.

SECTION II. ELECTROCHEMISTRY

16. CYCLIC VOLTAMMETRY AND ELECTROLYSIS OF
THE RU-EDTA SYSTEM

To try and understand the redox behavior of Ru3Y, a cyclic voltammogram (CV) of a 1.00 mM solution of Ru3Y at pH 5.50 was performed using a basal-plane graphite (BPG) electrode (see Figure 20). The initial potential was +0.200 V vs. SCE (all potentials will be reported vs. SCE, the saturated calomel electrode) and the potential was scanned to -1.000 V, whereupon, the scan direction was reversed and scanned to +1.500 V. The scan was reversed again and continued back to -0.750 V, reversed, and scanned back up to +1.500 V, and then scanned repetitively between +0.500 V and +1.500 V.

The initial scan yielded the expected reversible Ru3/2Y couple (waves I and II) with $E^\circ = -0.225$ V (3,4). The wave at +1.000 V (III) had roughly the same peak current as the Ru3/2Y couple, but the return wave (IV) was much smaller. The "pre-wave" (V) at -0.050 V was roughly the same height as IV, but exhibited no anodic wave upon reversal at -0.150 V (not shown). The original wave (I) then appeared after scanning past V, followed by II upon scan reversal. Another new wave (VI) was observed when the solution was scanned repetitively between +0.500 V and +1.500 V. This wave paired with IV to yield a quasi-reversible couple with $E^\circ = +0.900$ V ($\Delta E_p = 80$ mV). The peak currents for this

Figure 20

Cyclic Voltammogram of Ru₃Y-OH₂

Conditions: 1.18 mM Ru₃Y-OH₂

50 mM acetate buffer, pH 5.50

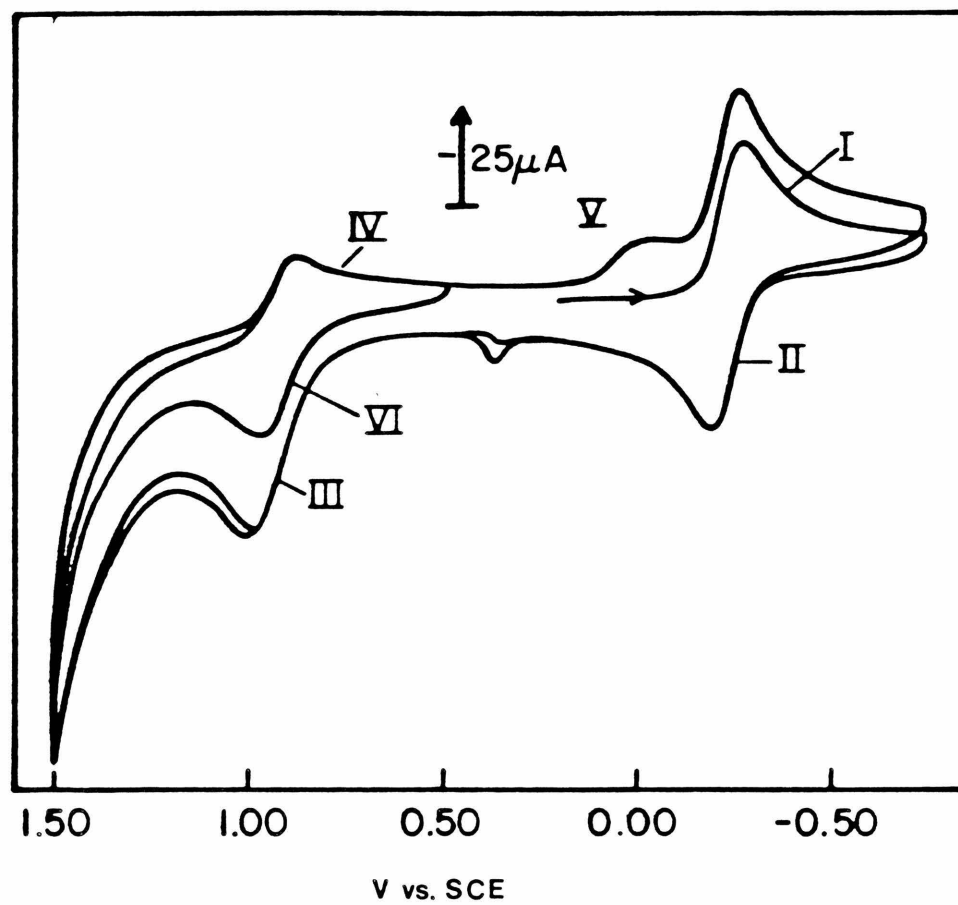
Total ionic strength = 0.200 N with NaTFA

BPG electrode

Initial potential: +0.200 V

Scan rate: 100 mV/sec

Figure 20



couple were not equal, with VI being greater than IV, and both were less than the peak currents for I and II. The solvent oxidation current at +1.500 V was also much greater than that observed in the absence of Ru3Y (not shown). This CV, thus, serves to illustrate the complex electrochemical behavior exhibited by Ru3Y upon oxidation and then reduction. Several electroactive species are produced depending upon the scan direction and the potentials that were scanned and the description and characterization of these processes will be the subject of the next few sections

In an attempt to characterize the complex, or complexes produced upon oxidation of Ru3Y-OH₂, an electrolysis was performed with an unbuffered solution initially at pH 5.00. The electrolysis was performed using a platinum gauze working anode held at +1.000 V. The electrolysis was stopped periodically and the optical spectrum and pH were measured. As the electrolysis continued, the pH of the solution dropped, while the solution turned the greenish-yellow color of the [34] dimer. After one-half of a Faraday per mole of Ru3Y-OH₂ had been consumed, the optical spectrum reached a maximum and changed no further. The final spectrum was identical to that obtained for the [34] dimer by oxidizing Ru3Y-OH₂ by chemical means (see Figure 2). The formation of the [34] dimer is thus seen to be produced electrochemically in the same manner as by chemical means: one Faraday per two moles of ruthenium and the evolution of protons at pH 5.

The electrolysis was then continued until nearly 2.5 Faradays per mole of ruthenium had been consumed. No change in the optical spectrum was observed during this stage of the electrolysis. The back-titration of the total acid generated during the whole electrolysis yielded 1.1 moles of H^+ per Faraday. The formation of the [34] dimer from Ru_3Y-OH_2 has been previously determined by other methods to generate 1 H^+ per 1 mole of ruthenium (see equation 14), so that the subsequent oxidation process must also generate one proton per electron consumed.

The lack of any change in the optical spectrum indicates that the [34] dimer was not being destroyed during this stage of the electrolysis and that the solvent was being oxidized. The possible oxidation products of water include hydrogen peroxide, or dioxygen, and protons. Hydrogen peroxide formation from water would yield the observed proton to Faraday ratio, but the applied potential of +1.100 V is too low for the production of hydrogen peroxide, $E^\circ = +1.160$ V for the H_2O_2/H_2O couple at pH 5. The likely reaction, therefore, is dioxygen evolution from the oxidation of water. The thermodynamic potential for the O_2/H_2O couple at this pH is $E^\circ = +0.690$ V.

The small surface area of the platinum electrode, coupled with the length of time required for any measureable quantities of dioxygen to be produced (greater than one hour), made this method of dioxygen evolution ineffective for easy monitoring. As described earlier, the inability to

rigidly keep atmospheric dioxygen out of a vessel that is not under positive pressure of an inert gas prevents the quantitative detection of catalytically evolved dioxygen. Dioxygen is, however, being evolved catalytically in the presence of the [34] dimer at this potential since none was produced in its absence.

A similar set of experiments was performed on a Ru₃Y solution in a pH 7.70 buffered solution with a platinum gauze electrode. A CV (see Figure 21) obtained on a graphite disk electrode also present in the solution was essentially identical to that of the pH 5.50 solution upon reduction to Ru₂Y-OH₂ (I and II), but it also exhibited different behavior upon oxidation (waves I and II).

The post wave present at -0.425 V was identified as being due to adsorption of Ru₃Y-OH₂ to the electrode surface (either BPG, or mercury). The wave height for I increased at a rate proportional to the square root of the scan rate indicating a diffusion controlled, nernstian process (60), while the post wave increased roughly, linearly with scan rate (20 mV/sec -10 V/sec) indicating an adsorption process. The post wave was present only at pH's 7.5 ±0.5 using phosphate and borate buffers, but not above, or below these pH's. It was, however, not present when edta was the buffer at pH 7.5. When phosphate was added to the edta-buffered solution, then the post-wave was observed to grow in. This indicates that some sort of Ru₃Y-OH/phosphate, or borate complex is produced that induces adsorption. The effect is

Figure 21

Cyclic voltammogram of Ru₃Y-OH₂ at pH 7.70

Conditions: 0.890 mM HRu₃Y-OH₂

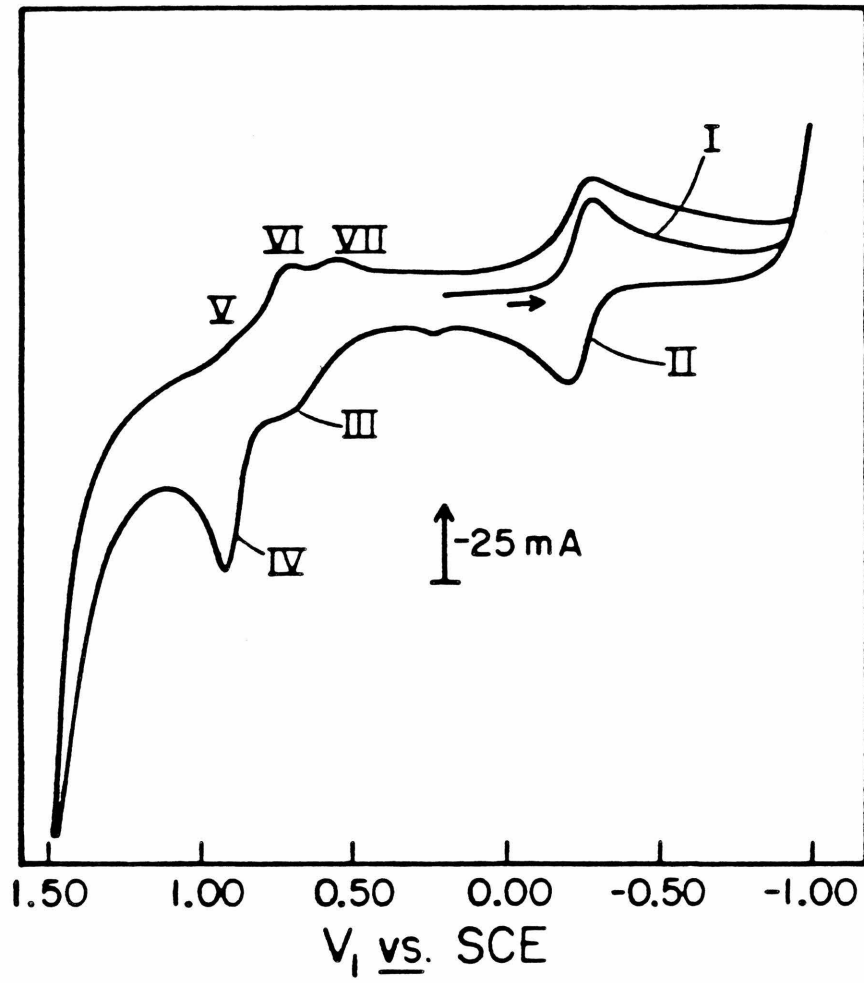
50 mM phosphate buffer, pH 7.70

total ionic strength = 0.200 N with NaTFA

BPG electrode

scan rate: 100 mV/sec

Figure 21



more pronounced on mercury than BPG and the exact mechanism of the adsorption process is unclear. The $\text{Ru}_2\text{Y-OH}_2$ complex, however, does not appear to adsorb since there is no evidence of an adsorption wave upon the return scan.

Considering the oxidation behavior, a large, broad "pre-wave" (III) before the large oxidation wave at +0.950 V (IV) was observed at +0.700 V for Ru_3Y at this pH. This wave did not exhibit a return reduction wave when the scan was reversed at +0.800 V (not shown). Upon extending the scan to +1.500 V and then reversing the scan direction, three small waves were observed (V, VI and VII).

To try and identify the species produced at III, an electrolysis was performed on this solution with a platinum gauze anode held at +0.750 V, and the optical spectrum of the solution was measured periodically. After the removal of one Faraday per two moles of ruthenium complete conversion of Ru_3Y to the yellow-green, [34] dimer was observed. The oxidation ceased at this point.

A series of CV's was recorded at different scan rates (20-500 mV/s) between +0.200 and +1.200 V on the oxidized solution (not shown). Waves IV and V appeared to be coupled since when the scan rate was increased, more of the product at wave IV was present to be reduced. It was difficult to extract any exact peak height currents due to the poorly defined background current, thereby preventing any detailed analysis of these waves. The apparent E° for these two waves is +0.860 V (70 mV separation at 500 mV/sec).

Waves VI and VII may be adsorption waves, but it is difficult to establish clearly the true nature of each wave using cyclic voltammetry. Waves VI and VII are also not present in the CV's at lower pH's. Cyclic voltammetry was, therefore, used only as a qualitative method to characterize the electrochemistry of the ruthenium-edta system.

After the solution had been electrolyzed at +0.750 V, the electrode potential was adjusted to +1.000 V and the electrolysis restarted. As the electrolysis continued, the color of the solution changed to an intense, emerald-green (see Figure 22). The electrolysis was continued for several hours and a small number of bubbles formed on the electrode. This was taken to indicate dioxygen formation. As the electrolysis was continued, the optical spectrum was measured periodically. A new spectrum exhibiting maxima at 308 nm ($32,500 \text{ cm}^{-1}$, $\epsilon_{308} = 8,390 \text{ M}^{-1} \text{ cm}^{-1}$), 393 nm ($25,400 \text{ cm}^{-1}$, $\epsilon_{393} = 5,820 \text{ M}^{-1} \text{ cm}^{-1}$) and 644 nm ($15,500 \text{ cm}^{-1}$, $\epsilon_{644} = 1900 \text{ M}^{-1} \text{ cm}^{-1}$) was observed to grow in. The greenish-yellow [34] dimer was observed to reappear with time with two isosbestic points at 322 nm ($31,000 \text{ cm}^{-1}$, $\epsilon_{322} = 7,490 \text{ M}^{-1} \text{ cm}^{-1}$) and 518 nm ($19,300 \text{ cm}^{-1}$, $\epsilon_{518} = 596 \text{ M}^{-1} \text{ cm}^{-1}$) indicating the presence of just two species in solution. The decay process was evidently not very rapid and required nearly 4 hours to return fully to the [34] dimer. The oxidized complex is unstable towards decomposition to the [34] dimer, but its spectrum is different than the one observed when excess Ce(IV) was used as the oxidant. This new oxidized

Figure 22

UV/Vis of [34] dimer after electrolysis at +1.100 V

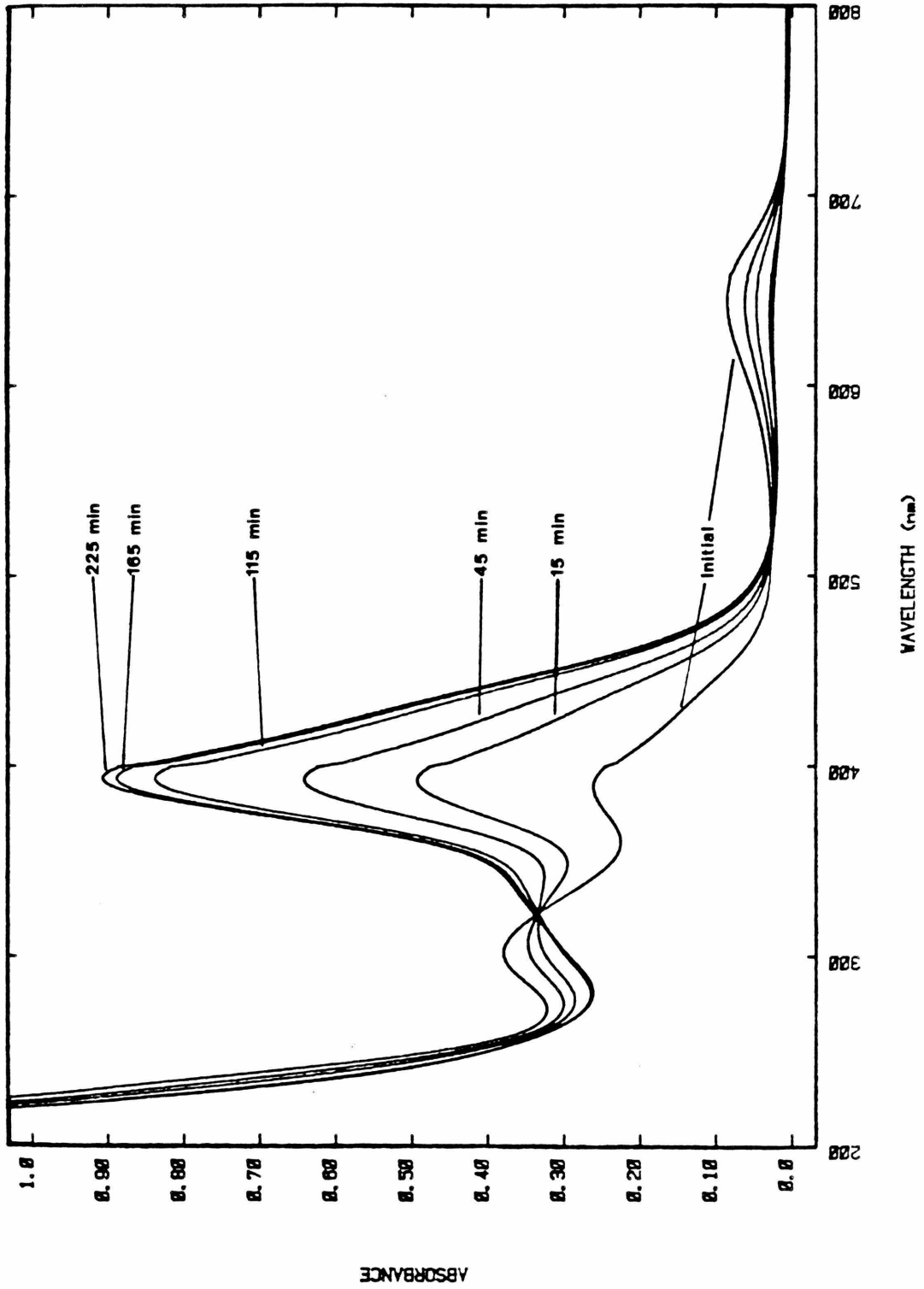
Conditions: 0.890 mM HRu3Y-OH₂

50 mM phosphate buffer, pH 7.70

total ionic strength = 0.200 N with NaTFA

200-800 nm

Figure 22



complex was not able to be identified by this experiment but is taken as another form of the [44] dimer. The coordinated edta is apparently not being consumed during the oxidation since the initial [34] spectrum was eventually regenerated. Once again, the catalytic oxidation of the solvent to produce dioxygen seems to be most likely.

To try and determine which oxidation waves were attributable to the [34] dimer and which ones were due to Ru3Y-OH_2 , CV's of several different pH solutions containing the [34] dimer were studied. The [34] dimer study was made, either on electrochemically generated solutions, or by dissolving some solid [34] dimer. Identical results were obtained for each.

A CV of the [34] dimer yielded nearly the same results as that for Ru3Y at any given pH. At $\text{pH} \leq 5$, the same behavior was observed for the [34] dimer in the +1.000 V region as for Ru3Y-OH_2 (see Figure 20). The large oxidation wave (III), was observed on the initial pass and a reversible couple (waves IV,VI) of smaller magnitude appeared upon repetitive cycling between +0.400 V and +1.500 V. For $7 \leq \text{pH} \leq 10$, however, there was a difference between the CV's of [34] dimer and Ru3Y-OH_2 . The large "pre-wave", III (see Figure 21) was no longer evident upon scanning from +0.200 V out to +1.200 V, while the large oxidation wave, IV, still appeared. Waves V, VI, and VII were still evident upon reversing the scan. As the scan rate was increased, the CV's showed an increase in the ratio of the currents of

wave V to wave IV. It was not possible to quantify this amount of current since the solvent oxidation wave distorted the baseline. Qualitatively, the CV's indicated that at faster scan rates a greater amount of the species that was oxidized at wave IV was still present to be reduced at wave V. This type of behavior is indicative of a chemical reaction occurring after the [34] dimer had been oxidized. The follow-up chemical reaction was not fast enough to consume all of the oxidized dimer since at slow scan rates (20mV/sec) there was no evidence of wave V. The chemical reaction was taken to be catalytic water oxidation to produce dioxygen and the [34] dimer since dioxygen was detected at a YSL O₂ probe in the solution during the electrolysis.

An electrolysis was also performed at +1.000 V on a solution of the [34] dimer at pH 10. After 30 minutes, bubbles were seen to form on the surface of the BPG disk without any change in the optical spectrum and the YSL O₂ probe indicated the evolution of dioxygen. The rate of dioxygen evolution at this pH is apparently faster than at pH 5. The quantitative detection of dioxygen was not possible, but it is clear that in the presence of the [34] dimer, dioxygen is catalytically evolved from water at potentials greater than +1.000 V.

As was the case for Ru3Y-OH₂, cyclic voltammograms were not used for quantitative measurements of the oxidation processes. The CV's did, however, provide a qualitative

description of the oxidative electrochemistry of the [34] dimer. At all pH's between 1 and 10, a large oxidation wave was present at +1.000 V. For $\text{pH} \geq 7$, a reversible couple at more negative potentials was seen to emerge from this wave. The reversible couple is attributed to the oxidation of the [34] dimer to the [44] dimer, while the large oxidation wave is ascribed to the catalytic evolution of dioxygen from water.

As can be seen from the above results, the electrochemistry of the ruthenium-edta system is very complicated and exhibits several waves in the CV's of the [34] dimer and $\text{Ru}_3\text{Y-OH}_2$. The number and peak currents of these waves were greater at higher pH's and this made it very difficult to assign the waves to a particular electrochemical process. This problem was most evident in the +0.200 V to +1.500 V region, and an alternative method of studying these waves was needed. Rotating ring-disk electrode voltammetry provided this means, and will be discussed in a later section.

The reduction of the [34] dimer occurs at sufficiently negative potentials to allow its cyclic voltammetry to be examined at a hanging mercury drop electrode (HMDE). A typical CV of the [34] dimer at pH 10 is shown in Figure 23. The redox couple at -0.870 V was not always present and depended on the sample used. This wave sometimes amounted to 15% of the total ruthenium concentration. This was determined by a comparison of the peak currents for wave I

Figure 23

Cyclic voltammogram of the [34] dimer at pH 9.96

Conditions: 0.432 mM [34] dimer

50 mM borate buffer, pH 9.96

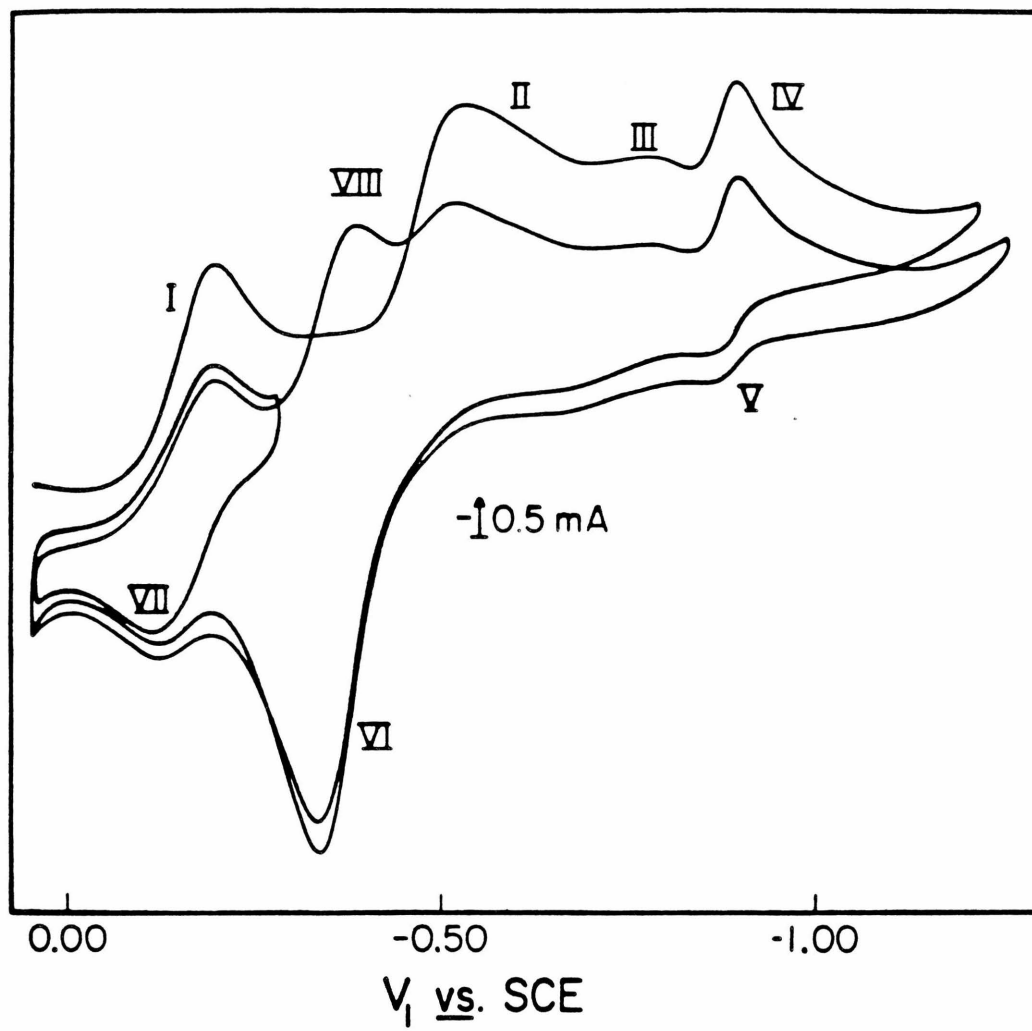
total ionic strength = 0.200 N with NaTFA

HMDE electrode: area = 0.032 cm²

scan region: +0.050 <---> -1.250 V

scan rate: 50 mV/sec

Figure 23



in Figure 23, to a solution lacking the redox couple at -0.800 V.

The CV scan was started at $+0.050$ V and proceeded to -1.200 V. Several waves were present in the initial scan. Upon reversing the scan and returning to the initial potential, three anodic waves were observed. Reversing the scan direction once again, yielded a new cathodic wave, VIII, between waves I and II.

Repetitive cycling between $+0.050$ V and -0.275 V showed waves I and VII to be coupled. At typical CV scan rates (20 - 500 mV/sec), the peak heights for waves I and VII were very nearly equal and the peak separation was approximately 70 mV indicating a reversible, one-electron process. Waves I and VII were therefore taken to be due to the $[34]/[33]$ redox couple. The wave height of VII was also a function of pH and was not present at scan rates up to 1 V/sec at pH's < 5 . The $[33]$ dimer apparently splits into two Ru_3Y monomers rather fast, since, even at pH 10, an electrolysis performed at -0.290 V on a solution of the $[34]$ dimer yielded only $\text{Ru}_3\text{Y-OH}$; as determined by its optical spectrum and cyclic voltammetry. An electrolysis performed at -0.150 V on a solution of the $[34]$ dimer at pH 10 required one-half a Faraday per mole of the $[34]$ dimer to produce two moles of $\text{Ru}_3\text{Y-OH}$. This further substantiates the dimeric, mixed-valence, composition of the oxidized species of Ru_3Y .

Repetitive scans on a solution of the $[34]$ dimer between $+0.050$ V and -1.200 V at pH's > 7 , yielded a decrease in

waves I, II, III, and VII, with a concomitant increase in VIII. There was also no change in waves VI, IV and V (when the latter two were present). This effect is evident at any scan rate, but it is enhanced at higher scan rates. The following scenario is proposed to account for this behavior. Wave II is ascribed to the reduction of the [33] dimer to a [32] dimer. There is then a fast, following chemical reaction with decomposition of the [32] dimer yielding $\text{Ru}_3\text{Y-OH}$ and $\text{Ru}_2\text{Y-OH}_2$ (at pH 10). This accounts for there never being any evidence of a reoxidation wave for a [32] dimer. Only the presence of the monomeric $\text{Ru}_2/3\text{Y}$ redox couple was detected (waves VI and VIII). Cyclic voltammetry did not offer a reasonable method for determining accurate values for the rate constants associated with these chemical processes and details of the mechanism of the breakup of the various dimers will be discussed in the section on the rotating ring-disk electrode.

After the [34] dimer had been reduced to produce the monomeric $\text{Ru}_3\text{Y-OH}_2$ (or $\text{Ru}_3\text{Y-OH}$, depending on the pH) a scan rate study of the resultant solution was performed. Depending upon the purity of the solution, either one, or two species were present in solution. Only the $\text{Ru}_3/2\text{Y}$ couple (waves VI and VIII) was observed, unless there was some impurity present, in which case waves IV and V were present. The optical spectrum of this solution was similar to that expected for $\text{Ru}_3\text{Y-OH}$ at pH 10 for wavelengths greater than 280 nm, but the end absorbance in the

ultraviolet was continually rising instead of exhibiting the expected shoulder at 232 nm ($43,100 \text{ cm}^{-1}$). The difference in the absorbance cannot be attributed to the presence of the "impurity", since even in the absence of the "impurity" the absorbance in the ultraviolet was still rising.

Waves VI and VIII yielded linear plots of oxidation peak current vs. the square root of scan rate indicating simple nernstian behavior. The peak positions did not change with scan rate, and in the case of the Ru₃/2Y couple, the peak current ratio for the two waves was equal and separated by 65 mV. The smaller waves near -0.900 V, however, had a varying ratio of anodic to cathodic peak current as a function of scan rate. At higher scan rates (200 mV/sec), the ratio was nearly equal to one. The peak separation, however, was only 35 mV. These factors indicate that this couple corresponds to a two-electron process with a following chemical reaction. The exact nature of this species was not characterized in these studies, but appears to be a different form of a [33] dimer.

If the Ru₃Y-OH solution is reduced at -0.500 V, then a spectrum similar to Ru₂Y-OH₂ started to appear and stopped changing at 1.0 moles of ruthenium. In the presence of the "impurity" the far ultraviolet, however, exhibited a rising absorbance with an inflection at 233 nm ($42,900 \text{ cm}^{-1}$), instead of the symmetric peak at 290 nm characteristic of pure Ru₂Y-OH₂. The CV's of this solution showed, as expected, no change from before the electrolysis. The rest

potential, however, had shifted from -0.150 V to -0.500 V indicating that the $\text{Ru}_3\text{Y-OH}$ had been reduced totally to $\text{Ru}_2\text{Y-OH}_2$.

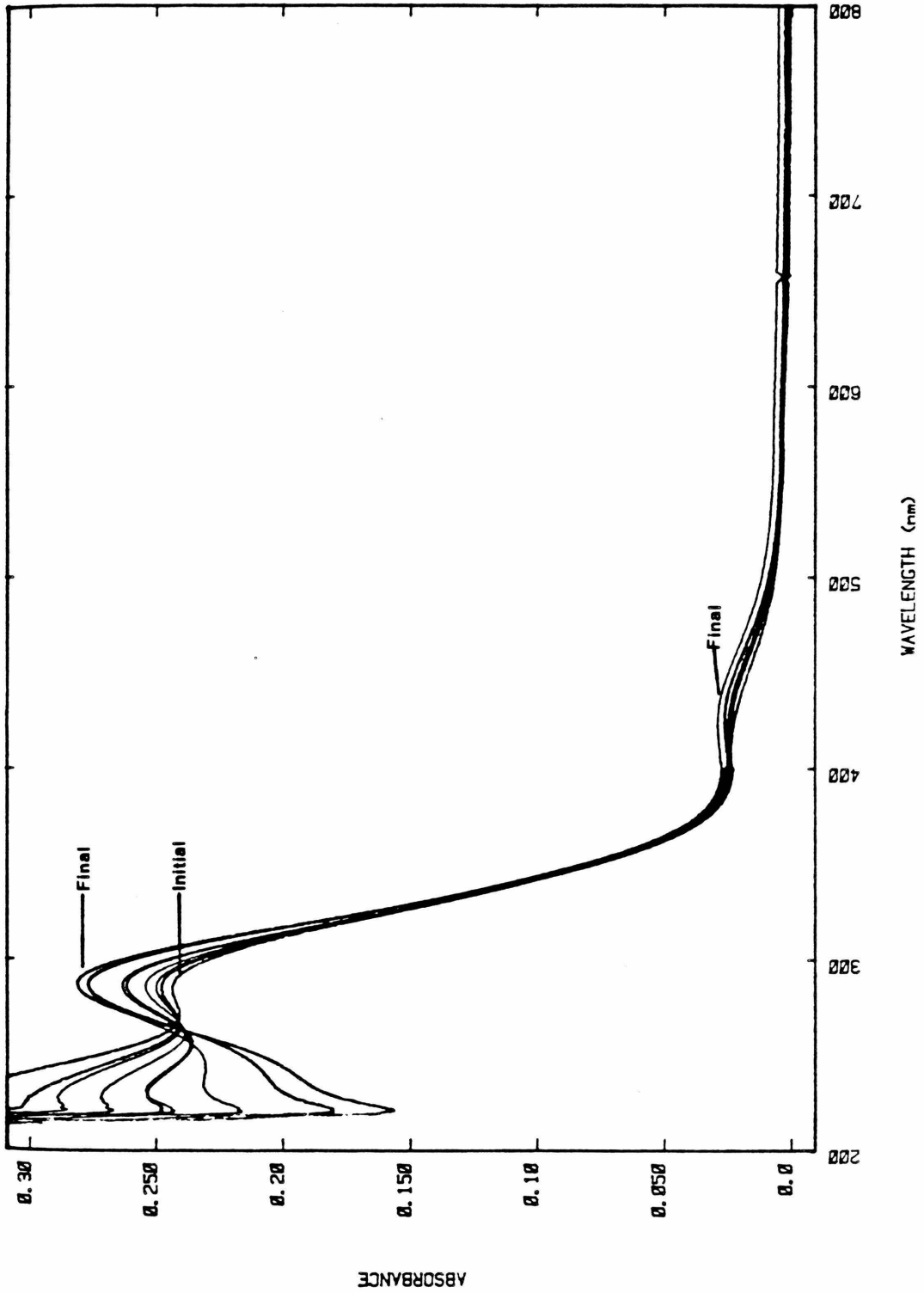
When a solution containing the "impurity" was electrolyzed at -1.050 V, then the spectrum (see Figure 24) and the CV changed, resulting in only $\text{Ru}_2\text{Y-OH}_2$ being observed. The wave at -1.050 V eventually disappeared during the electrolysis. The final concentration of $\text{Ru}_2\text{Y-OH}_2$, determined by the known extinction coefficient for $\text{Ru}_2\text{Y-OH}_2$ at 290 nm, was equal to the total amount of ruthenium in the sample as determined by chemical analysis and showed that up to 15%, depending upon the sample, of the ruthenium was involved in the reduction of the "impurity". The number of coulombs was not corrected for background reductions and did not correlate well with the ruthenium content for the impurity. The spectra in Figure 24 indicate that the final form of the species reduced at -1.050 V was $\text{Ru}_2\text{Y-OH}_2$. The rising end absorbance in the optical spectrum for the solution before electrolysis at -1.050 V was initiated is very similar to that exhibited by $\text{Ru}_3\text{Y-OH}_2$. This band is most likely due to a LMCT transition from the coordinated carboxylate-group oxygen to the ruthenium(III). The impurity may, therefore, have some ruthenium(III) character to it, which adds further to the classification of the impurity as a fairly stable [33] dimer with a structure different from the [33] species produced upon reduction of the [34] dimer.

Figure 24

UV/VIS of a [34] dimer solution after reduction at
-1.050 V ("impurity" present)

Conditions: 0.432 mM [34] dimer
50 mM borate buffer, pH 9.96
total ionic strength = 0.200 N with NaTFA
200-800 nm

Figure 24



In total, the electrolysis and spectral results indicate that the [34] dimer is reduced by one electron to the [33] dimer, which then breaks up to yield two Ru₃Y monomers (on the electrolysis time scale). The Ru₃Y monomer can then simply be reduced to Ru₂Y-OH₂. The CV's indicated that the [33] and the [32] forms of the dimer were produced upon successive reduction steps of the [34] dimer and that they were stable long enough to be observed on this technique's time scale ($t_{\frac{x}{2}} < 1$ sec), but not long enough to be observed during a bulk electrolysis.

In various samples, an impurity was also observed in amounts varying from zero to 15%. The impurity apparently requires two electrons to be reduced, whereupon, it breaks up to give Ru₂Y-OH₂. The impurity is, thus, taken to be a [33] dimer, but with a different structure than the [33] dimer that is produced upon reduction of the [34] dimer. This new [33] dimer is also much more difficult to reduce than the "simple", oxo-bridged species.

17. POLAROGRAPHY

During the pH study of the cyclic voltammetric response of the [34] dimer, all of the reduction waves were observed to shift as a function of pH. To identify clearly which waves were due to the Ru₃/2Y couple, a study of the polarography of the monomer as a function of pH was undertaken. Polarographic techniques utilized were Tast and normal pulse since the use of cyclic voltammetry, even on mercury, is not as accurate at determining the half-wave potentials, and the diffusion coefficients. A diffusion coefficient was determined for Ru₃Y-OH and found to vary by less than 10% from that for Ru₃Y-OH₂ (5.50 E-6 vs. 6.00 E-6 cm²/sec, respectively). The half-wave potentials were determined roughly by cyclic voltammetry, and then determined accurately by a wave shape analysis of the polarographic wave (153).

$$E = E_{\frac{1}{2}} + \left(\frac{0.059}{n} \right) \log \left(\frac{(i_1 - i)}{(i - i_0)} \right) \quad (38)$$

where,

E = the applied potential (V)

$E_{\frac{1}{2}}$ = the half-wave potential (V)

$$= E^\circ + \left(\frac{0.059}{n} \right) \log \left(\frac{D_r}{D_o} \right)$$

E° = the formal potential (V)

n = number of electrons involved in the redox couple

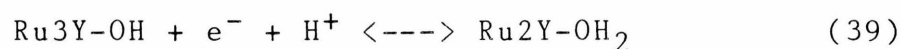
D_i = diffusion coefficients of the redox couple species (cm^2/sec)

i_d = limiting current (μamp)

i_0 = baseline current (μamp)

i = measured current at a given potential (μamp)

The results of this analysis are plotted in Figure 25, along with the results for the [34] dimer. Also included are $E_{1/2}$ values for Ru3Y-OH_2 for several pH's between 1 and 5 determined by Shimizu, et al (3,4). A pKa of 7.7 is indicated for Ru3Y-OH_2 in Figure 25. This value agrees very well with the spectroscopically, and potentiometrically determined value of 7.65. The $E_{1/2}$ for the $\text{Ru3Y-OH}/\text{Ru2Y-OH}_2$ couple are seen to vary by -60 mV/pH above this value. This is due to the inclusion of one proton in the redox reaction



$$E = E^\circ + \left\{ \frac{0.059}{n} \right\} \log \left\{ \frac{[\text{Ru2Y-OH}_2]}{[\text{Ru3Y-OH}_2]} \right\} + \left\{ \frac{0.059}{n} \right\} \text{pH} \quad (40)$$

A typical normal pulse polarogram for the [34] dimer is shown in Figure 26. Four distinct limiting current plateaus are evident at this pH (8.51). Not all of the polarograms yielded such well-separated waves, however, since all of the waves exhibited variable pH behavior.

Wave shape analysis plots of the first wave exhibited slopes of 55-65 mV indicating a one-electron, reversible

Table 9

Polarography results for Ru3Y and the [34] dimer

Table 9

<u>pH</u>	<u>$E_{\frac{1}{2}}$</u> V vs SCE	<u>slope</u> mV	<u>i</u> μ amps	<u>conc</u> mM	<u>r^2</u>	<u>D</u> cm ² /sec
5.00	-0.003	59.5	0.390	0.401	0.999	3.34 E-6
	-0.239	48.5	1.345		0.999	
	-0.719	58.7	1.448		0.990	
6.82	-0.115	62.2	0.420	0.408	0.997	3.75 E-6
	-0.298	61.1	1.235		0.993	
	-0.584	55.0	1.288		1.000	
	-0.818	45.0	1.398		0.996	
7.69	-0.131	59.6	0.280	0.280	0.996	3.54 E-6
	0.358	62.0	0.765		0.985	
	-0.588	53.0	0.830		0.999	
	-0.810	40.5	0.940		0.997	
8.51	-0.145	59.5	0.388	0.379	0.998	3.71 E-6
	-0.408	56.7	0.958		0.999	
	-0.592	54.5	1.138		0.996	
	-0.835	37.0	1.276		1.000	
9.17	-0.157	58.0	0.318	0.302	0.999	3.91 E-6
	-0.441	53.0	0.770		0.999	
	-0.605	58.2	0.970		0.998	
	-0.848	41.0	1.038		0.999	

-continued on next page-

Table 9

<u>pH</u>	$E_{\frac{1}{2}}$	slope	i	conc	r^2	D
	<u>V vs SCE</u>	<u>mV</u>	<u>μamps</u>	<u>mM</u>		<u>cm^2/sec</u>
10.00	-0.159	66.5	0.300	0.293	0.996	3.47 E-6
	-0.493	77.0	0.748		0.998	
	-0.763	50.0	0.850		0.999	
	-0.878	37.0	0.930		0.998	
11.30	-0.225	57.5	0.360	0.354	0.996	3.46 E-6
	-0.560	49.0	0.673		0.999	
	-0.945	30.0	0.863		1.000	
12.55	-0.313	61.0	0.490	0.495	0.996	3.60 E-6
	-0.639	60.0	0.800		1.000	

D = 3.60±0.18 E-6

* This table includes data for the "impurity".
The concentration given is for the [34] dimer

Figure 25

Plot of $E_{\frac{1}{2}}$ vs. pH for the [34] dimer and Ru3Y

Figure 25

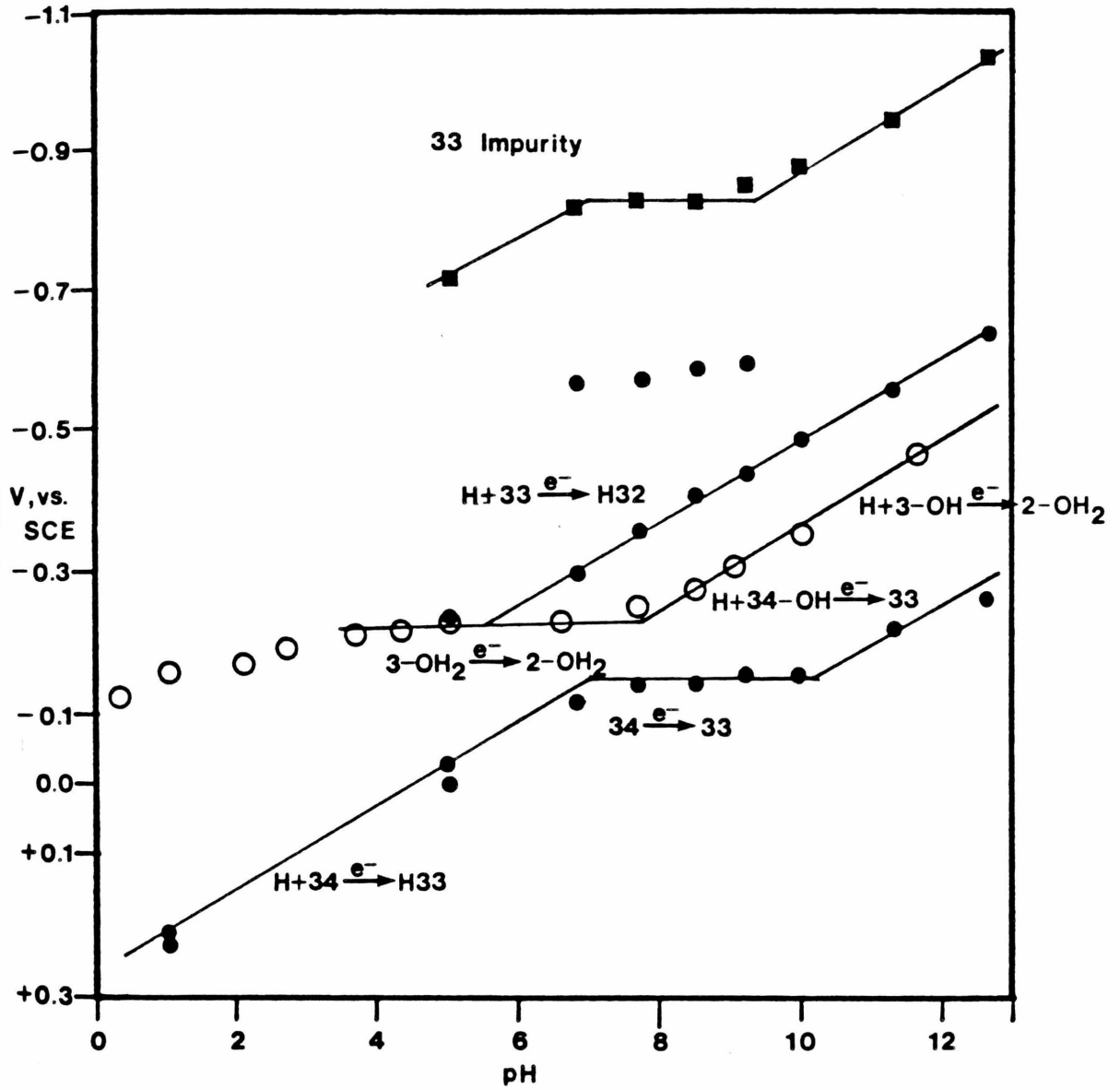


Figure 26

Normal pulse polarograms of the [34] dimer

Conditions: 0.379 mM [34] dimer

50 mM phosphate buffer, pH 8.51

total ionic strength = 0.200 N with NaTFA

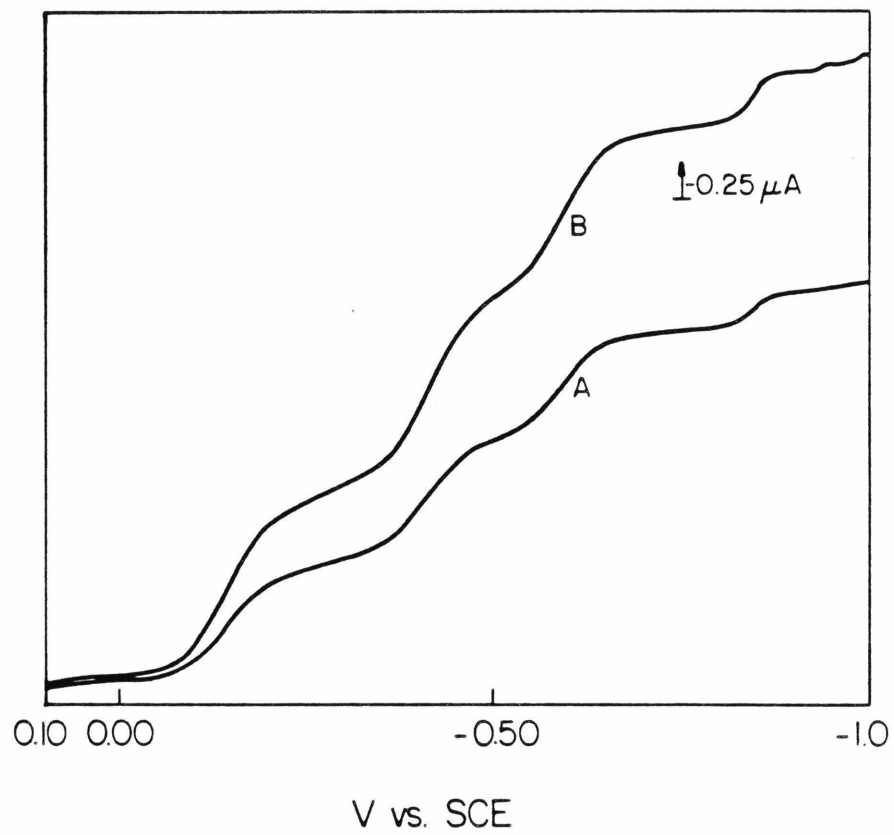
drop time, flow rate:

A. 0.5 sec, 0.637 mg/sec

B. 1.0 sec, 0.650 mg/sec

initial potential: +0.100 V

Figure 26



process (see Figure 27). The diffusion coefficient for the [34] dimer was also determined in this series of experiments and found to be $3.80 \pm 0.20 \text{ E-6 cm}^2/\text{sec}$. The diffusion coefficient was also found to be pH independent between pH 5 and 12.6.

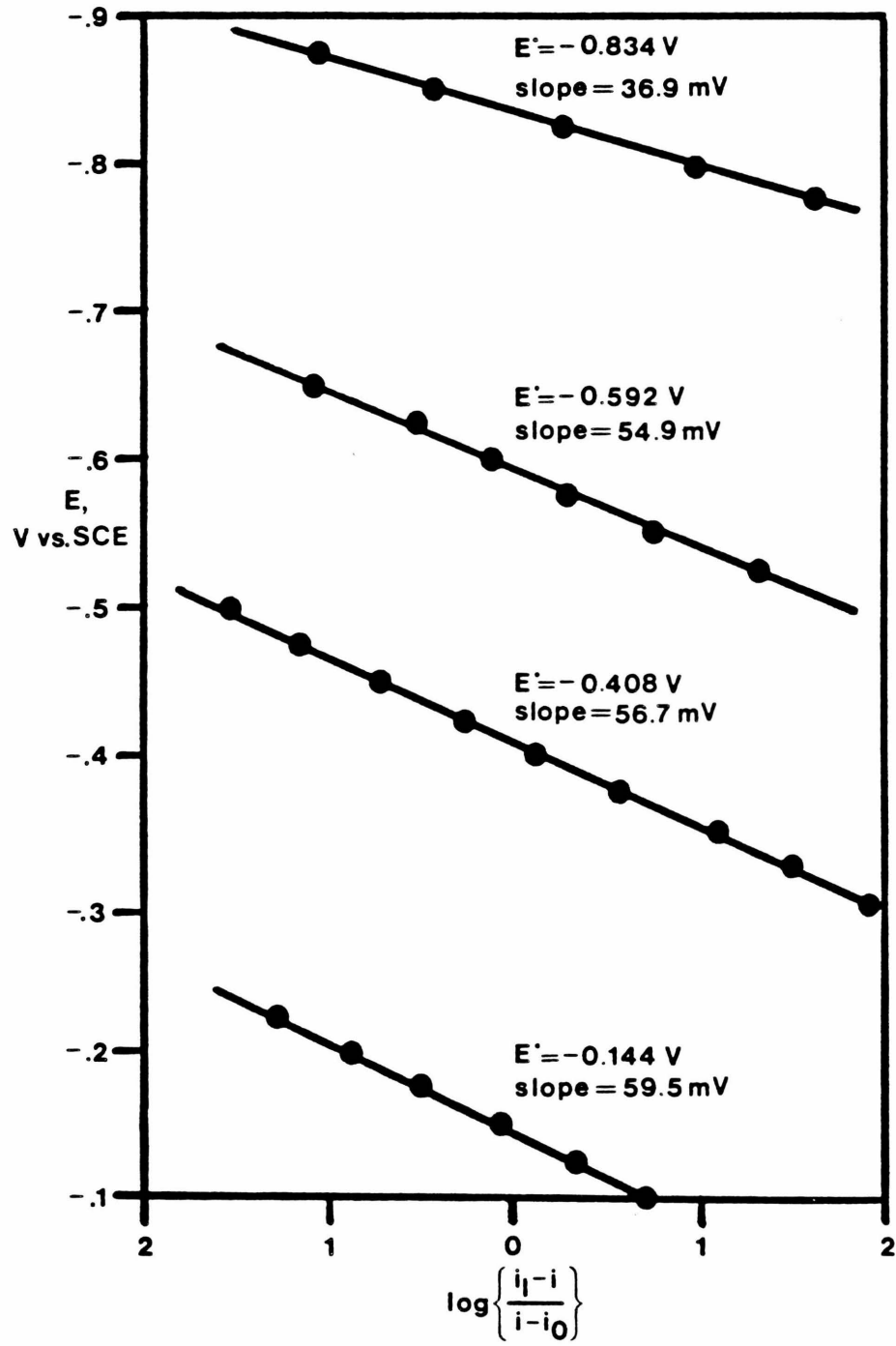
In the Tast polarograms, the second wave also analyzed for one electron (see Table 9 and Figure 27), but the ratio of the total limiting current of the second plateau to the first varied from 2.42 at pH 10, to up to 3.45 for pH 5. At pH's above 10, the ratio was less than two. The reasons for this latter result are unclear. The wave shape plots were also non-linear for other than the first wave in this pH region. When a third wave appeared with $E_{\frac{1}{2}} -0.700 \text{ V}$, then it analyzed as one electron and the total limiting current was three times that of the first wave. The smaller wave past -0.700 V (the previously discussed "impurity") was found to have a wave shape plot slope of 37-45 mV indicating a two-electron process. This result concurs with the previous CV observation of a reversible, two-electron redox couple near -0.800 V .

As the pH was changed, several variations were observed in the polarographic responses of the different oxidation states of the dimer (see Figure 25). The first wave exhibited a -60 mV/pH variation for its half-wave potential between pH 1 and 7 (the pH 1 values were taken from rotating ring-disk electrode results). A pK_a near 7.0 ± 0.4 was indicated by a leveling off of the $E_{\frac{1}{2}}$ vs. pH behavior

Figure 27

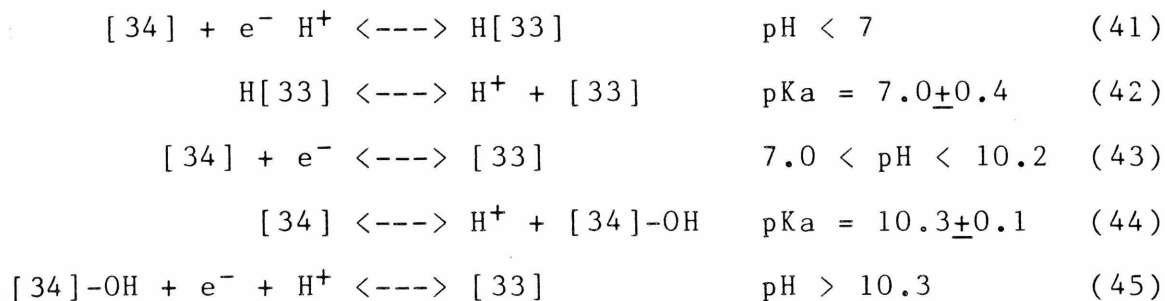
Wave shape analysis plots of pH 8.51 Tast polarogram

Figure 27



between pH 7 and pH 10. Another pKa of 10.2 ± 0.2 was indicated at the higher pH's, and above pH 10 the half-wave potential varied by -60 mV/pH . The following reaction scheme is proposed to account for the behavior of the first wave.

SCHEME I



where,

[34] = mixed-valence dimer

H[33] = protonated, one-electron reduced dimer

[34]-OH = μ -oxo, μ -hydroxo bridged mixed
valence dimer

It is expected that the free-acetate arms of the [34] dimer would have pKa's near 3, but, as was the case for Ru3Y-OH_2 , that their degree of protonation would have little effect on the half-wave potential (3,4). It is, therefore, unlikely that the pH dependence of the first wave involves an acetate group.

As discussed earlier, there was no spectroscopic evidence for protonation of any coordinated, oxo-containing ligand on the [34] dimer at $\text{pH} < 7$. Thus, the proton-coupled reduction of the [34] dimer below pH 7

involves the protonation of the [33] dimer. Equations 41 and 42 take this into account. The [33] dimer is, most likely, protonated at the μ -oxo position (abbreviated H[33]) to give a μ -hydroxo bridged dimer. Protonation of the bridging μ -oxo group then destabilizes the dimer and leads to its breakup to produce two $\text{Ru}_3\text{Y-OH}_2$'s. The bridging μ -hydroxo group in the [33] dimer is seen to have a pKa of 7.0, so that above pH 7 there should not be any pH dependence on the half-wave potential (equation 43). This behavior is observed between pH 7 and 10. The resultant [33] dimer is unstable enough, however, that it still breaks up. The rate of breakup is slower, however, than at lower pH's as indicated by the increased anodic current for the return wave in the CV's of the [34]/[33] redox couple at pH's > 7 (see Figure 23).

The second inflection in the half-wave potential plot for the first wave is due to the deprotonation of the [34] dimer to form the μ -oxo, μ -hydroxo bridged species (abbreviated [34]-OH) described earlier (see equation 44). Upon reduction, the [34]-OH dimer is protonated to produce the μ -oxo bridged [33] dimer (see equation 45). A return wave is still seen in the CV at these higher pH's, but an electrolysis indicated that the [33] dimer is still unstable enough that only the $\text{Ru}_3\text{Y-OH}$ monomer is observed as the final product after reducing at the first wave.

A second wave attributable to a [33]/[32] couple becomes apparent for pH's ≥ 7.0 . Below this pH, the breakup of the

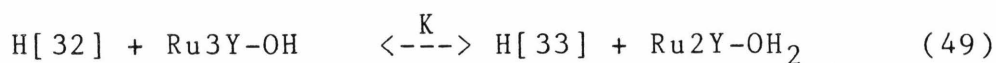
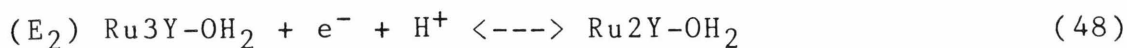
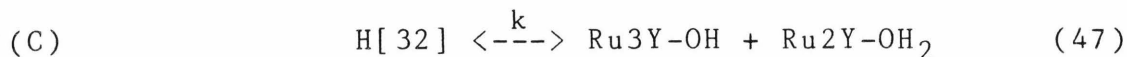
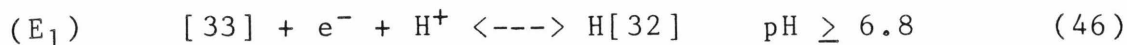
[33] dimer is so fast that only $\text{Ru}_3\text{Y-OH}_2$ is present and the second wave exhibits half-wave potentials identical to Ru_3Y (see Figures 25 and 26). Above pH 7, the half-wave potential for the second wave determined by polarography no longer coincided with the half-wave potentials for Ru_3Y . The CV's also showed that the Ru_3Y did not appear until after the reduction process of the second wave had occurred (see Figure 23). These results indicate that the [33] dimer is long-lived enough so that it can be reduced further by one-electron to give the [32] dimer. The lack of any return oxidation wave in the CV for the [32] dimer indicates that it is short-lived on CV time scales and splits up to give $\text{Ru}_3\text{Y-OH}$ and $\text{Ru}_2\text{Y-OH}_2$. A CV also showed that $\text{Ru}_2\text{Y-OH}_2$ was the only species present upon the return oxidation scan.

The [33]/[32] couple displays a -60 mV/pH variation of $E_{1/2}$ with no apparent pKa inflection for $\text{pH} < 12.6$. The [32] dimer is taken to be μ -hydroxo bridged and the pH dependence of the half-wave potential is due to protonation of the [32] form of the dimer. An inflection in the $E_{1/2}$ at $\text{pH} < 7$ would be expected for this wave due to the pKa of the [33] dimer, but the instability of the [33] dimer toward monomerization at these pH's prevents its observation.

Referral to Figure 25 shows that the half-wave potential for the [33]/[32] couple is negative of the $\text{Ru}_3/2\text{Y}$ couple. This means that when the [32] dimer monomerizes to produce $\text{Ru}_3\text{Y-OH}$ and $\text{Ru}_2\text{Y-OH}_2$, that $\text{Ru}_2\text{Y-OH}_2$ cannot reduce either the [33], or the [32] dimer, but that the [32] dimer can reduce

Ru3Y-OH to produce Ru2Y-OH₂ and the [33] dimer.

SCHEME II

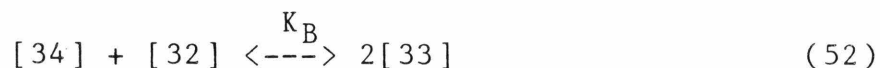
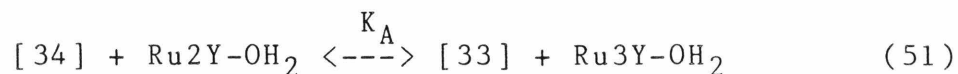


This is an ECE mechanism (E stands for an electron transfer reaction at the electrode, and C for an intervening, chemical process) where the last step, equation 49, is a homogeneous electron transfer reaction. The equilibrium constant for equation 49 is defined by the difference in the redox couples for the two half-reactions described by equations 46 and 48.

$$K_{eq} = 10^{-\left(\frac{E_1 - E_2}{0.059}\right)} \quad (50)$$

where E_1 corresponds to the reduction potential of equation 46 and E_2 to equation 48 and both are given in volts. For this system, $K_{eq} = 130$, for $\text{pH} \geq 6.8$. Thus there is a net regeneration of a [33] dimer and production of Ru2Y-OH₂ from Ru3Y-OH, produced by either [33] or [32] monomerization reactions, encounters a still undecomposed [32] dimer. This reaction will then affect the concentration profiles of all of the species before reacting at the electrode. It is difficult to determine exactly what effect it will have,

since it is not possible to generate a stable solution of the [33] dimer, and since both $\text{Ru}_2\text{Y-OH}_2$ and the [32] dimer can react in a homogeneous electron transfer reaction with the bulk species, the [34] dimer.



Between pH 7 and 10, the total limiting current of the second wave was 2.4 times as large as the limiting current of the first wave. More quantitative information about this mechanism and the individual steps will be covered in the section on the RRDE.

A third wave at -0.600 V was observed in the polarograms of the [34] dimer between pH 6.8 and 9.3. Wave shape plots yielded slopes of 53-58 mV, indicating a one-electron reaction. The half-wave potential was pH independent in this region. At pH 10, the half-wave potential shifted to -0.763 V, and then the wave became indistinct, with a steadily increasing current. When the current could be measured easily, the total limiting current of this wave, when compared to the first wave, yielded a ratio of 3.0. The [34] dimer is apparently totally reduced to its [22] form. This wave is tentatively assigned to the [32]/[22] redox couple. The lack of any pH dependence between pH 6.8 and 9.3 can be attributed to the structural limitations of the dimer. The [32] dimer is probably bridged by a μ -

hydroxide group, which is incapable of any further protonation. The [22] dimer is more than likely very unstable and decomposes in a very fast follow-up chemical reaction, with the subsequent pickup of a proton to form two $\text{Ru}_2\text{Y}-\text{OH}_2$'s.

The behavior of this wave above pH 10 is rather unusual. Little work other than the single polarographic measurements at pH 11 and 12.6 was done and the results are included here for future reference.

As mentioned earlier, in several of the samples, a two-electron wave was observed at very negative potentials. Its identity remains unclear, but its pH behavior is included in Figure 25, and Table 10. Two pKa's are indicated at 6.8 and 9.5. The slopes of the lines are nearly -60 mV/pH indicating a one proton per electron ratio during the reduction step, which was previously determined to be a two electron process. Little else, unfortunately, can be said about this wave, and a systematic means of producing this "impurity" is needed to aid in studying it further.

The polarographic study yielded much useful information about the redox potentials of the different oxidation state dimers produced upon reduction of the [34] dimer. Several pKa's were determined and were attributed to protonation and deprotonation of the [34], the [33], the [32], and the [22] dimers. Taken in conjunction with the pH dependent, half-wave potential behavior of $\text{Ru}_3\text{Y}-\text{OH}_2$, various pathways for

the decomposition of each of the dimers were proposed. The half-wave potentials determined for Ru₃/2Y above pH 7 also completed the full pH behavior of this couple between pH 1 and 12. The expected, -60 mV/pH shift for the Ru₃Y-OH/Ru₂Y-OH₂ couple was observed.

The diffusion coefficients for Ru₃Y-OH and the [34] dimer were also determined polarographically. The value for Ru₃Y-OH did not vary much from that of Ru₃Y-OH₂, with both near 6.0 E-6 cm²/sec, while the [34] dimer had a value of 3.6±0.2 E-6 cm²/sec. The larger size of the [34] dimer most likely accounts for the decreased value when compared to Ru₃Y-OH₂.

The actual amounts of limiting current observed for each of the waves in the reduction of the [34] dimer is, at the first several glances, very confusing. The ratio of the current for the second reduction wave of the [34] dimer to the current for the first wave are reproducibly, non-integral, and generally greater than two, and, sometimes three. Above pH 10, this ratio drops to below two. The reasons for many of these responses were eventually elucidated by utilization of the rotating ring-disk electrode (RRDE), and computer simulations of the complicated pathways indicated by the above experiments. More about this follows in a later section.

18. SPECTRO-ELECTROCHEMISTRY

Optically transparent thin-layer electrolysis cells (OTTLE) afford a rapid and accurate means of simultaneously monitoring the optical response of an electrolyzed solution. Cyclic voltammetry, bulk electrolysis, and a Ce(IV) titration of the [34] dimer showed that there was an oxidized form of the [34] dimer, but that it was unstable and eventually decayed back to the [34] dimer. In an attempt to detect the oxidized species before it decayed back to the [34] dimer, an OTTLE cell was used with the HP-8450 UV/Visible spectrophotometer to rapidly measure (1 sec) the full optical response (200-800 nm) of the [34] dimer upon oxidation.

A 0.450 mM solution of the [34] dimer in 0.1 M HTFA (total ionic strength was adjusted to 0.200 N with NaTFA) was monitored while varying the applied potential to the cell (see Figure 28). The cell was allowed to equilibrate for 300 seconds before obtaining the final reading for a given potential. This length of time satisfied the condition for a thin-layer cell where the cell pathlength is smaller than the diffusion-layer thickness enabling mass transfer effects within the cell to be neglected, and thereby resulting in bulk electrolysis conditions (148).

$$x \ll (2Dt)^{\frac{1}{2}} \quad (53)$$

where,

$$x = \text{cell pathlength (cm)}$$

Figure 28

Spectroelectrochemical response of the [34] dimer at pH 1

Conditions: 0.450 mM [34] dimer

0.100 M HTFA

total ionic strength = 0.200 N with NaTFA

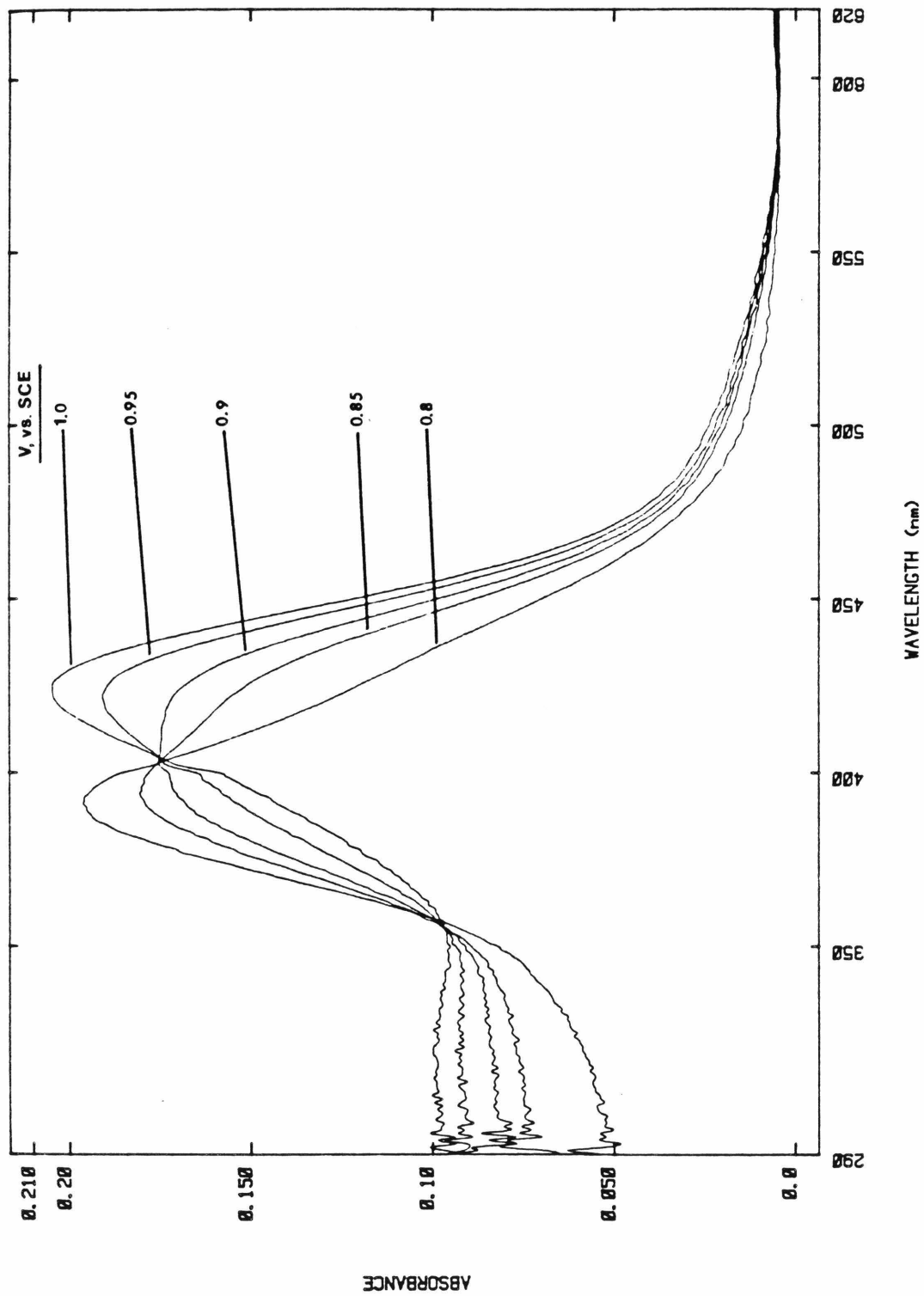
scan range: 290-620 nm

applied potentials: +0.800, 0.900, 0.925,

0.950, AND 1.000 V

equilibration time: 300 sec

Figure 28



D = diffusion coefficient of electroactive species (cm^2/sec)

t = length of time of the experiment

The OTTLE cell pathlength was determined to be 0.213 mm by comparing the absorbance of the [34] dimer in this and a 1.00 mm cell. Taking the diffusion coefficient of the [34] dimer as $3.6 \text{ E-}6 \text{ cm}^2/\text{sec}$, t is calculated to be 63 seconds, substantiating the thin-layer cell conditions for this experiment.

Two isosbestic points, 404 nm ($24,800 \text{ cm}^{-1}$, $\epsilon_{404} = 18,100 \text{ M}^{-1} \text{ cm}^{-1}$) and 356 nm ($28,100 \text{ cm}^{-1}$, $\epsilon_{356} = 10,100 \text{ M}^{-1} \text{ cm}^{-1}$) were observed during the electrolysis indicating the presence of just two species in solution. These two species were taken to be the [34] dimer and its oxidized form.

For a given potential, the concentration of the two halves of a redox couple are given by the Nernst equation which can be modified to include the absorbance of the solution at 25°C .



$$E = E^\circ + \left(\frac{0.059}{n}\right) \log \left(\frac{[\text{Ox}]}{[\text{Red}]}\right) \quad (55)$$

$$E = E^\circ + \left(\frac{0.059}{n}\right) \log \left(\frac{[A_{\text{r}} - A]}{[A - A_0]}\right) \quad (56)$$

where,

[Ox] = concentration of oxidized species

[Red] = concentration of reduced species

n = the number of electrons involved in the redox

E = a given potential (volts)

E° = the formal reduction potential (volts)

A_r = the absorbance of the fully reduced species

A_o = the absorbance of the fully oxidized species

A = the absorbance at a given potential where both halves of the redox couple are present

The derivation of equation 56 follows the same procedures applied to equations 17-22 discussed in the base titration section. A Nernst plot is then made where the log term is plotted vs. the applied potential. The slope is thus a function of the number of electrons involved in the redox couple, and the E° is determined when the log term is zero. If the standard assumption is made that the diffusion coefficient for both halves of the redox couple are equal, then E° can be taken as $E_{\frac{1}{2}}$ (148).

$$E_{\frac{1}{2}} = E^\circ + \left(\frac{0.059}{2n} \right) \log \left(\frac{D_r}{D_o} \right) \quad (57)$$

where,

D_r = diffusion coefficient of the reduced species

D_o = diffusion coefficient of the oxidized species

A Nernst plot of the two absorbance maxima at 393 nm (for the [34] dimer) and 424 nm (for the oxidized dimer) yielded a 56 mV slope indicating that the oxidized species

is the one-electron, oxidized [44] dimer (see Figure 29).

The [44] dimer is thus produced upon oxidation of the [34] dimer at potentials greater than 1.000 V at pH 1. The [44] dimer produced by this method was also observed to decay back to the [34] dimer after the cell was turned off. This precludes the existence of any other higher oxidation state forms of the dimer. The catalytic species for dioxygen evolution is therefore concluded to be the [44] form of the dimer.

This is in contrast to the results of Meyer's ruthenium-bipyridine, oxo-bridged dimer (47), where he claims that a [55] dimer is the catalytic species. His conclusion is based on the observation that four equivalents of Ce(IV) per mole of [33] dimer are necessary before any dioxygen evolution is detected. There was also no mention made of any of the intermediate oxidation state dimers during the oxidation process. Based on the spectral similarities between the ruthenium-edta and ruthenium-bipyridine dimers in the [34] oxidation states, the differences between the two systems upon oxidation is puzzling. More experiments are needed to determine the stoichiometry involved for the ruthenium-bipyridine dimer. Since the system studied by Meyer did not react very fast, the use of an OTTLE cell may also prove useful in determining the oxidation state of the reactive species.

Referring to the spectra in Figure 28, a shift to lower energy is seen for the intense charge transfer band upon

Figure 29

Nernst plot of the oxidation of the [34] dimer

Legend:

solid circles: 393 nm absorbance data

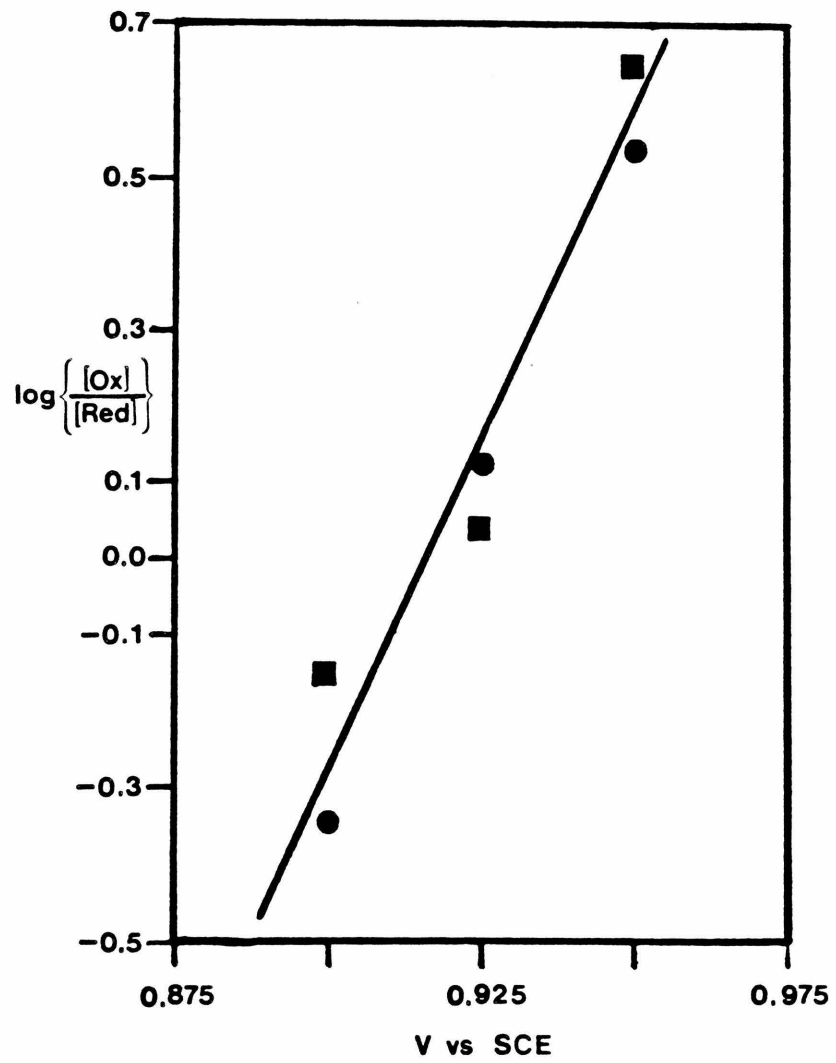
solid squares: 424 nm absorbance data

r^2 : 0.951

intercept: 0.917 V

slope: 56.3 mV

Figure 29



oxidation. In the absence of any structural changes, the charge-transfer bands for the [44] dimer would be expected to be at higher energy than for the [34] dimer. Yet, in this case, the prominent band for the [34] dimer at 393 nm ($25,400 \text{ cm}^{-1}$) is shifted to lower energy (424 nm, $23,600 \text{ cm}^{-1}$). A possible reason for this unexpected shift is that there is a change in the coordination environment around the ruthenium centers. Since the carboxylate arms coordinated to Ru3Y-OH_2 are known to be labile, similar behavior may be occurring for the dimer and a water molecule may then substitute to bind to the dimer upon oxidation. If this were the case, then the coordinated water would be likely to deprotonate, producing a hydroxide, or even a bridging hydroxide, in a manner similar to that proposed for the [34] dimer at higher pH's. The incorporation of a hydroxide, or a water would then be expected to shift the charge transfer band to lower energy relative to the energy for a coordinated carboxylate.

The incorporation of a water, or hydroxide may also be the means by which the catalytic cycle proceeds. A shift in the half-wave potential for the [44]/[34] couple would be expected for this kind of coordination change upon oxidation and the RRDE was used to investigate this; a shift was observed. More about this will be discussed in the next section.

One other possibility could be that the coordination geometry around each of the rutheniums changes upon

oxidation to form a seven-coordinate complex. This could involve either the incorporation of a water molecule, or one of the free-acetate arms. The formation of a seven-coordinate complex could then lead to the observed red-shift of the charge transfer band. There is precedence for seven-coordinate metal-edta complexes (149-151), but the unstable nature of the [44] dimer makes it difficult experimentally to determine its structure.

19. ROTATING RING-DISK ELECTRODE VOLTAMMETRY

The rotating ring-disk electrode (RRDE) provides a very powerful means for studying complicated chemical and electrochemical reactions (149). The RRDE enables the species generated at the disk to be monitored afterwards at the ring. Any complicating chemical, or subsequent electrochemical processes, will affect the disk current, and hence, the ring current. Several factors can lead to changing the disk and ring currents from the simple, hydrodynamically controlled Levich behavior.

$$i_{D,lim} = 0.62nFAC_b D^{\frac{2}{3}} \omega^{\frac{1}{2}} \nu^{-\frac{1}{6}} \quad (58)$$

where,

$i_{D,lim}$ = limiting current at the disk electrode (μ amps)

n = number of electrons involved in the redox couple

F = Faraday's constant

A = area of the disk electrode (cm^2)

C_b = bulk concentration of the electroactive species (mole/cm^3)

D = diffusion coefficient (cm^2/sec)

ν = kinematic viscosity of the solvent (cm^2/sec)

ω = rotation rate of the RRDE (rad/sec)

Chemical pre-equilibrium, following chemical reactions, multiple electrochemical steps, and surface phenomena will alter the measured currents from the Levich behavior. Typically, the ring potential is set at a potential that

will cause the reverse of the initial electrochemical disk reaction to occur. The ring current is simply a function of the electrode's geometry so that any electrochemical, or chemical process occurring at the disk will be reflected in the ring's response. This is reflected in the quantity, N , the collection efficiency.

$$N = -\left(\frac{i_r}{i_d}\right) \quad (59)$$

where,

i_r = the ring current

i_d = the disk current

The complicated electrochemical response of the ruthenium-edta monomers and dimers was investigated using the RRDE in the hopes of unravelling the myriad of reactions occurring during oxidation and reduction of the various species. Since very few reaction mechanism involving chemical complications can be described by a closed-form mathematical solution, digital simulation was required to aid in modelling the system and to extract homogeneous chemical rate constants. The methods originally developed by Feldberg (55), and expanded upon by Bard and Prater (52-54) were used to model the RRDE. A more detailed description of the method and its application to the systems discussed below will be described in a later chapter.

A typical series of RRDE voltammograms is illustrated in Figure 30 for a pH 1 solution of HRu3Y-OH_2 . In Figure 30a,

Figure 30

RRDE of RU3Y-OH_2 at pH 1

Conditions: BPG disk, platinum ring

0.368 mM RU3Y-OH_2

0.100 N HTFA

total ionic strength = 0.200 N with NaTFA

scan rate 0.5 V/min

ring potential: +0.400 V

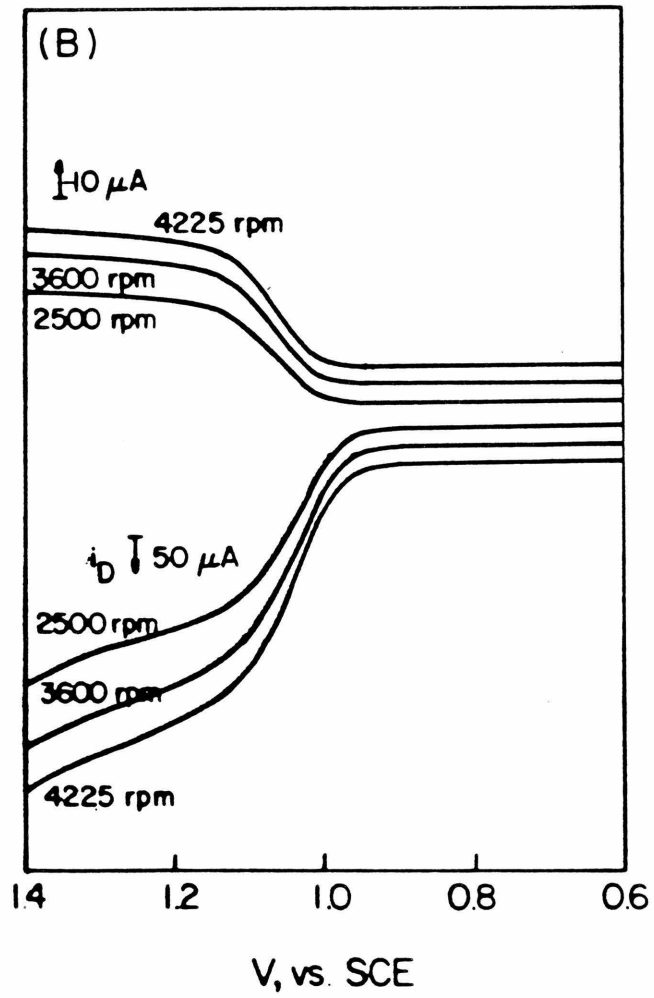
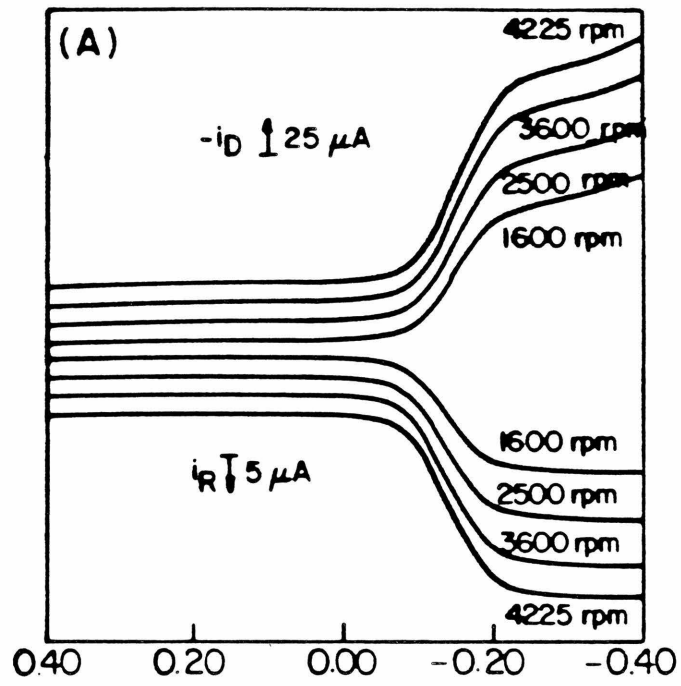
A) disk scan range: +0.400 ---> -0.400 V

rotation rates: 1600, 2500, 3600, 4225 rpm

B) disk scan range: +0.400 ---> +1.400 V

rotation rates: 2500, 3600, 4225 rpm

Figure 30



a 0.386 mM solution was scanned from +0.400 V to -0.500 V at the disk, while the ring potential was set at +0.400 V. The rotation rate in this, and the following RRDE voltammograms was varied, typically, between 100 and 4625 rpm, while the scan rate was always 0.50 V/min. Figure 30b is a series of voltammograms of the same solution with the disk scanned from +0.400 V to +1.300 V and the ring set at +0.400 V. The limiting ring and disk currents were then plotted vs. the square root of the rotation rate (Levich plots) (see Figure 31). The diffusion coefficient was calculated from the Levich slope for the reduction of Ru3Y-OH₂ at -0.300 V and found to be 5.92 E-6 cm²/sec, which concurs with the value determined previously by polarography.

The response of the reduction of Ru3Y-OH₂ to Ru2Y-OH₂ also serves as a convenient internal means of calibrating the collection efficiency of the RRDE for a one-electron redox reaction. The observed collection efficiency for the electrode was found to be 0.168 vs. the calculated value of 0.176. The calculated value was obtained either by the simulation program in the absence of any chemical complications, or by an equation given by Albery and Hitchman (49).

$$N = 1 - F\left(\frac{\alpha}{\beta}\right) + \beta^{\frac{2}{3}} [1 - F(\alpha)] - (1 + \alpha + \beta)^{\frac{2}{3}} \cdot F\left[\left(\frac{\alpha}{\beta}\right)(1 + \alpha + \beta)\right] \quad (60)$$

Figure 31

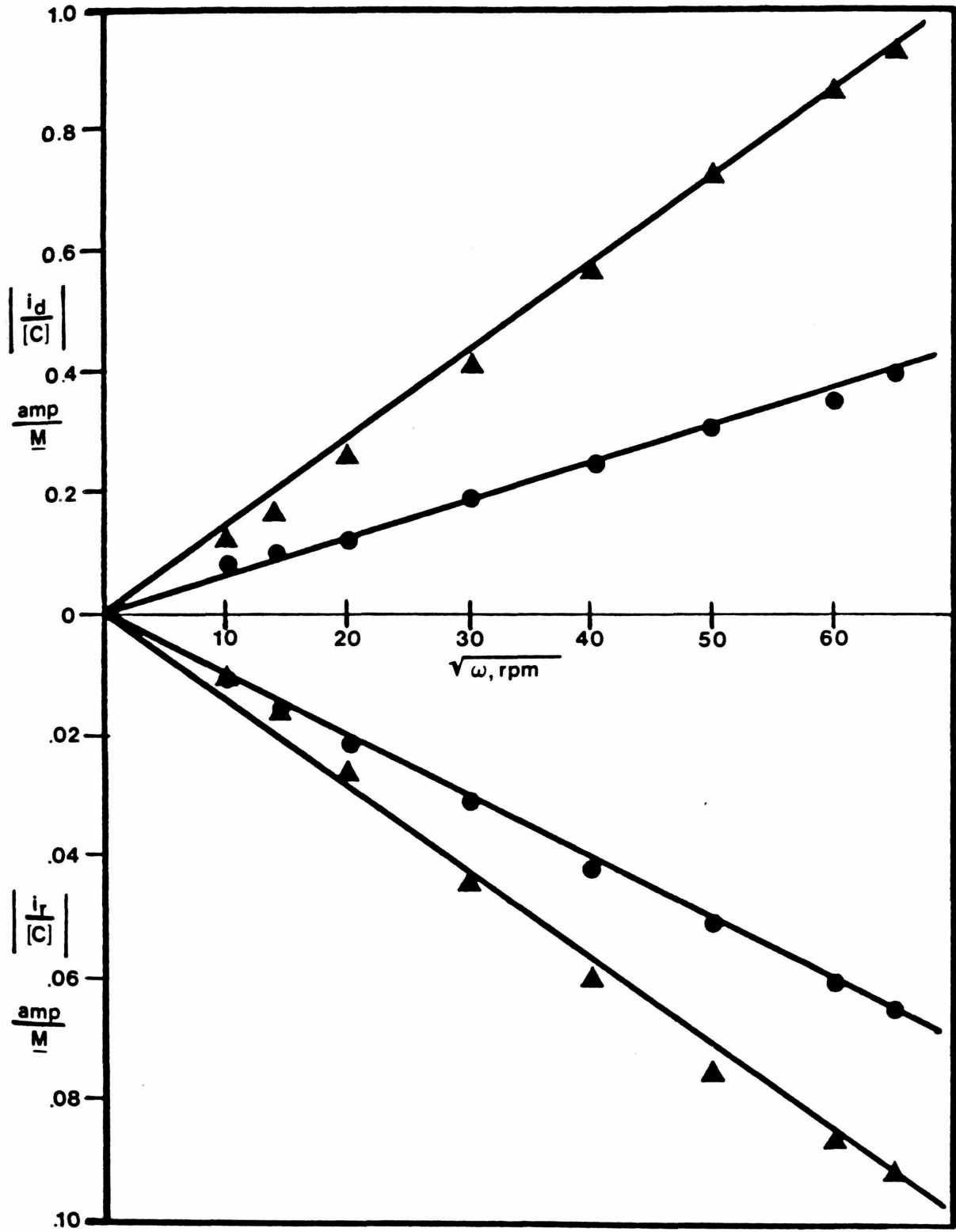
Levich plots of RU3Y-OH_2 at pH 1.00

Legend:

solid circles: -0.300 V

solid triangles: +1.200 V

Figure 31



where,

$$\alpha = \left(\frac{r_1}{r_2}\right)^3 - 1$$

$$\beta = \left(\frac{i_r}{i_d}\right)^{\frac{3}{2}} = \left(\frac{r_3}{r_1}\right)^3 - \left(\frac{r_2}{r_1}\right)^3$$

r_1 = disk radius

r_2 = inner radius of the ring

r_3 = outer radius of the ring

$$F(\theta) = \left(\frac{\sqrt{3}}{4\pi}\right) \ln\left(\frac{(1+\theta^{\frac{1}{3}})^3}{1+\theta}\right) + \frac{3}{2\pi} \arctan\left(\frac{2\theta^{\frac{1}{3}}-1}{\sqrt{3}}\right) + \frac{1}{4}$$

The Levich plots of the limiting disk currents at +1.200 V exhibited slightly more than twice the disk current at -0.300 V, while the ring current was roughly 1.5 times larger than when the disk potential was -0.300 V. The collection efficiency for this wave was thus calculated to be 0.105. These results indicate that there is a following chemical reaction affecting the currents at +1.200V. Previously, it was shown that the final product upon oxidation of Ru3Y-OH₂ at +1.200 V was the [34] dimer. The overall stoichiometry of the dimerization reaction of the [34] dimer from Ru3Y-OH₂ was also determined to involve two protons, so that a pH dependence for the oxidation and dimerization might be expected. Evidence for a [44] dimer was also found by cyclic voltammetry and by spectro-electrochemistry at this potential. Furthermore, the [44]

dimer was apparently the catalytic species for the evolution of dioxygen. Before the catalytic process could be studied by RRDE voltammetry, however, an understanding of the dimerization process was required so that the current due to dimerization could be accounted for and subtracted from the total limiting current at the disk at +1.200 V.

The CV's of Ru3Y had indicated that there was a separation of the wave due to the formation of the dimer and the catalytic wave at $\text{pH} \geq 7$. At lower pH's, the waves were not separated and little could be ascertained from the electrochemical response about the dimerization reaction. Several RRDE experiments were, therefore, performed on Ru3Y-OH₂ solutions at various pH's to help understand the dimerization reaction.

The reduction waves for Ru₃/2Y were observed at potentials identical with those obtained by polarography and typical rotation rate behavior and Levich plots are shown in Figures 32 and 33 for pH 7.70. The anodic behavior of Ru3Y-OH₂, however, was different than at pH 1. A smaller "pre-wave" was seen to emerge from the larger wave at +1.000 V above pH 5. By pH 7.7 the wave was defined clearly and was not observed to change upon raising the pH. The shifts of the half-wave potentials for the waves observed by RRDE are listed in Table 10. The half-wave potentials were determined by the wave shape analysis procedure described earlier for polarographic waves. The anodic "pre-wave" was seen to shift roughly -90 mV/pH, between pH 3 and pH 7, but

Figure 32

RRDE of RU3Y-OH₂ at pH 7.70

Conditions: BPG disk, platinum ring

0.431 mM RU3Y-OH₂

50 mM phosphate buffer

total ionic strength = 0.200 N with NaTFA

scan rate 0.5 V/min

ring potential: +0.400 V

A) scan range: +0.400 ---> -0.600 V

rotation rates: 2500, 3600, 4625 rpm

B) scan range: +0.200 ---> +1.200 V

rotation rates: 2500, 3600, 4625 rpm

Figure 32

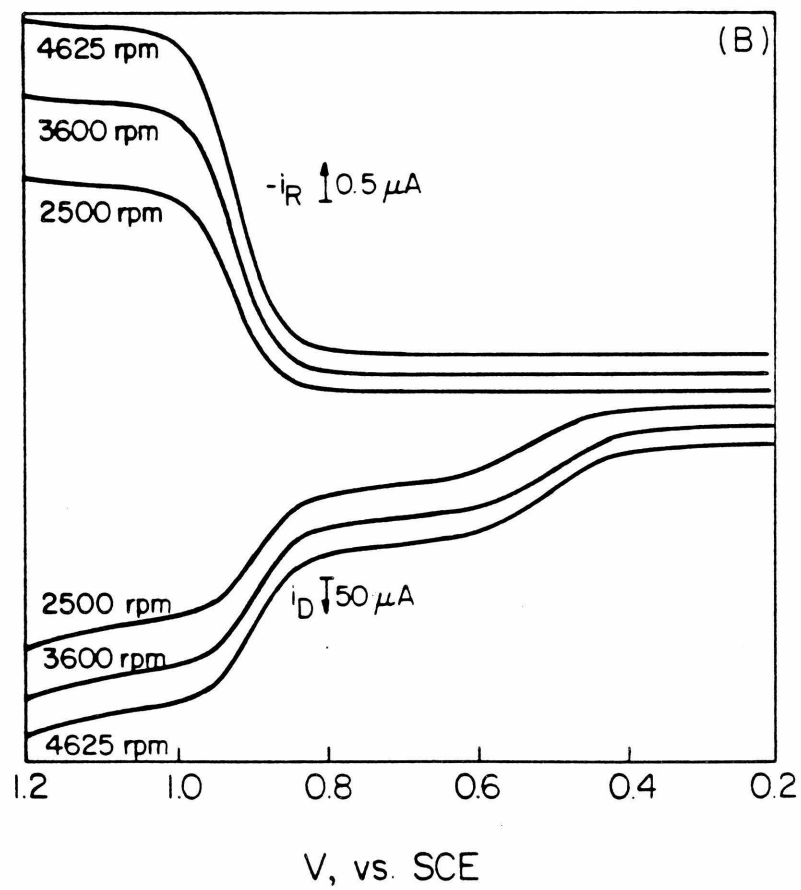
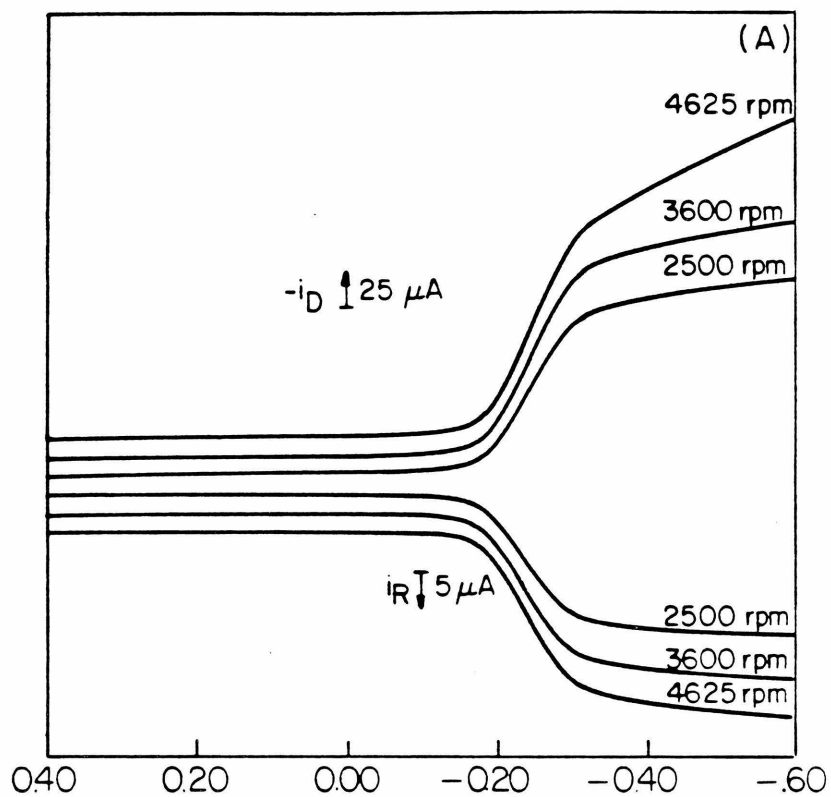


Figure 33

Levich plot of RU3Y-OH_2 at pH 7.70

Legend:

solid circles:	-0.400V
solid squares:	+0.700 V
solid triangles:	+1.050 V

Figure 33

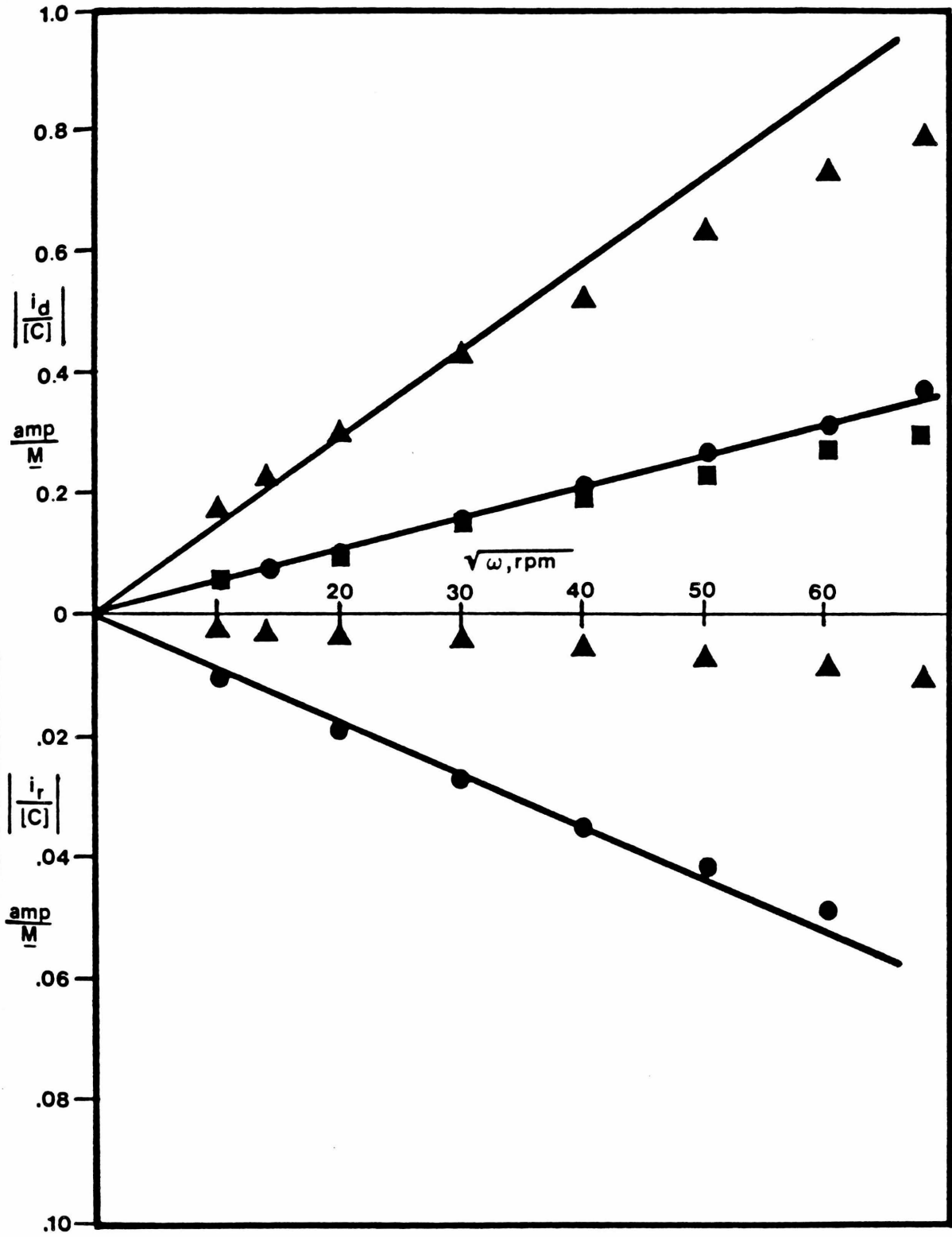


Table 10

RRDE wave shape analysis of $\text{Ru}_3\text{Y-OH}_2$ and the [34] dimer

Table 10*

Ru3Y			
<u>pH</u>	<u>$E_{\frac{1}{2}}$, (V vs SCE)</u>	<u>slope, (mV)</u>	<u>r^2</u>
1.00	-0.155	62.2	1.000
	+1.048	72.9	0.992
5.00	-0.232	66.3	0.998
	+0.648	85.4	0.998
	+0.892	83.4	0.999
7.70	-0.253	65.8	0.998
	+0.479	86.1	0.995
	+0.887	77.0	0.999
9.25	-0.314	61.8	0.997
	+0.537	112.9	0.999
	+0.909	61.8	0.998

--continued on next page--

Table 10*

[34] dimer

pH	$E_{\frac{1}{2}}$, (V vs SCE)	slope, (mV)	r^2
1.00	-0.166	60.8	0.996
	+0.222	63.0	0.998
	+0.979	70.8	1.000
5.00	-0.287	72.9	1.000
	-0.036	72.7	1.000
	+0.897	83.5	0.998
7.70	-0.376	65.2	0.998
	-0.156	74.0	0.994
	+0.981	81.6	0.999
9.25	-0.179	86.8	0.993
	+0.907	71.7	1.000

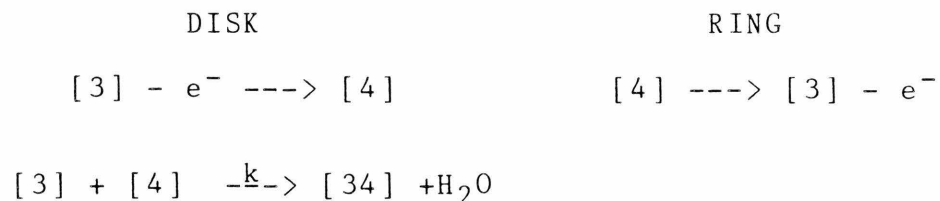
* 3600 rpm wave analyzed for all samples

the exact pH dependence was not determined due to the limited number of pH's studied. Since the number of electrons involved at +0.700 V for pH 7.70 has been determined previously by coulometry to be one, it is not clear if this is a one-electron, two proton (-120 mV/pH), or a one-electron, one proton (-60 mV/pH) coupled reaction. The involvement of at least one proton in the electron transfer step is, however, indicated by these results.

For even the fastest rotation rate, 4625 rpm, there was no evidence of any ring current (<0.05 μ amps), with the ring held at +0.400 V. This indicates that the disk product that is produced while scanning over the "pre-wave" reacts rapidly to produce a species that is electro-inactive at this ring potential. Cathodic ring current is not observed until the ring is set at a potential where the [34] dimer is reduced to the [33] dimer (see Figure 25). This further substantiates the argument that the final product upon oxidation of Ru3Y-OH₂ is the [34] dimer.

In an effort to determine the disk and ring response and the rate of dimer formation, the following Scheme (III) was simulated.

SCHEME III



A plot of the collection efficiency, N , and the dimensionless disk current, ZD , vs. the dimensionless, simulation rate constant, $XKTC$, is shown in Figure 34.

$$XKTC = \left(\frac{kC}{\omega} \right) \left(\frac{\nu}{D} \right)^{\frac{1}{3}} (0.51)^{-\frac{2}{3}} \quad (61)$$

where,

k = second-order dimerization rate
constant ($\underline{M}^{-1} \text{ sec}^{-1}$)

C = bulk concentration of species [34] (moles/liter)

ω = rotation rate (rad/sec)

ν = kinematic viscosity of the solvent (cm^2/sec)

D = diffusion coefficient (cm^2/sec)

Using the current values (normalized for concentration) for pH 7.70 it is seen that even for the fastest rotation rate, 4625 rpm, that there was no observable ring current. This implies an $XKTC$ of at least 50. Using the bulk concentration of Ru3Y-OH of 0.430 $\underline{\text{mM}}$, $\nu=0.01 \text{ cm}^2/\text{sec}$ for water, and $D=5.92 \text{ E-6 cm}^2/\text{sec}$ for the diffusion coefficient, a minimum, second-order rate constant of $k = 3.0 \text{ E+6 } \underline{\text{M}}^{-1} \text{ sec}^{-1}$ is calculated. The disk current, however, is predicted to be between 0.50 and 0.60 times the disk current for the uncomplicated redox reaction. This is not observed (see Figure 33). The disk current varies between 1.00 and 0.74 times the uncomplicated redox reaction.

If the disk current is used to fit the simulation, then a significant amount of ring current would be expected (at least one-third of the Levichian ring current), due to the

Figure 34

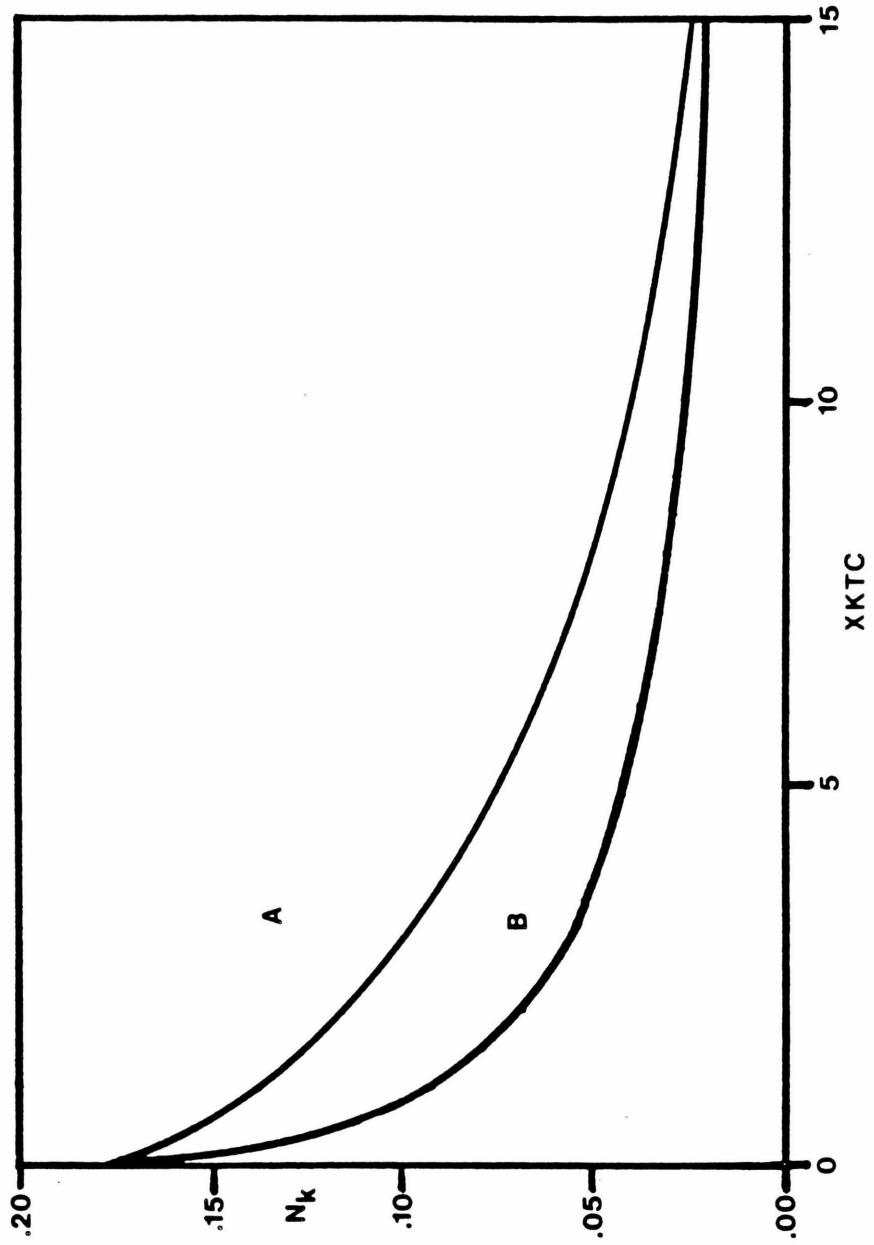
Simulated collection efficiency, N_k , vs. XKTC

for Scheme III and Scheme V

A. Scheme III

B. Scheme V

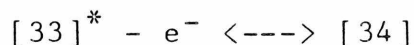
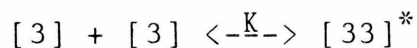
Figure 34



reduction of [4] back to [3]. It is hard to account for the enhanced disk, and the diminished ring response with this scheme. It thus appears likely that another dimerization mechanism is operable.

Another possible mechanism that was investigated involves a prior pre-equilibrium between two Ru₃Y-OH monomers to dimerize, or to form some sort of a precursor complex, which is then oxidized to produce the [34] dimer.

SCHEME IV



where,



$$K = \left(\frac{[33]^*}{[3]^2} \right) = \left(\frac{k_f}{k_b} \right)$$

Solutions exist for a first-order pre-equilibrium with a following redox reaction, but the second order case has yet to be solved (153). A first-order pre-equilibrium can be ruled out, however, since the oxidized species, Ru₄Y, would still have to react with an incoming Ru₃Y, which would lead to, in the absence of any measureable ring current, a predicted disk limiting current near one-half the Levich

current. This is clearly not observed.

In general, for a preceding chemical reaction, even for the first order case, only a quantity containing the complicated product of the equilibrium constant with the rate constants can be obtained by analyzing the disk current behavior. The Levich plot for a prior pre-equilibrium would then be expected to exhibit a "bending over" of the disk current from the Levich line of the uncomplicated redox reaction towards a kinetically limited current. This trend is what is observed.

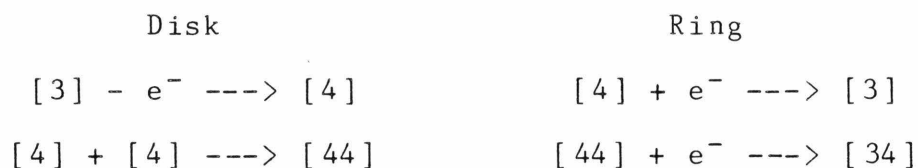
Typically, for a first-order preceding chemical reaction, a Koutecky-Levich plot (153) is made (a plot of $(1/i \text{ vs. } 1/\omega^{\frac{1}{2}})$) and, if a linear plot is obtained, then the inverse slope is the Levich slope, while the intercept contains information about the equilibrium and rate constants (153). An independent method is then needed, however, to determine one of the unknown rate, or equilibrium constants to help determine the others.

Unfortunately, there is no evidence in the optical spectrum for a stable [33] dimer formed in the presence of Ru3Y-OH. Furthermore, the observed, half-wave potential of the [34]/[33] couple near -0.150 V also indicates that the wave at +0.700 V is not due to the oxidation of the [33] dimer. In addition, the limiting current for this mechanism would still be predicted to be only one-half of the Levich current at -0.300 V. The measured disk current is thus too large to correspond to the formation of a precursor [33]

dimer with a following oxidation step.

One final mechanism was considered to try and account for the one-electron Levich current observed for the wave at +0.700 V. This involved the oxidation of Ru₃Y to Ru₄Y with the subsequent dimerization occurring between two Ru₄Y monomers to give a [44] dimer. This sequence is outlined in Scheme V and the simulation results are plotted in Figure 34.

SCHEME V



Scheme V, however, does not account for the absence of any ring current. Two species, [4], and [44], are capable of being reduced at the applied ring potential of +0.400 V. It is possible that a rapid decomposition of the [44] dimer to the [34] dimer follows the dimerization step. This would imply, however, that one Faraday could be required per mole of ruthenium to produce the [34] dimer, but a bulk electrolysis described earlier showed that only one Faraday per two moles of ruthenium was required to produce the [34] dimer. Scheme V is thus ruled out as incompatible with the bulk electrolysis and chemical oxidation stoichiometry.

It appears, therefore, that Schemes III and V are ruled out by the RRDE and spectral results. Scheme IV also appears to be ruled out by the lack of any evidence of a

precursor complex and by the one-electron Levichian disk current. The reasons for the discrepancy between the measured currents and the simulated currents may be due to surface effects on the disk electrode that masks the current due to simple mass-transfer, or else there is an alternate mechanism that is operative. The most plausible mechanisms were considered and simulated so that the former situation seems most likely. This is further substantiated by the CV results that showed definite surface kinetic complications. The investigation of surface kinetic phenomena is very involved and was beyond the scope of this study. Thus, the measured data do not allow a definitive description of the [34] dimerization process to be made and only the overall stoichiometry determined earlier can be considered valid.

A consideration of the half-wave potentials for the "pre-wave" between +0.500 and +1.000 V (see Table 10) shows that dioxygen is thermodynamically capable of oxidizing $\text{Ru}_3\text{Y-OH}_2$ to the [34] dimer between pH 1 and roughly, pH 9. My results have shown, however, that dioxygen reacts very slowly with $\text{Ru}_3\text{Y-OH}_2$ at $\text{pH} \leq 5$. Less than 3% conversion of $\text{Ru}_3\text{Y-OH}_2$ to the [34] dimer was observed after two days in a dioxygen saturated solution containing 1.00 mM $\text{Ru}_3\text{Y-OH}_2$ buffered at pH 5, while a 0.500 mM $\text{HRu}_3\text{Y-OH}_2$ solution at pH 1 was stable in air for weeks. Between pH 7 and 9, however, the reaction between dioxygen and $\text{Ru}_3\text{Y-OH}$ to form the [34] dimer was shown to proceed rapidly. This indicates that the reaction is slowed significantly in the presence of acid.

The limiting step does not appear to be the oxidation of the ruthenium, however, since permanganate and hydrogen peroxide produced the [34] dimer immediately upon mixing at pH 5, and with Ce(IV) and permanganate doing likewise in pH 1 solutions of HRu3Y-OH₂. With the lack of any indication of a kinetically limited pre-equilibrium between two Ru3Y monomers at any of the pH's studied, the reduction of dioxygen in the presence of acid appears to be the rate-limiting step.

The electrochemical process occurring near +1.000 V also presented difficulty in its analysis. To try and separate the effects of the "pre-wave" from the large oxidation wave, a series of RRDE experiments were performed at various pH's on solutions of the [34] dimer prepared from the isolated salt. The RRDE's of the [34] dimer did not exhibit the "pre-wave" upon scanning from +0.400 V to +1.500 V (see Figure 35). The RRDE response for the disk scanned from +0.400 to -0.600 V are shown in Figure 36, and the Levich plots for both scan directions appear in Figure 37.

When compared to the disk response for the [34]/[33] redox couple (near 0.000 V) at pH 1, the limiting disk response for the wave at +1.000 V is seen to be 2 to 2.5 times as large. This implies that this is either a two-electron process, or that there is some chemical step after the first oxidation followed by another oxidation step. The former possibility can be ruled out based on the wave shape analysis which shows this is to be a one-electron process

Figure 35

Oxidative RRDE behavior of the [34] dimer

Conditions: BPG disk, platinum ring

scan rate 0.5 V/min

ring potential +0.400 V

pH 1.00

0.123 mM [34] dimer

total ionic strength = 0.200 N with NaTFA

scan range: +0.400 ---> +1.400 V

rotation rates: 1600, 2500, 3600, 4225 rpm

Figure 35

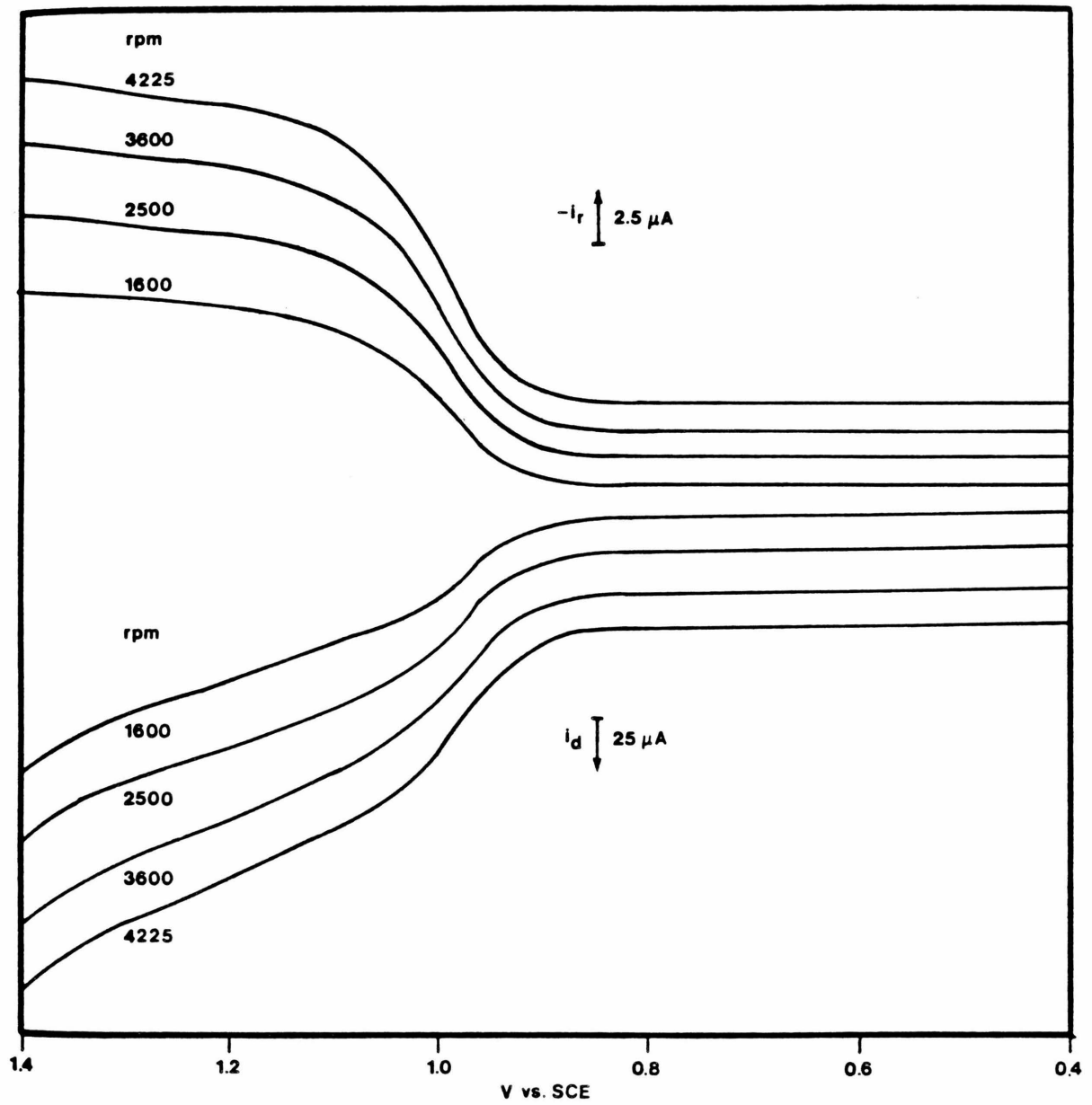


Figure 36

Reductive RRDE behavior of the [34] dimer

Conditions: BPG disk, platinum ring

scan rate 0.5 V/min

ring potential +0.400 V

1) pH 1.00

0.123 mM [34] dimer

total ionic strength = 0.200 N with NaTFA

scan range: +0.400 ---> -0.400 V

rotation rates: 1600, 2500, 3600, 4225 rpm

2) pH 7.70

0.148 mM [34] dimer

50 mM phosphate buffer

total ionic strength = 0.200 N with NaTFA

scan range: +0.400 ---> -0.600 V

rotation rates: 2500, 3600, 4625 rpm

Figure 36

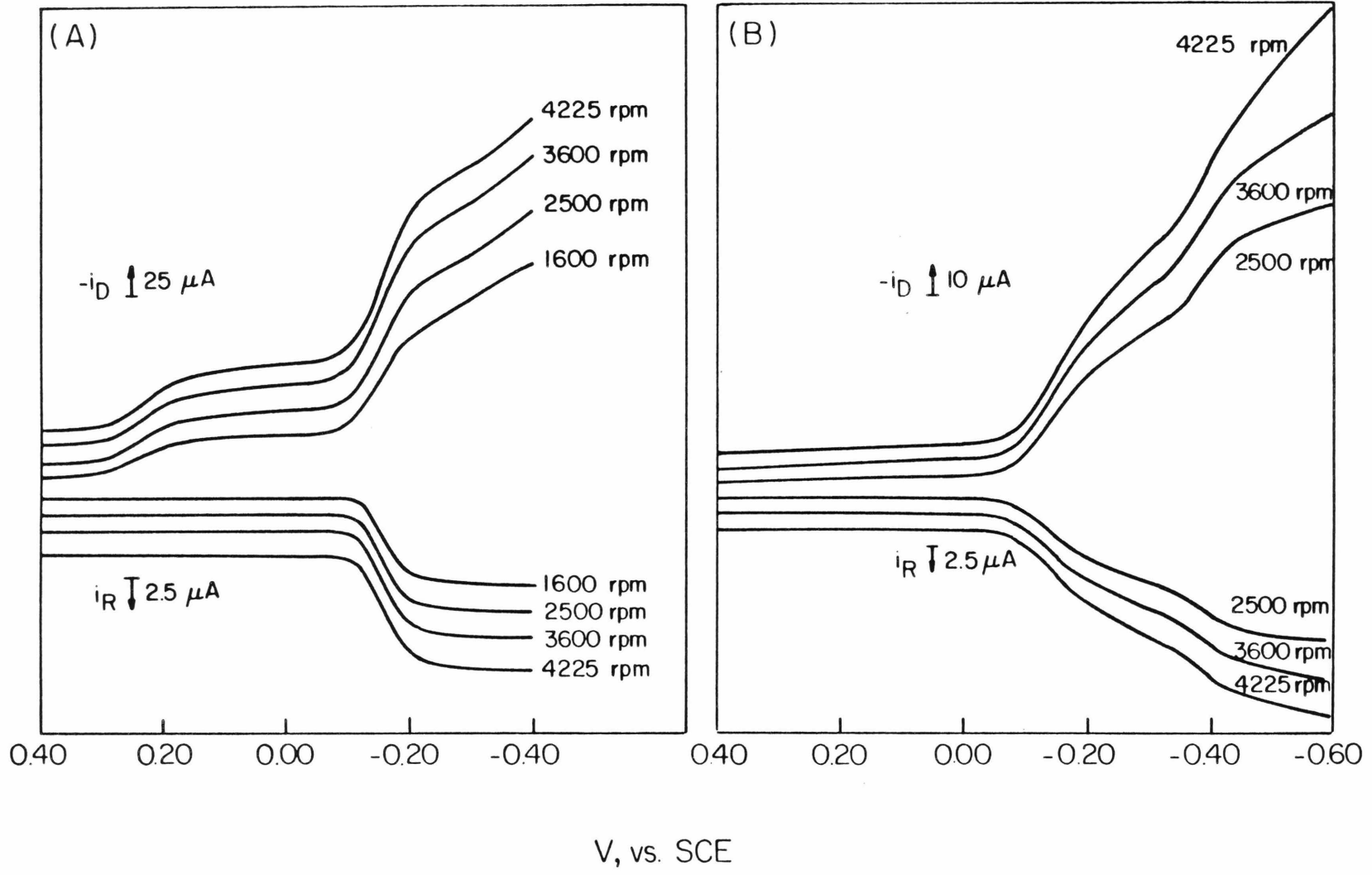


Figure 37

Levich plots of the [34] dimer

A. pH 1.00

$n_1 = 1$, one-electron Levich line

solid circles: +0.050 V

solid squares: -0.300 V

open circles: +1.150 V

B. pH 7.70

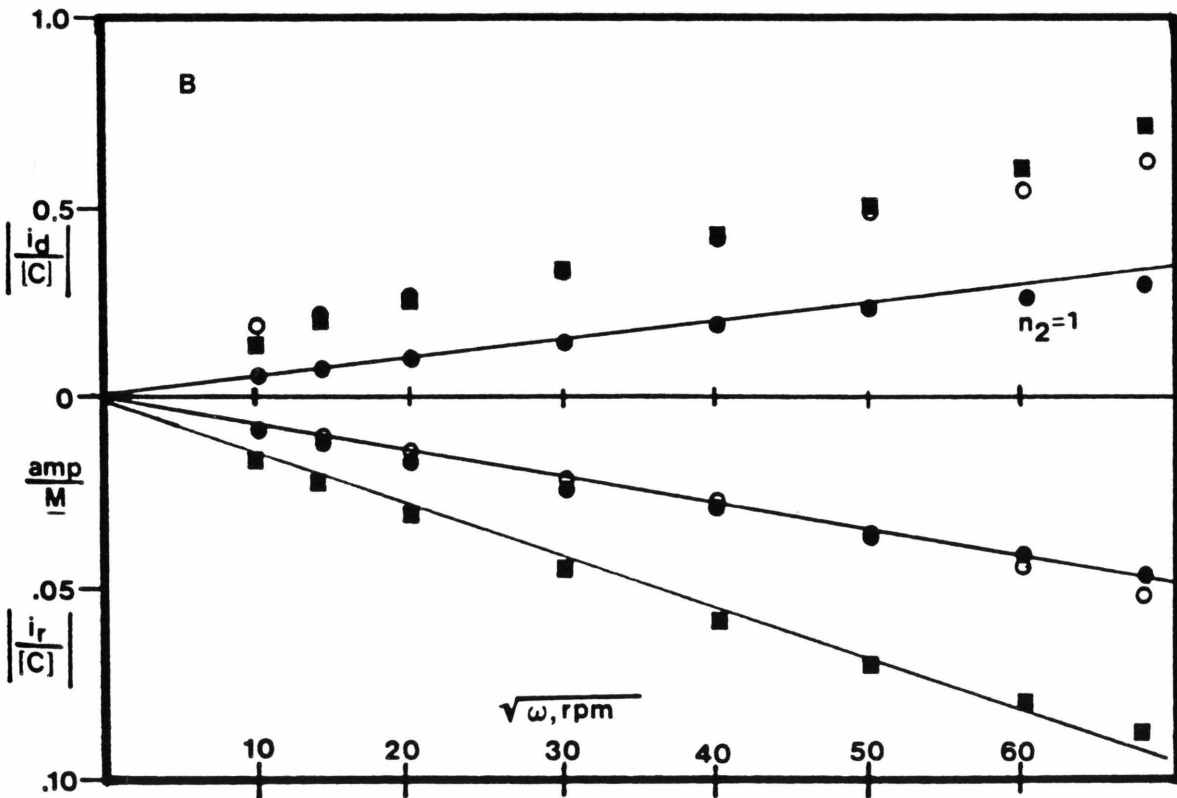
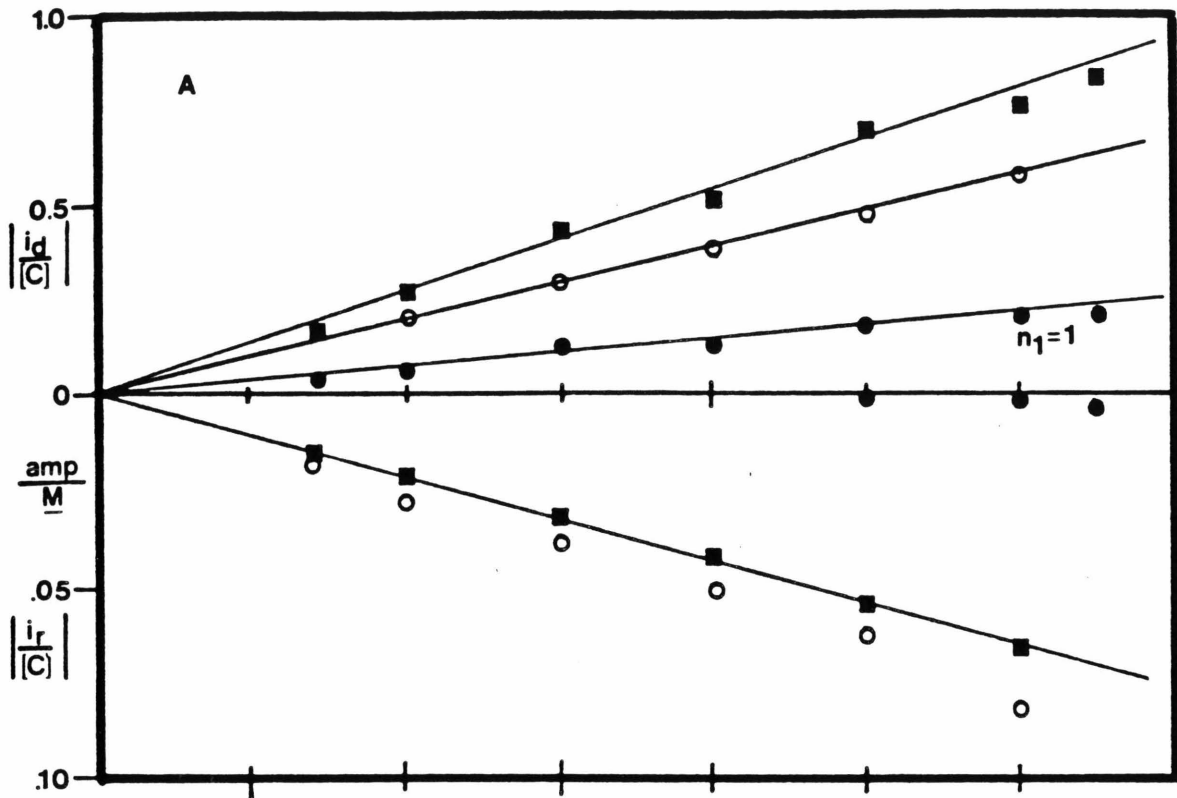
$n_2 = 1$, one-electron Levich line

solid circles: -0.225 V

solid squares: -0.450 V

open circles: +1.050 V

Figure 37

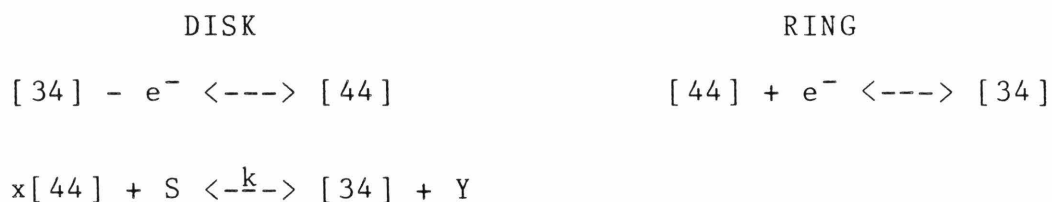


(the slope at any pH is 70-80 mV).

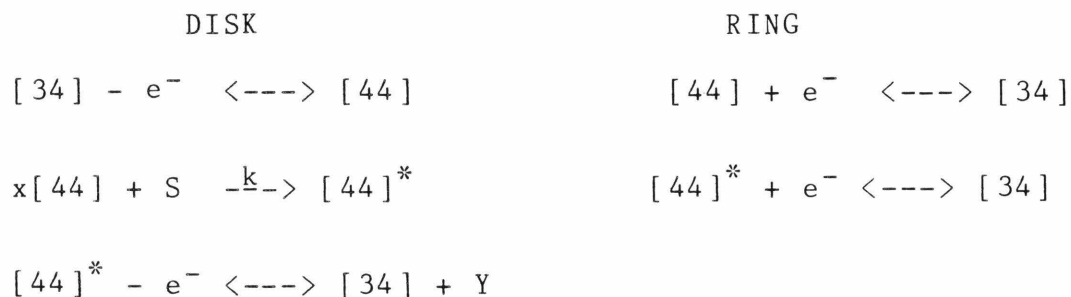
The second scenario presents several possibilities that could lead to the increased limiting disk current. Given that dioxygen evolution was observed to occur at this potential during electrolysis, a catalytic mechanism is indicated as the most likely process. The actual sequence of reactions is difficult to predict from just the disk response, and the ring response is needed to help determine the mechanism. To predict the disk and ring responses as a function of rate constant and rotation rate, a simulation must be performed.

Several catalytic mechanisms were simulated and their predicted responses compared with the observed results. The following mechanisms were simulated.

SCHEME VI



SCHEME VII



where,

[34],[44] and [44]^{*} are electroactive

S = substrate

Y = non-electroactive, oxidized product

k = the rate constant of the chemical step

x = the number of species, [44], that react with
substrate, S

Scheme VI is an $E_r C_{cat}$ mechanism, while Scheme VII is an $E_r C_i E_{cat}$ mechanism. Scheme VI considers that the oxidized species, [44], is the catalytic species that reacts with the substrate to generate the oxidized, non-electroactive product, Y, regenerating the initial electroactive species, [34]. Scheme VII considers that the oxidized species reacts with the substrate, S, to produce an electroactive intermediate, [44]^{*}, which can be further oxidized to produce an oxidized, non-electroactive product, Y, and then regenerate the electroactive species, [44]. The overall stoichiometry for the catalytic reaction is considered by the input variable, x. Four electrons are needed to produce dioxygen from water, while two electrons are needed to produce hydrogen peroxide from water, so that the value of x was set at four, two, and one for comparison. The resulting disk, ring and collection efficiencies for these simulations are listed in Tables 11 and 12.

For the simulations, XKTC is a dimensionless parameter that contains the second-order rate constant,

$$XKTC = \left(\frac{xkC}{\omega} \right) \left(\frac{\nu}{D} \right)^{\frac{1}{3}} (0.51)^{-\frac{2}{3}} \quad (61)$$

Table 11

Simulation data for $E_r C_{cat}$ mechanism

Table 11^a $E_r C_{cat}$

<u>XKTC</u>	<u>DISK</u>	<u>RING</u>	<u>COLLECTION EFFICIENCY</u>
0.000	1.001	1.001	0.176
0.100	1.530	0.707	0.081
0.200	0.930	0.529	0.048
0.300	2.257	0.410	0.032
0.400	2.534	0.325	0.023
0.500	2.778	0.263	0.017
0.600	2.995	0.216	0.013
0.700	3.192	0.180	0.010
0.800	3.372	0.151	0.008
0.900	3.537	0.128	0.006
1.000	3.690	0.109	0.005

a. Stoichiometry factor ($xB + C \rightarrow A + Y$) : 1.00
 Electrode geometry: 100,104,110; step size: 50;
 maximum # iterations: 150; convergence; 1.0 E-4
 M: 10; DMA, DMB, DMC: 0.45;

--continued on next page--

Table 11^b $E_r C_{cat}$

<u>XKTC</u>	<u>DISK</u>	<u>RING</u>	<u>COLLECTION EFFICIENCY</u>
0.000	1.001	1.000	0.176
0.100	1.540	0.703	0.080
0.200	1.964	0.518	0.046
0.300	2.318	0.394	0.030
0.400	2.625	0.306	0.021
0.500	2.898	0.242	0.015
0.600	3.146	0.194	0.011
0.700	3.374	0.158	0.008
0.800	3.585	0.129	0.006
0.900	3.782	0.107	0.005
1.000	3.967	0.089	0.004

b. Stoichiometry factor ($xB + C \rightarrow A + Y$) : 2.00
 Electrode geometry: 100,104,110; step size: 50;
 maximum # iterations: 150; convergence; 1.0 E-4
 M: 10; DMA, DMB, DMC: 0.45;

-- continued on next page--

Table 11^c $E_r C_{cat}$

<u>XKTC</u>	<u>DISK</u>	<u>RING</u>	<u>COLLECTION EFFICIENCY</u>
0.000	1.001	1.000	0.176
0.100	1.545	0.701	0.080
0.200	1.981	0.512	0.045
0.300	2.350	0.385	0.029
0.400	2.673	0.296	0.019
0.500	2.963	0.232	0.014
0.600	3.229	0.183	0.010
0.700	3.474	0.147	0.007
0.800	3.704	0.119	0.006
0.900	3.919	0.097	0.004
1.000	4.122	0.079	0.003

c. Stoichiometry factor ($x\text{B} + \text{C} \rightarrow \text{A} + \text{Y}$) : 4.00
 Electrode geometry: 100,104,110; step size: 50;
 maximum # iterations: 150; convergence; 1.0 E-4
 M: 10; DMA, DMB, DMC: 0.45;

Table 12

Simulation data for $E_r C_i E_{cat}$ mechanism

Table 12^a $E_r C_i E_{cat}$

<u>XKTC</u>	<u>DISK</u>	<u>RING</u>	<u>COLLECTION EFFICIENCY</u>
0.000	1.001	1.000	0.176
0.100	1.124	0.963	0.150
0.200	1.244	0.926	0.131
0.300	1.360	0.893	0.115
0.400	1.472	0.860	0.102
0.500	1.582	0.826	0.092
0.600	1.688	0.793	0.082
0.700	1.791	0.761	0.075
0.800	1.891	0.728	0.068
0.900	1.987	0.696	0.061
1.000	2.080	0.662	0.058

a. $C + ne \rightarrow A$: $n = 2.00$

Electrode geometry: 100,104,110; step size: 50;

maximum # iterations: 150; convergence; $1.0 \text{ E-}4$

M: 10; DMA, DMB, DMC: 0.45;

--continued on next page--

Table 12^b $E_r C_i E_{cat}$

<u>XKTC</u>	<u>DISK</u>	<u>RING</u>	<u>COLLECTION EFFICIENCY</u>
0.000	1.001	1.000	0.176
0.100	1.247	0.964	0.135
0.200	1.484	0.921	0.109
0.300	1.710	0.868	0.089
0.400	1.922	0.807	0.074
0.500	2.119	0.737	0.061
0.600	2.303	0.661	0.050
0.700	2.590	0.777	0.053
0.800	2.641	0.513	0.034
0.900	2.798	0.441	0.028
1.000	3.195	0.699	0.038

b. $C + ne \rightarrow A$: $n = 4.00$

Electrode geometry: 100,104,110; step size: 50;

maximum # iterations: 150; convergence; $1.0 \text{ E-}4$

M: 10; DMA, DMB, DMC: 0.45;

where all of the above terms have been defined previously. The simulated disk and ring currents are normalized to the uncomplicated, Levich response, and N is the collection efficiency. In the $E_r C_{cat}$ simulations, the value of M ($=[S]/[34]$) was taken as 10.0. This accounts for the fact that the substrate for these simulations is the solvent, thereby, yielding pseudo first-order conditions. The value of $M = 10$ has been found to produce this limiting case in the simulations (52-54). The simulation also considers the standard Pine electrode with $r_2/r_1 = 1.04$, and $r_3/r_1 = 1.10$.

A comparison of the experimental results (see Figure 35) with the values predicted by any of the simulations indicates that these mechanisms do not appear to be operative for this system. In all cases, the simulated disk and ring currents do not coincide with the measured disk and ring currents. If just the observed disk currents are used then several of the simulations fit the data. It is the ring current that defines the operative mechanism. For either of the mechanisms that were simulated a decrease in the ring current from the Levich ring current is expected. The measured ring currents were all "too large" for any of the simulations. In several instances the measured currents were actually larger than the Levich ring current, which indicates that the concentration profile of the electroactive species reaching the ring was much greater than can be accounted for by these mechanisms. One possible reason for the enhanced ring currents may be that the dimer is

splitting into monomers during the catalytic process. This possibility was not able to be substantiated by any other means and the reason for the observed ring response is unclear at this time.

Since the measured disk current was larger than the Levich disk current, this indicates that there must be some coupled chemical reaction accompanying the oxidation of the [34] dimer. The production of dioxygen from water indicates that part of the process must also be catalytic. Unfortunately, the experimental data do not correlate well with any of the simulations making the positive identity of the mechanism difficult.

A possible cause of the inability to determine the reaction mechanism of the dimerization and the catalysis may be due to complications introduced by surface effects at the BPG disk. These heterogeneous chemical effects could lead to a masking of the mass-transfer controlled currents. The CV's showed a series of complicated waves at higher pH's that were ascribed to surface phenomena and adsorption waves. These complications may make any analysis that only considers homogeneous kinetics insufficient. Heterogeneous kinetics can be included in the simulations, but a knowledge of the adsorption properties of the system are needed. This information is not always easily obtainable, and was beyond the scope of this study. A new technique that promises to aid in measuring only the current related to the homogeneous kinetics in the presence of heterogeneous kinetics is the

modulated rotating disk electrode (153-156). In this technique, the rotation rate of the disk electrode is modulated about a center frequency and the amplitude of the modulated current is measured. This technique has the attractive feature that the measured modulated current is free from double-layer charging and processes associated with oxidation and reduction of the electrode or of adsorbed species, and that it is relatively insensitive to the anodic and cathodic background currents (153). Since the modulated disk current is proportional to the unmodulated disk current, the amount of current due to just mass-transfer effects can then be calculated and fit to simulated data to obtain a homogeneous rate constant. In light of the heterogeneous problems associated with the dimerization reaction, and the catalytic evolution of dioxygen from water, it does not seem likely that any kinetic information will be able to be determined without the use of this technique.

Not all of the applications of the RRDE simulations yielded inconclusive results. The complicated mechanism of the reduction of the [34] dimer represented an opportunity where mechanistic data could be extracted from the experimental data using the simulation programs.

The RRDE voltammograms for the reduction of the [34] dimer at pH 1 and pH 7.7 are illustrated in Figure 36. The first reduction wave is attributed to the [34]/[33] couple. The Levich plots of the disk currents show that depending

upon the pH, there are two different Levich lines for this process. The lower line (labelled $n_1 = 1$) is due to the response of the [34] dimer at pH 1, while the upper line (labelled $n_2 = 1$) corresponds to the response for pH's 5.00 and 7.70. For the higher pH's, a diffusion coefficient of, $3.60 \text{ E-}6 \text{ cm}^2/\text{sec}$ was obtained for the [34] dimer, which is the same as the value obtained by polarography. At pH 1, however, the diffusion coefficient was determined to be $2.70 \text{ E-}6 \text{ cm}^2/\text{sec}$. (The pH 1 diffusion coefficient for the [34] dimer was not determined by polarography since the [34] dimer is capable of oxidizing mercury). The smaller diffusion coefficient is probably due to the fact that the overall charge of [34] dimer is zero at pH 1 which, taken in conjunction with the large size of the [34] dimer, would lead to a decrease in its mobility in solution when compared to $\text{pH} \geq 3$, where it is a tri-anion and it would be expected to have greater mobility.

The stability of the [33] dimer produced upon reduction of the [34] dimer has been shown by cyclic voltammetry to break up to form $\text{Ru}_3\text{Y-OH}_2$ at a rate that is pH sensitive. The RRDE affords a convenient way of monitoring the amount of the [33] dimer that has not decayed to the monomer and with the use of the simulations a way of determining the rate of its breakup.

In a typical experiment, the disk was scanned from $+0.400 \text{ V}$ to -0.600 V , while the ring was held at $+0.400 \text{ V}$ (see Figures 36 and 37). The ring was set at a potential

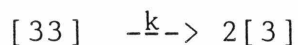
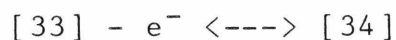
where the [33] dimer was reoxidized back to the [34] dimer, but where the monomer is electro-inactive.

To account for the observed ring and disk response, the following first-order decay process was used to model the reduction of the [34] dimer and its subsequent breakup.

SCHEME VIII

DISK

RING



A plot of the collection efficiency v_s. the dimensionless kinetic parameter, XKT,

$$XKT = \left(\frac{k}{\omega} \right) \left(\frac{v}{D} \right)^{\frac{1}{3}} (0.51)^{-\frac{2}{3}} \quad (62)$$

is shown in Figure 38, while the data for the systems studied are listed in Table 13.

The calculated first-order rate constant exhibits a decrease between pH 1 and 7.70 from 81. to 3.6 sec⁻¹, and then remains constant at this value at pH 9.25. The results indicate that the half-life of the [33] dimer for even the slowest rate of the breakup is only 200 msec, while the fastest rate yields a half-life of 9 msec. These results, thus, substantiate the observations made earlier concerning the instability of the [33] dimer towards monomerization to form Ru3Y.

Figure 38

Simulated collection efficiency, N_k , vs. XKT
for Scheme VIII

Figure 38

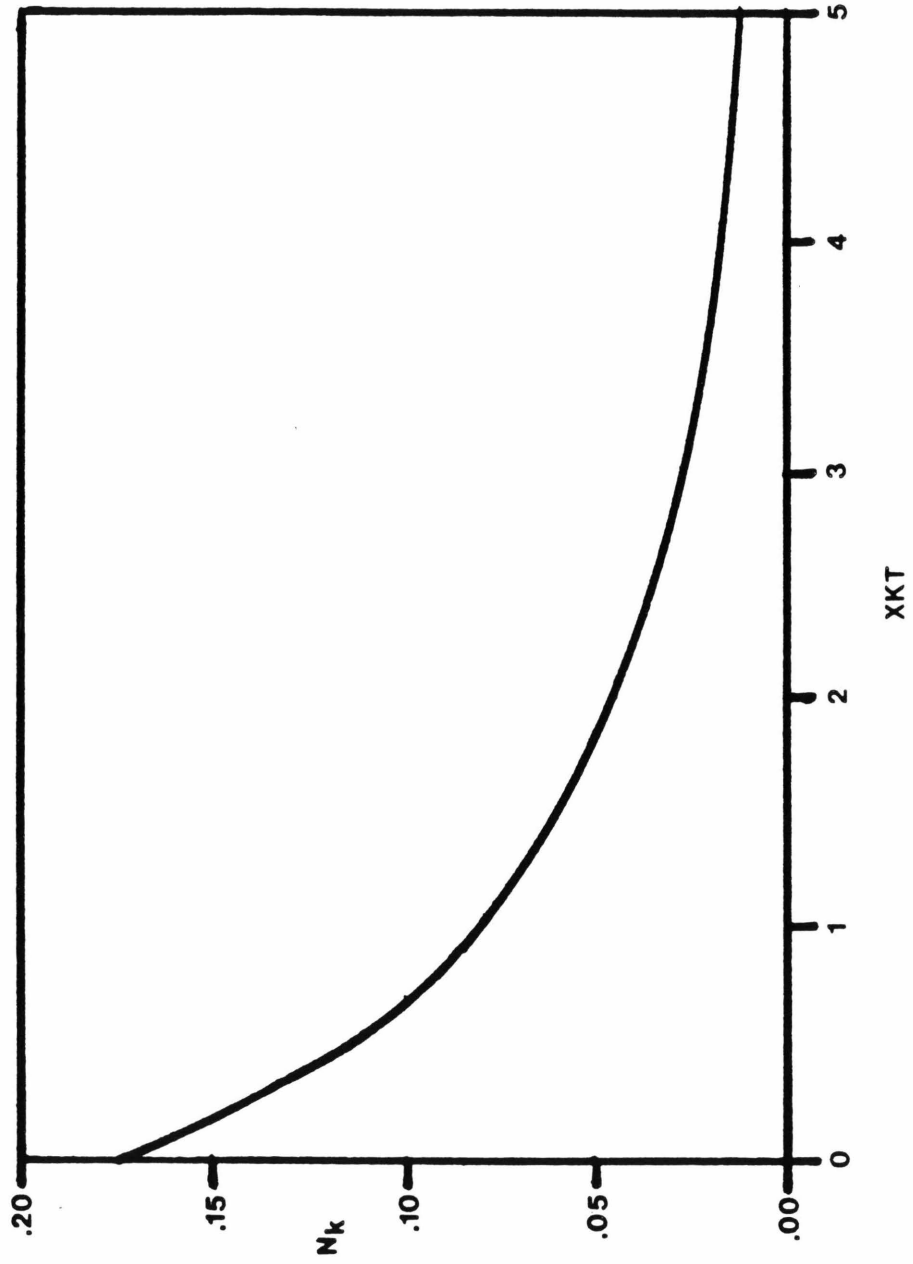


Table 13

Data for the breakup of the [34] dimer

- a. pH 1.00
- b. pH 5.00
- c. pH 7.70
- d. pH 9.25

Table 13^a

<u>pH</u>	<u>Conc.</u>	<u>ω, rpm</u>	<u>$\frac{i_{\text{disk}}}{\text{conc.}}$</u>	<u>$\frac{i_{\text{ring}}}{\text{conc.}}$</u>	<u>Coll. Eff.</u>	<u>XKT</u>	<u>$k, M^{-1} s^{-1}$</u>
1.00	0.123	1600	0.138	0.0006	0.004	10.	70.
		2500	0.193	0.0012	0.006	7.1	77.
		3600	0.211	0.0017	0.009	6.2	96.
							k(ave) = 81.±13.
5.00	0.244	400	0.109	0.0059	0.054	1.85	3.6
		900	0.150	0.0080	0.053	1.68	7.3
		1600	0.193	0.0092	0.048	1.63	12.5
		2500	0.234	0.0097	0.042	1.58	19.0
		3600	0.277	0.0102	0.037	1.55	26.8
							k(ave) = 19.5±10.0
5.00	0.424	400	0.087	0.0041	0.048	1.84	3.53
		900	0.129	0.0050	0.039	1.81	7.82
		1600	0.159	0.0050	0.032	1.68	12.9
		2500	0.186	0.0056	0.030	1.56	18.7
		3600	0.218	0.0050	0.023	1.52	19.3
							k(ave) = 12.4±6.8

a. $\frac{i_{\text{disk}}}{\text{conc.}}$, $\frac{i_{\text{ring}}}{\text{conc.}}$ = amp/M; coll. eff. = collection efficiency

$$\text{XKT} = \left(\frac{k}{\omega} \right) \left(\frac{v}{D} \right)^{\frac{1}{3}} (0.51)^{-\frac{2}{3}}$$

--continued on next page--

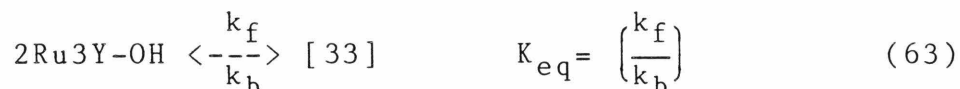
Table 13^b

<u>pH</u>	<u>Conc.</u>	<u>ω, rpm</u>	$\frac{i_{\text{disk}}}{\text{conc.}}$	$\frac{i_{\text{ring}}}{\text{conc.}}$	<u>Coll. Eff.</u>	<u>XKT</u>	<u>$k, M^{-1}S^{-1}$</u>
7.70	0.146	900	0.144	0.0163	0.113	0.537	2.40
		1600	0.185	0.0201	0.085	0.586	4.60
		2500	0.226	0.0223	0.098	0.489	6.00
		3600	0.274	0.0240	0.088	0.397	7.00
<hr/>							$k(\text{ave}) = 5.00 \pm 2.00$
7.70	0.148	1600	0.193	0.0291	0.151	0.177	1.38
		2500	0.237	0.0361	0.152	0.166	2.03
		3600	0.271	0.0415	0.153	0.159	2.79
		4625	0.301	0.0457	0.152	0.171	3.86
<hr/>							$k(\text{ave}) = 2.51 \pm 1.06$
9.25	0.172	400	0.070	0.0096	0.138	0.289	0.565
		900	0.096	0.0134	0.139	0.273	1.20
		1600	0.116	0.0139	0.120	0.461	3.60
		2500	0.139	0.0195	0.140	0.273	3.33
		3600	0.155	0.0226	0.146	0.218	3.83
		4625	0.168	0.0241	0.143	0.241	5.44
<hr/>							$k(\text{ave}) = 2.99 \pm 1.80$

a. $\frac{i_{\text{disk}}}{\text{conc.}}$, $\frac{i_{\text{ring}}}{\text{conc.}}$ = amp/M; coll. eff. = collection efficiency

$$\text{XKT} = \left(\frac{k}{\omega} \right) \left(\frac{V}{D} \right)^{\frac{1}{3}} (0.51)^{-\frac{2}{3}}$$

The establishment of the rate of the breakup of the [33] dimer, taken in conjunction with the observation that there was no evidence of dimer formation from the optical spectra of Ru3Y-OH₂ at pH's 7.70 and 9.25 for concentrations up to 10 mM, fixes an upper value for the equilibrium and forward rate constants for Ru3Y towards dimerization.



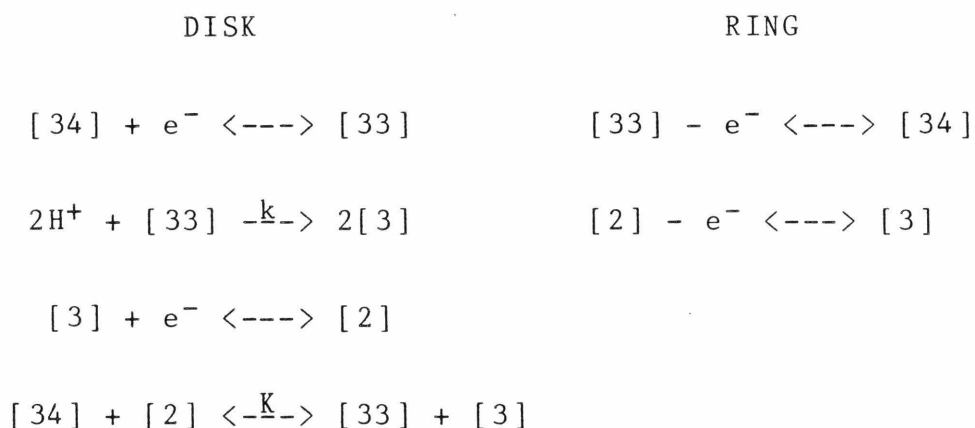
Assuming that the limit of the optical determination of the dimer is 1% conversion of the monomer to form the dimer, then for a 10 mM solution of Ru3Y-OH at pH 9.25, $K_{\text{eq}} = 1 \text{ M}^{-1}$. This fixes the forward rate constant as $k_f = 3.75 \text{ M}^{-1} \text{ sec}^{-1}$. At lower pH's, the introduction of a $[\text{H}]^+$ dependent term is also required. This is an upper limit for both of these values and it is likely that the true values are lower.

Using the upper value for the equilibrium constant and a typical concentration used for the RRDE experiments (0.500 mM), the maximum amount of [33] dimer present in solution is calculated to be 0.2 μM. This indicates that less than 0.4% of the monomer is present as the [33] dimer at the concentrations used in the electrochemical experiments. This would also tend to rule out a pre-equilibrium step as necessary for the dimerization reaction (see scheme IV).

The rate of breakup is accelerated for $\text{pH} \leq 5$ and all that is observed on the second wave of the RRDE is the reduction of Ru3Y-OH₂. This resulted in an interesting phenomenon in

the electrochemical response at pH 1 and pH 5. The total limiting disk current was observed to be more than three times the limiting current of the first reduction wave (see Figure 36, and reference 44). Since the final electrolysis product of the [34] dimer was shown to be $\text{Ru}_2\text{Y-OH}_2$, and to only require 3 Faradays per mole of dimer, the RRDE, and the polarographic results were initially puzzling. To try and account for the RRDE results, the following scheme was simulated.

SCHEME IX



where protons are involved in the chemical step to produce $\text{Ru}_3\text{Y-OH}_2$ monomers, which can then be reduced to $\text{Ru}_2\text{Y-OH}_2$. This mechanism considers the rate of breakup of the [33] dimer, and it also takes into account the homogeneous reaction between [2] and [34], which has an equilibrium constant determined by the half-wave potentials for the reduction of [34] and [3] (see equation 50). Using the half-wave potentials determined by polarography (see Figure 25 and Table 9), the equilibrium constant was found to be at

Figure 39

Simulation data for Scheme IX

A. Collection efficiency, N_k , vs. XKT

B. Disk Current, ZD , vs. XKT

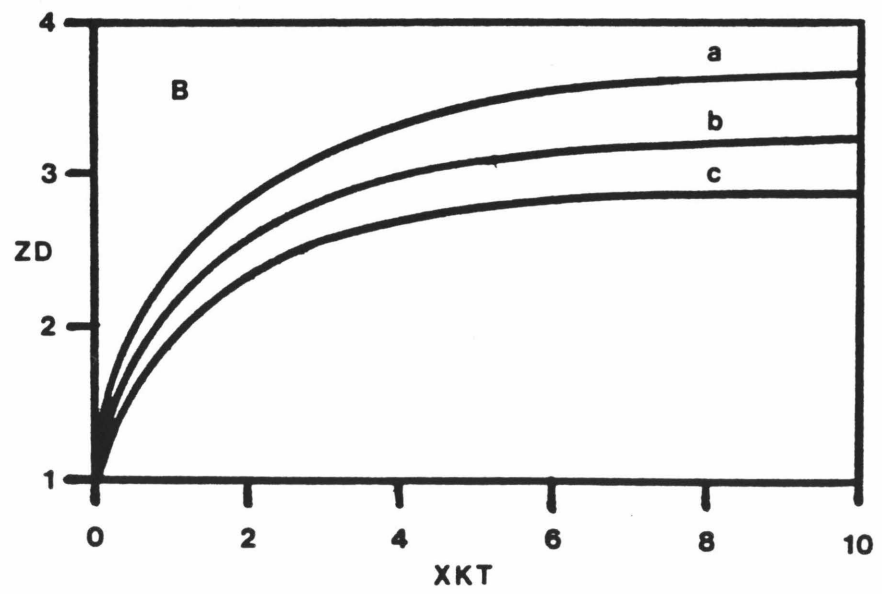
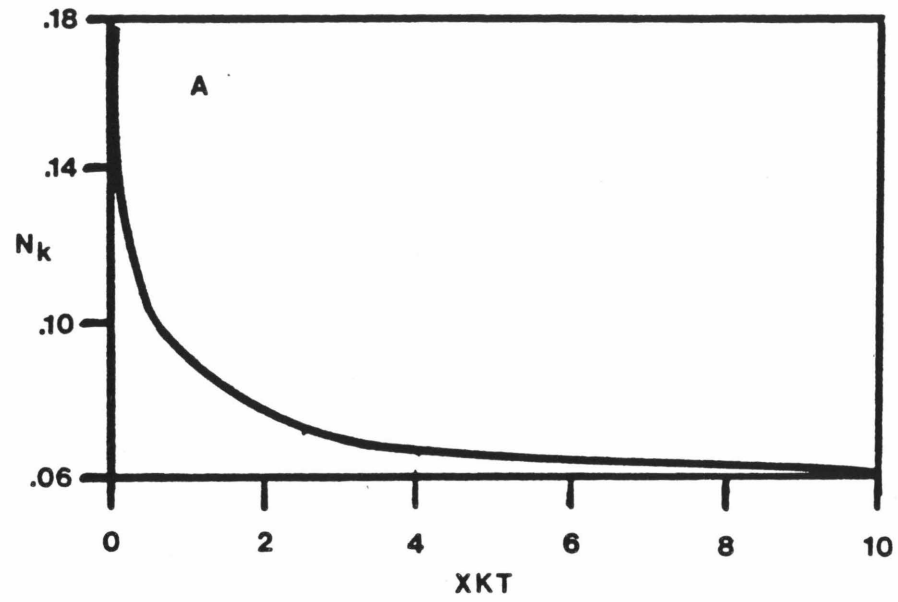
Conditions: $\left(\frac{D_{\text{dimer}}}{D_{\text{monomer}}} \right) = 0.45, 0.67, 1.00$

$K = 1000.$

Diffusion Coefficients

	[34]	[33]	[3]	[2]
a.	0.20	0.20	0.45	0.45
b.	0.30	0.30	0.45	0.45
c.	0.45	0.45	0.45	0.45

Figure 39



least 1000 ($\Delta E^\circ > 180$ mV).

The results are pictured in Figure 39, and they indicate that the limiting current is, indeed, supposed to be greater than 3.0 for most rate constants, and that the limiting value for the disk current varies as a function of the difference of the diffusion coefficients for the monomer and the dimer. The following cases with different ratios of the diffusion coefficients for the dimer and the monomer were simulated above:

$$\text{i) } D_{\text{dimer}} = 2.7 \text{ E-6 cm}^2/\text{sec},$$

$$\text{ii) } D_{\text{dimer}} = 4.0 \text{ E-6 cm}^2/\text{sec},$$

$$\text{iii) } D_{\text{dimer}} = 6.0 \text{ E-6 cm}^2/\text{sec},$$

with $D_{\text{monomer}} = 6.0 \text{ E-6 cm}^2/\text{sec}$ throughout. The disk currents are illustrated in Figure 39a, while the collection efficiencies are illustrated in Figure 39b. The limiting currents were found to be 4.0, 3.5, and 3.0, respectively, for the three cases considered. When the diffusion coefficients are identical, the limiting current is, in the limit, exactly equal to three. The limiting current goes up from there when the monomer has a larger diffusion coefficient than the dimer.

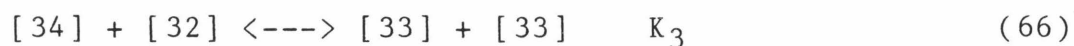
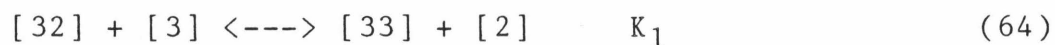
This can be explained by considering that the reduced monomer, [2], diffuses out into the solution faster than the reduced dimer, [33], where it can then react with an oxidized dimer, [34], to produce a [33] dimer and a [3]

monomer. The reduced monomer is thus effectively acting as a fast charge carrier capable of reducing the bulk species. The concentration profile of the electroactive species reaching the electrode is then altered by this. This then leads to a total limiting disk current greater than three. The experimental data were fit to the appropriate simulation curve and the average value for the rate constant of the breakup of the [33] dimer was determined to be, for i) (pH 1), $83 \pm 25 \text{ sec}^{-1}$, which agreed very well with the rate constant determined from just the first wave.

The measured value determined for ii) (pH 5), however, exhibited an average normalized, limiting, disk current slightly larger than the predicted value, 3.78 vs. 3.50. This may be due to a slight amount of $\text{Ru}_3\text{Y-OH}_2$ present in the sample used. This would increase the observed amount of ring and disk currents. The predicted limiting disk currents for the rate constant determined from the first wave should have varied from a high value of 3.30 for 400 rpm, to a low value of 2.40 for 3600 rpm.

It is interesting to note that a purer sample of the [34] dimer yielded a ratio of 3.45 in polarography for the limiting current of the second reduction wave to the first reduction wave. This experiment should approximate the zero rotation rate, or the limiting rate ratio for the RRDE, as it apparently does. This adds further credence to this mechanism as the means by which the [34] dimer is reduced at lower pH's.

Above pH 7, another mechanism for the breakup of the [33] dimer upon reduction needs to be considered. Referring to Figure 25, it is seen that for these pH's the reduction of the Ru3Y-OH monomer occurs at potentials positive of the [33]/[32] couple. This means that any of the Ru3Y-OH that is produced from the [33] dimer, or the [32] dimer split-up, can react with the [32] dimer to produce a [33] dimer and Ru2Y-OH₂. The other homogeneous electron transfer reactions that can occur include [2] monomer reacting with the bulk species, [34] dimer, to produce [33] dimer and [3] monomer, and [32] dimer reacting with the bulk species, [34], to produce two [33] dimers. These last two reactions are favored thermodynamically to give, essentially, 100% conversion to the listed products. The series of homogeneous reactions are given by equations 64-66.

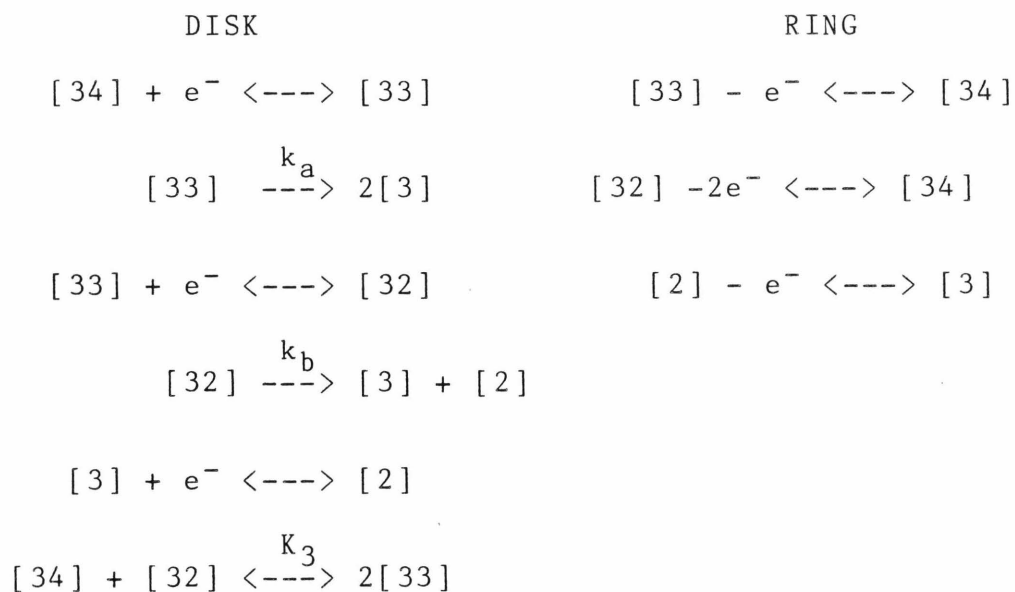


If the product of K_1 and K_2 is greater than one, then this is just K_3 (equation 65). The values for K_1 , and K_2 were determined from the half-wave potentials and for pH>7.7 the product was greater than 1000. Thus, the overall homogeneous chemical reaction for this simulation was taken as $K_3=1000$.

The following scheme was then used to simulate the disk

and ring response.

SCHEME X



where,

[34], [33], [32], [3] and [2] all have their usual meanings

k_a = first-order rate constant, which is fixed for a given simulation

k_b = first-order rate constant, which is varied in the simulation

K_3 = homogeneous equilibrium constant that is fixed for a given simulation

The first rate constant, k_a , is determined from the formal potential for the first reduction and the EC mechanism simulation (see Table 13).

The value of k_a was taken as 3.75 sec⁻¹, which was determined previously for pH 7.7-9.25, and K_3 was input as 1,000 for the simulations. The disk response, and the

collection efficiency are plotted vs. the dimensionless parameter, XKTC (defined above), in Figure 40. Several other values for k_a were used to test the simulation and they are also plotted in Figure 40. The tabulated values for two separate samples of the [34] dimer at pH 7.70 are listed in Table 14.

The simulation results were fit very well by the data leading to a value for the second rate constant, $k_b = 6.3 \pm 3.3 \text{ sec}^{-1}$. The RRDE voltammograms at pH 9.25 were very poorly defined due to a steadily sloping background and thus were not useful. This problem may be overcome by the use of the previously described, modulated, RDE technique, which would enable the surface effect problems to be eliminated. (153-156). As was the case with the reduction of the [34] dimer at lower pH's, the ratio of the limiting disk current for the second wave compared to the first was larger than the expected value of 2.0 for two, consecutive one-electron reductions of the [34] dimer. The kinetics and the thermodynamics are seen to lead to an increase in the disk current over this value, as well as accounting for the ring response. The increased disk current is, once again, seen to be due to the homogeneous reactions, and the difference in diffusion coefficients for the monomers and the dimer.

The use of the RRDE and the simulation programs has proved to be very successful in determining the homogeneous chemical reactions of the [34] dimer upon reduction. The enhanced currents for the second reduction wave in the RRDE,

Figure 40

Simulation data for Scheme X

A. Collection efficiency, N_k , vs. XKTC

B. Disk current, ZD, vs. XKTC

Conditions: $K = 1,000$

$$\left(\frac{D_{\text{dimer}}}{D_{\text{monomer}}} \right) = 0.50$$

$$k_a = \text{a. } 0.75$$

$$\text{b. } 3.75$$

$$\text{c. } 10.0$$

$$\text{d. } 20.0$$

$$\text{e. } 75.0$$

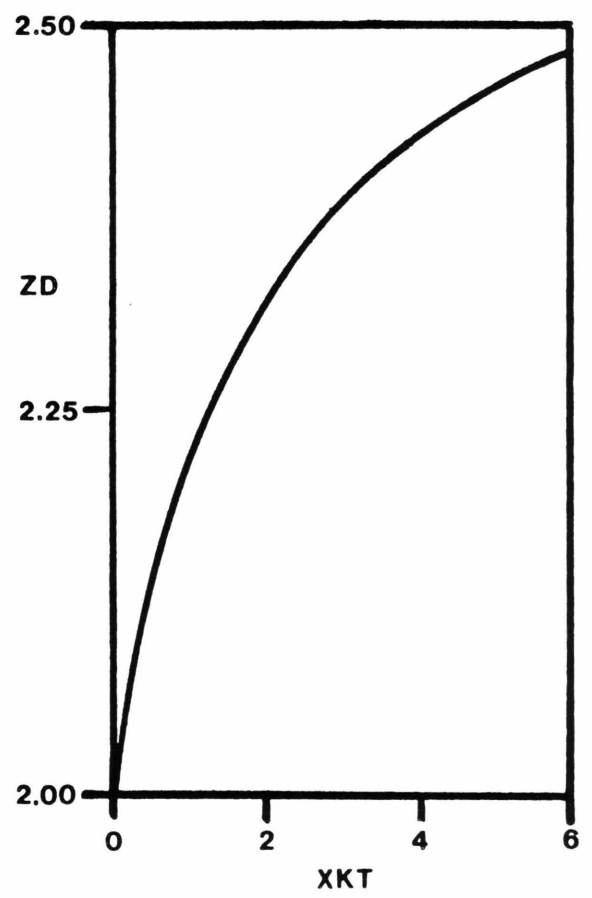
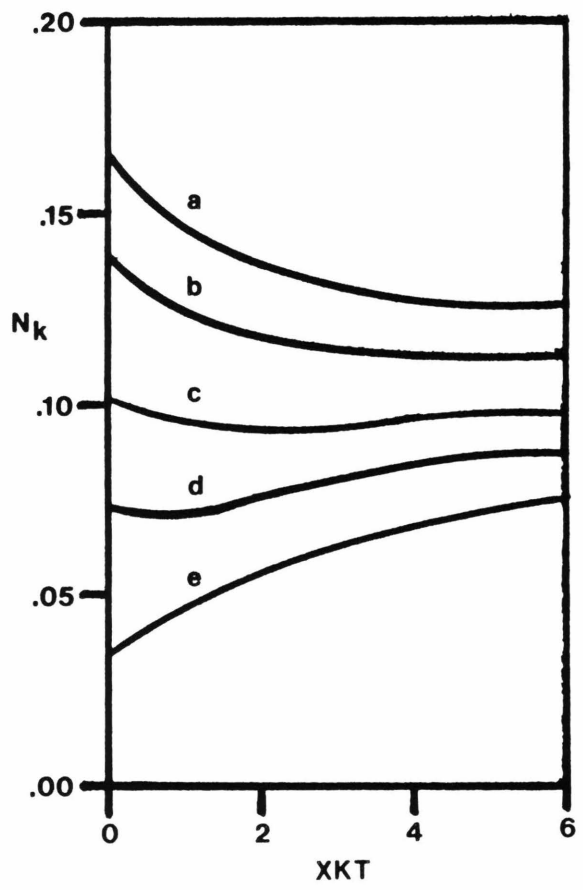


Figure 40

Table 14

Experimental RRDE data for Scheme X

Table 14*

<u>pH</u>	<u>Conc.</u>	<u>ω, rpm</u>	$\frac{i_{\text{disk}}}{\text{conc.}}$	$\frac{i_{\text{ring}}}{\text{conc.}}$	<u>Coll. Eff.</u>	<u>XKT</u>	<u>$k, M^{-1} s^{-1}$</u>
7.70	0.146	200	0.202	0.0198	0.098	2.30	2.20
		400	0.243	0.0245	0.101	1.60	3.10
		900	0.336	0.0336	0.100	2.00	8.70
		1600	0.422	0.0414	0.098	1.50	11.
		2500	0.501	0.0471	0.094	0.90	11.
		3600	0.614	0.0528	0.086	1.1	±9.
		4225	0.672	0.0544	0.081	1.8	37.

$$k(\text{ave}) = 7.2 \pm 4.3$$

7.70	0.148	200	0.203	0.0223	0.110	3.00	2.90
		400	0.257	0.0311	0.121	1.70	3.30
		900	0.345	0.0453	0.131	1.50	6.50
		1600	0.423	0.0582	0.138	0.90	7.0
		2500	0.507	0.0697	0.137	0.60	7.3
		3600	0.602	0.0798	0.133	1.0	±7.

$$k(\text{ave}) = 5.4 \pm 2.1$$

$$k(\text{total}) = 6.3 \pm 3.3$$

* $\frac{i_{\text{disk}}}{\text{conc.}}$, $\frac{i_{\text{ring}}}{\text{conc.}}$ = amp/M; coll. eff. = collection efficiency

$$\text{XKT} = \left(\frac{k}{\omega} \right) \left(\frac{v}{D} \right)^{\frac{1}{3}} (0.51)^{-\frac{2}{3}}$$

the CV, and the polarographic experiments has been shown to be due to the difference in the diffusion coefficients between the monomeric Ru3Y-OH_2 , and the dimer. Without the simulations, however, the unravelling of the disk and ring responses in the RRDE voltammograms would have been impossible. The simulations also serve to illustrate why other electrochemical techniques yielded limiting, or peak currents greater than expected for simple electron transfer reactions. The effect of homogeneous chemical kinetics between two species with different diffusion coefficients can lead to unusual electrochemical responses and this effect can be reasonably accounted for only by digital simulation. The combined use of the simulations and the RRDE thus makes this a very powerful means of studying complicated electrochemical processes and an increase in their combined use is advocated, since it is relatively easy to include the heterogeneous, and the homogeneous kinetics into a simulation of the desired mechanism.

20. SUMMARY AND CONCLUSION

The electrochemical response of Ru₃Y was investigated at several pH's. The E's for the Ru₃/2Y couple were determined by polarographic techniques and found to vary by -60 mV/pH above the indicated pK_a of 7.70 (see Figure 25). The oxidative behavior of Ru₃Y was investigated by cyclic voltammetry, electrolysis and RRDE voltammetry, but it was not as easily interpretable.

The oxidative electrolysis of Ru₃Y at +1.00 V to produce the [34] dimer at pH 1-7 yielded the same stoichiometry as by chemical means: one Faraday was required per two moles of Ru₃Y with the net evolution of protons. The CV's of a solution of Ru₃Y indicated that there was an oxidation wave always present at +1.00 V with more current than for the one-electron reduction of Ru₃Y to produce Ru₂Y. Repetitive cycling between +0.40 V and +1.40 V showed, at scan rates near 200 mV/sec, that a reversible wave ($\Delta \approx 70$ mV) grew in at slightly more negative potentials than the large wave. The peak currents for this wave were now less than for the Ru₃/2Y couple. At slower scan rates (20 mV range), the small wave was less well-defined while the larger wave remained the same. The larger wave was taken to be due to the catalytic evolution of dioxygen from water, since an electrolysis performed with the potential fixed past this wave yielded measurable amounts of dioxygen, while the smaller wave was attributed to the reversible oxidation of the [34] to the [44] dimer.

The oxidative RRDE behavior of Ru₃Y at pH 1-9.25 was investigated to try and determine the mechanism of the formation of the [34] dimer. Several different mechanisms were simulated by a digital method to try and account for the observed disk currents, but none of them were fit well by the experimental data. The reason for the discrepancy was attributed to surface effects at the electrode that were masking the mass-transfer controlled current. There was also an absence of any ring current until the potential was set to reduce the [34] dimer. This indicated that there was no oxidized Ru₃Y present to be reduced at the ring and that the formation of the dimer was very rapid. There was no spectral evidence of formation of a precursor [33] dimer that was then subsequently oxidized to produce the [34] dimer. There was also no evidence that the oxidized Ru₃Y, probably Ru₄Y, reacted with itself to initially form a [44] dimer which then decayed to produce the [34] dimer and some other, unidentified, oxidized species. This mechanism also would not fit the electrolysis results, since one Faraday would have been required per mole of Ru₃Y to produce the final [34] dimer. It seems most likely that the formation of the [34] dimer involves the reaction between a Ru₃Y and a Ru₄Y. It was, however, not possible to definitively describe the mechanism of formation of the [34] dimer due to surface effects. Similar problems were also encountered for the larger oxidation wave near +1.00 V and it was not possible to determine the mechanism involved in the

catalytic production of dioxygen.

The electrochemistry of the [34] dimer was also investigated. The oxidative RRDE and CV behavior of the [34] dimer yielded inconclusive mechanistic results. A spectro-electrochemical oxidation of the [34] dimer at pH 1 showed that the oxidized form of the [34] dimer was the one-electron product, the [44] dimer. The spectrum of the [44] dimer was also identical with the spectrum that was produced when an excess of Ce(IV) was added to a solution of the [34] dimer, which was then observed to evolve dioxygen catalytically. This indicates that the [44] dimer is the catalytic species in the production of dioxygen from water.

Using a ruthenium-bipyridine dimer, Meyer, et al (47) concluded that the catalytic species for the evolution of dioxygen from water using Ce(IV) as the oxidant was the [55] form of the dimer. This result was only given in a short communication and further work was reported in progress. When it is considered that the best current dioxygen evolution catalyst, ruthenium dioxide, contains oxo-linked Ru(IV) units, it seems likely that Ru(IV) containing molecules will exhibit catalytic dioxygen evolution behavior. The ruthenium-edta [44] dimer supports this idea, and it is my guess that the catalytic form of the ruthenium-bipyridine dimer studied by Meyer will also turn out to be the [44] dimer.

The electrochemical reduction of the [34] dimer provided more easily interpretable results than did its oxidation. A

cyclic voltammogram of the [34] dimer yielded several reduction waves (see Figure 23). An electrolysis performed with the potential set just past the first wave yielded only Ru3Y, as evidenced by its optical spectrum, after one-half a Faraday per mole of the [34] dimer. The total reduction of the [34] dimer required three Faraday's per mole of dimer and resulted in the production of Ru2Y, exclusively. These results further substantiated the dimeric, mixed-valence nature of the [34] dimer.

The polarographic response of the [34] dimer at pH 5-12.6 was also investigated (see Figure 26) and each of the waves exhibited a different dependence on the pH. The E° for each of the waves was determined by the standard polarographic wave shape analysis described earlier. The E° for the first wave exhibited two inflection points indicating two different proton coupled steps during the one-electron reduction of the [34] dimer (see Figure 25). Between pH 1-7, the E° changed by -60 mV/pH, and then remained at a constant value until pH 10.3, whereupon a -60 mV/pH change occurred between pH 10.3 and 12.6. The first pH dependence is ascribable to the proton coupled reduction of the [34] dimer to produce a protonated form of the [33] dimer. Since the [34] dimer is most likely μ -oxo bridged between pH 1 and 10, the protonation of the [33] dimer is taken to lead to a μ -hydroxo-bridged dimer below pH 7. The pKa of 7.0 is then due to the deprotonation of the bridging group. Above pH 7 and below pH 10.3 there is no pH

dependence since now both forms of the redox couple are μ -oxo bridged. The pKa of 10.3 was established earlier by spectroscopic means as being due to the deprotonation of the [34] dimer to, most likely, form a μ -oxo, μ -hydroxo-bridged dimer ([34]-OH). The second proton coupled reduction is then due to protonation of the [34]-OH dimer to produce the μ -oxo bridged [33] dimer.

The RRDE behavior of the first reduction process of the [34] dimer was also investigated between pH 1-9.25. The following mechanism was then simulated to try and describe the disk and ring response:

SCHEME VIII

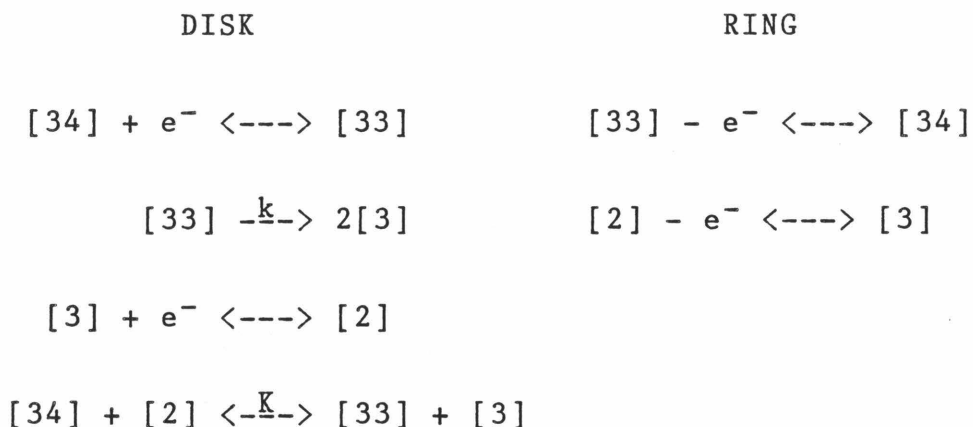


The experimental data were seen to fit the simulation results very well and the following rates of breakup for the [33] dimer were determined: i) pH 1, $k = 81 \text{ M}^{-1} \text{ sec}^{-1}$, ii) pH 5, $k = 17 \text{ M}^{-1} \text{ sec}^{-1}$, iii) pH 7.70, $k = 3.6 \text{ M}^{-1} \text{ sec}^{-1}$.

The second reduction wave also exhibited a pH dependence. Below pH 5, the E' was exactly the same as that for $\text{Ru}_3/2\text{Y-OH}_2$. The limiting current of the second wave was also greater than three times the first. The use of the simulation program offered an explanation as to why this occurred. The following scheme was used to model the

reduction and breakup of the dimer at the second wave:

SCHEME IX

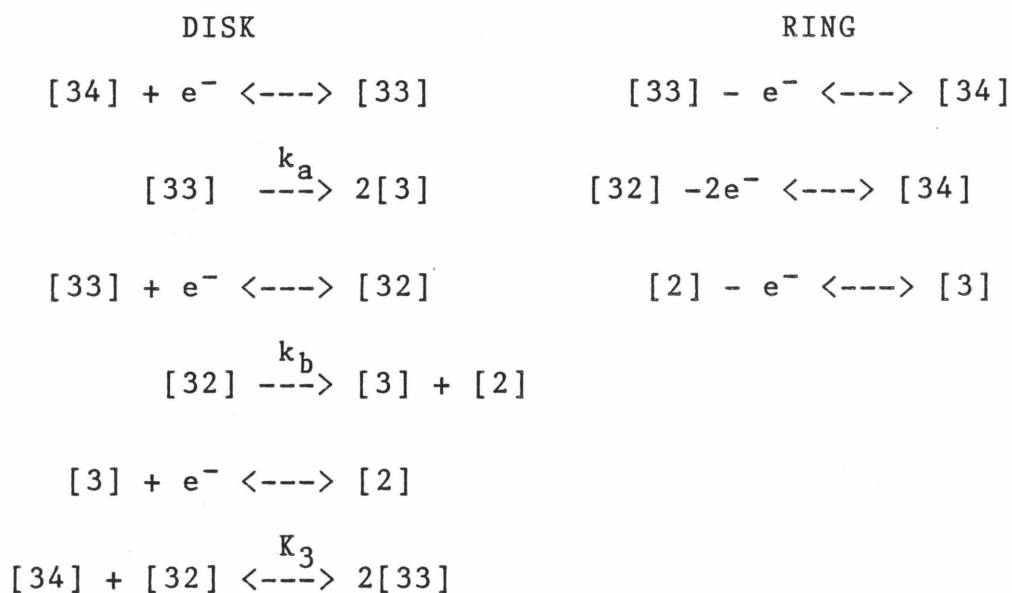


The equilibrium constant is determined by the difference in the E^0 's for the [34]/[33] and the Ru₃/2Y couples. When the difference in the diffusion coefficients for the monomer and the dimer is considered, then the large observed current for the second wave when compared to the first wave, is predicted by the simulation program. The diffusion coefficient for the [34] dimer was determined to be 3.6\0.2 cm²/sec by both polarography and by an analysis of the first wave of the RRDE voltammogram. The rate constants that were determined by the use of the simulation program were seen to match those found by an analysis of just the first wave.

At pH 7.70, a different mechanism was determined to be operable. A cyclic voltammogram showed that the [33] dimer was long-lived enough that it could be reduced to the [32] dimer. The [32] dimer could then break up to produce Ru₃Y and Ru₂Y monomers. The interesting phenomenon here is that the E^0 for the Ru₃/2Y couple is positive of that for the

[33]/[32] couple. This means that Ru₂Y cannot reduce the [33] dimer, but that the [33] dimer and Ru₃Y can react to produce the [32] dimer and Ru₂Y by a homogeneous electron transfer reaction. The following scheme was then simulated:

SCHEME X



The first rate constant, k_a , was determined by an analysis of the first wave and was input into the simulation as a constant, as was the difference in the diffusion coefficients, and the equilibrium constant, K_3 . Once again, the observed disk and ring currents fit the simulation data well and an average value of $6.3 \text{ M}^{-1} \text{ sec}^{-1}$ was determined for two different samples of the [34] dimer.

These last few results indicate the versatility and usefulness of digital simulations with RRDE voltammetry in being able to describe complicated electrochemical systems. The ease with which the programs can be modified to include

varying chemical complications and properties of the system being studied makes these two techniques very potent probes of the mechanistic details of electrochemical systems.

The characterization of the [34] dimer has been detailed in the previous chapters. The spectral similarities between the ruthenium-edta dimer and other ruthenium containing dimers in their higher oxidation states has already been detailed earlier, while the last few chapters have dealt with the electrochemical response. The present work also affords the first detailed attempt at systematically describing the formation and fission of a ruthenium, oxo-bridged dimer using electrochemical methods. The applicability of these techniques to the other dimeric ruthenium systems that have been studied is not very difficult and it is advocated that these systems be investigated similarly.

21. RRDE SIMULATION DISCUSSION

The use of digital simulations in the analysis of RRDE data has been described in the previous two chapters. One of the advantages of the digital simulations was that they enabled different diffusion coefficients for the reactive species to be taken into account. This is unlike analytical solutions for the RRDE in which the simplifying assumption is made that all the diffusion coefficients are equal. The digital simulations also allowed homogeneous reactions between the disk products and the bulk species to be considered, as well as the inclusion of several kinetic chemical steps and variable substrate concentrations. Using these modifications, several mechanisms were simulated and the results compared with the experimental data to successfully extract chemical kinetic information.

Several methods have been proposed to model the RRDE (153) by digital means. These include the point method advocated by Britz (157), the collocation method (158), and the "box" method of finite difference simulation. The latter method was developed initially by Feldberg (55), and then expanded upon by Bard and Prater (52-54,153,159).

The first method has been shown to work extremely well for a one-dimensional array system that takes into account only the layer below the disk (157). The inclusion of a second-dimension to account for the radial layers extending out towards the ring has not been attempted for this system, however, due to the complicated programming necessary, and

the considerable computation time that would be required to perform the simulation (157). The collocation method (158), on the other hand, promises to afford a very rapid means of solving complex RRDE simulations. It requires considerable programming time, however, due to its complicated matrix algebra approach and, consequently, there has been little work performed on this method, other than the theoretical foundation for the technique.

The technique used in the present study was the "box" method. This method considers dividing up the volume below the RRDE into finite elements with a fixed-size. The diffusion and convection terms for the mass transfer are then considered for each species by taking the difference between adjacent boxes for a given time interval (52,55). Fick's second law is then used to describe the concentration gradient which then leads to the diffusion effects between two adjacent boxes (equation 67)

$$\begin{aligned} \Delta F_i(j,k) = & DM_i [F_i(j+1,k) - F_i(j,k)] \\ & - DM_i [F_i(j,k) - F_i(j,k)] \end{aligned} \quad (67)$$

where,

$F_i(j,k)$ = concentration of the i^{th} species
in box, (j,k)

DM_i = dimensionless diffusion coefficient

$$= \left(\frac{D_i \Delta t}{(\Delta x)^2} \right) \quad (68)$$

The dimensionless diffusion coefficient is related to the real diffusion coefficient, D_i , by the width of one layer, Δx , and the time length, Δt , for each iteration (52), while the iteration time length is determined by considering the equation for the velocity of convective fluid flow normal to the electrode (equation 69)

$$V_x = \frac{dx}{dt} = -0.51\omega^{\frac{3}{2}}\nu^{-\frac{1}{2}}X^2 \quad (69)$$

where,

ω = rotation rate (rad/sec)

ν = kinematic viscosity (cm^2/sec)

X = distance from the electrode (cm)

The radial convection is considered in a similar manner.

The initial and boundary conditions for the experiment being simulated are then taken into account. At the end of each iteration, a simulated current is calculated and the electrolyzed species at the electrode's surface is converted to its redox partner. The whole process is then repeated until the difference for the simulated current between two successive iterations is less than a specified amount, or until a predetermined number of iterations are performed. The final simulated output then includes the disk and ring currents, and the collection efficiency. Complications such as chemical kinetics and homogeneous equilibria can also be added to each iteration after all of the mass transfer effects have been considered, and before the currents are calculated. In the absence of any kinetic complications,

the theoretical collection efficiency for the modelled electrode's geometry is obtained.

Once the main body of the program has been set up to calculate the Levich behavior, it becomes a simple matter to add or delete reactive species into the model. The same effects are applied to each species; only the coefficient of the species in question is changed. Boundary values, initial conditions, and diffusion coefficients can also be changed easily, and chemical complications, both kinetic and thermodynamic, can be included into the simulation. The series of iterations is then repeated for each simulated rate constant, XKT or $XKTC$ (described in the RRDE section) (equations 61 and 62), or thermodynamic value, and the resulting currents and collection efficiency are then calculated.

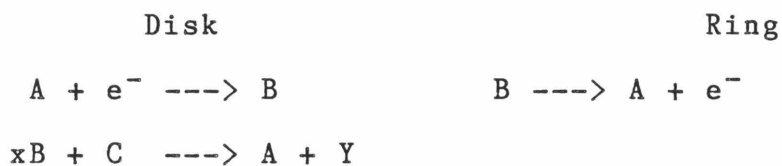
For several systems it was also instructive to list the concentrations for each of the species above the disk to help understand the resulting simulated disk response. The concentrations can be included in the output by simply adding a very short routine at the end of the program. This routine is listed in the appendix, where a sample of the output with, and without, this routine is also included.

During the course of using the Bard and Prater programs, several limitations to the programs were encountered. At large values for the rate constant, the finite difference method becomes unstable and is no longer feasible as a means of describing the kinetic term. The use of the integrated

form of the rate expression first described by Flanagan and Marcoux was then used (56). This method, too, had drawbacks. Primarily, this method required longer computation times, and was, therefore, used only when large kinetic terms were needed. A comparison of the simulated values using the two kinetic expressions yielded, essentially, identical values at medium to small values for the rate term. One anomaly was encountered when the Flanagan and Marcoux expression was employed. When the added substrate-to-reactant ratio was equal to one, then in a very limited range of the simulated second-order rate expression, $XKTC = 1.0 \pm 0.5$, the Flanagan and Marcoux method yielded erratic current fluctuations that precluded its use in this region. The values of XKTC on both sides of this region, however, were stable and gave values comparable to the finite difference expression of Bard and Prater. The reasons for this instability are unclear, and the integrated rate method was not used for $M = [\text{substrate}]/[\text{catalyst}] = 1$ when values in this region were required.

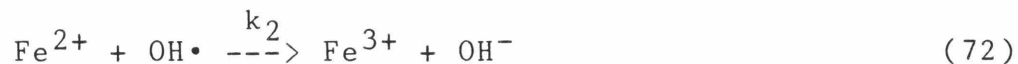
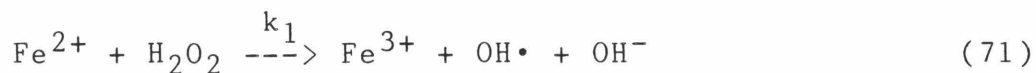
My initial interest in the use of the digital simulations was to model the catalytic system to aid in extracting a rate constant for the [34] dimer catalyzed production of dioxygen from water.

Catalytic Mechanism



where the variables A and B are a redox couple, and C is the substrate that is oxidized by x species of B to produce the electro-inactive product, Y, and to regenerate the bulk species, A. The remaining oxidized species, B, is then reduced at the ring to regenerate A.

The early work of Bard and Prater included a simulation for the catalytic mechanism (54) and a listing of their program was obtained for possible use in understanding the [34] catalytic reaction. This program was modified to include interactive input of data to aid in easily changing several of the program variables, as well as to include the integrated rate expression discussed above. The program was also later modified to consider several different reaction mechanisms (some were discussed in earlier sections) and a listing of these programs is included in the appendix. In a recent work by Skinner, et al (57), a correction of a factor of two was made to the rate expression for the catalytic disproportionation of hydrogen peroxide by iron (II) originally given by Bard and Prater (54). This factor was needed to account for the stoichiometry of the iron and the hydrogen peroxide.



Applying the steady-state approximation to $[\text{OH}\cdot]$ the following kinetic expression is obtained:

$$\frac{-d[\text{Fe}^{2+}]}{dt} = 2k_1[\text{Fe}^{2+}][\text{H}_2\text{O}_2] = \frac{-d[\text{Fe}^{3+}]}{dt} \quad (74)$$

The stoichiometry factor is taken into account in the simulations that follow by the user selectable value of x defined above. Skinner, et al then measured the disk and ring currents for several peroxide to iron ratios and calculated a "corrected" value for rate constant. They also used the experimental data given by Bard and Prater and recalculated the rate constant for this data. The resulting "corrected" values for the rate constant were given typically as $250 \text{ M}^{-1} \text{ sec}^{-1}$. This is, however, several times higher than the values of $40\text{-}70 \text{ M}^{-1} \text{ sec}^{-1}$ obtained by other groups by different methods (57,161,162). The reasons for this were not clear and Skinner, et al, suggested that possible experimental difficulties in measuring the current contributed to this discrepancy.

One of the main attractions of the simulations was the ability to input different values for the diffusion coefficient of each species. This capability, and the effect it could have on the measured disk and ring currents was demonstrated rather dramatically in the previous section dealing with the reduction of the [34] dimer. In all of the previous uses of the catalytic simulation programs, identical diffusion coefficients had used for all of the

species. It was felt that since the diffusion coefficients of the Fe^{2+} , and the hydrogen peroxide are so different, the use of different diffusion coefficients was required to accurately model this system. By not including the different diffusion coefficients, the concentration of peroxide in a given volume element was being underestimated. This would then lead to a misleading, and high value for the rate constant. The effect of varying the diffusion coefficients was thus investigated for the catalytic systems described by Bard and Prater (54), and Skinner (57). An example of the catalytic simulation using the Bard and Prater electrode geometry (54) is given in Figure 41. The following three cases were considered:

- i) no stoichiometry correction, $\text{DMi} = 0.45$
- ii) stoichiometry correction = 2, $\text{DMi} = 0.45$
- iii) stoichiometry correction = 2, $\text{DMA} = 0.125$,
 $\text{DMB} = 0.125$, $\text{DMC} = 0.45$

In all of the systems that were compared, the diffusion coefficient of Fe^{3+} was taken as $5 \text{ E-}6 \text{ cm}^2/\text{sec}$, while for hydrogen peroxide, a value of $1.8 \text{ E-}5 \text{ cm}^2/\text{sec}$ was used. In terms of the simulated diffusion coefficients, the values were input as 0.125 for DMA and DMB, and 0.45 for DMC.

The reason for selecting these simulation values was that a value less than 0.5 is required for all of the diffusion coefficients in the finite element model, otherwise, instabilities occur. The instabilities are due

Figure 41

Comparison of Simulations for the Catalytic Mechanism
for the Bard and Prater Electrode (54)

A. Collection efficiency vs. XKTC

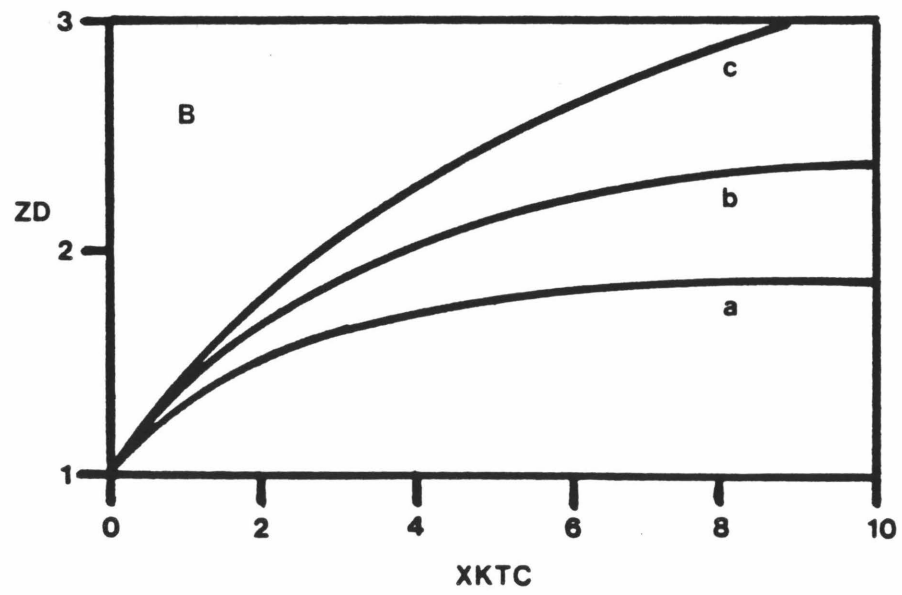
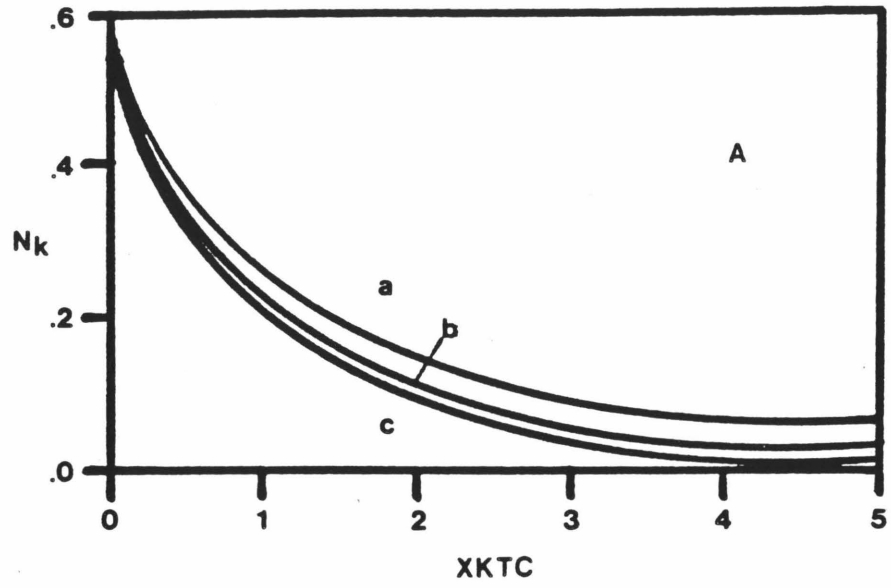
B. Disk Current, ZD, vs. XKTC

a. $x=1$, $DMA = DMB = DMC = 0.45$

b. $x=2$, $DMA = DMB = DMC = 0.45$

c. $x=2$, $DMA = DMB = 0.125$, $DMC = 0.45$

Figure 41



to "too much" species being transferred between boxes, and the propagation of successively larger errors during each iteration (157).

In the original derivation of the RRDE program, a value of DMA = 0.45 was used. With DMA equal to 0.45 and the step size, L, equal to 1000, a steady-state current value that was 99.5% of the Levich current was obtained after 25 minutes of computer time.

$$\Delta t = \frac{t_k}{L} \quad (75)$$

where,

t_k = real time variable

Δt = simulated time variable

L = step size, or number of iterations necessary to simulate the time variable

Bard and Prater determined that they could shorten the computation time by a factor of 60 by using modified convection equations (52). With the correction factors, a value of L=50 for DMA = 0.45 was used in the original simulations, which, after only three times the step size number of iterations, yielded a limiting current value that was 99.5% of the Levich current (52). If the value of DMA was adjusted in the simulations to account for a faster moving species (such as the substrate C in the catalytic mechanism, which is then set a fixed value of 0.45 for DMC), but without adjusting the time interval, then the simulated

limiting Levich behavior was not observed. It was therefore, necessary to redefine the time variable in relationship to the new, lower diffusion coefficient for DMA to account for the proper time interval for each iteration. This factor was derived by considering equations 2 and 4 so that the new value yielded the same time variable.

$$\text{DMA}(1)L(1) = \text{DMA}(2)L(2) = \frac{\tau_k D_A}{(\Delta X)^2} \quad (76)$$

where,

DMA(1) and L(1) are 0.45 and 50, respectively, DMA(2) is the new lower diffusion coefficient, and L(2) is the new, calculated number of iterations necessary for a given real time interval. For the iron-peroxide system the step size was thus increased to 180, and the maximum number of iterations was, therefore, increased to 540. This adjustment then yielded the Levich current to within 99.5% of the steady state value. In addition, this change increased significantly the length of time needed to perform each simulation when compared to the DMA = 0.45, L = 50 parameters.

The catalytic mechanism program was then run after including the stoichiometric factor introduced by Skinner, and by considering the proper values for the diffusion coefficients. The geometries of the electrodes for Skinner's and Bard and Prater's systems, and an electrode used in our labs, the standard Pine electrode, were

simulated. Skinner's, and Bard and Prater's data were then fitted to the corrected simulations (see Tables 15 and 16 and Figure 41). Much lower rate constants than those obtained by the previous workers were found for both sets of data. These new values were also much more consistent with the values determined previously by spectroscopic methods.

It can now be seen that the experimental data for both groups were reasonably good, and that with some minor corrections, the simulation program is correct, but that it must be applied correctly to the experimental conditions. The recalculated values for Skinner's runs for the iron system with the following peroxide-to-iron(II) ratios of 0.1, 0.2, 1.0(twice), 2.0 and 9.8 yielded $k = 55.8 \pm 7.7$, 69.4 ± 14.7 , 82.3 ± 13.1 , 79.0 ± 6.4 , 105 ± 18 , and 135 ± 38 . For the Bard and Prater data, with a ratio of 1:1, k was recalculated to be 43.4 ± 3.5 . The lower ratio experiments yield values that agree very well with those obtained by other techniques, while the two higher ratio results are a little bit larger. The reasons for the last two results are unclear.

As a further test of the programs, recalculated results for the copper system studied by Skinner (using a diffusion coefficient of $5 \text{ E-}6 \text{ cm}^2/\text{sec}$) at several concentrations and temperatures are included in Table 17. These data yielded rate constants similar to the iron system, while the value for the activation energy was analyzed by an Arrhenius plot to be 5.65 kcal/mole. This is lower than the 8.5 kcal/mole

Table 15

RRDE catalytic simulation results for Skinner (57) data

Table 15^a

RRDE results in 2.0 M HCl
 25°C 12.94 mM FeCl₃ 1.28 mM H₂O₂

ω	N	XKTC	k
9.4	0.308	2.55	46.9
23	0.347	1.10	49.5
37	0.359	0.755	54.7
62	0.367	0.555	67.3
90	0.377	0.318	56.0
138	0.380	0.250	67.5
182	0.385	0.145	51.8
219	0.386	0.123	52.6
254	0.383	0.189	93.8
284	0.390	0.0385	21.38

$$k(\text{ave}) = 55.8 \pm 7.7$$

$$k(\text{Skinner}) = 230 \pm 60$$

a. ω (rad/sec), N = collection efficiency, k ($\text{M}^{-1}\text{sec}^{-1}$),

$$\text{XKTC} = \left\{ \frac{2kC_A^0}{\omega} \right\} \left(\frac{\nu}{D} \right)^{\frac{1}{3}} (0.51)^{-\frac{2}{3}}$$

$$D(\text{Fe}) = 5 \text{ E-6 cm}^2/\text{sec}; D(\text{H}_2\text{O}_2) = 1.8 \text{ E-5 cm}^2/\text{sec}$$

$$\nu = 0.01 \text{ cm}^2/\text{sec};$$

Electrode Radii: 100, 110, 143; M: 0.1

DMA=0.125, DMB=0.125, DMC=0.45

Step size = 180; # iterations = 540

Table 15^b

RRDE results in 2.0 M HCl

25°C 6.45 mM FeCl₃ 1.28 mM H₂O₂

<u>ω</u>	<u>N</u>	<u>XKTC</u>	<u>k</u>
9.5	0.273	1.81	67.6
22	0.341	0.597	51.6
36	0.340	0.611	86.4
61	0.364	0.300	71.9
88	0.369	0.245	64.8
134	0.381	0.111	58.5
174	0.380	0.122	83.4
216	0.386	0.060	50.9
257	0.380	0.122	123
300	0.389	0.030	35.3

$$k(\text{ave}) = 69.4 \pm 14.7$$

$$k(\text{Skinner}) = 250 \pm 70$$

b. ω (rad/sec), N = collection efficiency, k (M⁻¹sec⁻¹),

$$\text{XKTC} = \left(\frac{2kC_A^0}{\omega} \right) \left(\frac{\nu}{D} \right)^{\frac{1}{3}} (0.51)^{-\frac{2}{3}}$$

$$D(\text{Fe}) = 5 \text{ E-}6 \text{ cm}^2/\text{sec}; D(\text{H}_2\text{O}_2) = 1.8 \text{ E-}5 \text{ cm}^2/\text{sec}$$

$$\nu = 0.01 \text{ cm}^2/\text{sec};$$

Electrode Radii: 100, 110, 143; M: 0.2

DMA=0.125, DMB=0.125, DMC=0.45

Step size = 180; # iterations = 540

Table 15^c

RRDE results in 2.0 M HCl
 25°C 6.48 mM FeCl₃ 6.40 mM H₂O₂

<u>ω</u>	<u>N</u>	<u>XKTC</u>	<u>k</u>
9.4	0.064	2.37	87.1
22	0.167	0.852	73.2
36	0.215	0.557	78.4
62	0.246	0.416	101
90	0.295	0.240	84.6
137	0.320	0.167	89.6
182	0.344	0.106	75.1
222	0.356	0.077	67.0
258	0.353	0.084	84.9
290	0.350	0.091	103
299	0.367	0.052	61.0

$$k(\text{ave}) = 82.3 \pm 13.1$$

$$k(\text{Skinner}) = 210 \pm 30$$

c. ω (rad/sec), N = collection efficiency, k (M⁻¹sec⁻¹),

$$\text{XKTC} = \left(\frac{2kC_A^0}{\omega} \right) \left(\frac{\nu}{D} \right)^{\frac{1}{3}} (0.51)^{-\frac{2}{3}}$$

$$D(\text{Fe}) = 5 \text{ E-}6 \text{ cm}^2/\text{sec}; D(\text{H}_2\text{O}_2) = 1.8 \text{ E-}5 \text{ cm}^2/\text{sec}$$

$$\nu = 0.01 \text{ cm}^2/\text{sec};$$

Electrode Radii: 100,110,143; M: 1.0

DMA=0.125, DMB=0.125, DMC=0.45

Step size = 180; # iterations = 540

Table 15^d

RRDE results in 2.0 M HCl

25°C 3.30 mM FeCl₃ 3.30 mM H₂O₂

<u>ω</u>	<u>N</u>	<u>XKTC</u>	<u>k</u>
20	0.229	0.490	75.2
32	0.274	0.309	76.0
56	0.310	0.196	84.1
80	0.327	0.148	91.2
122	0.357	0.075	70.2
131	0.361	0.066	81.3
200	0.367	0.050	76.8
233	0.363	0.061	110
262	0.379	0.025	50.3
270	0.374	0.037	77.0

$$k(\text{ave}) = 79.0 \pm 6.4$$

$$k(\text{Skinner}) = 220 \pm 20$$

d. ω (rad/sec), N = collection efficiency, k (M⁻¹sec⁻¹),

$$\text{XKTC} = \left(\frac{2kC_A^0}{\omega} \right) \left(\frac{\nu}{D} \right)^{\frac{1}{3}} (0.51)^{-\frac{2}{3}}$$

$$D(\text{Fe}) = 5 \text{ E-6 cm}^2/\text{sec}; D(\text{H}_2\text{O}_2) = 1.8 \text{ E-5 cm}^2/\text{sec}$$

$$\nu = 0.01 \text{ cm}^2/\text{sec};$$

Electrode Radii: 100,110,143; M: 1.0

DMA=0.125, DMB=0.125, DMC=0.45

Step size = 180; # iterations = 540

Table 15^e

RRDE results in 2.0 M HCl
 25°C 6.45 mM FeCl₃ 12.8 mM H₂O₂

<u>ω</u>	<u>N</u>	<u>XKTC</u>	<u>k</u>
9.5	0.0173	2.34	87.5
22	0.077	0.924	79.8
36	0.121	0.600	84.8
62	0.174	0.384	93.5
88	0.207	0.290	100
134	0.254	0.187	98.7
179	0.264	0.169	119
221	0.288	0.129	131
289	0.301	0.11	125
299	0.305	0.104	122

$$k(\text{ave}) = 105 \pm 18$$

$$k(\text{Skinner}) = 250 \pm 50$$

e. ω (rad/sec), N = collection efficiency, k (M⁻¹sec⁻¹),

$$\text{XKTC} = \left(\frac{2kC_A^0}{\omega} \right) \left(\frac{\nu}{D} \right)^{\frac{1}{3}} (0.51)^{-\frac{2}{3}}$$

$$D(\text{Fe}) = 5 \text{ E-}6 \text{ cm}^2/\text{sec}; D(\text{H}_2\text{O}_2) = 1.8 \text{ E-}5 \text{ cm}^2/\text{sec}$$

$$\nu = 0.01 \text{ cm}^2/\text{sec};$$

Electrode Radii: 100,110,143; M : 2.0

DMA=0.125, DMB=0.125, DMC=0.45

Step size = 180; # iterations = 540

Table 15^f

RRDE results in 2.0 M HCl

25°C	1.31 mM FeCl ₃		12.8 mM H ₂ O ₂
ω	N	XKTC	k
13.7	0.0324	0.306	81.2
25	0.069	0.191	92.5
47	0.130	0.110	99.6
75	0.172	0.077	111
102	0.200	0.061	120
149	0.236	0.045	129
192	0.248	0.040	149
232	0.261	0.035	158
271	0.267	0.033	173
293	0.269	0.033	185
297	0.269	0.032	186

$$k(\text{ave}) = 135 \pm 38$$

$$k(\text{Skinner}) = 310 \pm 70$$

f. ω (rad/sec), N = collection efficiency, k ($\text{M}^{-1}\text{sec}^{-1}$),

$$\text{XKTC} = \left(\frac{2kC_A^0}{\omega} \right) \left(\frac{\nu}{D} \right)^{\frac{1}{3}} (0.51)^{-\frac{2}{3}}$$

$$D(\text{Fe}) = 5 \text{ E-6 cm}^2/\text{sec}; D(\text{H}_2\text{O}_2) = 1.8 \text{ E-5 cm}^2/\text{sec}$$

$$\nu = 0.01 \text{ cm}^2/\text{sec};$$

Electrode Radii: 100, 110, 143; M: 9.8

DMA=0.125, DMB=0.125, DMC=0.45

Step size = 180; # iterations = 540

Table 16

RRDE catalytic simulation results for Bard and
Prater data (54)

Table 16*

RRDE results in 2.0 M HCl

25°C 6.40 mM FeCl₃ 6.40 mM H₂O₂

ω	N	XKTC	k
21.4	0.300	0.473	40.1
32.6	0.351	0.334	43.1
43.9	0.383	0.260	45.2
53.6	0.416	0.194	41.2
62.8	0.436	0.157	39.1
91.4	0.450	0.133	48.2
97.8	0.458	0.121	46.7

$$k(\text{ave}) = 43.4 \pm 3.5$$

$$k(\text{Skinner}) = 202 \pm 15$$

$$k(\text{Bard and Prater}) = 105 \pm 5$$

*. ω (rad/sec), N = collection efficiency, k ($\text{M}^{-1}\text{sec}^{-1}$),

$$\text{XKTC} = \left(\frac{2kC_A^0}{\omega} \right) \left(\frac{\nu}{D} \right)^{\frac{1}{3}} (0.51)^{-\frac{2}{3}}$$

$$D(\text{Fe}) = 5 \text{ E-6 cm}^2/\text{sec}; D(\text{H}_2\text{O}_2) = 1.8 \text{ E-5 cm}^2/\text{sec}$$

$$\nu = 0.01 \text{ cm}^2/\text{sec};$$

Electrode Radii: 83, 94, 159; M: 1.0

DMA=0.125, DMB=0.125, DMC=0.45

Step size = 180; # iterations = 540

Table 17

RRDE catalytic simulation results for Skinner data (57)
of Copper system

Table 17^a

RRDE results in 2.0 M HCl

15°C	6.70 <u>mM</u> CuCl ₂	6.70 <u>mM</u> H ₂ O ₂	
	<u>ω</u>	<u>N</u>	<u>XKTC</u>
	9.1	0.086	1.83
	22	0.182	0.747
	36	0.235	0.463
	63	0.281	0.286
	90	0.304	0.213
	138	0.327	0.148
	182	0.340	0.116
	224	0.342	0.111
	257	0.353	0.084
	282	0.360	0.068
	286	0.360	0.068

$$k(\text{ave}) = 73.4 \pm 9.5$$

$$k(\text{Skinner}) = 154 \pm 20$$

a. ω (rad/sec), N = collection efficiency, k ($\text{M}^{-1}\text{sec}^{-1}$),

$$\text{XKTC} = \left(\frac{2kC_A^0}{\omega} \right) \left(\frac{\nu}{D} \right)^{\frac{1}{3}} (0.51)^{-\frac{2}{3}}$$

$$D(\text{Cu}) = 5 \text{ E-}6 \text{ cm}^2/\text{sec}; D(\text{H}_2\text{O}_2) = 1.8 \text{ E-}5 \text{ cm}^2/\text{sec}$$

$$\nu = 0.01 \text{ cm}^2/\text{sec};$$

Electrode Radii: 100, 110, 143; M : 1.0

DMA=0.125, DMB=0.125, DMC=0.45

Step size = 180; # iterations = 540

Table 17^b

RRDE results in 2.0 M HCl
 15°C 6.22 mM CuCl₂ 62.4 mM H₂O₂

<u>ω</u>	<u>N</u>	<u>XKTC</u>	<u>k</u>
9.1	0.000	-----	-----
22	0.0042	0.724	64.8
36	0.143	0.456	66.8
63	0.040	0.223	57.2
90	0.064	0.200	73.3
138	0.105	0.137	76.8
182	0.133	0.107	79.3
224	0.154	0.089	80.8
257	0.168	0.079	83.0
282	0.179	0.073	83.2
286	0.181	0.071	83.0

$$k(\text{ave}) = 74.8 \pm 9.1$$

$$k(\text{Skinner}) = 140 \pm 15$$

b. ω (rad/sec), N = collection efficiency, k (M⁻¹sec⁻¹),

$$\text{XKTC} = \left\{ \frac{2kC_A^0}{\omega} \right\} \left(\frac{\nu}{D} \right)^{\frac{1}{3}} (0.51)^{-\frac{2}{3}}$$

$$D(\text{Cu}) = 5 \text{ E-}6 \text{ cm}^2/\text{sec}; D(\text{H}_2\text{O}_2) = 1.8 \text{ E-}5 \text{ cm}^2/\text{sec}$$

$$\nu = 0.01 \text{ cm}^2/\text{sec};$$

Electrode Radii: 100,110,143; M: 10.0

DMA=0.125, DMB=0.125, DMC=0.45

Step size = 180; # iterations = 540

Table 17^c

RRDE results in 2.0 M HCl

25°C 6.83 mM CuCl₂ 6.83 mM H₂O₂

<u>ω</u>	<u>N</u>	<u>XKTC</u>	<u>k</u>
9.1	0.0500	2.87	96.9
21	0.137	1.11	86.2
35	0.189	0.703	91.2
60	0.257	0.372	82.7
86	0.275	0.306	97.5
132	0.302	0.219	107
174	0.326	0.151	97.5
214	0.330	0.141	112
247	0.334	0.131	120
273	0.337	0.123	124
285	0.336	0.126	133

$$k(\text{ave}) = 104 \pm 16$$

$$k(\text{Skinner}) = 260 \pm 45$$

c. ω (rad/sec), N = collection efficiency, k (M⁻¹sec⁻¹),

$$\text{XKTC} = \left(\frac{2kC_A^0}{\omega} \right) \left(\frac{\nu}{D} \right)^{\frac{1}{3}} (0.51)^{-\frac{2}{3}}$$

$$D(\text{Cu}) = 5 \text{ E-}6 \text{ cm}^2/\text{sec}; \quad D(\text{H}_2\text{O}_2) = 1.8 \text{ E-}5 \text{ cm}^2/\text{sec}$$

$$\nu = 0.01 \text{ cm}^2/\text{sec};$$

Electrode Radii: 100, 110, 143; M: 1.0

DMA=0.125, DMB=0.125, DMC=0.45

Step size = 180; # iterations = 540

Table 17^d

RRDE results in 2.0 M HCl
 25°C 6.37 mM CuCl₂ 63.7 mM H₂O₂

<u>ω</u>	<u>N</u>	<u>XKTC</u>	<u>k</u>
9.1	0.000	-----	-----
21	0.000	-----	-----
35	0.0045	0.706	98.3
60	0.153	0.443	106
86	0.037	0.285	97.6
132	0.067	0.195	102
174	0.082	0.168	116
214	0.098	0.144	123
247	0.106	0.136	133
273	0.110	0.131	143
283	0.110	0.131	148

$$k(\text{ave}) = 118 \pm 19$$

$$k(\text{Skinner}) = 230 \pm 2$$

d. ω (rad/sec), N = collection efficiency, k (M⁻¹sec⁻¹),

$$\text{XKTC} = \left(\frac{2kC_A^0}{\omega} \right) \left(\frac{\nu}{D} \right)^{\frac{1}{3}} (0.51)^{-\frac{2}{3}}$$

$$D(\text{Cu}) = 5 \text{ E-}6 \text{ cm}^2/\text{sec}; D(\text{H}_2\text{O}_2) = 1.8 \text{ E-}5 \text{ cm}^2/\text{sec}$$

$$\nu = 0.01 \text{ cm}^2/\text{sec};$$

Electrode Radii: 100,110,143; M: 10.0

DMA=0.125, DMB=0.125, DMC=0.45

Step size = 180; # iterations = 540

Table 17^e

RRDE results in 2.0 M HCl

35°C 6.66 mM CuCl₂ 6.67 mM H₂O₂

<u>ω</u>	<u>N</u>	<u>XKTC</u>	<u>k</u>
9.0	0.0319	3.91	134
22	0.122	1.41	118
35	0.165	0.867	115
60	0.225	0.508	116
87	0.247	0.411	136
134	0.290	0.256	130
179	0.301	0.222	151
226	0.318	0.173	148
254	0.320	0.167	162
280	0.317	0.176	187
287	0.329	0.143	156

$$k(\text{ave}) = 141 \pm 22$$

$$k(\text{Skinner}) = 402 \pm 71$$

e. ω (rad/sec), N = collection efficiency, k (M⁻¹sec⁻¹),

$$\text{XKTC} = \left(\frac{2kC_A^0}{\omega} \right) \left(\frac{\nu}{D} \right)^{\frac{1}{3}} (0.51)^{-\frac{2}{3}}$$

$$D(\text{Cu}) = 5 \text{ E-}6 \text{ cm}^2/\text{sec}; D(\text{H}_2\text{O}_2) = 1.8 \text{ E-}5 \text{ cm}^2/\text{sec}$$

$$\nu = 0.01 \text{ cm}^2/\text{sec};$$

Electrode Radii: 100,110,143; M: 1.0

DMA=0.125, DMB=0.125, DMC=0.45

Step size = 180; # iterations = 540

Table 17^f

RRDE results in 2.0 M HCl
 35°C 6.25 mM CuCl₂ 58.0 mM H₂O₂

<u>ω</u>	<u>N</u>	<u>XKTC</u>	<u>k</u>
9.0	0.000	-----	---
35	0.00099	1.10	160
87	0.024	0.360	130
134	0.055	0.220	120
179	0.076	0.180	130
254	0.111	0.130	135
287	0.121	0.120	140

$$k(\text{ave}) = 135 \pm 13$$

$$k(\text{Skinner}) = 338 \pm 15$$

f. ω (rad/sec), N = collection efficiency, k (M⁻¹sec⁻¹),

$$XKTC = \left[\frac{2kC_A^0}{\omega} \right] \left(\frac{\nu}{D} \right)^{\frac{1}{3}} (0.51)^{-\frac{2}{3}}$$

$$D(\text{Cu}) = 5 \text{ E-}6 \text{ cm}^2/\text{sec}; \quad D(\text{H}_2\text{O}_2) = 1.8 \text{ E-}5 \text{ cm}^2/\text{sec}$$

$$\nu = 0.01 \text{ cm}^2/\text{sec};$$

Electrode Radii: 100, 110, 143; M: 10.0

DMA=0.125, DMB=0.125, DMC=0.45

Step size = 180; # iterations = 540

value for this system calculated previously by Skinner. These results imply that the mechanisms for the two systems are the same, and that the activation energy for copper is only about one-half the value for iron (9.65 kcal/mole) (163). Based on these recalculations, a reworking of the experiments for both the iron and the copper systems utilizing the catalytic program with the corrected stoichiometry, and diffusion coefficients is warranted to verify these results.

Listed in Table 18 is a calculation of the rate constant for the data of Geiger and Anson (160) measured in their study of the cobalt-cyclam catalysis of hydrogen peroxide disproportionation. The sum of the values at several concentrations was determined to be $2.1(\pm 0.4)E+3 \text{ M}^{-1} \text{ s}^{-1}$, which is in good agreement with the value determined by Espenson, $1.92 E+3 \text{ cm}^2/\text{sec}$ (161). The ease with which the RRDE data can be obtained and then fit with a simulation curve makes this a straightforward way of determining the rate constant when an electrochemical response can be measured.

The simulation programs can also aid in determining the experimental conditions necessary to make a meaningful measurement. They enable upper limits for rate constants to be set. For example, considering the mechanism studied above (this mechanism can also apply to the two-electron reduction of dioxygen to hydrogen peroxide by a metal catalyst) with equimolar concentrations of substrate and

Table 18

Simulated catalytic mechanism for a cobalt-cyclam
system using the data of Geiger and Anson.

Table 18^aRRDE results in 2.0 M HCli) 22°C 1.4 mM Co-cyclam 0.50 mM H₂O₂

ω	N	XKTC	k
10.5	0.067	5.40	±020
94.2	0.116	1.40	2390
262	0.145	0.50	2370

$$k(\text{ave}) = 2380 \pm 7$$

ii) 22°C 1.4 mM Co-cyclam 0.99 mM H₂O₂

ω	N	XKTC	k
10.6	0.029	6.20	1200
41.9	0.065	2.20	1700
94.2	0.092	1.10	2000
167	0.110	0.75	2300
262	0.120	0.59	2800

$$k(\text{ave}) = 2180 \pm 480$$

a. ω (rad/sec), N = collection efficiency, k (M⁻¹sec⁻¹),

$$XKTC = \left(\frac{2kC_A^0}{\omega} \right) \left(\frac{\nu}{D} \right)^{\frac{1}{3}} (0.51)^{-\frac{2}{3}}$$

$$D(\text{Co}) = 5 \text{ E-}6 \text{ cm}^2/\text{sec}; D(\text{H}_2\text{O}_2) = 1.8 \text{ E-}5 \text{ cm}^2/\text{sec}$$

$$\nu = 0.01 \text{ cm}^2/\text{sec};$$

$$\text{Electrode Radii: } 100, 104, 110; M(\text{i})=0.36; M(\text{ii})=0.71$$

$$\text{DMA}=0.125, \text{ DMB}=0.125, \text{ DMC}=0.45$$

$$\text{Step size} = 180; \# \text{ iterations} = 540$$

Table 18^b

iii) 22°C 1.4 mM Co-cyclam 0.99 mM H₂O₂

<u>ω</u>	<u>N</u>	<u>XKTC</u>	<u>k</u>
10.5	0.015	4.1	780
41.9	0.037	1.9	1400
94.2	0.060	1.1	1900
167	0.083	0.66	2000
262	0.102	0.44	2100

$$k(\text{ave}) = 1600 \pm 400$$

$$k(\text{ave, total}) = 2100 \pm 400$$

b. ω (rad/sec), N = collection efficiency, k (M⁻¹sec⁻¹),

$$\text{XKTC} = \left(\frac{2kC_A^0}{\omega} \right) \left(\frac{\nu}{D} \right)^{\frac{1}{3}} (0.51)^{-\frac{2}{3}}$$

$$D(\text{Co}) = 5 \text{ E-}6 \text{ cm}^2/\text{sec}; D(\text{H}_2\text{O}_2) = 1.8 \text{ E-}5 \text{ cm}^2/\text{sec}$$

$$\nu = 0.01 \text{ cm}^2/\text{sec};$$

Electrode Radii: 100, 104, 110; M: 1.4

DMA=0.125, DMB=0.125, DMC=0.45

Step size = 180; # iterations = 540

Co-cyclam = trans-[Co([14]aneN₄(OH₂)₂)]³⁺

catalyst, a detectable upper limit of roughly $k = 1 \text{ E}+6 \text{ M}^{-1} \text{ cm}^{-1}$ is found (ring current = 0.7 μ amps, [catalyst] = 1.00 mM , rotation rate = 3600 rpm, disk area = 0.458 cm^2 , collection efficiency = 0.176). The simulation shows that the limiting disk current is 5.20 times the uncatalyzed disk current, while the ring current is only 1.5% of the Levich ring current. For this rate constant, the disk limiting current will essentially remain constant at lower rotation rates and yield the limiting current given by the equation:

$$\left(\frac{i_{k,\text{lim}}}{i_{0,\text{lim}}}\right) = 1 + \left(\frac{x[S]}{[C]}\right) \left(\frac{D_S}{D_C}\right)^{\frac{1}{3}} \quad (76)$$

where,

$i_{k,\text{lim}}$ = limiting kinetic current

$i_{0,\text{lim}}$ = Levich current in the absence of kinetics

[S] = substrate concentration

[C] = catalyst concentration

D_S = diffusion coefficient of the substrate

D_C = diffusion coefficient of the catalyst

x = the number of catalytic species that react
with the substrate

Thus, a plot of the disk current vs. the square root of the rotation rate will be linear with a zero intercept, as is the case with the uncatalyzed case, but with a value 5.20 times that of the uncatalyzed reaction. By lowering the substrate to catalyst ratio to 0.36, then for the same rate constant used above, the disk current is 2.39 times the

uncatalyzed disk, and the ring current is 16% of the Levich ring current. The upper limit for the rate constant using the ring current (0.7 μ amps, ie. 1.5% of the Levich ring current) now becomes $5 \text{ E}+6 \text{ M}^{-1}\text{cm}^{-1}$. The disk current only goes up to 2.70 times the uncatalyzed disk current. This shows how the disk current is not very discriminating for very fast reactions, and that the ring current must be considered to accurately determine the rate constant. Higher values determined by use of the RRDE (164), should therefore be considered suspect and a careful re-examination of the experimental conditions and data needs to be considered.

As can be seen from these results, and in the characterization of the [34] dimer, the use of the simulation programs in conjunction with the RRDE is a very powerful means of quantitatively defining the electrochemical properties of a chemical system. The ease in changing parameters, and the straightforward correlation of real and simulated conditions by the finite difference method would seem to make this the method of choice for simulations. The combined use of these techniques is, therefore, advocated for the study of any kinetically complicated electrochemical system.

22. APPENDIX

A. PH TITRATION PROGRAM LISTING AND SAMPLE OUTPUT

The following section includes a listing of the program used for the titration curve plotted in Figure 6 as well as an example of the output generated by the program. The program requires that the HP 41-C calculator be configured with the quad memory module, the extended functions module and a printer. The storage of the program on magnetic cards is also recommended, thereby, necessitating the use of the magnetic card reader.

The calculator then must be configured as follows:

User mode: on
Size: 030
Printer: manual

To start the program:

XEQ TITRN

The calculator will then prompt for the following information, whereupon the information is entered and the program is restarted by pushing the Run/Stop button (R/S):

Acid Y/N
pKa =

Several pKa's can be accommodated by the program. After all of the pKa's have been entered, the 'A' button is pushed to

continue the program.

Volume<ML>=?

Normality= (of the titrated species)

Base Normality=?

Increment=iii.fffcc

where,

iii = the starting volume of base

fff = the final volume of base

cc = the increment of base added

After the increment has been entered the the R/S button pushed, the program will start to calculate the values for the pH titration.

The listing is given in Figure 42.

Figure 42

Program listing and output for pH titration simulation

Figure 42

01*LBL "TITRN"	47 ST+ 25	93 FRA	139 STO 25
02 FIX 3	48 112	94 CLA	140 ISG 25
03 "*****"	49 XTOA	95 ADV	141 RCL IND 25
04 112	50 "K _a ="	96 STO 21	142 RCL 20
05 XTOA	51 PROMPT	97 RCL 25	143 +
06 "PH TITRATION"	52 FIX 2	98 1	144 .5
07 "I *****"	53 ARCL X	99 +	145 ST- 25
08 XEQ "PRA"	54 XEQ "PRA"	100 STO 00	146 RDN
09 CLA	55 CLA	101 0	147 DSE 25
10 ADV	56 CHS	102 "INCREMENT="	148 RCL 25
11 "ACID Y/N"	57 10IX	103 "HIII.FFFCC"	149 RCL 22
12 AGN	58 STO IND 25	104 PROMPT	150 *
13 PROMPT	59 GTO E	105 STO 27	151 -
14 AOFF	60*LBL A	106 CLA	152 RCL IND 25
15 ASTO X	61 "VOLUME"	107*LBL B	153 *
16 "Y"	62 "K<ML>=?"	108 ARCL 26	154 1 E-14
17 ASTO Y	63 PROMPT	109 "HBASE="	155 -
18 CF 00	64 STO 23	110 RCL 27	156*LBL b
19 X=Y?	65 -6	111 INT	157 DSE 25
20 SF 00	66 AROT	112 FIX 0	158 GTO 00
21 CLRG	67 ASHF	113 ARCL X	159 RCL 07
22 CLA	68 X<>Y	114 1 E-3	160 X<> 25
23 12	69 "I="	115 *	161 X<>Y
24 XTOA	70 FIX 3	116 CF 02	162 RCL 25
25 100	71 ARCL X	117 X=0?	163 10
26 XTOA	72 32	118 SF 02	164 +
27 32	73 XTOA	119 RCL 21	165 RDN
28 XTOA	74 109	120 X<>Y	166 STO IND T
29 ASTO 26	75 XTOA	121 *	167 DSE 07
30 CLA	76 100	122 LASTX	168 GTO c
31 32	77 XTOA	123 RCL 23	169 RCL 00
32 XTOA	78 XEQ "PRA"	124 +	170 STO 25
33 32	79 CLA	125 /	171 RCL 01
34 XTOA	80 "MOLARITY="	126 STO 20	172 RCL 20
35 112	81 PROMPT	127 RCL 24	173 +
36 XTOA	82 ENG 3	128 LASTX	174 STO 10
37 72	83 ARCL X	129 /	175 RCL 01
38 XTOA	84 XEQ "PRA"	130 STO 22	176 RCL 22
39 61	85 CLA	131 R↑	177 *
40 XTOA	86 RCL 23	132 STO 00	178 SQR
41 32	87 *	133 RCL 00	179 FS?C 02
42 XTOA	88 STO 24	134 STO 07	180 GTO 01
43 ASTO 18	89 "BASE"	135*LBL c	181 GTO B
44 CLA	90 "NORMALITY="	136 RCL 07	182*LBL 00
45*LBL E	91 PROMPT	137 .5	183 RCL IND 25
46 1	92 ARCL X	138 +	184 *

--continued on the next page--

Figure 42

185 GTO b	231 ABS	277 RCL 10	<p>**** pH TITRATION ****</p> <p>pKa= 10.30 VOLUME= 25.000 ml MOLARITY= 500.0E-6 BASE NORMALITY= 110.0E-3</p> <p>μl BASE= 0 pH= 6.73 μl BASE= 5 pH= 8.81 μl BASE= 10 pH= 9.12 μl BASE= 15 pH= 9.30 μl BASE= 20 pH= 9.44 μl BASE= 25 pH= 9.55 μl BASE= 30 pH= 9.63 μl BASE= 35 pH= 9.71 μl BASE= 40 pH= 9.78 μl BASE= 45 pH= 9.84 μl BASE= 50 pH= 9.90 μl BASE= 55 pH= 9.95 μl BASE= 60 pH= 9.99 μl BASE= 65 pH= 10.04 μl BASE= 70 pH= 10.08 μl BASE= 75 pH= 10.12 μl BASE= 80 pH= 10.16 μl BASE= 85 pH= 10.19 μl BASE= 90 pH= 10.22 μl BASE= 95 pH= 10.26 μl BASE= 100 pH= 10.29</p>
186+LBL a	232 1	278 4	
187 2	233 X<=Y?	279 XEQ 06	
188 FS? 00	234 SF 02	280 RCL 11	
189 CHS	235 RCL 09	281 3	
190 ST+ 00	236 FS?C 02	282 XEQ 06	
191+LBL B	237 GTO 01	283 RCL 12	
192 RCL 08	238 LOG	284 2	
193 XEQ d	239 CHS	285 XEQ 06	
194 CHS	240 XEQ d	286 RCL 13	
195 10IX	241 ARCL 10	287 XEQ 08	
196+LBL 01	242 FIX 2	288 RCL 13	
197 ENTER↑	243 ARCL X	289 XEQ 07	
198 ENTER↑	244 PRA	290 RCL 14	
199 GTO IND 25	245 CLA	291 GTO 09	
200+LBL 05	246 ISG 27	292+LBL 03	
201 6	247 GTO B	293 4	
202 *	248 STOP	294 *	
203 RCL 10	249+LBL d	295 RCL 10	
204 5	250 FS? 00	296 3	
205 XEQ 06	251 RTN	297 XEQ 06	
206 RCL 11	252 14	298 RCL 11	
207 4	253 X<>Y	299 2	
208 XEQ 06	254 -	300 XEQ 06	
209 RCL 12	255 RTN	301 RCL 12	
210 3	256+LBL 06	302 XEQ 08	
211 XEQ 06	257 *	303 RCL 13	
212 RCL 13	258+LBL 07	304 GTO 09	
213 2	259 +	305+LBL 02	
214 XEQ 06	260 *	306 3	
215 RCL 14	261 RTN	307 *	
216 XEQ 08	262+LBL 08	308 RCL 10	
217 RCL 13	263 +	309 2	
218 XEQ 07	264 STO 16	310 XEQ 06	
219 RCL 14	265 CLX	311 RCL 11	
220 XEQ 07	266 RCL 10	312 SF 02	
221 RCL 15	267 XEQ 07	313 GTO 08	
222+LBL 09	268 RCL 11	314 .END.	
223 +	269 XEQ 07		
224 RCL 16	270 RCL 12		
225 /	271 FS?C 02		
226 -	272 GTO 09		
227 X<0?	273 GTO 07		
228 GTO a	274+LBL 04		
229 STO 09	275 5		
230 %CH	276 *		

B. CATALYTIC PROGRAM LISTING AND SAMPLE OUTPUT

The basic program first described by Bard and Prater (52-54) was used and modified. The following information must be input as a batch file to run the program, or else it is input as it is prompted on a monitor (default values are in parenthesis):

Step size (50):

Iteration limit (150):

Convergence criterion of the disk current (E-4):

Diffusion coefficient for species A, B, C: maximum of 0.45

Substrate:Catalyst ratio = $M = C/A$:

Low limit for XKTC (0.0):

High Limit for XKTC (10.0):

XKTC increment (10.0/M):

Electrode Radii: --IR1,IR2,IR3-- must be integers

Stoichiometric factor: for $x\text{B} + \text{C} \rightarrow \text{A}$

The program then starts running and the data is output onto the user-assigned device, or data file.

The program is annotated to describe the function of each section of the program and follows in Figure 43 with a sample output that also lists the concentration of the three species, A, B, C above the disk.

Figure 43

Catalytic program listing and output

Figure 43

```

c      PROGRAM CATALYTIC-3
c      This program simulates a catalytic mechanism where the chemical
c      step involves the disk product B reacting with substrate C
c      to regenerate species A. This simulation uses only one box
c      for the disk. Controlled potential step to the limiting current
c      plateau at the disk.
c
c      A + e --> B          at the disk
c      xB + C --> A
c
c      B - e --> A          at the ring
c
c      dimension fa(25,100),fb(25,100),fc(25,100),
c      *      fj(25),xdif(25),rdif(25,100),ik(25,100),ikk(25,100)
c
c      real m
c
c      8      format(f12.6)
c      9      format(i)
c
c      10     type '( Step size (50): %s)'
c      read (5,9,end=2000),l
c      if (l .eq. 0)l=50
c
c      type '( Iteration limit (150; -1=infinite): %s)'
c      accept q,limit
c      if (limit .eq. 0) limit=150
c      if (limit .lt. 0) limit=2**30+(2**30-1)
c
c      type '( Convergence criterion of disk current(e-4): %s)'
c      accept p,conv
c      if (conv .eq. 0.) conv=0.1e-3
c
c      type '( Diffusion coefficient for species A,B,C: %s)'
c      accept *,dma,dmb,dnc
c
c      type '( Substrate:Catalyst ratio (C/A=M): %s)'
c      accept s,m
c      if (m .eq. 0.) m=1.000001
c      if (m .eq. 1.0) m=1.000001
c
c      type '( Low limit for XKTC (C.0): %s)'
c      accept s,xktclow
c
c      11     type '( High limit for XKTC (10./M; -1.=low limit): %s)'
c      accept s,xktchigh
c      if (xktchigh .eq. 0.)xktchigh=10./m
c      if (xktchigh .lt. 0.)xktchigh=xktclow
c      if (xktchigh .lt. xktclow) goto 11
c
c      12     type '( XKTC Increment ((high limit-low limit)/10): %s)'
c      accept s,xktcincr
c      if (xktcincr .le. 0.)xktcincr=(xktchigh-xktclow)/10.
c      if (xktcincr .eq. 0)goto 12
c
c      type '( Electrode radii: %s)'
c      accept *,ir1,ir2,ir3
c
c      type '( Stoichiometric factor (xB + C --> A): %s)'
c      accept s,bccoeff
c      if (bccoeff .eq. 0)bccoeff=1.
c
c      Initialize the variables and start the program.
c      x1=1
c      jmaxm=0
c      za=sqrt(x1/dma)
c      zr=0.
c      znorw=0.62/(0.51)**(1.0/3.0)
c
c      convection velocity normal to the electrode.
c      vnaut=1./sqrt(dma*x1**3)
c
c      Define the electrode regions.
c      ir4=ir3+10
c      k2c=ir2-ir1+1
c      k3i=k20+1
c      k30=ir3-ir1+1
c      k4i=k3c+1
c      k4c=ir4-ir1+1
c      k5=k40-1
c      r1=ir1
c
c      Disk area.
c      ad=(r1-.5)**2

```

--continued on the next page--

Figure 43

```

zdanor=dma*za
zrbnor=dmb*za/ad
* type 1010,ir1,ir2,ir3,i,limit,conv,dma,dmb,dmc,m,
  bccoeff,xktclow,xktchigh,xktcincr
* write(6,1010)ir1,ir2,ir3,i,limit,conv,dma,dmb,dmc,m,
  bccoeff,xktclow,xktchigh,xktcincr
1010 format(' ', 'CATALYTIC SIMULATION-3',/,
  qx, 'A + e --> B at the disk',/,
  rx, 'xB + C --> A',/,
  qx, 'B - e --> A at the ring',/,
  ' SIMULATION PARAMETERS',/,
  ' RRDE with R1=',15,3x,'R2=',15,3x,'R3=',15,/,
  ' Step size=',15,2x,'Maximum # of steps=',15,
  2x,'Convergence:',G10.2,/,
  ' x',DMA=',f10.6,5x,'DMB=',f10.6,5x,'DMC=',f10.6,/,
  ' Substrate:Catalyst (M=C/A ratio)=',f7.3,/,
  ' Stoichiometry factor: (xB + C --> A)=',f6.3,/,
  ' XKTC=',f12.6,' to ',f12.6,' by steps of ',f12.6,/,/,
  ' XKTC',7x,' 7D ',5x,' ZR ',5x,' ZRatio ',
  3x,'Convergence')
c Calculate ZR,ZD,and ZRatio for each value of XKTC.
do 999 xktc=xktclow,xktchigh,xktcincr
  xktc1=xktc/x1
  jmax=24
c Effects of convection normal to the electrode.
do 87 j=1,jmax
  xj=j-1
  xj=xj/(1.-(1.11*vnaut*xj))
  jj=xj+1.
  dj=j-1
  xd(f(j))=xjj-djj
  jj(j)=jj
82 continue
c Effects of radial convection.
do 92 j=1,jmax
  xj=j-1
  do 91 k=1,k40
    rk=k-2+ir1
    rkk=rk/exp(1.03*vnaut*xj)
    kk=rkk+1.
    dkk=kk-1
    rdif(j,k)=rkk-dkk
    ff(kk-ir1)93,94,94
93 ik(j,k)=1
    ikk(j,k)=1
    goto 91
94 ik(j,k)=kk-ir1+1
    ikk(j,k)=ikk(j,k)+1
91 continue
92 continue
c Initial conditions.
do 150 j=1,25
  do 140 k=1,k40
    fa(j,k)=1.
    fb(j,k)=0.
    fc(j,k)=m
140 continue
150 continue
c Change the boundary conditions at the disk at the
c initiation of electrolysis for a potential step
c to the limiting current plateau.
fa(1,1)=0.
fb(1,1)=1.
fc(1,1)=m
zd=1./x1
zold=0.
c Start the iterations.
do 999 i=2,limit
c Update the boundary conditions at the disk
c due to diffusion.
zold=zd
fb(1,1)=fb(1,1)+dma*fa(2,1)-dmb*(fb(1,1)-fb(2,1))
fc(1,1)=fc(1,1)-dmc*(fc(1,1)-fc(2,1))

```

--continued on the next page--

Figure 43

```

c      Update the boundary conditions at the ring
c      due to diffusion.
do 210 k=k31,k30
  fa(1,k)=fa(1,k)+dmb*fb(2,k)-dma*(fa(1,k)-fa(2,k))
  fb(1,k)=0.
  fc(1,k)=fc(1,k)-dmc*(fc(1,k)-fc(2,k))
210  continue

c      Update the gap region at the electrode
c      due to diffusion.
do 220 k=2,k20
  fa(1,k)=fa(1,k)-dma*(fa(1,k)-fa(2,k))
  fb(1,k)=fb(1,k)-dmb*(fb(1,k)-fb(2,k))
  fc(1,k)=fc(1,k)-dmc*(fc(1,k)-fc(2,k))
220  continue

c      Update the region past the ring at the
c      electrode due to diffusion.
do 230 k=k4i,k40
  fa(1,k)=fa(1,k)-dma*(fa(1,k)-fa(2,k))
  fb(1,k)=fb(1,k)-dmb*(fb(1,k)-fb(2,k))
  fc(1,k)=fc(1,k)-dmc*(fc(1,k)-fc(2,k))
230  continue

c      Update the remaining layers for
c      diffusion effects.
do 340 k=1,k40
  dropa=fa(2,k)+dma*(fa(3,k)-2.*fa(2,k)+fa(1,k))
  dropb=fb(2,k)+dmb*(fb(3,k)-2.*fb(2,k)+fb(1,k))
  dropc=fc(2,k)+dmc*(fc(3,k)-2.*fc(2,k)+fc(1,k))
  jmax=23
  j=3
  do while (j .le. jmax)
    dripa=fa(j,k)+dma*(fa(j+1,k)-2.*fa(j,k)+fa(j-1,k))
    dripb=fb(j,k)+dmb*(fb(j+1,k)-2.*fb(j,k)+fb(j-1,k))
    dripc=fc(j,k)+dmc*(fc(j+1,k)-2.*fc(j,k)+fc(j-1,k))
    fa(j-1,k)=dropa
    fb(j-1,k)=dropb
    fc(j-1,k)=dropc
    dropa=dripa
    dropb=dripb
    dropc=dripc
    if((dropa-.999999) .eq. 0.)then
      jmax=j+1
    else if ((dropa-.999999) .gt. 0.)then
      jmax=j
      if((jmax-jmax).gt. 0) jmax=jmax
      goto 340
    else
      jmax=j+1
    endif
  340  j=j+1
  end do
  fa(jmax,k)=dropa
  fb(jmax,k)=dropb
  fc(jmax,k)=dropc
350  continue

c      Update for convection normal to the electrode.
do 102 j=1,jmaxm
  jj=i(j)
  jjj=jj+1
  do 101 k=1,k40
    fa(j,k)=fa(j,j,k)+(fa(j,jj,k)-fa(j,j,k))*xdif(j)
    fb(j,k)=fb(j,j,k)+(fb(j,jj,k)-fb(j,j,k))*xdif(j)
    fc(j,k)=fc(j,j,k)+(fc(j,jj,k)-fc(j,j,k))*xdif(j)
101  continue
102  continue

c      Update for radial convection.
do 202 j=1,jmaxm
  do 201 kinv=1,k5
    k=k40-kinv
    kk=ik(j,k)
    kkk=ikk(j,k)
    fa(j,k)=fa(j,kk)+(fa(j,kkk)-fa(j,kk))*rdif(j,k)
    fb(j,k)=fb(j,kk)+(fb(j,kkk)-fb(j,kk))*rdif(j,k)
    fc(j,k)=fc(j,kk)+(fc(j,kkk)-fc(j,kk))*rdif(j,k)
201  continue
202  continue

c      Update for the kinetics.
do 400 k=1,k40
  do 480 j=1,jmaxm
    ff(fb(j,k))480,480,410

```

--continued on the next page--

Figure 43

```

410      If (fc(j,k)) 480,480,420
420      del=xk*ci+fb(j,k)*fc(j,k)
      Yb(j,k)=fb(j,k)-del
      fc(j,k)=fc(j,k)-del/bccoeff
      fa(j,k)=fa(j,k)+del
480      continue
490      continue

c      Calculate the disk current.
      zd=fa(2,1)*zdanor+fa(1,1)*za/2.0
      fb(1,1)=fb(1,1)+fa(1,1)
      fa(1,1)=0.

c      Calculate the ring current.
      zr=0.
      do 510 k=k31,k30
          rk=k-2+ir1
          zr=zr+(((rk+.5)**2)-((rk-.5)**2))*fb(2,k)*zrbnor
510      continue

c      Calculate the ZRatio.
      zratio=zr/zd

      If(abs(zd-zold) .le. conv) goto 9998

999      continue

9998     type 1510,xk*ci,zd/znorw,zr,zratio,zd-zold
1510     write(6,1510)xk*ci,zd/znorw,zr,zratio,zd-zold
      format(' ',f10.3,5x,4(f10.6,5x),6l0.3)

9999     continue
2000     stop
      end

```

--continued on the next page--

Figure 43

CATALYTIC SIMULATION-3

A + e --> P at the disk
 xR + C --> A
 B - e --> A at the ring

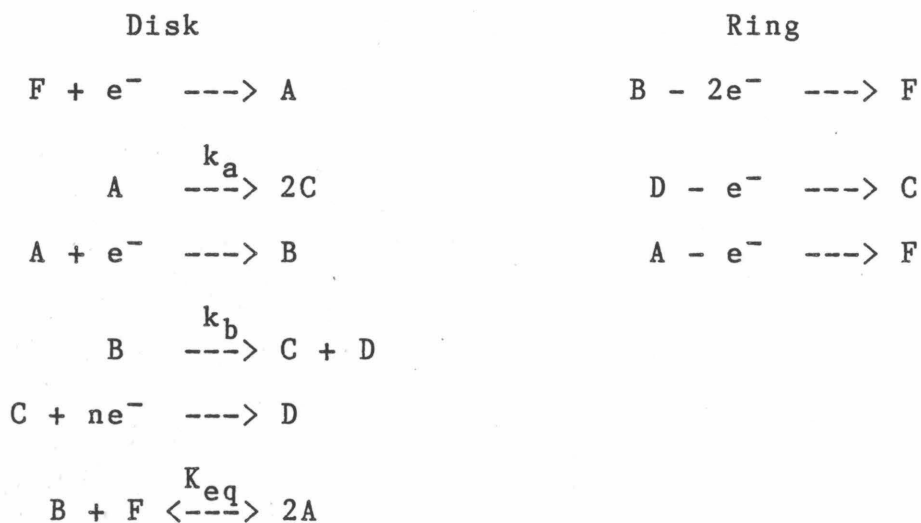
SIMULATION PARAMETERS

PRDF with R1= 100 R2= 104 R3= 110
 Step size= 50 Maximum # of steps= 150 Convergence: 0.10E-03
 CMA= 0.450000 DMR= 0.450000 CMC= 0.450000
 Substrate:Catalyst (M=C/A ratio)= 1.000
 Stoichiometry factor: (xR + C --> A)= 2.000
 XKTC= 0.000000 to 100.000000 by steps of 50.000000

XKTC	ZD	ZP	ZRatio	Convergence
0.000	1.001489	0.1364C7	0.175519	-C.000097
fa(j,1)	fb(j,1)	fc(j,1)		
0.000000	1.000000	1.000001		
0.163241	C.236159	1.000001		
0.325969	0.674031	1.000001		
0.481612	C.512389	1.000001		
0.623945	0.376056	1.000001		
0.745287	C.254113	1.000001		
0.842765	0.157735	1.000001		
0.911483	C.022517	1.000001		
0.955947	C.044053	1.000001		
0.981021	C.018969	1.000001		
0.993171	C.C06829	1.000001		
0.998052	0.001948	1.000001		
0.999600	0.000400	1.000001		
0.999953	C.C00047	1.000001		
0.999999	0.000001	1.000001		
1.000000	0.000000	1.000001		
50.000	2.844281	0.002247	0.004008	-0.C00093
fa(j,1)	fb(j,1)	fc(j,1)		
0.000000	1.000000	0.045272		
0.419772	0.580229	C.090806		
0.712157	0.281844	0.174105		
0.891162	0.108838	0.310250		
0.967257	0.032743	0.477034		
0.992252	C.007749	C.639591		
0.998519	0.001481	0.774884		
0.999765	C.000235	0.873735		
0.999968	0.000032	0.937567		
0.999996	C.000004	C.973661		
1.000000	0.000000	C.991072		
1.000000	0.000000	C.998314		
1.000000	0.000000	1.000001		
1.000000	C.000000	1.000001		
1.000000	C.000000	1.000001		
1.000000	C.000000	1.000001		
1.000000	C.000000	1.000001		
100.000	2.936168	0.002993	0.001314	-C.000093
fa(j,1)	fb(j,1)	fc(j,1)		
0.000000	1.000000	0.019720		
C.447241	C.552759	C.052272		
0.769327	0.230674	C.131162		
0.935509	C.064491	C.277890		
0.988518	0.011482	0.461636		
0.992661	C.C01339	0.636725		
0.999891	0.000109	0.778624		
0.999993	C.000007	C.881070		
1.000000	0.000000	0.946764		
1.000000	C.000000	C.984596		
1.000000	0.000000	1.000001		
1.000000	C.000000	1.000001		
1.000000	0.000000	1.000001		
1.000000	C.000000	1.000001		
1.000000	C.000000	1.000001		
1.000000	C.000000	1.000001		
1.000000	C.000000	1.000001		

C. SCHEME X PROGRAM LISTING AND SAMPLE OUTPUT

The listing of this program is included as an example of the type of complicated electrochemical systems that can be accommodated by this simulation technique. The mechanism that was simulated is listed below:



The values for k_a and K_{eq} are input as constants and the value of k_b is varied by the program. The same general pattern for the input of data is followed for this program as for the catalytic program. This program also includes the added, and labelled section that takes the homogeneous electron transfer reaction into account. If the homogeneous reaction were to yield two different species (say x and a), instead of the example listed here where both products are the same, then the program is written such that one of the two $fa(j,k)$ terms is converted into $fx(j,k)$. An example of the integrated form of the rate expression is also used by this program.

Figure 44

Scheme X program listing and sample output

Figure 44

```

vnaut=1./sqrt(dma*xl**3)
c Define the electrode regions.
lr4=lr3+10
k20=lr2-ir1+1
k31=k20+1
k30=lr3-ir1+1
k47=k30+1
k40=lr4-ir1+1
k5=k40-1
r1=ir1
c Disk area.
ad=(r1-.5)**2
zdanor=dma*za
zdfnor=dmf*za
zdcnor=dmc*za
zrdnor=dmd*za/ad
zrbnor=dmb*za/ad
zranor=dma*za/ad
* type 1C10,xk,n,xkeq,ir1,ir2,ir3,l,limit,conv,n,dma,
  * dnb,dmc,dmd,dmf,xktlow,xkthigh,xktincr
* write(6,1010)xk,n,xkeq,ir1,ir2,ir3,l,limit,conv,n,
  * dma,dnb,dmc,dmd,dmf,xktlow,xkthigh,xktincr
1C10 format(' ','ECECE-KIET SIMULATION',/,
  * 9x,'F + e --> A at the disk',/,
  * 13x,'A --> 2C fixed dimensionless rate, k=',g10.3,/,
  * 9x,'A + e --> B',/,
  * 17x,'A --> C + D',/,
  * 9x,'C + l1,e --> D',/,
  * 9x,'B + F <--> A + A Keq=',g10.3,/,/,
  * 9x,'D - e --> C at the ring',/,
  * 9x,'B -2e--> F',/,
  * 9x,'A - e --> F',/,
  * ' SIMULATION PARAMETERS',/,
  * ' RDE with R1=',14,' R2=',14,' R3=',14,/,
  * ' Step size=',15,2x,'Maximum # of steps=',110,
  * 2x,'Convergence: ',G10.2,/,
  * 2x,'n=',11,/,
  * 5x,'DMA=',f6.3,5x,'DMR=',f6.3,5x,'DMC=',f6.3,
  * 5x,'DMD=',f6.3,5x,'DMF=',f6.3,/,
  * 'XKT=',f10.3,' to ',f10.3,' by steps of ',f10.3,/,/,
  * 6x,'XKT',12x,'ZD',13x,'ZR',11x,'ZRATIO',5x,'CONVERGENCE')
c Calculate ZR,ZD,and ZRatio for each value of XKTC.
do 999 xkt=xktlow,xkthigh,xktincr
  xktl=xkt/xl
  xk1=xk/xl
  jmax=24
c Effects of convection normal to the electrode.
do 92 j=1,jmax
  xj=j-1
  xjj=xj/(1.-(1.11*vnaut*xj))
  jj=xjj+1
  djj=jj-1
  xdf(j)=xjj-djj
  j(j)=jj
82 continue
c Effects of radial convection.
do 92 j=1,jmax
  xj=j-1
  do 91 k=1,k40
    rk=k-2+ir1
    rkk=rk/exp(1.03*vnaut*xj)
    kk=rkk+1.
    dkk=kk-1
    rdiff(j,k)=rkk-dkk
    if(kk-ir1)93,94,94
  93 ik(j,k)=1
    ikk(j,k)=1
    goto 91
  94 ik(j,k)=kk-ir1+1
    ikk(j,k)=ikk(j,k)+1
  91 continue
  92 continue
c Initial conditions.
do 150 j=1,25
  do 140 k=1,k40

```

--continued on the next page--

Figure 44

```

      ff(j,k)=1.
      fa(j,k)=0.
      fb(j,k)=0.
      fc(j,k)=0.
      fd(j,k)=0.
140      continue
150      continue

c      Change the boundary conditions at the disk at the
c      initiation of electrolysis for a potential step
c      to the limiting current plateau for the second
c      electrolysis step.

      ff(1,1)=0.
      fa(1,1)=0.
      fb(1,1)=1.
      fc(1,1)=0.
      fd(1,1)=0.

      zd=1./xi
      zoid=0.

c      Start the iterations.
      do 999 i=2,limit

c      Update the boundary conditions at the disk
c      due to diffusion.
      zoid=zd
      fb(1,1)=fb(1,1)+dmf*ff(2,1)+dma*fa(2,1)-dmb*(fb(1,1)-fb(2,1))
      fd(1,1)=fd(1,1)+dmc*fc(2,1)-dmd*(fd(1,1)-fd(2,1))

c      Update the boundary conditions at the ring
c      due to diffusion.
      do 210 k=k31,k30
      fa(1,k)=0.
      fb(1,k)=0.
      fc(1,k)=fc(1,k)+dmd*fd(2,k)-dmc*(fc(1,k)-fc(2,k))
      fd(1,k)=0.
210      ff(1,k)=ff(1,k)+dma*fa(2,k)+dmb*fb(2,k)-dmf*(ff(1,k)-ff(2,k))
      continue

c      Update the gap region at the electrode
c      due to diffusion.
      do 220 k=2,k20
      fa(1,k)=fa(1,k)-dma*(fa(1,k)-fa(2,k))
      fb(1,k)=fb(1,k)-dmb*(fb(1,k)-fb(2,k))
      fc(1,k)=fc(1,k)-dmc*(fc(1,k)-fc(2,k))
      fd(1,k)=fd(1,k)-dmd*(fd(1,k)-fd(2,k))
220      ff(1,k)=ff(1,k)-dmf*(ff(1,k)-ff(2,k))
      continue

c      Update the region past the ring at the
c      electrode due to diffusion.
      do 230 k=k41,k40
      fa(1,k)=fa(1,k)-dma*(fa(1,k)-fa(2,k))
      fb(1,k)=fb(1,k)-dmb*(fb(1,k)-fb(2,k))
      fc(1,k)=fc(1,k)-dmc*(fc(1,k)-fc(2,k))
      fd(1,k)=fd(1,k)-dmd*(fd(1,k)-fd(2,k))
230      ff(1,k)=ff(1,k)-dmf*(ff(1,k)-ff(2,k))
      continue

c      Update the remaining layers for
c      diffusion effects.
      do 350 k=1,k40
      dropa=fa(2,k)+dma*(fa(3,k)-2.*fa(2,k)+fa(1,k))
      dropb=fb(2,k)+dmb*(fb(3,k)-2.*fb(2,k)+fb(1,k))
      dropc=fc(2,k)+dmc*(fc(3,k)-2.*fc(2,k)+fc(1,k))
      dropd=fd(2,k)+dmd*(fd(3,k)-2.*fd(2,k)+fd(1,k))
      dropf=ff(2,k)+dmf*(ff(3,k)-2.*ff(2,k)+ff(1,k))
      jmax=23
      j=3
      do while (j .le. jmax)
      dripa=fa(j,k)+dma*(fa(j+1,k)-2.*fa(j,k)+fa(j-1,k))
      dripb=fb(j,k)+dmb*(fb(j+1,k)-2.*fb(j,k)+fb(j-1,k))
      dripc=fc(j,k)+dmc*(fc(j+1,k)-2.*fc(j,k)+fc(j-1,k))
      dripd=fd(j,k)+dmd*(fd(j+1,k)-2.*fd(j,k)+fd(j-1,k))
      dripf=ff(j,k)+dmf*(ff(j+1,k)-2.*ff(j,k)+ff(j-1,k))
      fa(j-1,k)=dropa
      fb(j-1,k)=dropb
      fc(j-1,k)=dropc
      fd(j-1,k)=dropd
      ff(j-1,k)=dropf
      dropa=dripa
      dropb=dripb
      dropc=dripc

```

--continued on the next page--

Figure 44

```

dropd=drifd
dropf=drifd
if((dropf-.999999).eq. 0.)then
  jmax=j+1
else if ((dropf-.999999).gt. 0.)then
  jmax=j
if((jmax-jmax).gt. 0) jmax=jmax
goto 340
else
  jmax=j+1
endif
340  j=j+1
      end do
      fa(jmax,k)=dropa
      fb(jmax,k)=dropb
      fc(jmax,k)=dropc
      fd(jmax,k)=dropd
      ff(jmax,k)=dropf
350  continue
c    Update for convection normal to the electrode.
do 102 j=1,jmax
  j1=j
  j2=j+1
  do 101 k=1,k40
    fa(j,k)=fa(j1,k)+(fa(j1,k)-fa(j2,k))*xdif(j)
    fb(j,k)=fb(j1,k)+(fb(j1,k)-fb(j2,k))*xdif(j)
    fc(j,k)=fc(j1,k)+(fc(j1,k)-fc(j2,k))*xdif(j)
    fd(j,k)=fd(j1,k)+(fd(j1,k)-fd(j2,k))*xdif(j)
    ff(j,k)=ff(j1,k)+(ff(j1,k)-ff(j2,k))*xdif(j)
101  continue
102  continue
c    Update for radial convection.
do 202 j=1,jmax
  do 201 kinv=1,k5
    k=k40-kinv
    kk=k(j,k)
    kkk=kk(j,k)
    fa(j,k)=fa(j,kk)+(fa(j,kkk)-fa(j,kk))*rdif(j,k)
    fb(j,k)=fb(j,kk)+(fb(j,kkk)-fb(j,kk))*rdif(j,k)
    fc(j,k)=fc(j,kk)+(fc(j,kkk)-fc(j,kk))*rdif(j,k)
    fd(j,k)=fd(j,kk)+(fd(j,kkk)-fd(j,kk))*rdif(j,k)
    ff(j,k)=ff(j,kk)+(ff(j,kkk)-ff(j,kk))*rdif(j,k)
201  continue
202  continue
c    Update for the heterogeneous kinetics.
if((xkeq.lt.1.0000001).and.(xkeq.gt.0.999999)) goto610
do 660 k=1,k40
  do 670 j=1,jmax
    a=(xkeq-1.0)
    b=(fa(j,k)+fa(j,k)+xkeq*(fb(j,k)+ff(j,k)))
    c=(xkeq*fb(j,k)+ff(j,k)-fa(j,k)*fa(j,k))
    delta=(-b+sqrt((b**2.0)-4.0*a*c))/(2.0*a)
    fa(j,k)=fa(j,k)-delta
    fb(j,k)=fb(j,k)+delta
    ff(j,k)=ff(j,k)+delta
    fa(j,k)=fa(j,k)-delta
670  continue
660  continue
    goto 679
  do 620 k=1,k40
    do 630 j=1,jmax
      delta=(fa(j,k)*fa(j,k)-fb(j,k)*ff(j,k))/
        (fa(j,k)+fb(j,k)+ff(j,k)+fa(j,k))
      fa(j,k)=fa(j,k)-delta
      fb(j,k)=fb(j,k)+delta
      ff(j,k)=ff(j,k)+delta
      fa(j,k)=fa(j,k)-delta
630  continue
620  continue
c    Update for the kinetics of A-> 2C using the supplied value.
do 879 k=1,k40
  do 881 j=1,jmax
    fff(fa(j,k))880,880,885
    delxk=fa(j,k)*(1.0-exp(-xk1))
    fa(j,k)=fa(j,k)-delxk
    fc(j,k)=fc(j,k)+2.0*delxk
881  continue
880  continue
c    Update for the kinetics using the solution for the
c    first order differential equation.

```

--continued on the next page--

Figure 44

```

do 490 k=1,k40
do 480 j=1,jmax
  if(fb(j,k))480,480,410
410  del=fb(j,k)*(1.0-exp(-xkt))
460  fb(j,k)=fb(j,k)-del
  fc(j,k)=fc(j,k)+del
  fd(j,k)=fd(j,k)+del
480  continue
490  continue

c Calculate the disk current.
zdzd=ff(2,1)*zdfnor*2.0+fa(2,1)*zdanor+n*fc(2,1)*zdcnor+
* (n*fc(1,1)+fa(1,1)+ff(1,1)*2.0)*za/2.
  fd(1,1)=fd(1,1)+fc(1,1)
  fb(1,1)=fb(1,1)+fa(1,1)+ff(1,1)
  fc(1,1)=0.
  fa(1,1)=0.
  ff(1,1)=0.

c Calculate the ring current.
zr=0.
do 510 k=k31,k30
  rk=k-2+ir1
  zr=zr+(((rk+.5)**2)-((rk-.5)**2))*((fd(2,k)*zrdnor
* +fb(2,k)*zrbnor*2.0+zranor*fa(2,k))
* +(fa(1,k)+fb(1,k)*2.0)*za/2.0*ad)
510  continue

c Calculate the ZRatio.
zratio=zr/zd

999  if(abs(zd-zold) .le. conv)goto 9998
continue

9998  type 1510,xkt,zd/znorm,zr,zratio,zd-zold
1510  write(6,1510)xkt,zd/znorm,zr,zratio,zd-zold
format(' ',f10.3,5x,4(f10.6,'x'),G10.3)

9999  continue
2000  stop
end

```

--continued on the next page--

Figure 44

```

ECECE-KIFT SIMULATION
  F + e --> A      at the disk
  A + e --> 2C     fixed dimensionless rate, k= 20.0
  C + 1e --> D
  B + F <--> A + A      Keq= 0.100E+04
  D - e --> C      at the ring
  R - 2e --> F
  A - e --> F

SIMULATION PARAMETERS
RRDE with R1= 100 R2= 104 R3= 110
Step size= 75 Maximum # of steps= 225 Convergence: 0.10E-03
n=1
XKT= DMA= 0.300 DMB= 0.300 DMC= 0.450 DMD= 0.450 DMF= 0.300
      0.000 to 5.000 by steps of 0.500

XKT      ZD      ZR      ZRATIO      CONVERGENCE
0.000    1.992589  0.113865  0.073639  -0.000096
0.500    2.136194  0.117552  0.070917  -0.000100
1.000    2.225419  0.122551  0.070964  -0.000098
1.500    2.285984  0.129611  0.073063  -0.000099
2.000    2.329719  0.136986  0.075771  -0.000098
2.500    2.363058  0.143498  0.078254  -0.000100
3.000    2.389803  0.148873  0.080276  -0.000098
3.500    2.412791  0.153541  0.082004  -0.000100
4.000    2.432566  0.157775  0.083580  -0.000097
4.500    2.449691  0.161555  0.084985  -0.000097
5.000    2.464386  0.164824  0.086187  -0.000097

```

23. REFERENCES

1. M. Mukaida, H. Okuno and T. Ishimori, Nippon Kagaku Zashi 1965, 86, 56.
2. N. A. Ezerskaya and T. P. Solovykh, Russ. J. Inorg. Chem. 1966, 11, 991.
3. K. Shimizu, T. Matsubara, and G. P. Satô, Bull. Chem. Soc. Jap. 1974, 47, 1651.
4. K. Shimizu, Bull. Chem. Soc. Jap. 1977, 50, 2921.
5. T. Matsubara and C. Creutz, J. Am. Chem. Soc. 1978, 100, 6255.
6. Y. Yoshino, T. Uehiro and M. Saito, Chem. Soc. Jap. Chem. Letters 1978, 487.
7. T. Matsubara and C. Creutz, Inorg. Chem. 1979, 18, 1956.
8. Y. Yoshino, T. Uehiro and M. Saito, Bull. Chem. Soc. Jap. 1979, 52, 1060.
9. P. Ford, De F. P. Rudd, R. Gaunder and H. Taube, J. Am. Chem. Soc. 1968, 90, 1187.
10. A. M. Zwickel and C. Creutz, Inorg. Chem. 1971, 10, 2395.
11. H. Taube, Survey of Prog. in Chem. 1973, 6, 1.
12. H. S. Lim, D. J. Barclay and F. C. Anson, Inorg. Chem. 1972, 11, 1460.
13. J. B. Godwin and T. J. Meyer, Inorg. Chem. 1971, 10, 471.
14. J. N. Armor and H. Taube, J. Am. Chem. Soc. 1970, 92, 6170.

15. C. Creutz and H. Taube, J. Am. Chem. Soc. 1969, 91, 3988.
16. R. E. Shepherd and H. Taube, Inorg. Chem. 1973, 12, 1392.
17. S. Isied and H. Taube, Inorg. Chem. 1974, 7, 1545.
18. T. R. Weaver, T. J. Meyer, S. A. Adeyami, G. M. Brown, R. P. Eckberg, W. E. Hatfield, E. C. Johnson, R. W. Murray and D. Untereker, J. Am. Chem. Soc. 1975, 97, 3039.
19. C. G. Kuehn and H. Taube, J. Am. Chem. Soc. 1976, 98, 689.
20. T. Matsubara and P. C. Ford, Inorg. Chem. 1976, 15, 1107.
21. S. S. Isied and H. Taube, Inorg. Chem. 1976, 15, 3070.
22. H. Taube, Coord. Chem. Rev. 1978, 26, 33.
23. W. Bottcher, G. M. Brown and N. Sutin, Inorg. Chem. 1979, 18, 1447.
24. C. K. Poon and D. A. Isabirye, J. Chem. Soc. 1977, 2115.
25. C. A. Stein, Ph. D. Thesis, Stanford University, 1978.
26. F. Basolo and R. G. Pearson, "Mechanisms of Inorganic Reactions", second edition, Wiley, New York, 1967, p. 124 ff.
27. Y. Sulfab, R. S. Taylor and A. G. Sykes, Inorg. Chem. 1976, 15, 2388.
28. N. Oyama and F. C. Anson, J. Electroanal. Chem. 1978, 88, 289.

29. N. Oyama and F. C. Anson, J. Am. Chem. Soc.
1979, 101, 1634.
30. N. Oyama and F. C. Anson, J. Am. Chem. Soc.
1979, 101, 1634.
31. Personal observations.
32. P. J. Peerce, H. B. Gray and F. C. Anson, Inorg. Chem.
1979, 18, 2593.
33. C. A. Stein and H. Taube, J. Am. Chem. Soc.
1978, 101, 1635.
34. C. A. Stein and H. Taube, Inorg. Chem. 1979, 18, 2212.
35. C. A. Stein and H. Taube, Inorg. Chem. 1979, 18, 1168.
36. B. P. Parkinson and F. C. Anson, Anal. Chem. 1978, 50,
1886.
37. N. A. Ezerskaya and T. P. Solovykh, Russ. J. Inorg.
Chem. 1966, 11, 1168.
38. N. A. Ezerskaya and T. P. Solovykh, Russ. J. Inorg.
Chem. 1966, 11, 1379.
39. N. A. Ezerskaya and T. P. Solovykh, Russ. J. Inorg.
Chem. 1967, 12, 1547.
40. N. A. Ezerskaya and T. P. Solovykh, Russ. J. Inorg.
Chem. 1968, 13, 96.
41. A. Y. Karmulov, N. A. Ezerskaya, L. K. Shubochkin,
R. N. Shchelokov and A. L. Buchachenko, Koord.
Khim. 1977, 3, 1079.
42. A. A. Diamantis and J. V. Dubrawski, Inorg. Chem.
1981, 20, 1142.

43. M. M. T. Khan and G. Ramachandraiah, Inorg. Chem. 1982, 21, 2109.
44. M. Ikeda, K. Shimizu and G. P. Sato, Bull. Chem. Soc. Jap. 1982, 55, 797.
45. M. M. T. Khan, Pure and Appl. Chem. 1983, 55, 159.
46. J. A. Baumann and T. J. Meyer, Inorg. Chem. 1983, 19, 345.
47. S. W. Gersten, G. J. Samuels and T. J. Meyer, J. Am. Chem. Soc. 1982, 104, 4029.
48. R. N. Adams, "Electrochemistry at Solid Electrodes", Marcel Dekker, New York, 1969, pp. 67-114.
49. W. J. Albery and M. L. Hitchman, "Ring-Disc Electrodes", Clarendon Press, Oxford, 1971.
50. V. G. Levich, "Physicochemical Hydrodynamics", Prentice-Hall, Englewood Cliffs, New Jersey, 1962.
51. L. K. J. Tong, K. Liang and W. R. Ruby, J. Electroanal. Chem. 1967, 13, 245.
52. K. B. Prater and A. J. Bard, J. Electrochem. Soc. 1970, 117, 207.
53. K. B. Prater and A. J. Bard, J. Electrochem. Soc. 1970, 117, 335.
54. K. B. Prater and A. J. Bard, J. Electrochem. Soc. 1970, 117, 1517.
55. S. W. Feldberg, "Computers in Chemistry and Instrumentation", Vol. 2, ed. J. S. Mattson, H. B. Marks, Jr., H. C. MacDonald, Jr., Marcel Dekker, Inc., 1972, Chapter 7.

56. J. B. Flanagan and L. Marcoux, J. Phys. Chem. 1973, 77, 1051.
57. J. F. Skinner, A. Glasel, L. Hsu and B. L. Funt, J. Electrochem. Soc. 1980, 127, 315.
58. H. N. Po and N. Sutin, Inorg. Chem. 1968, 7, 621.
59. B. Figgis and J. Lewis, "Techniques in Inorganic Chemistry," ed H. Jonassen and A. Weissberger, Volume IV, Interscience, New York (1965).
60. R. N. Adams, "Electrochemistry at Solid Electrodes," Marcell Dekker, New York, 1969.
61. L. Meites, "Polarographic Techniques", John Wiley and Sons, New York, New York, 1965.
62. J. H. Christie, R. A. Osteryoung, and F. C. Anson, J. Electroanal. Chem. 1967, 13, 236.
63. M. D. Ryan, J. Electroanal. Chem. 1977, 79, 105.
64. C. W. Anderson, H. B. Halsall and W. R. Heineman, Anal. Biochem. 1979, 93, 366.
65. V. T. Taniguchi, W. R. Ellis, Jr., V. Cammarata, J. Webb, F. C. Anson and H. B. Gray, ACS Adv. in Chem. Series, No. 201; ACS: Washington, D. C., 1982, pp. 51-68.
66. J. L. Woodhead and J. M. Fletcher, J. Chem. Soc. 1961, 5039.
67. J. L. Hoard, M. Lind and J. V. Silverton, J. Am. Chem. Soc. 1961, 83, 2770.
68. D. W. Phelps, E. M. Kahn and D. Hodgson, Inorg. Chem. 1975, 14, 2486.

69. R. J. H. Clark, M. L. Franks and P. C. Turtle, J. Am. Chem. Soc. 1977, 99, 2473.
70. I. M. Kohthoff, E. B. Sandell, E. J. Meehan and S. Bruckenstein, "Textbook of Quantitative Inorganic Analysis", Fourth edition, The MacMillan Company, New York, New York, 1969.
71. G. L. Brennan, J. Chem. Ed. 1968, 51, 812.
72. K. Krishnan and R. A. Plane, J. Am. Chem. Soc. 1968, 90, 3195.
73. G. C. Allen and N. S. Hush, Prog. Inorg. Chem. 1967, 8, 357.
74. N. S. Hush, Prog. Inorg. Chem. 1967, 8, 391.
75. M. B. Robin and P. Day, Adv. Inorg. Chem. Radiochem., 1967, 10, 247.
76. J. Woodward, Philos. Trans. R. Soc. London 1974, 33, 15.
77. T. J. Meyer, Chem. Phys. Lett. 1979, 64, 417.
78. B. P. Sullivan and T. J. Meyer, Inorg. Chem. 1980, 19, 752.
79. P. George and J. S. Griffith, "The Enzymes", Vol. 1, P. D. Boyer et al., ed., Academic Press, New York, New York, 1959, p. 347.
80. C. Creutz, Prog. Inorg. Chem., submitted for publication.
81. N. S. Hush, Electrochim Acta 1968, 13, 1005.
82. T. J. Meyer, Acc. Chem. Res. 1978, 11, 94.
83. J. E. Burdett, Comments Inorg. Chem. 1981, 1, 85.

84. J. Lauher, Inorg. Chim. Acta 1980, 39, 119.
85. B. Mayoh and P. Day, J. Am. Chem. Soc. 1972, 94, 2885.
86. B. Mayoh and P. Day, Inorg. Chem. 1974, 13, 2273.
87. M. Ratner and M. J. Ondrechen, Mol. Phys. 1976, 32, 1233.
88. M. A. Ratner, Int. J. Quant. Chem. XIV 1978, 675.
89. S. B. Piepho, E. R. Krausz and P. N. Schatz, J. Am. Chem. Soc. 1978, 100, 2006.
90. K. Y. Wong, P. N. Schatz and S. B. Piepho, J. Am. Chem. Soc. 1979, 101, 2793.
91. K. Y. Wong and P. N. Schatz, Prog. Inorg. Chem. 1981, 28, 369.
92. E. Buhks, Ph. D. Thesis, Tel Aviv University, 1980.
93. J. K. Beattie, N. S. Hush and P. R. Taylor, Inorg. Chem. 1976, 15, 992.
94. N. S. Hush, A. Edgar and J. K. Beattie, Chem. Phys. Lett. 1980, 69, 128.
95. B. C. Bunker, R. S. Drago, D. N. Hendrickson, R. M. Richman and S. L. Kessell, J. Am. Chem. Soc. 1978, 100, 3805.
96. C. Creutz and H. Taube, J. Am. Chem. Soc. 1973, 95, 1086.
97. J. H. Elias and D. Drago, Inorg. Chem. 1972, 11, 415.
98. C. Creutz, M. L. Good and S. Chandra, Inorg. Nucl. Chem. Lett. 1973, 9, 171.
99. W. P. Griffith, Coord. Chem. Rev. 1970, 5, 459.

100. J. R. Ferraro and W. R. Walker, Inorg. Chem.
1965, 4, 1382.
101. J. R. Ferraro, R. Driver, W. R. Walker and W. Wozniak,
Inorg. Chem. 1967, 6, 1586.
102. R. J. Majiste and E. A. Meyers, J. Phys. Chem.
1970, 74, 3497.
103. R. M. Wing and K. P. Callahan, Inorg. Chem. 1969, 8,
871.
104. F. P. Dwyer, H. A. Goodwin and E. C. Gyarfás, Aust. J.
Chem. 1963, 16, 544.
105. P. M. Smith, T. Fealey, J. E. Earley, and J. V.
Silverton, Inorg. Chem. 1971, 10, 1943.
106. A. McL. Mathieson, D. P. Mellor and N. C. Stephenson,
Acta Cryst. 1952, 5, 185.
107. F. A. Cotton and J. T. Mague, Inorg. Chem. 1966, 5, 317.
108. J. M. Fletcher, W. E. Gardner, B. F. Greenfield, M. J.
Holdoway and M. H. Rand, J. Chem. Soc. A
1968, 653.
109. J. D. Dunitz and L. E. Orgel, J. Chem. Soc. 1953, 2594.
110. C. K. Jorgenson and L. E. Orgel, Mol. Phys. 1961, 4,
215.
111. J. R. Campbell and R. J. H. Clark, Mol. Phys.
1978, 36, 1133.
112. J. S. Filippo, Jr., P. J. Fagan and F. J. DiSalvo,
Inorg. Chem. 1977, 16, 1016.
113. S. J. Lippard, H. J. Schugar and C. Walling, Inorg.
Chem. 1967, 6, 1825.

114. H. J. Schugar, G. R. Rossman, C. G. Barraclough and H. B. Gray, J. Am. Chem. Soc. 1972, 94, 2683.
115. R. Shandles, E. O. Schlemper and R. K. Murmann, Inorg. Chem. 1971, 10, 2785.
116. D. L. Toppen and R. K. Murmann, Inorg. Nucl. Chem. Lett. 1970, 6, 139.
117. C. K. Jorgenson, Inorg. Chem. 1970, 12, 101.
118. C. K. Jorgenson, Mol. Phys. 1959, 2, 309.
119. Z. Harzion and G. Navon, Inorg. Chem. 1980, 19, 2236.
120. G. Lodi, E. Silvieri, A. De Battisti and S. Trasatti, J. Appl. Electrochem. 1978, 125, 1093.
121. A. Mills and M. L. Zeeman, J. C. S. Chem. Comm. 1981, 948.
122. J. P. Collman, M. Marrocco, P. Denisevich, C. Koval and F. C. Anson, J. Am. Chem. Soc. 1980, 103, 6027.
123. D. J. Hewkin and W. P. Griffith, J. Chem. Soc. A 1966, 472.
124. I. S. Filippo, Jr., R. L. Graysen and H. L. Sniadoch, Inorg. Chem. 1976, 15, 269.
125. A. V. Khedakar, J. Lewis, F. E. Mabbs and H. Weigold, J. Chem. Soc. A 1967, 1561.
126. A. Earnshaw and J. Lewis, J. Chem. Soc. 1961, 396.
127. K. Nakamoto, "Infrared and Raman Spectra of Inorganic and Coordination Compounds", Third Edition, John Wiley and Sons, Inc., New York, 1978.

128. T. R. Bhat and M. Krishnamurthy, J. Inorg. Nucl. Chem. 1963, 25, 1147.
129. O. K. Medhi and U. Agarwala, Inorg. Chem. 1980, 19, 1387.
130. A. Hudson and M. J. Kennedy, J. Chem. Soc. A 1969, 1116.
131. I. A. Miller and E. L. Offenbacher, Phys. Rev. 1968, 166, 269.
132. S. Wherland, Ph. D. Thesis, California Institute of Technology, 197_.
133. K. W. H. Stevens, Proc. Roy. Soc. A 1953, 219, 242.
134. J. S. Griffith, Mol. Phys. 1971, 21, 135.
135. C. P. S. Taylor, Biochim et Biophysica Acta 1977, 491, 137.
136. C. Walling, R. E. Partch and T. Weil, Proc. Nat. Acad. Sci. USA 1975, 72, 140.
137. B. A. Moyer, M. S. Thompson and T. J. Meyer, J. Am. Chem. Soc. 1980, 102, 2310.
138. B. A. Moyer and T. J. Meyer, Inorg. Chem. 1981, 20, 436.
139. G. J. Samuels and T. J. Meyer, J. Am. Chem. Soc. 1981, 103, 307.
140. M. S. Thompson and T. J. Meyer, J. Am. Chem. Soc. 1982, 104, 5070.
141. R. E. DeSimone and R. S. Drago, J. Am. Chem. Soc. 1970, 92, 2343.

142. H. M. McConnell and R. E. Robertson, J. Chem. Phys. 1958, 29, 1361.
143. F. F. L. Ho, L. E. Erickson, S. R. Watkins, and C. N. Reilly, Inorg. Chem. 1970, 9, 1139.
144. L. E. Erickson, F. F. L. Ho, and C. N. Reilley, Inorg. Chem. 1970, 9, 1148.
145. L. E. Erickson, D. C. Young, F. F. L. Ho, S. R. Watkins, J. B. Terrill, and C. N. Reilley, Inorg. Chem. 1971, 10, 446.
146. R. S. Drago, "Physical Methods in Chemistry", W. B. Saunders Co., Philadelphia (1977), Chapter 12.
147. "NMR of Paramagnetic Molecules", ed. G. N. LaMar, W. D. Horrocks, Jr., and R. H. Holm, Academic Press, New York (1973).
148. P. M. Smith, T. Fealey, J. E. Earley, and J. V. Silverton, Inorg. Chem. 1971, 10, 1943.
149. M. D. Lind, M. J. Hamor, and J. L. Hoard, Inorg. Chem. 1964, 3, 34.
150. J. J. Stezowski, R. Countryman, and J. L. Hoard, Inorg. Chem. 1973, 12, 1749.
151. M. Saito, T. Uehiro, F. Ebina, T. Iwamoto, A. Ouchi, and Y. Yoshino, J. Chem. Soc. Jap. Chem. Lett. 1979, 997.
152. A. McL. Mathieson, D. P. Mellor and N. C. Stephenson, Acta Cryst. 1952, 5, 185.

153. A. J. Bard and L. R. Faulkner, "Electrochemical Methods--Fundamentals and Applications", John Wiley and Sons, New York, 1980.
154. S. Bruckenstein and B. Miller, J. Electrochem. Soc. 1970, 117, 1032.
155. B. Miller and S. Bruckenstein, Anal. Chem. 1974, 46, 2026.
156. K. Toduda, S. Bruckenstein, and B. Miller, J. Electrochem. Soc. 1975, 122, 1316.
157. D Britz, "Lecture Notes in Chemistry--Digital Simulation in Electrochemistry", ed. B. Berthier, M. J. S. Dewar, H. Fischer, K. Fukui, G. G. Hall, H. Hartmann, J. J. Jaffe, J. Jortner, W. Kutzelnigg, K. Ruedenberg, E. Scrocco, Springer-Verlag, New York, 1981.
158. L. F. Whiting and P. W. Carr, J. Electroanal. Chem. 1977, 81,1.
159. V. J. Puglisi and A. J. Bard, J. Electroanal. Chem. Soc. 1972, 119,833.
160. T. Geiger and F. C. Anson, J. Am. Chem. Soc. 1981, 103, 7489.
161. A. Bakac and J. H. Espenson, Inorg. Chem. 1983, 22, 779.
162. C. Walling and S. Kato, J. Am. Chem. Soc. 1971, 93,4275.
163. T. J. Hardwick, Can. J. Chem. 1957, 35,428.

164. P. A. Forshey and T. Kuwana, Inorg. Chem. 1983, 22, 699.

PROPOSITIONS

R. Baar Thesis

Proposition 1

It is proposed that the series of ruthenium tetroxide complexes (RuO_4 , RuO_4^- , and RuO_4^{2-}) be investigated by EXAFS to determine the effect of the oxidation state of the ruthenium on the K-shell absorption edge, the ruthenium-oxygen bond lengths and the Debye-Waller factor.

The use of EXAFS has proven to be very useful in the determination of the coordination environment of inorganic metal complexes (1-3). Typically, a K-shell electron is removed from the central-atom and the scattering of the resulting photoelectron wave by the surrounding atoms is measured. The absorption spectrum of the sample is then measured as the energy of the incoming X-rays is varied. The EXAFS are then analyzed by use of the following equation:

$$\chi(k) = - \sum_j \frac{N_j}{kr_j^2} |f_j(k, \pi)| \sin[2kr_j + \varphi_j(k) + 2\delta'(k)] \\ \times \exp(-2\sigma_j^2 k^2) \exp(-2r_j/\lambda_j(k))$$

where,

k = photoelectron wave vector

$$= \hbar^{-1} [2m(\hbar\omega - E_0)]^{1/2}$$

$\chi(k)$ = the x-ray frequency

E_0 = the threshold energy of the absorption

edge

N_j = the number of atoms at a distance, r .

\hat{e} = polarization direction

r = distance of central atom to the atom of interest

$f_j(k, \pi)$ = back-scattering amplitude

$\phi_j(k)$ = phase shift due to back-scattering from the j^{th} neighboring atom

$2\delta_1^j$ = central-atom phase shift

$\exp(-2\sigma_j^2 k^2)$ = Debye-Waller factor

$\exp(-2r_j/\lambda_j(k))$ = inelastic losses factor

The amplitude and phase components of this equation have been considered in detail both theoretically and experimentally (1, 4, and the references therein). The inelastic loss factor is fit empirically to the data to account for the losses in intensity of the absorbance due to multielectron excitation and inelastic scattering of the excited-state photoelectron wave (5). Only recently, however, has the effect of the Debye-Waller factor on the EXAFS spectrum been considered (1,5-7).

The EXAFS Debye-Waller factor differs from the Debye-Waller factor for X-ray diffraction (1). It is the mean-square average of the difference of displacements and may, in general, be different from the mean-square displacement.

$$\sigma_j^2(k) = \langle (\hat{f}_j^0 \cdot \mathbf{u}_j)^2 + (\hat{f}_j^0 \cdot \mathbf{u}_0)^2 \rangle - 2 \langle (\hat{f}_j^0 \cdot \hat{\mathbf{u}}_0) (\hat{f}_j^0 \cdot \mathbf{u}) \rangle \quad (2)$$

The last term in the above equation is the correlation term and vanishes if the central atom and the scattering atom

move independently. In covalently bonded systems the nearest neighbor is strongly bonded and such coherence effects are very important (1). For example, in the case of Ge a different Debye-Waller factor must be assigned to the first shell compared with other shells (1, 8).

The Debye-Waller factor can be determined from the vibrational spectra of model compounds (9-12). The Debye-Waller factor is then incorporated into the amplitude function and used in the EXAFS curve fitting procedure. Since the amplitude function contains information about the number of scatterers, inclusion of the Debye-Waller factor enables a more accurate assessment of the coordination environment around the metal. An example of this enhanced precision was demonstrated recently by Cramer, et al (9), where they analyzed 15 Mo-S compounds and showed a correlation between the bond length and the calculated root-mean-square deviation in the Debye-Waller factor.

Another important area of analysis of the EXAFS of a complex is its edge absorption spectrum. The edge absorption yields information about the oxidation state of the metal, its electronic structure, and its coordination geometry, while the position of the edge provides information about the oxidation state (1-3, 9). Some metal-oxo containing compounds have also exhibited a characteristic low-energy shoulder in their edge spectra. The intensity of this feature results from unresolved, bound-state transitions from the metal $1s$ orbital to vacant

molecular orbitals oriented along the metal-oxo bond. The detailed electronic aspects of these features have been discussed (2, 3, 9).

The series of ruthenium tetroxides provides an opportunity to study the effect of just the oxidation state on the edge spectrum of structurally similar complexes. All of the complexes have been found to be tetrahedral (either by X-ray spectroscopy, or by analysis of their vibrational spectra). Several studies have appeared that consider the vibrational spectra of these complexes (13-15) and the Debye-Waller factors can then be calculated from these spectra and used in the analysis of the EXAFS. A more refined picture of the amplitude and phase parameters for the Ru-O bond will also be able to be determined. This will have applications to the study of oxygen-containing ruthenium catalysts, such as ruthenium dioxide (which has also been studied by EXAFS (16-19)) and will provide more experimental results to compare with the results and theory described by Kutzler, et al (2, 3).

In addition, the study of the edge spectra will provide information about the effect of the oxidation state of the ruthenium on the position of the edge. The presence of any ruthenium-oxo groups should also show up in the edge spectra as a low-energy shoulder. A comparison of the parameters determined for KRuO_4 by EXAFS, X-ray crystallography and vibrational spectroscopy with the results for the other two ruthenium tetroxides will also enable a bond distance to be

determined for these two complexes. A comparison of these results with the previous EXAFS results for ruthenium dioxide will then provide an extensive base of comparison for oxygen-containing ruthenium complexes in several oxidation states.

REFERENCES

1. P. A. Lee, P. H. Citrin, P. Eisenberger and B. M. Kincaid, Rev. of Mod. Phys. **1981**, 53, 769.
2. F. W. Kutzler, C. R. Natoli, D. K. Misener, S. Doniach, and K. O. Hodgson, J. Chem. Phys. **1980**, 73, 3274.
3. F. W. Kutzler, R. A. Scott, J. M. Berg, K. O. Hodgson, S. Doniach, S. P. Cramer and C. H. Chang, J. Am. Chem. Soc. **1981**, 103, 6083.
4. Boon-Keng Tao and P. A. Lee, J. Am. Chem. Soc. **1979**, 101, 2815.
5. S. P. Cramer, R. Wahl and K. V. Rajagopalan, J. Am. Chem. Soc. **1981**, 103, 7721.
6. P. Eisenberger and B. Lengeler, Phys. Rev. B **1980**, 21, 5521.
7. E. A. Stern, B. A. Bunker and S. M. Heald, Phys. Rev. B **1980**, 21, 5521.
8. P. Rabe, L. Tolkiehn and A. Werner, J. Phys. C12 **1979**, L545.
9. S. P. Cramer, K. O. Hodgson, W. O. Gillum, and L. E. Mortenson, J. Am. Chem. Soc. **1978**, 100, 3398.
10. A. Muller and B. Nagarajan, Z. Naturforsch., B: Anorg. Chem., Org. Chem., Biochem., Biophys. **1966**, 21B, 508.
11. S. J. Cyvin, "Molecular Vibrations and Mean Square Amplitudes", Elsevier, Amsterdam, 1968.
12. R. W. James, Z. Phys. **1932**, 33, 737.

13. F. Gonzalez-Vilchez and W. P Griffith, J. C. S. Dalton **1972**, 1416.
14. R. S. McDowell, L. B. Asprey and L. C. Hoskins, J. Chem. Phys. **1972**, 56, 5712.
15. F. A. Cotton and R. M. Wing, Inorg. Chem. **1965**, 4, 867.
16. M. D. Silverman and H. A. Levy, J. Am. Chem. Soc. **1954**, 76, 3317.
17. D. B. Rogers, R. D. Shannon, A. W. Sleight and J. L. Gillson, Inorg. Chem. **1969**, 8, 841.
18. F. A. Cotton and J. T. Mague, Inorg. Chem. **1966**, 5, 317.
19. F. W. Lytle, H. Via, and I. H. Sinfelt, J. Chem. Phys. **1977**, 67, 3831.

Proposition 2

Abstract: A ruthenium-edta mixed-valence dimer catalyzes dioxygen evolution from water when an appropriate voltage is applied to the solution. It is proposed that by comparing the EXAFS of the mixed-valence dimer with a series of model compounds containing similar Ru-ligand and possible Ru-bridge-Ru-moieties, the dimer's bridging structure will be attempted to be determined. The first time use of an X-ray transparent thin electrochemical cell will also allow the in situ generation of the catalytic form of the dimer and a determination of its structure. This will provide information concerning the relationship between the dimer's structure and its catalytic activity. The structure determination of the catalytic form of the dimer is also not feasible by other standard spectroscopic, or diffraction techniques.

Recently, attempts at devising catalysts which aid in the oxidation of water, a key reaction in photosynthesis (1), and which can aid in the photochemical splitting of water into dioxygen and dihydrogen have received much attention (2).



$E^0 = +1.23 \text{ V vs. Normal Hydrogen Electrode (NHE)}$



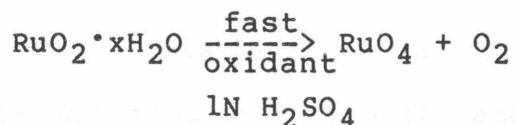
$E^0 = +0.000 \text{ V (the Normal Hydrogen Electrode)}$



The interest in the reverse of the last reaction lies in its use for storing solar energy in chemical bonds for later use as an efficient and clean fuel source.

Ruthenium containing compounds have frequently been used as dioxygen evolution catalysts. The accessibility of several oxidation states (necessary for the four electron oxidation of water), the substitution inertness of the chelated ligands, and the possibility of photochemical coupling has led to the extensive amount of work using this metal. Several attempts have been made to characterize the mechanism of reaction of these ruthenium-containing catalysts (1-9).

One of the best catalysts which aids in the evolution of dioxygen from water is ruthenium dioxide, $\text{RuO}_2 \cdot x\text{H}_2\text{O}$ (3). The actual mechanism is not known although recent evidence suggests the possibility of ruthenium tetroxide, RuO_4 , as the active species for a suspension of ruthenium dioxide (4).





When ruthenium dioxide is bound to TiO_2 , however, the catalytic activity goes up (15) and there is not any evidence of RuO_4 formation (4). Based upon electrochemical (6) and XPS (7) results, the following mechanism has been proposed for RuO_2 as a catalyst:



The interaction of dioxygen with metallic ruthenium has been characterized by EXAFS and shown to lead to the formation of ruthenium dioxide as the catalytic species on silica support (8).

Meyer and coworkers (9) have prepared the $[(\text{bipy})_2(\text{pyr})\text{RuO}]^{2+}$ ion which can apparently oxidize water to dioxygen. The presence of ruthenyl, $\text{Ru}=\text{O}$, functionality was listed by Meyer as being necessary for dioxygen evolution (9). This assertion coincides with the RuO_4 intermediate observed by Mills (4) and the RuO_3 intermediate

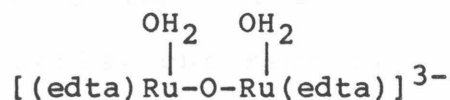
proposed by Lodi, et al (6), and Augustynski, et al (7). Meyer, et al, did not, however, observe the evolution of dioxygen in their system. Conclusive evidence of the actual mechanism and the structure of the active species in all of these systems is, as of yet, unavailable.

In the process of studying the aqueous electrochemistry of $[\text{Ru(III)(edta)(OH}_2)]^-$, it was observed that dioxygen could be generated catalytically after oxidation of the ruthenium-edta monomer to a mixed-valence dimer (formally, Ru(3.5)-Ru(3.5)) (10). The dimer could also be generated by the addition of hydrogen peroxide to an acidic solution containing $[\text{Ru(edta)(OH}_2)]^-$ (10-12). The following stoichiometry is observed in the production of the mixed-valence dimer (10):

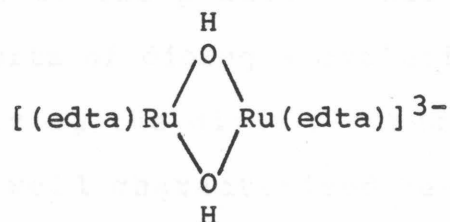


[3,4] = mixed-valence Ru(edta) dimer

Spectral and magnetic measurements have established that the formal oxidation state on each ruthenium is 3.5. This indicates that two of the three possible unpaired electrons [Ru(III) is d^5 , low spin, while Ru(IV) is d^4 , low spin] have paired in a molecular orbital upon dimer formation, while the remaining unpaired electron is delocalized over both metal centers. There is one titratable proton per dimer with a pKa of 10.3. The following structures are proposed:



-or-



Further oxidation yields the catalytic evolution of dioxygen and protons from water in neutral to basic solutions. The reaction is suppressed by acid, and, at pH 1, the one-electron oxidized [4,4] dimer decays slowly back to the [3,4] dimer. The existence of the [44] dimer has been detected by the use of spectroelectrochemical technique (13).

Using an optically transparent, thin-layer electrochemical cell, a potential of +1.14-1.24 vs. NHE was applied to an acidic solution of the mixed-valence dimer. The large electrode surface area to solution volume ratio, coupled with the slow decay of the [4,4] dimer, led to the equilibrium concentration of the [4,4] dimer being reached in a few minutes. A Nernst plot of the concentration of the ratio of the unoxidized to the oxidized forms of the dimer (proportional to the measured absorbance) vs. applied potential yields a line with a slope of 60 millivolts, indicating a one-electron oxidation (13).

Attempts at isolating a crystal of the mixed-valence dimer have been futile, but recently, a small amount of amorphous powder was isolated. The existence of a "ruthenyl" moiety ($\text{Ru}=\text{O}$) was not indicated when an infrared spectra was taken of the powder. This is not consistent with previous reports of dioxygen evolution catalysts and a way of characterizing the dimer's structure is necessary. There are not any well characterized $\text{Ru}-\text{O}-\text{Ru}$, or $\text{Ru}(\text{OH})_2\text{Ru}$ bands in the infrared or Raman spectral regions and insight into the bridging structure has not been possible by these techniques. The use of NMR, or ESR (down to liquid helium temperatures) has also been uninformative (10).

EXAFS affords a method to characterize the structures of both the [3,4] and the [4,4] dimers. The [3,4] dimer can be studied as both the solid and in aqueous solution at pH values above and below the pK_a of the dimer to see if there is any change in the structure in the presence, or absence of the titratable proton. Utilizing an X-ray transparent (lucite) spectroelectrochemical cell, the catalytic [4,4] dimer will be generated, in situ, and insight into its structure obtained.

The EXAFS of a $\text{Ru}-\text{O}-\text{Ru}$ moiety vs. those of a $\text{Ru}(\text{OH})_2\text{Ru}$ moiety should be distinctly different due to the different ruthenium-ruthenium distances in each. Comparisons with model ruthenium compounds containing these structures should aid in the determination of the dimers' bridging structure. The position and shape of the ruthenium edge will also be

investigated since they provide information about the oxidation state, the bonding orbital scheme and the coordination geometry of the ruthenium in the dimer (14,15).

Cramer, et al (14) have observed a shoulder in the edge spectra of molybdenum compounds when a Mo=O bond is present. This effect has been attributed to the excitation of a core electron to a low-lying bound state molecular orbital due to the Mo=O interaction and should appear in other systems with similar bonding schemes (14,15). The presence of a Ru=O moiety in the catalytic [4,4] dimer can be determined by a study of the ruthenium edge shape and position (14,15) and compared with the evidence for its existence in other catalytic ruthenium systems (4, 6, 7, 9).

The combined use of an electrochemical cell with EXAFS has not been previously attempted. This combination of techniques has much promise in solution structure determinations since electrochemistry provides a clean and efficient means of oxidizing, or reducing a sample while remaining in the X-ray beam. This would allow for minimum sample manipulation when different oxidation states of a dissolved complex are required (especially useful for air sensitive compounds), the ability to coulometrically oxidize, or reduce a sample at a pre-determined, potentiostated potential, the generation, in solution, of species that are not stable in the solid state, and with the use of standard electrochemical sampling techniques such as cyclic voltammetry and polarography (13), would provide an

easy way to establish and maintain the identity of an electroractive species.

To aid in identifying the structure of the Ru(edta) dimers, a series of model ruthenium compounds of known crystal structures will also need to be measured. To establish the Ru-N parameters, Ru(III)(NH₃)₆Cl₃ (16), Ru(II)(NH₃)₆Cl₂ (16) and Ru(bipyridine)₃Cl₂ (17) will be used. The linear and slightly bent Ru-O-Ru moiety's parameters will be established by measuring [Ru(bipyridine)₂(NO₂)]₂O (21), K₄[Cl₅Ru]₂O (22), and K[(NH₃)₅RuORu(NH₃)₄ORu(NH₃)₅] (23), while the Ru(O)₂Ru moiety's parameters will be determined by using RuO₂ (24). To characterize the Ru-Ru parameters, Ru₂(O₂C-butyl) (25), will be used, while for Ru-Cl, K₂RuCl₆ (26) will be used.

In this series of model compounds the formal oxidation state of the ruthenium varies from II to VIII. Questions concerning the transferability of phase and amplitude parameters, Debye-Waller factors, edge properties, and correlations with ab initio (15,27) calculations will be addressed, as well as the application of these parameters to the structure determinations of the unknown compounds.

REFERENCES

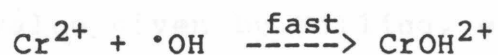
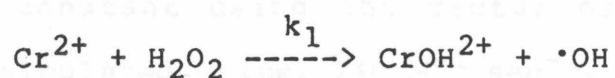
1. G. Renger, FEBS Lett. **1977**, 81, 223; M. M. Morrison and D. T. Sawyer, Inorg. Chem. **1978**, 17, 333; F. K. Fong and L. Galloway, J. Am. Chem. Soc. **1978**, 100, 3594.
2. J. Kiwi and M. Gratzel, Angew. Chem., Int. Ed. Engl. **1978**, 17, 860; J. O. M. Bockris and K. Vosaki, Adv. Chem. Ser. **1977**, No 163, 3-70; V. Bolzani, L. Moggi, M. F. Manfrin, F. Bolletta and M. Gleria, Science (Washington, D. C.) **1975**, 189, 852.
3. J. Kiwi and M. Gratzel, Chem. Phys. Lett. **1981**, 78, 241, and the references therein.
4. A. Mills and M. L. Zeeman, J. Chem. Soc. Chem. Commun. **1981**, 948.
5. K. Kalyanasundaram, E. Borgarello and M. Gratzel, Helv. Chem. Acta **1981**, 64, 362.
6. G. Lodi, E. Sivieri, A. De Battisti, and S. Trasatti, J. Appl. Electrochem. **1978**, 8, 135.
7. J. Augustynski, L. Balsenc and J. Hinden, J. Electrochem Soc. **1978**, 125, 1093.
8. F. W. Lytle, G. H. Via and J. H. Sinfelt, J. Chem. Phys. **1977**, 67, 3831.
9. B. A. Moyer and T. J. Meyer, Inorg. Chem. **1981**, 20, 436.
10. R. Baar thesis, California Institute of Technology, Pasadena, California, 1983.

11. N. A. Ezerskaya and T. P. Solovykh, Russ. J. Inorg. Chem. **1967**, 12, 1547.
12. N. A. Ezerskaya and T. P. Solovykh, R ss. J. Inorg. Chem. **1966**, 11, 1168.
13. A. J. Bard and L. R. Faulkner, "Electrochemical Methods--Fundamentals and Applications", John Wiley and Sons, New York, 1980 and the references therein.
14. S. P. Cramer, R. Wahl and K. V. Rajagopalan, J. Am. Chem. Soc. **1981**, 10, 7721.
15. P. A. Lee, P. H. Citrin, P. Eisenberger and B. M. Kincaid, Rev. Mod. Phys. **1981**, 53, 769, and the references therein.
16. H. C. Stynes and J. A. Ibers, Inorg. Chem. **1971**, 10, 2304.
17. D. P. Rillema and D. S. Jones, J. Chem. Soc. Chem. Commun. **1979**, 849.
18. D. Silverman and H. A. Levy, J. Am. Chem. Soc. **1954**, 76, 3317.
19. J. L. Woodhead and J. M. Fletcher, J. Chem. Soc. **1961**, 5039.
20. G. Chao, R. L. Sime and R. J. Sime, Acta Cryst. **1973**, B29, 2845.
21. D. W. Phelps, E. M. Kahn and D. J. Hodgson, Inorg. Chem. **1971**, 10, 1943.
22. A. McL. Mathieson, D. P. Mellor, and N. C. Stephenson, Acta Cryst. **1952**, 5, 185.

23. P. M. Smith, T. Fealey, J. E. Earley, and J. V. Silverton, Inorg. Chem. **1971**, 101, 1943.
24. D. B. Rogers, R. D. Shannon, A. W. Sleight and J. L. Gillson, Inorg. Chem. **1969**, 8, 84.
25. M. J. Bennett, K. G. Carlton and F. A. Cotton, Inorg. Chem. **1969**, 8, 1.
26. D. Adams and D. P. Mellor, Austr. J. Sci. Res. **1952**, 5A, 577.

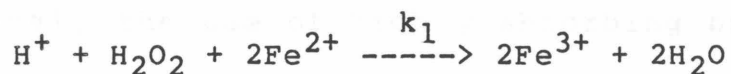
PROPOSITION 3

It is proposed that the rotating ring-disk electrode (RRDE) (1) be used in conjunction with computer simulations to study the catalytic reduction of hydrogen peroxide by Cr(II). Several different studies have considered this reaction (2-6) and investigated its behavior by spectroscopic methods. The following mechanism has been proposed:



The rate constants reported for the first reaction are $k_1 = (2.8 \pm 0.7) \text{ E}+4 \text{ M}^{-1} \text{ sec}^{-1}$ (6) and $(7.06 \pm 0.04) \text{ E}+4 \text{ M}^{-1} \text{ sec}^{-1}$ (3). Bakac and Espenson's noted that a factor of two was left out of the analysis by Samuni, et al, and their resultingly low value was attributed to small absorbance changes in the stopped-flow experiment and the high reaction rate (2).

This factor of two was also pointed out by Skinner, et al (6) as having been neglected in Bard and Prater's analysis of the catalytic reduction of peroxide by Fe^{2+} (10). Both Skinner, et al, and Bard and Prater used the rotating ring-disk electrode in conjunction with computer simulations of the catalytic mechanism to determine the rate of chemical catalysis.



Skinner, et al, pointed out a similar lack of use of the factor of two in the kinetic equation for the reduction of the peroxide by Bard and Prater in their simulation. Skinner used the data of Bard and Prater and recalculated the value for the rate constant using the factor of two, but the subsequent recalculated value, $240 \text{ M}^{-1} \text{ sec}^{-1}$, was higher than the reported value given by Walling, et al (8,9), $45\text{-}70 \text{ M}^{-1} \text{ sec}^{-1}$. Skinner, et al, also performed new experiments where the ratio of the iron:peroxide ratio varied from 0.1 to 10. The values that they obtained were also near $250 \text{ M}^{-1} \text{ sec}^{-1}$, and the reason for these high values was not well understood in the report.

It was subsequently shown that the reason for the discrepancy between the early spectroscopically determined rates, and the electrochemically determined rates was not only the need to include the stoichiometric factor of two, but also the lack of inclusion of the correct diffusion coefficients for the reactive species (11). When the necessary modifications for the inclusion of the diffusion coefficients into the simulation programs was made, then using the experimental data of Skinner, et al, and Bard and Prater, values of $75\text{-}110 \text{ M}^{-1} \text{ sec}^{-1}$, and $45 \text{ M}^{-1} \text{ sec}^{-1}$, respectively, were recalculated (11). These values are in much closer agreement with the spectroscopically determined

values.

In general, the use of highly absorbing bands in the optical region have been used to monitor the rate of the catalytic reaction by stopped-flow techniques. Flash techniques were also frequently required, as were rather involved data analysis procedures. A pure solution of the reduced metal species, which is typically very oxygen sensitive, and which therefore necessitates the use of elaborate inert atmosphere techniques was also required. These requirements made it difficult to easily determine the rate of reaction for the catalytic reduction of peroxide by metal systems.

The use of the RRDE, on the other hand, allows the oxidized form of the metal system to be used as the starting material and only requires standard deaerating techniques for an electrochemical cell for the experiment to be performed. An accessible reduction potential for the catalytic form of the metal complex is then required to initiate the reaction.

The simulation program does not require much time to be input into the computer and the running of the program does not require much computer time. A form of the program is available that allows the input of variable diffusion coefficients, chemical stoichiometries and substrate-to-catalyst ratios (11). A series of working curves can then be generated to accommodate any chemical conditions which can then be compared to the resultant disk and ring currents for the catalytic reaction.

The investigation of the rate of catalysis by Cr(II) by the use of the RRDE can then be compared with the previously reported values. Using some typical experimental conditions the following results for the normalized disk and ring currents (when compared to the uncatalyzed reduction of Cr^{2+}) and collection efficiencies ($N = i_{\text{ring}}/i_{\text{disk}}$) are predicted for the Cr(II) system:

M	ω (rpm)	XKTC	disk	ring	N
0.36	200	23.5	2.12 (135 μamp)	0.048 (3.9 μamp)	.029
	3600	1.31	1.23 (333 μamp)	0.119 (39.6 μamp)	.119
1.4	200	23.5	4.93 (314 μamp)	0.002 (0.18 μamp)	.001
	3600	1.31	1.82 (493 μamp)	0.074 (26.1 μamp)	.074

where,

$$\text{XKTC} = \left(\frac{\text{xkC}}{\omega} \right) \left(\frac{\nu}{D} \right)^{\frac{1}{3}} (0.51)^{\frac{2}{3}}$$

is the dimensionless rate constant used in the simulation, and,

$$C = 0.5 \text{ mM } \text{Cr}^{2+}$$

$$D = 5 \text{ E-6 cm}^2/\text{sec}$$

$$x = 2, \text{ the stoichiometry factor}$$

$$\nu = 0.01 \text{ cm}^2/\text{sec}, \text{ the solution kinematic viscosity}$$

$$k = \text{rate constant of } 5 \text{ E+4 } \text{M}^{-1} \text{ sec}^{-1}$$

$$M = \text{substrate-to-catalyst ratio}$$

$$\omega = \text{rotation rate (Hz used for XKTC, rpm in the chart)}$$

and the standard Pine electrode is used (disk radius = 0.382 cm, area = 0.46 cm², inner and outer ring radii = 0.399 and 0.422 cm, respectively, and the uncatalyzed collection efficiency is 0.176). The listed currents are the predicted amounts for the simulation variables used.

It can be seen that both the ring and the disk currents should provide information about the catalysis, but that at slower rotation rates for higher values of M the ring current is very small and probably undetectable. The disk current, however, is nearly five times as large as the uncatalyzed disk current. As the value of M is increased even further than, then it becomes more difficult to measure any disk current different from the "limiting value" of 5.70 times the uncatalyzed disk current:

$$i_{lim} = \frac{(nC_{cat}D_{cat}^{\frac{2}{3}}) + (nxC_{sub}D_{sub}^{\frac{2}{3}})}{(nC_{cat}D_{cat}^{\frac{2}{3}})}$$

The use of the RRDE will also allow for the easy use of thermostated cells to enable activation energies and entropies for the Cr²⁺ catalyzed reaction to be determined in a straightforward manner (7).

It is felt that the use of the RRDE in conjunction with the computer simulation programs will enable the rapid and detailed investigation of the chromium-peroxide system to be made without much of the experimental difficulties encountered in spectroscopic methods.

REFERENCES

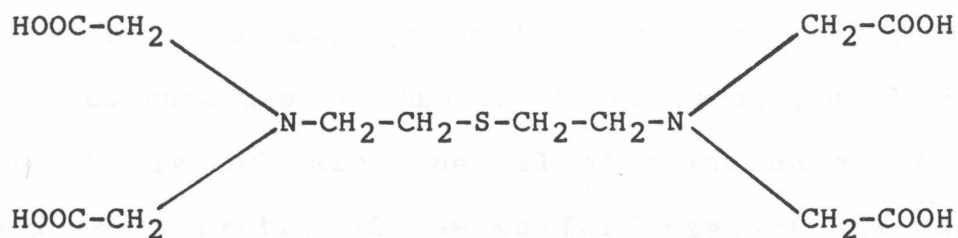
1. S. Bruckenstein and B. Miller, Acc. Chem. Res. **1977**, 10, 54.
2. A. Bakac and J. P. Espenson, Inorg. Chem. **1983**, 22, 779.
3. M. Ardon and R. A. Plane, J. Am. Chem. Soc. **1959**, 81, 3179.
4. L. B. Anderson and R. A. Plane, Inorg. Chem. **1964**, 3, 1470.
5. A. C. Cahill and J. Taube, J. Am. Chem. Soc. **1952**, 74, 2312.
6. A. Samuni, D. Meisel and C. J. Czapski, J. Chem. Soc. Dalton Trans. **1972**, 1273.
7. J. F. Skinner, A. Glasel, L. Hsu and B. L. Funt, J. Electrochem. Soc. **1980**, 127, 315.
8. C. Walling, R. E. Partch and T. Weil, Proc. Nat. Acad. Sci., USA **1975**, 72, 140.
9. C. Walling and S. Kato, J. Am. Chem. Soc. **1971**, 93, 4275.
10. K. B. Prater and A. J. Bard, J. Electrochem. Soc. **1970**, 117, 1517.
11. R. Baar Thesis, California Institute of Technology, Pasadena, California, 1983.

PROPOSITION 4

Abstract: It is proposed to prepare the selenium analogue of tedta and then utilize it as a multidentate ligand. By various spectroscopic and electrochemical techniques the similarities attributable to the metal-selenium interaction and the metal-sulfur interaction can then be used to infer the nature of the metal-sulfur moiety.

Recently, the study of metal-sulfur complexes and their interactions has been very intense (1-3). With the realization that metal-sulfur interactions are very important in biological processes, many attempts have been made to synthesize compounds modelled after what are thought to be the active sites (3, 7). These studies have also used the amino acids, methionine and cysteine, and their derivatives with various metals to directly coordinate the known active amino acid to a certain metal (4-6). The ability to characterize the structure and interactions of these compounds and their solutions has been very difficult and needs to be elucidated.

With this in mind, molecules that would force, or emphasize metal-sulfur coordination have been devised. One of these is a modification of ethylenediaminetetraacetate (edta), called thio, bis-ethylenediaminetetraacetate (tedta) (32,33) which has the following structure:



tedta

Thus, it is hoped that by the chelation effect, due to the edta part of the ligand, metal-sulfur coordination will be induced.

The problem, however, of identifying the metal-sulfur bond (a thioether in this case, but also for thiolates) by chemical, electrochemical or spectroscopic techniques has defied unambiguous characterization. It is proposed that due to the similarity of selenium and sulfur in organic compounds, and in the few recent metal-seleno complexes that have been studied (7, 8) that the selenium analogue of tedta be synthesized and coordinated to various metals.

This ligand, to be called sedta, has apparently been prepared (10), but other than its stability constants with H^+ , Ca^{2+} , Mg^{2+} , and Sr^{2+} , no other published results have appeared. A comparison of the pKa values of sedta with tedta shows that the selenium has a minor effect on the proton affinity as compared to the sulfur.

Complex	Temp, C	Medium	K_1	K_2	K_3	K_4	Ref
tedta	20	0.1 KNO_3	1.8	2.52	8.47	9.42	9
sedta	25	0.1 KNO_3	2.02	2.65	8.78	9.37	10

Being unable to find a copy of the U.S.A.E.C. (10) report to see how Kroll, et al, synthesized the ligand, a procedure similar to that used to prepare tedta is suggested (32,33).

The utility of using the selenium analogues of sulfur compounds as probes of the sulfur interactions has been explored in many different analytical and spectroscopic techniques. A few examples follow below.

I. Infrared Spectroscopy

In general, the intensities of Se bands are rather low and occur below 1100 cm^{-1} . This makes them rather hard to separate from the many other vibrations that can occur in this region, but comparing the sulfur and selenium analogues the shifts for a given vibration are rather large. Almost all of the shifts to lower energy for selenium substitution can be accounted for by the increase in the molecular weight (34).

From molecular studies and heats of formation, it has been found that the angles become more acute for selenium (approximately 2-5) (7, 14) and that the bonds formed are weaker. These couple to give smaller force constants, but the differences are not nearly as significant as in the increased mass. Table I includes some examples that illustrate this elemental shift.

The substitution of selenium does, however, also affect the symmetric deformation and rocking modes of the alkyl groups next to it (11). Since these vibrations, as well as

Table I.

Infrared Band Comparisons of S and Se (Y = S, Se)

Band	S (cm ⁻¹)	Se (cm ⁻¹)	Compounds
$\nu(\text{Y-H})$	2550-2605	2280-2330	R-Y-H
$\delta(\text{C-Y-H})$	802	712	CH ₃ -Y-H
$\nu(\text{C-H})$	710	590	CH ₃ -Y-H
		550-610	R-Y-R
		530-625	R-YO-R
	660-750	-	R-YO ₂ -R
		507-584	R-Y-R
$\nu(\text{Y-Y})$	505-540	286-293	R-Y-Y-R
$\delta(\text{C-Y-C})$	284	233	CH ₃ -Y-CH ₃
$\nu(\text{C=Y})$	1510	1267	CS ₂ , CSe ₂
	700-800	600-700	Thio- and seleno- amides, ureas
$\nu_{\text{as}}(-\text{CY}_2)^-$	900-1050	800-950	Dithio and diseleno carbamates
$\nu(\text{M-Y})$	300-350	240-270	[M=Pd(II), Pt(II)], [Y=(CH ₃) ₂ S, (CH ₃) ₂ Se]

those due to selenium appear in the same region and are also shifted to lower energies, care must be taken in deciding upon assigning a certain vibration.

Paetzold, et al (16), have pointed out that the intensity of the carbon-selenium stretch is highly dependent upon the formal charge on the selenium so that if there was any attachment of selenium to a metal, large shifts would be expected. This has been observed (17-21) in a few cases.

A further study on the formal charge of the selenium and the effect of metal coordination would be to use ESCA (36). This has been done for a few selenium ligands by Malmuster, et al (22), and due to the larger cross section of selenium than for sulfur (35), more information could be collected more easily and then correlated to electron densities and formal charges (37). Using ESCA to identify the relative oxidation state of the selenium, as well as of the metal, and then comparing these to the intensities, positions, and relative shifts of the infrared absorptions would then lead to a better understanding of the type of bonding interactions.

II. Structure Determination

There has been some structural work done on organo-selenium and organo-sulfur analogues. These crystal structure determinations show that the selenium analogue is generally longer in bond lengths by about 0.13 angstroms (the difference in the covalent radii) and that the bond

angles are more acute by roughly 2-5 degrees (14). A few examples of this are shown in Table II.

Recently, Bobrick, et al (7), have synthesized the selenium analogues of $[\text{Fe}(\text{S})_4(\text{SR})_4]^{2-}$ and determined the crystal structure of $[\text{Fe}(\text{Se})_4(\text{SPh})_4]^{2-}$ and compared it with $[\text{Fe}_4(\text{S})_4(\text{SPh})_4]^{2-}$. These results are shown in Table III. These complexes exhibited a slight lengthening of the Fe-X bond and a decrease in bond angles. Included in Table III are also some more values that show the interchangeability of sulfur and selenium and the minor changes that result.

III. Magnetic Resonance

When applicable, the NMR of selenium compounds is very informative (13). Much work has been done comparing selenium and sulfur organic compounds using proton NMR, and as seen from Table IV, the correlations of the electronegativity with the chemical shift shows their similarity. This is to be expected since the chemical shift is sensitive to the surrounding magnetic and electric fields and, hence, to the nature and the spatial arrangements of the substituents. The coupling constants depend only on the electric fields and so are sensitive to the conformation, the bond angles, the bond lengths and the electronegativity of the substituents.

Since the first three factors have been shown to be pretty much identical, and as it will be shown the electronegativities are nearly identical, the comparison of

Table II.

Selected Bond Lengths

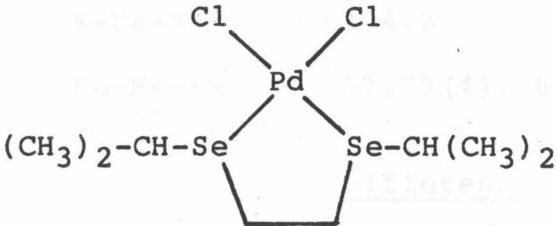
Compound	Y-C (Å)	(C-Se-C) ^o
CH ₃ -Se-CH ₃	1.98±0.1	98±10
CH ₃ -Se-Se-CH ₃	1.953±.005	98±3.5
Se Se	1.99±0.04	98±3.5
	2.04±0.06	
	1.98	98.7±2.2
	2.03±0.5	100.4±2.0
	2.04	
	2.10	
CH ₃ -S-CH ₃	1.81±0.01	

Table III.

A Comparison of $[\text{Fe}_4\text{S}_4(\text{SPh})_4]^{2-}$ vs. $[\text{Fe}_4\text{Se}_4(\text{SPh})_4]^{2-}$

<u>Parameter</u>	$[\text{Fe}_4\text{X}_4(\text{SPh})_4]^{2-}$	
	<u>X = S</u>	<u>X = Se</u>
Fe-S	2.263 Å	2.273 Å
Fe-X	2.267 (4), 2.296 (8)	2.385 (4), 2.417 (8)
Fe···Fe	2.730 (2), 2.739 (4)	2.773 (2), 2.788 (4)
S-Fe-X	115.1°	112.3°
Fe-X-Fe	73.50	70.55
X-Fe-X	104.3	106.4
Fe-Fe-Fe	59.79 (4), 60.11 (8)	59.65 (4), 60.18 (8)
	<u>Difference</u>	
$\text{M}(\text{Y}_2\text{CNET})_2$	0.11 Å	M = Ni, Cu, Zn
$\text{Mo}(\text{Y}_2\text{C}_2\text{R}_2)_3$	0.16	

Table IV.

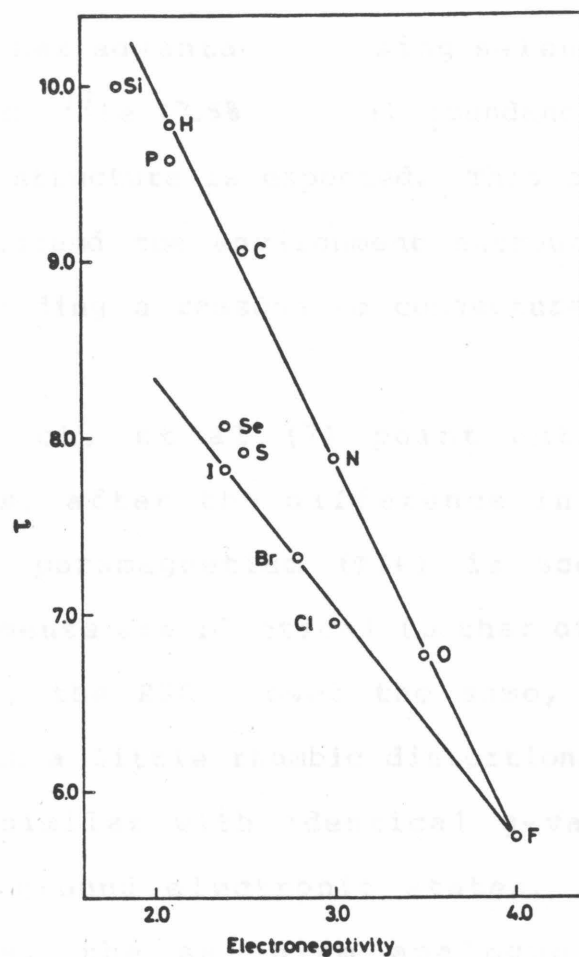


FIG. XVD-2 A plot of proton chemical shifts (τ -values) of compounds (dilute CCl_4 solutions) with the general formula $(\text{CH}_3)_n\text{X}$ vs. Pauling electronegativity of X. The chemical shifts, except for X = Se and P, are from Appendix B of ref. 7. The data for $(\text{CH}_3)_2\text{Se}$ are from the work of Mila and Laurent,¹ and for $(\text{CH}_3)_3\text{P}$ from the work of McCoy and Allred.⁹

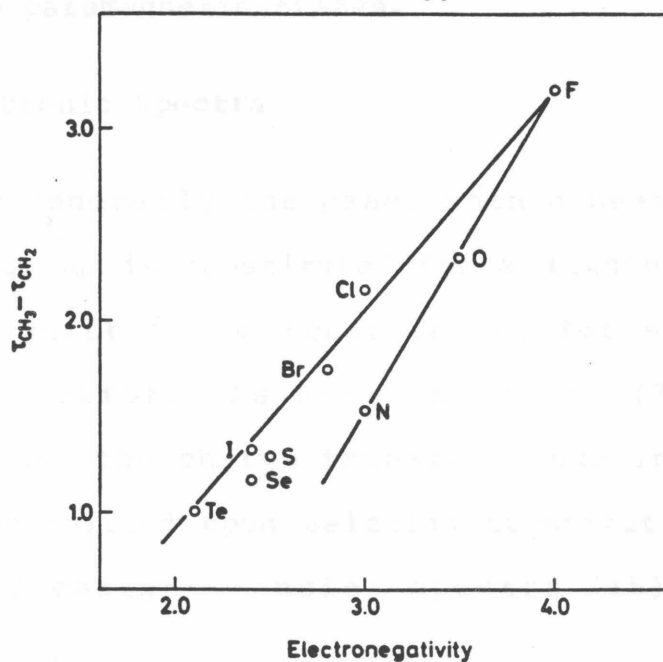


FIG. XVD-3 A plot of the internal chemical shift difference ($\tau_{\text{CH}_3} - \tau_{\text{CH}_2}$) in ethyl derivatives, $(\text{CH}_3\text{CH}_2)_n\text{X}$, vs. Pauling electronegativity of X. The data are from the work of Narasimhan and Rogers,¹⁰ except for X = Se and Te, which are from the work of Breuninger *et al.*¹¹

selenium with sulfur can be made.

One further advantage of using selenium is that one of its isotopes, ^{77}Se (7.5% natural abundance) has $I = 1/2$ and a satellite structure is expected. This can then be used to better understand the environment surrounding the selenium thereby providing a reasonable conjecture as to the sulfur environment.

As Bobrick, et al (7) point out in the seleno-ferrodoxins, after the difference in the temperature independent paramagnetism (TIP) is accounted for, the magnetic moments are identical to that of the ferrodixins. Furthermore, the ESR showed the same, basically axial, spectrum with a little rhombic distortion. The line shapes were very similar with identical g-values; indicating equivalent ground electronic states. Thus, as in the ferrodixins, the selenium analogue leads to anti-ferromagnetic coupling, giving a ground state singlet with low-lying paramagnetic states.

IV. Electronic Spectra

As is generally the case, when a heavier member of a periodic group is substituted for a lighter cogenitor, the spectral shift is to lower energy for selenium when it replaces sulfur. As Bobrick, et al (7) saw in their ferrodoxins, the charge transfer bands in the 300-500 nm region red-shifted upon selenium substitution. Jorgensen's theory of charge transfer spectra (15) using optical

electronegativities and some previous estimates lead to the prediction of (23-25):

$$\Delta E_{CT}(\text{cm}^{-1}) = 30,000 (\text{cm}^{-1}) [\chi_{\text{opt}}(\text{S}) - \chi_{\text{opt}}(\text{Se})] \cong 0.1$$

Using the data obtained for the ferredoxins fixed this value as being even lower; at 0.03-0.04. This further illustrates the near similarity, but distinct differences between selenium and sulfur.

For the particular case at hand, the thio- and seleno-ether complexes, the use of selenium should help red-shift those bands attributed to Cr-S (38) and Co-S (39) that appear in the ultraviolet. It is hoped that these bands will be separated enough from the other large charge transfer bands in that region that could obscure this shift. Another check would be to apply Jorgensens charge transfer theory with the values obtained by Bobrick, et al (7).

One other very useful technique that would be very susceptible to elemental substitution is EXAFS (40). Due to the larger size of the selenium and the accessibility of the K, and L-shell electrons to excitation at low X-ray energies, the double check of the interference pattern of the metal on the selenium, and vice-versa, will help in identifying the environments of these two elements (in solution as well as in the solid state). The low energy flux required for selenium EXAFS also makes it desirable on a practical level, since higher energy X-ray fluxes are hard to come by.

In theory, this could be done for sulfur (41) (and many attempts have been made), but its smaller size makes it a smaller absorber and harder to work with. Also, one of the requirements for the use of EXAFS in determining unknown structures is well characterized crystal structures of compounds with $M-X$, or R_2X-M ($X = S, Se$) formulas. This can generally be accomplished by using dithiocarbamates and the diselenocarbamates with the desired metal to be studied.

V. Electrochemistry

One of the reasons that *tedta* was employed as a ligand for metals was the hope that by utilizing sulfurs adsorptive behavior on mercury, the chelated metal could be observed in different oxidation states (33). Also, it was hoped that by understanding the chemistry of the attached redox couple, it could be used in selective electrode catalysis. In general, the adsorption of selenium should be stronger on mercury than sulfur due to the increased polarizability, and this behavior is observed. Nygard (26-31) has compared quite a few sulfur and selenium analogues and found their electrochemistry to be very similar (including cysteine and cystine). Bobrick, et al (7), also compared the ferredoxin electrochemistry (they used carbon disks in DMF) and found that selenium substitution led to an anodic shift of the redox couple of up to 60 mV. The shapes of the couples remained the same as did their reversibility. Thus, the lower oxidation state is slightly stabilized in the selenium

case, relative to the sulfur, as would be expected for the more polarizable atom.

VI. Conclusion

The ability to synthetically substitute selenium for sulfur has been exhibited many times. The differences that result have been generally characterized and it is proposed that they be utilized to infer the type and the extent of metal-sulfur interactions. Specifically, it would address the problems that have confronted Peerce, et al (33) (Cr), Hodgson (42) (Cu) and Anson (43) (Ru) when utilizing tedta as a chelate. Generally, this could be used for any other metals. Also, selenium substitution can be used in other organo-sulfur ligands. This would especially seem desirable after Stein and Taube's (44) recent hypotheses of through-space interactions between ruthenium and 1, 8-thiocane.

REFERENCES

1. a) L. H. Jensen, Ann. Rev. Biochem. **1974**; b) G. N. Schrauzer, Nat. Eng. **1978**.
2. W. Orme-Johnson, Ann. Rev. Biochem. **1973**, 42, 149; G. Palmer, "The Enzymes," Vol XII, 3rd ed., P. D. Boyer, Ed., Academic Press, New York, N. Y., 1975.
3. C. L. Hill, J. Renaud, R. H. Holm, and L. E. Mortenson, J. Am. Chem. Soc. **1977**, 99, 2549 and the references cited therein.
4. C. A. McAuliffe, J. V. Quagliano, and L. M. Vallarino, Inorg. Chem. **1966**, 5, 1996.
5. P. de Meester, D. J. Hodgson, H. C. Freeman, and C. J. Moore, Inorg. Chem. **1977**, 16, 1494.
6. C. A. McAuliffe and S. G. Murray, Inorg. Chim. Acta Rev. **1972**, 103.
7. M. A. Bobrick, E. J. Laskowski, R. W. Johnson, W. D. Gillium, J. M. Berg, K. O. Hodgson, and R. H. Holm, Inorg. Chem. **1978**, 17, 1402.
8. Y. Sugima, K. Ishizu, T. Kimura, and H. Tanaka, Bioinorg. Chem. **1975**, 4, 291.
9. B. Anderegg, Helv. Chim. Acta **1964**, 47, 1801.
10. H. Kroll, M. A. Lipson, and E. F. Bolton, U.S.A.E.C. Report TID-2271, March 11, 1966

11. K. A. Jensen, L. Henricksen, and P. H. Nielsen, in "Organic Selenium Compounds: Their Chemistry and Biology," L. L. Klayman and W. H. H. Gunther, Ed., Wiley, New York, N. Y. 1973, Chapter XV.
12. J. E. Kuder, ibid.
13. Ulla Svanholm, ibid.
14. I. L. Karle and J. K, ibid.
15. K. A. Jensen and C. K. Jorgensen, ibid., Chapter XVI.
16. R. Paetzold, U. Lindner, G. Bochman, and P. Reigh, Z. Anorg. Alleg. Cheml **1967**, 352, 295, 305.
17. P. J. Hendra and N. Sudasivan, Spectrochim. Acta **1965**, 21, 1127.
18. J. R. Alkins and P. J. Hendra, J. Chem. Soc. A **1965**, 1325.
19. N. N. Greenwood and G. Hunter, J. Chem. Soc. A **1967**, 1520.
20. N. N. Greenwood and G. Hunter, J. Chem. Soc. A **1969**, 929.
21. D. C. Goodall, J. Chem. Soc. A **1968**, 887.
22. G. Mamuster, I. Thoren, S. Hogberg, J. E. Bergmark, S. E. Karlsson, and E. Regane, Phys. Scr. **1971**, 3, 96.
23. C. Furlani, E. Cervone, F. D. Camassei, Inorg. Chem. **1968**, 7, 265.
24. K. A. Jensen, V. Krishnan, and C. D. Jorgensen, Acta Chem. Scand. Chem. **1970**, 24, 743.

25. R. Heber, R. Kirmse, and E. Hoter, Z. Anorg. Allg. Chem. **1972**, 393, 159.
26. B. Nygard, J. Olofsson and G. Bergson. Ark. Kemi **1967**, 393, 159.
27. B. Nygard, Acta Chem. Scand. **1966**, 20, 1710.
28. B. Nygard, Ark. Kemi **1967**, 27, 405.
29. B. Nygard, Ark. Kemi **1967**, 27, 341.
30. B. Nygard, Ark. Kemi **1967**, 27, 325.
31. B. Nygard, Acta Chem. Scand. **1967**, 15, 1039.
32. D. D. Smolin, L. M. Kaybitnaya and Y. Victovov, J. Gen. Chem. USSR **1964**, 34, 3762.
33. P. Peerce, H. B. Gray and F. C. Anson, submitted for publication.
34. See Table I.
35. S. A. Best, P. Brant, R. D. Feltham, T. B. Rauchfuss, D. M. Roundhill and R. A. Walton, Inorg. Chem. **1967**.
36. K. Siegbahn, C. Nordling, A. Fahlman, R. Norberg, K Hamrin, J. Hedman, G. Johansson, T. Bergmark, S. E. Karlsson, J. Lindgren and B. Lindberg, "ESCA Atomic Molecular and Solid State Structure Studies by Means of Electron Spectroscopy," Almquist and Wiksells AB, Stockholm, 1967.
37. F. N. Hendrickson, J. M. Hollander and W. L. Jolly, Inorg. Chem. **1970**, 9, 612.
38. G. J. Kennard and E. Deutsch, Inorg. Chem. **1978**, 17, 2225.

39. K. Yamanair, J. Hidaka and Y. Shimura, Bull. Chem. Soc. Jap. **1977**, 50, 2643.
40. P. Eisenberger and B. M. Kincaid, Science **1978**, 200, 1441.
41. S. P. Cramer, K. O. Hodgson, E. I. Stiefel and W. E. Newton, J. Am. Chem. Soc. **1978**, 100, 2748.
42. Private communication.
43. Private discussions.
44. C. Stein and H. Taube, J. Am. Chem. Soc. **1978**, 100, 1635.

Proposition 5

It is proposed that a study of the interaction between $[\text{Ru}(\text{edta})(\text{OH}_2)]$ and sulfur-containing compounds be investigated by spectroscopic and electrochemical techniques. In particular, the reactions between thioethers, thiolates, and sulfides will be studied and compared with the vast amount of information available on Ru-ammine complexes and their reactions with sulfur-containing compounds.

Many sulfur containing metal ion compounds, including some simple structural analogues of the active sites of sulfur containing enzymes, have been synthesized and characterized, but there have been relatively few studies concerning the reactivity of metal ion-sulfur bonds (1,2). A systematic study that utilized simple ligands containing sulfur in various oxidation states and their affinity for, and reactivity with $[\text{Ru}(\text{III})(\text{edta})(\text{OH}_2)]^{-/2-}$ is proposed as a way of further understanding metal ion-sulfur interactions. The ligands will include R_2S , HSR , H_2S , RS^- , HS^- , RSSR (where R is a hydrocarbon), methionine and cysteine. The effects of saturation, unsaturation and chelating moieties in R upon the reactivity of the sulfur and $[\text{Ru}(\text{edta})(\text{OH}_2)]^{-/2-}$ will also be explored.

The choice of $[\text{Ru}(\text{edta})(\text{OH}_2)]$ is based upon many

factors. The integrity of the penta-coordinate edta as the formal oxidation state varies from Ru(II) to Ru(IV) is maintained. The substitution inertia of Ru(II) and Ru(III) are such that substituted species, Ru(edta)L , may be generated, allowing the role of the metal oxidation state to be systematically explored. Comparison of the properties of the edta system with the ammine, bipyridine and aquo systems will also be made to gain some insight into the role the sulfur ligands play in the reactivity and the properties of the metal center.

It has been shown that the rate constants for the substitution reactions of $[\text{Ru(edta)(OH}_2)]^-$ can be up to 10 orders of magnitude greater than for other Ru(III) complexes containing oxygen and nitrogen donor atoms (4). In contrast to the $[\text{Ru(NH}_3)_5\text{OH}_2]^{3+}$ and $[\text{Ru(bipy)}_2(\text{OH}_2)]^{3+}$ systems, $[\text{Ru(edta)(OH}_2)]^-$ substitution reactions proceed by an associative rather than a dissociative mechanism (3, 4). This difference has been ascribed to steric effects (large negative entropies of activation for the edta system) and to hydrogen bonding between the unprotonated, dangling carboxylate of the edta and the coordinated water (4). The latter effect assists in removing the water from the ruthenium, while the crowded 7-coordinate intermediate is sensitive to the nature of the incoming ligand (4). If water is not the entering, or the leaving ligand, or if the dangling carboxylate is protonated, then a dissociative mechanism is observed to be operative and the enhanced

lability is diminished and comparable to the ammine system. For all of the systems, the Ru(II) form appears to proceed via a dissociative pathway with the substitution rate of the edta system being up to 100 times faster than for the ammine system. This is most likely due to the lower effective charge on the ruthenium in the edta system (4).

In contrast to the edta complexes of some first row transition series M(II)/M(III) couples (for V, Cr, and Fe), where the M(III) center is stabilized strongly over M(II), and, where M(II)(edta) complexes are very much stronger reducing agents (by 0.5-1.0 V) than their aquo counterparts, the Ru(III)/Ru(II) couple is not very different ($[\text{Ru}(\text{OH}_2)]^{3+/2+}$, 0.22 V; $[\text{Ru}(\text{edta})(\text{OH}_2)]^{-/2-}$, 0.05 V) (4, 5). Furthermore, the Ru(IV) state is also accessible without any major ligand reorganization (5). Two electron per ruthenium redox reactions now become a possibility, thereby overcoming the difficulty of bringing two, one-electron redox centers to the reactive site.

Some preliminary studies with various sulfur containing ligands have shown that $[\text{Ru}(\text{edta})(\text{OH}_2)]^{2-}$ behaves quite similarly to $[\text{Ru}(\text{NH}_3)_5(\text{OH}_2)]^{2+}$ in ligand affinity, and rates of substitution (7-9), but that $[\text{Ru}(\text{edta})(\text{OH}_2)]^{-}$ exhibits an enhanced reactivity and affinity for thioether ligands. In contrast with the Ru(III) ammines (8-10), dimethyl sulfide and 2, 2'-thiodiethanol spontaneously bind $[\text{Ru}(\text{edta})(\text{OH}_2)]^{-}$. Titrating $[\text{Ru}(\text{edta})(\text{OH}_2)]^{-}$ with 2, 2'-thiodiethanol (TDE), spectrophotometric and electrochemical measurements yielded

an affinity of 500 M^{-1} . In comparison, the affinity of $(\text{CH}_3)_2\text{S}$ for $\text{Ru}(\text{NH}_3)_5(\text{OH}_2)^{3+}$ was calculated to be $\sim 10^{-2} \text{ M}^{-1}$ (10) and was not observed to coordinate spontaneously ($k \cong 10^{-9} \text{ M}^{-1} \text{ sec}^{-1}$) (7). $[\text{Ru}(\text{NH}_3)_5\text{S}(\text{CH}_3)_2]^{3+}$ was obtained by first substituting the thioether onto $[\text{Ru}(\text{II})(\text{NH}_3)_5(\text{OH}_2)]^{2+}$ and then oxidizing $[\text{Ru}(\text{NH}_3)_5\text{S}(\text{CH}_3)_2]^{2+}$. The aquation of $[\text{Ru}(\text{NH}_3)_5\text{S}(\text{CH}_3)_2]^{3+}$ was observed to be $4.2 \times 10^{-9} \text{ sec}^{-1}$. In stark contrast, $[\text{Ru}(\text{edta})(\text{TDE})]^-$ aquated spontaneously upon dilution to produce $[\text{Ru}(\text{edta})(\text{OH}_2)]^-$, as monitored spectrally. The appearance of an isosbestic point at the same position as that observed during the substitution reaction indicates that the reaction only involves the substituted and the aquated forms of $\text{Ru}(\text{edta})$. Similar results were observed with dimethyl sulfide and $[\text{Ru}(\text{edta})(\text{OH}_2)]^-$. The different visible spectra for the coordinated thioethers of the edta and ammine systems raises the question of the manner of the $\text{Ru}(\text{III})\text{-SR}_2$ interaction and further investigations are warranted to systematize the effect of the auxiliary ligands on this interaction.

Comparing the pKa of coordinated SH_2 vs. OH_2 , it is seen that $[\text{Ru}(\text{edta})(\text{OH}_2)]^{3+}$ is a weaker sigma acid than $[\text{Ru}(\text{NH}_3)(\text{OH}_2)]^{3+}$ (7.6 vs. 4.0, respectively). Considering that SR_2 is a poorer sigma base than H_2O , the difference in affinity of $\text{Ru}(\text{III})(\text{edta})$ and $\text{Ru}(\text{III})(\text{NH}_3)_5$ ($=10^{-4}$) for thioethers seems reasonable.

The shift in redox potential upon thioether coordination to $[\text{Ru}(\text{edta})(\text{OH}_2)]^{-/2-}$ (-0.05 V vs. SCE from -0.22 V vs.

SCE) yields a calculated affinity of $3 \times 10^5 \text{ M}^{-1}$ for Ru(II). This value is comparable to the value obtained for thioether coordination to $[\text{Ru}(\text{NH}_3)_5(\text{OH}_2)]^{2+}$ of $\geq 1 \times 10^5 \text{ M}^{-1}$. Back-bonding effects still appear to dominate the reactivity of Ru(II) and thioethers.

To constrain the thioether moiety to be near the ruthenium, whether it is coordinated, or not, an edta analogue, tedta, that incorporates, $-\text{CH}_2-\text{S}-\text{CH}_2-$, symmetrically into the ethylenediammine backbone of edta was reacted with K_2RuCl_5 yielding an emerald-green complex, which was isolated as an amorphous solid (9). Its color, infrared spectrum and electrochemistry, however, have little in common with $[\text{Ru}(\text{edta})(\text{OH}_2)]^-$, or $[\text{Ru}(\text{edta})(\text{SR}_2)]^-$.

The cyclic voltammetry of Ru(tedta) produced very small currents relative to an equimolar concentration of $[\text{Ru}(\text{edta})(\text{OH}_2)]^-$, which has a reduction potential which is 200 mV negative of the $[\text{Ru}(\text{edta})(\text{SR}_2)]^{-/2-}$ couple. A catalytic dioxygen evolution wave similar to that for the oxidized, mixed-valence dimer of $[\text{Ru}(\text{edta})(\text{OH}_2)]^-$ was, however, observed (5). The actual structure of Ru(tedta) has yet to be determined, but the possibility of using a coordinated sulfur as a means of modifying the redox and catalytic behavior of ruthenium is suggestive.

Ru(tedta) was also observed to decompose very slowly in aqueous acid (months) yielding a brownish solution with the eventual appearance of a light colored precipitate. An interesting result when SH_2 is bubbled through a

$[\text{Ru}(\text{II})(\text{edta})(\text{OH}_2)]^{2-}$ solution has some bearing on the Ru(tedta) system. A visible spectrum different than $[\text{Ru}(\text{NH}_3)_5(\text{SH}_2)]^{2+}$ is observed when dimethyl sulfide is bubbled through the reduced Ru(edta) solution which then turns emerald-green upon air oxidation. The resulting complex then further reacts slowly (days) producing a brownish-orange solution similar to the final product observed for Ru(tedta) upon standing. These various complexes need to be isolated and then characterized to better understand the ruthenium-thioether interaction.

Other reactions of coordinated sulfur ligands will also be investigated. Coordinated thiolates are capable of being methylated, or dimerized to yield disulfides in simple metal-ion sulfur systems (1, 7) and enzymatically in the body (6), while thioethers can be oxidized to produce sulfoxides (1). These investigations may also shed some light on the unusual characteristics of Ru(tedta).

Some further observations present more questions concerning the nature of the Ru-S bond. Creutz has observed the coordination of thiocyanate to $[\text{Ru}(\text{edta})(\text{OH}_2)]^-$ (3, 4). By analogy to $[\text{Ru}(\text{NH}_3)(\text{OH}_2)]^{3+}$, the thiocyanate was assumed to be nitrogen bound. Adsorption experiments on mercury have shown the $[\text{Ru}(\text{edta})(\text{thiocyanate})]^{2-}$ complex to be adsorbed very much less than the ammine analogue (11). This is difficult to explain based on the charge difference of the two ions and implies that thiocyanate is sulfur bound to the ruthenium. This would explain the decreased adsorption

on mercury, since the uncoordinated nitrogen is known to be adsorbed poorly. Furthermore, a solution of $[\text{Ru}(\text{edta})(\text{OH}_2)]^-$ was titrated with $[\text{Cr}(\text{NCS})_6]^{3-}$ (which is known to be substitution inert with the nitrogen bound to the chromium), whereupon, a new spectrum was observed in the visible region indicating the existence of a bridged dimer with the sulfur bound to the ruthenium (9).

The possibility of building bridged metal systems utilizing the affinity of sulfur for ruthenium would enable the study of electron transfer rates and mechanism. Symmetrically and unsymmetrically bridged systems utilizing the $\text{Ru}(\text{edta})$ and $\text{Ru}(\text{NH}_3)_5$ ions could possibly be synthesized to study the effects of metal and sulfur electronic configurations, geometry and distance on inter- and intramolecular, and through-space charge transfer. The wealth of information available on $[\text{Ru}(\text{NH}_3)_5(\text{SR}_2)]^{2+/3+}$ and ruthenium ammine dithioethers (8, 12), as well as many other first and second row metal ion-sulfur complexes (1), will provide a basis for comparisons and understanding.

The understanding of the bonding and reactivity between metals and sulfur is still in its infancy. The role that sulfur plays in influencing and mediating electron transfer has only begun to be explored. This study will provide some insight into the ubiquitous nature of metal ion-sulfur interactions.

REFERENCES

1. C. G. Kuehn and S. S. Isied, Prog. in Inorg. Chem. **1980**, V27, S. Lippard (ed.), John Wiley and Sons, N. Y. , p. 153 and the references therein.
2. W. Stumm and J. J. Morgan, Aquatic Chemistry, 2^d ed., John Wiley and Sons, N. Y., 1981.
3. T. Matsubara and C. Creutz, J. Am. Chem. Soc. **1978**, 100, 6255.
4. T. Matsubara and C. Creutz, Inorg. Chem., **1979**, 18, 1956.
5. R. Baar thesis, California Institute of Technology, Pasadena, Ca., 1983.
6. L. Stryer, Biochemistry, W. H. Freeman and Co., San Francisco, 1975.
7. C. A. Stein and H. Taube, Inor. Chem. **1979**, 18, 2212.
8. C. Stein thesis, Stanford University, 1978.
9. Personal observations
10. C. G. Kuehn and H. Taube, J. Am. Chem. Soc. **1976**, 98, 689.
11. S. Gonzalez and F. Anson, J. Electroanal. Chem., in press.
12. C. A. Stein and H. Taube, J. Am. Chem. Soc. **1978**, 100, 1635.